DNA Nanostructures as Programmable Biomolecular Scaffolds for Enzymatic Systems

by

Yuhe Renee Yang

A Dissertation Presented in Partial Fulfillment
of the Requirements for the Degree
Doctor of Philosophy

Approved April 2016 by the
Graduate Supervisory Committee:

Hao Yan, Co-chair
Yan Liu, Co-chair
Julian Chen
Mark Hayes

ARIZONA STATE UNIVERSITY

May 2016

ABSTRACT

Nature is a master at organizing biomolecules in all intracellular processes, and researchers have conducted extensive research to understand the way enzymes interact with each other through spatial and orientation positioning, substrate channeling, compartmentalization, and more.

DNA nanostructures of high programmability and complexity provide excellent scaffolds to arrange multiple molecular/macromolecular components at nanometer scale to construct interactive biomolecular complexes and networks. Due to the sequence specificity at different positions of the DNA origami nanostructures, spatially addressable molecular pegboard with a resolution of several nm (less than 10 nm) can be achieved. So far, DNA nanostructures can be used to build nanodevices ranging from in vitro small molecule biosensing to sophisticated in vivo therapeutic drug delivery systems and multi-enzyme networks.

This thesis focuses on how to use DNA nanostructures as programmable biomolecular scaffolds to arranges enzymatic systems. Presented here are a series of studies toward this goal. First, we survey approaches used to generate protein-DNA conjugates and the use of structural DNA nanotechnology to engineer rationally designed nanostructures. Second, novel strategies for positioning enzymes on DNA nanoscaffolds has been developed and optimized, including site-specific/ non site-specific protein-DNA conjugation, purification and characterization. Third, an artificial swinging arm enzyme-DNA complex has been developed to mimic substrate channeling process. Finally, we extended to build a artificial 2D multi-enzyme network.

DEDICATION

First of all, I would like to thank my parents. For leading by example and providing me a loving home from my birth to now. My dad has set a great sample as a scientist and led me to the beauty chemistry world since I was a child. On the other hand, I want to thank my mom for not giving me any pressure in school work but let me learn other interesting things such as piano, dancing, singing, etc. I really appreciate their trust in me and their endless love.

I want to acknowledge my mentors, Dr. Hao Yan and Dr. Yan Liu. Their passion, dedication, and incredible drive are truly inspirational. Not only giving me professional guidance in science, I am also grateful for the trust they have in me, leaving me the room and giving me opportunities to think and work independently. I am also grateful to the members of my committee, Dr. Julian Chen, Dr. Mark Hayes, and Dr. Neal Woodbury, for their time and guidance. I also want to acknowledge Dr. Jinglin Fu for collaborating with me and guiding me in my first and second year as graduate student. Finally, I want to thank all the past and present graduate students, postdocs, and lab researchers who I have interacted with along the way. Their advice and support have been instrumental to my success.

ACKNOWLEDGMENTS

First of all, I would like to thank my parents. For leading by example and providing me a loving home from my birth to now. My dad has set a great sample as a scientist and led me to the beauty chemistry world since I was a child. On the other hand, I want to thank my mom for not giving me any pressure in school work but let me learn other interesting things such as piano, dancing, singing, etc. I really appreciate their trust in me and endless love.

I want to acknowledge my mentors, Dr. Hao Yan and Dr. Yan Liu. Their passion, dedication, and incredible drive are truly inspirational. Not only giving me professional guidance in science, I am also grateful for the trust they have in me, leaving me the room and giving me opportunities to think and work independently. I am also grateful to the members of my committee, Dr. Julian Chen, Dr. Mark Hayes, and Dr. Neal Woodbury, for their time and guidance. I also want to acknowledge Dr. Jinglin Fu for collaborating with me and guiding me in my first and second year as graduate student. Finally, I want to thank all the past and present graduate students, postdocs, and lab researchers who I have interacted with along the way. Their advice and support have been instrumental to my success.

TABLE OF CONTENTS

Page

LIST OF TABLES

Table Page

LIST OF FIGURES

Figure Page

Figure Page

LIST OF SCHEMES

Scheme Page

CHAPTER 1

DNA NANOSTRUCTURES AS PROGRAMMABLE BIOMOLECULAR SCAFFOLDS

Adapted with permission from Yuhe R. Yang, Yan Liu, and Hao Yan. **DNA Nanostructures as Programmable Biomolecular Scaffolds.** *Bioconjugate Chemistry* **2015** *26* (8), 1381-1395. Copyright 2015 American Chemical Society.

Abstract

This chapter focuses on how to use DNA nanostructures as scaffolds to organize biological molecules. First, we introduce the use of structural DNA nanotechnology to engineer rationally designed nanostructures. Second, we survey approaches used to generate protein-DNA conjugates. Third, we discuss studies exploring DNA scaffolds to create DNA nanodevices to analyze protein structures, to engineer enzyme pathways, to create artificial light-harvesting systems, and to generate nanomachines in vitro and in vivo. Future challenges and perspectives of using DNA nanostructures as programmable biomolecular scaffolds are addressed at the end.

1.1. Introduction

1.1.1. DNA nanotechnology

B-form double-stranded (ds) DNA has a well-defined structure with a helical repeat of 3.4 nm and diameter of 2 nm. Other than the simple dsDNA helices, more complex structures are realized by rational design of immobile Holliday Junctions, which was first brought up by Seeman[1]. Numerous kinds of DNA nanostructures have subsequently been developed, including double-crossover (DX) DNA tiles[2], triple-crossover (TX) tiles[3], 4×4 tiles[4], and three-point-star tiles[5], etc. The complexity of DNA nanostructures have increased even further by connecting DNA tiles in different ways using sticky ends, resulting in unique higher order nanostructures such as 2D lattices[4,6-8], nanotubes[9,10], and more complicated 3D structures such as polyhedra[5,11-13] and crystals formed by tensegrity triangle DNA tiles[14] (**Figure 1.1A**).

Scaffolded DNA origami was developed to construct spatially addressable, finite sized DNA nanostructures[15]. In this method, a long circular single stranded genome DNA was used as a scaffold to fold into various geometrical shapes with the help of hundreds of short oligonucleotides serving as 'staples' strands. With this technique, arbitrary shaped 2D nanostructures can be constructed with high yield. DNA origami technique was further developed to design[16] and create compact 3D DNA nanostructures[17-20] and elaborate architectures with complex curvatures[21] and gridiron like structures[22] (**Figure 1.1B**). As the complexity of DNA nanostructures increases, methods need to be exploited[23-27] to reveal their finer structural details.

More recently, a scaffold-free assembly strategy called single-stranded DNA tiles (SST) was developed by the Yin group[28] (**Figure 1.1C**). In this case, ssDNA was used as bricks to assemble or engrave into different shaped nanostructures. This method has also been employed to grow DNA lattices with controlled depth[29] (**Figure 1.1D**).

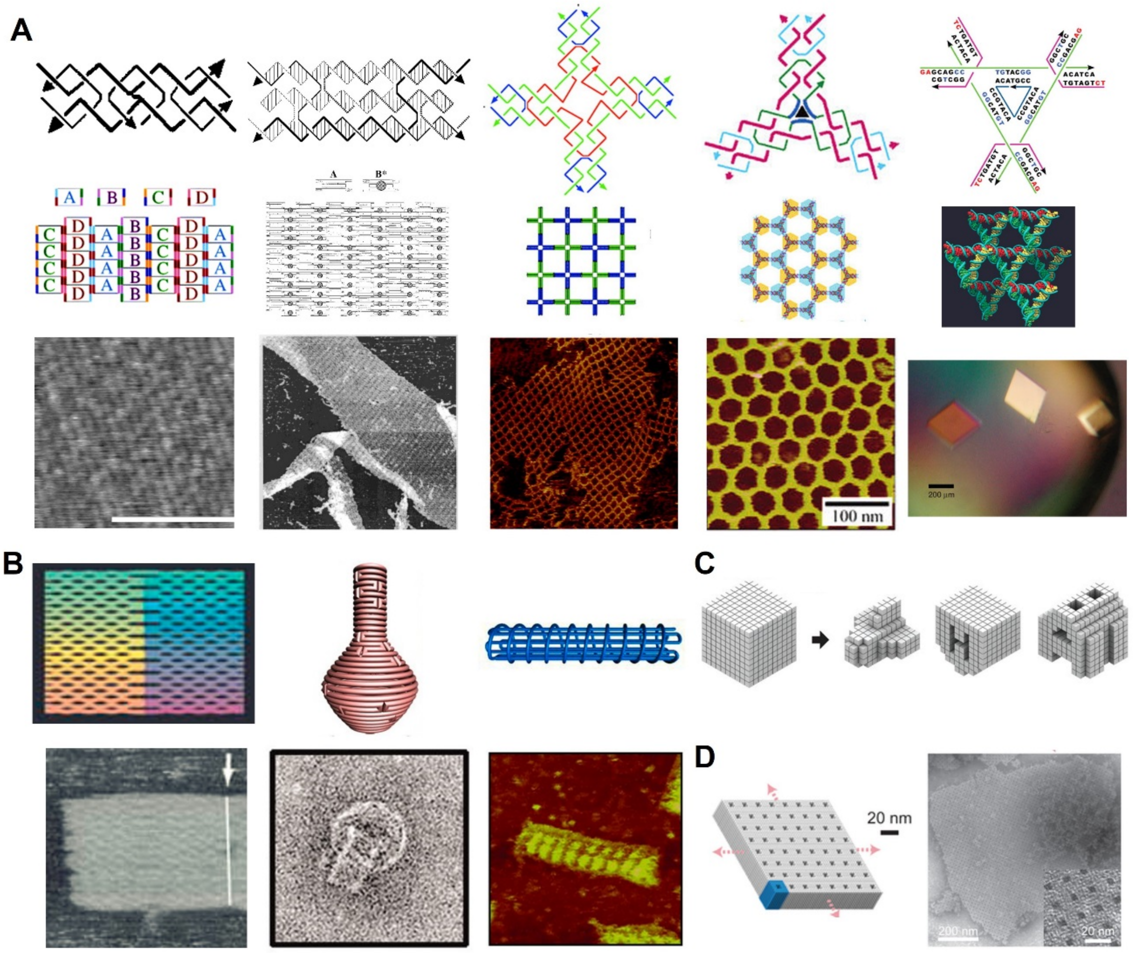

Figure 1.1. Examples of rationally designed DNA nanostructures. (A) DNA tile based periodic 2D lattices and 3D crystal (top, structures of motifs; middle, cartoon of 2D and 3D assembly patterns; bottom, AFM images of 2D lattices and optical image of 3D crystal). The building blocks (from left to right) include double-crossover (DX) DNA tile[2], triple-crossover (TX) tile[3], 4×4 tile[4], three-point-star tile[5], and tensegrity triangle tile[14]. **(B)** Schematics (top) and AFM /TEM images (bottom) of DNA origami nanostructures in 2D and 3D shapes, including (from left to right) a 2D rectangular DNA origami[15], a 3D DNA nanoflask structure with complex curvature[21], and a 3D screw like DNA gridiron

structure[22]. **(C)** Schematics of multiple single-stranded tile based 3D structures engraved from a cube[28]. **(D)** Schematics (left) and TEM images (right) of single-stranded tile based 2D crystals with controlled depth[29]. Images reproduced with permission: (A) left to right: ref 2, copyright (2003) Nature publishing group; ref 3, copyright (2000) American Chemical Society; ref 4, copyright (2003) American Association for the Advancement of Science; ref 5, copyright (2008) Nature publishing group; ref 14, copyright (2009) Nature publishing group; (B) left to right: ref 15, copyright (2006) Nature publishing group; ref 21, copyright (2011) American Association for the Advancement of Science; ref 22, copyright (2013) American Association for the Advancement of Science; (C) ref 28, copyright (2012) American Association for the Advancement of Science; (D) ref 29, copyright (2014) Nature publishing group.

1.1.2. DNA nanostructure as biomolecular scaffolds

Nature is a master at organizing biomolecules in all intracellular processes, and researchers have conducted extensive research to understand the way enzymes interact with each other through spatial and orientation positioning, substrate channeling, compartmentalization, and more.

DNA nanostructures of high programmability and complexity provide excellent scaffolds to arrange multiple molecular/macromolecular components at nanometer scale to construct interactive biomolecular complexes and networks. Due to the sequence specificity at different positions of the DNA origami nanostructures, spatially addressable molecular pegboard with a resolution of several nm (less than 10 nm) can be achieved. Peptides[30] and proteins[31] can be ordered with well controlled inter-molecular distances and relative ratios.

So far, scientists have studied distance-dependent molecular interactions, substrate channeling, and compartmentalization effects using DNA nanostructures as structural templates. DNA nanostructures can be used to build nanodevices ranging from *in vitro* small molecule biosensing to sophisticated *in vivo* therapeutic drug delivery systems and multi-enzyme networks.

1.2. Protein-DNA conjugation method

1.2.1. Introduction

The first technical challenge of building enzyme-DNA complexes is developing conjugation methods to link protein-of-interest and synthetic oligonucleotides. Because DNA molecules themselves display limited chemical functionality, scientists have developed different kinds of biomolecule-DNA coupling methods. The facile chemical modification of nucleic acids with various functional groups on ends or phosphate backbones enables functionalization of DNA nanostructures. Single-stranded DNA is easily functionalized, and oligonucleotides are normally stable during the organic synthesis process[32]. Most of the derivatives can be prepared by automated solid-phase synthesis and are commercially available. Functional groups include amine, thiol, azide, etc.

In contrast, protein modification requires more caution. All reactions have to be done in mild conditions so that the enzymes remain active, especially for functional proteins. Numerous methods for protein-DNA conjugation have been explored, including non-covalent/ covalent and non-site-specific / site-specific methods[33-35]. Each method has different advantages and disadvantages, so the choice depends on the applications. For more general conjugation methods that don’t require protein engineering, control of the conjugation site and stoichiometry is challenging. This is due to multiple lysine and cysteine residues displayed on the protein surface. In contrast, methods involving protein engineering provide site-specificity and exact stoichiometry, while protein engineering could be problematic and sometimes not successful due to insolubility or misfolding of the engineered protein. Here we categorize protein-DNA conjugation approaches into three groups: non-covalent binding, covalent binding without protein engineering (non-site specific), and covalent binding with protein engineering (site-specific).

1.2.2 Non-covalent site-specific conjugation method

1.2.2.1 Affinity tags

The most predominantly studied method for coupling proteins and DNA are through the non-covalent streptavidin (STV)-biotin interactions[36,37]. This is a convenient method because biotinylated oligonucleotides can be made by automated solid-phase synthesis and are commercially available, and STV-protein fusion can be obtained by protein engineering methods. Biotin-streptavidin binding also happens at mild conditions with very high affinity. The difficulty of controlling stoichiometry of DNA and protein can be overcome by an engineered monomeric avidin instead of the traditional tetrameric STV[38] (**Scheme 1.1A**).

Other Ligand-protein binding methods that are commonly used include NTA-Ni^{2+}-Histag, aptamer-protein binding, and antigen-antibody binding. One of which hexahistidine peptide (His_6) binds with nitrilotriacetic acid (NTA) ligand through nickel (II) ion[39] (**Scheme 1.1B**). Oligohistidine tags are commonly fused with proteins on N or C terminus using a nickel column for purification purposes[40-42]. One, two or three NTA ligand-modified ssDNA are prepared with different dissociation constants (kD)[43], and kD decreased from 120 nM to 6 nM between bis- and trisNTA–DNA and His$_6$-tagged GFP. Another advantage of this method is the reversibility of ion induced binding, which can be released by chelators, such as ethylenediaminetetraacetate (EDTA). Alternatively, a recent study using cobalt (III) as mediator ion achieved inert binding[44]. More specific aptamer-protein binding has been popular mainly because of convenience that the ligand is formed by nucleic acid itself so no chemical modification is needed (**Scheme 1.1C**). Binding affinity has been improved by assembling multivalent ligands with careful distance control on DNA nanostructures[45], which has allowed this technique to be used to build spatially addressable multiprotein nanoarrays.[46] In addition to aptamer-protein binding, another method with high specificity and affinity is antigen-antibody binding[47] (**Scheme 1.1D**), which has been used to immobilize antibodies on a DNA scaffold. A 2D antibody array has been built with Fluorescene-IgG interaction[48]. By modifying two antibodies in close proximity to one antibody, uniform orientation and high density (~20 nm) nanoarrays was achieved, compared to the traditional solid-surface immobilization method.

1.2.2.2 Apoenzymes reconstitution

For enzymes that have non-diffusible organic cofactors, an apo-enzyme reconstitution method has been a convenient way to generate protein-DNA conjugates[49]. The principle is straightforward (**Scheme 1.1E**): (1) extract the cofactor from the active enzyme, leading to an inactive apo-enzyme, (2) conjugate the cofactor with DNA, (3) reinsert DNA-cofactor into the apo-enzyme and achieve the active DNA-cofactor-enzyme conjugates. The enzyme activity is tuned with the DNA modified cofactor compared to wild type cofactors.

Among the cofactors, porphyrin and flavin derivatives have been studied intensively, including heme-apo-myoglobin[50,51], apo-HRP[52], and flavin-apo-flavin reductase[53]. The unique activation and inactivation properties expand the conjugation method with switchable properties for target DNA detection[53] and tuning of enzyme activities[54]. The chemically modified cofactor may interfere with enzyme activity.

1.2.2.3 Domain interactions: DNA-binding protein

Among a large number of DNA binding proteins, zinc-finger proteins (Zif) are one of the best characterized classes[55]. The zinc-finger protein has a DNA binding domain which binds a dsDNA region with specific sequences (~10 bp) with nanomolar affinity[56] (**Scheme 1.1F**). This technique requires protein engineering to fuse the DNA binding domain with the enzyme of interest. With a variety of Zif that recognize different sequences, this method has been used to target multiple proteins to specific locations on DNA origami nanostructures[56].

1.2.3. Covalent non site-specific conjugation method

Covalent protein-DNA conjugation methods are used to circumvent obstacles which result from dissociation of non-covalent, reversible interactions. A general method of wild type protein and DNA conjugation is achieved by a heterobifunctional crosslinkers. For the most commonly used Maleimide and N-hydroxysuccinimide (NHS) ester–derived crosslinkers, one end of the linker was covalently attached to the lysine side chains and the other maleimide-functionalized end was subsequently coupled to thiolated DNA strands[57]

(**Scheme 1.2**). N-Succinimidyl 3-(2-pyridyldithio)-propionate (SPDP) and Sulfo-Succinimidyl-4-(N-maleimidomethyl)cyclohexane-1-carboxylate (Sulfo-SMCC)[58] are commercial available crosslinkers, and the reaction procedures are mild and only take a few hours. This method only requires surface lysine residues and does not require protein engineering. Other than lysine, another crosslinker: dithiodipyridine reacts with the surface cystine and further link to thio-modified ssDNA[59]. This not only saves time, but also avoids the problem caused by fusion, i.e. protein may become insoluble after it is fused with tag.

DNA can be modified on any protein that has lysine/cysteine on its surface. One problem with this method is that the stoichiometric control is limited. An average of DNA labeling stoichiometry can be controlled by titrating the amount of crosslinkers, and the reaction yield relies on the number of lysines exposed on the protein surface. It requires an additional purification step to get the specific labeling ratio. It is hard to control the exact conjugation site, which can cause difficulty if the lysine is close to the active site, and enzymatic activity can be highly reduced (or altered) after modification. The alteration of enzyme activity depends on the nature of the protein of interest and it is difficult to avoid this problem.

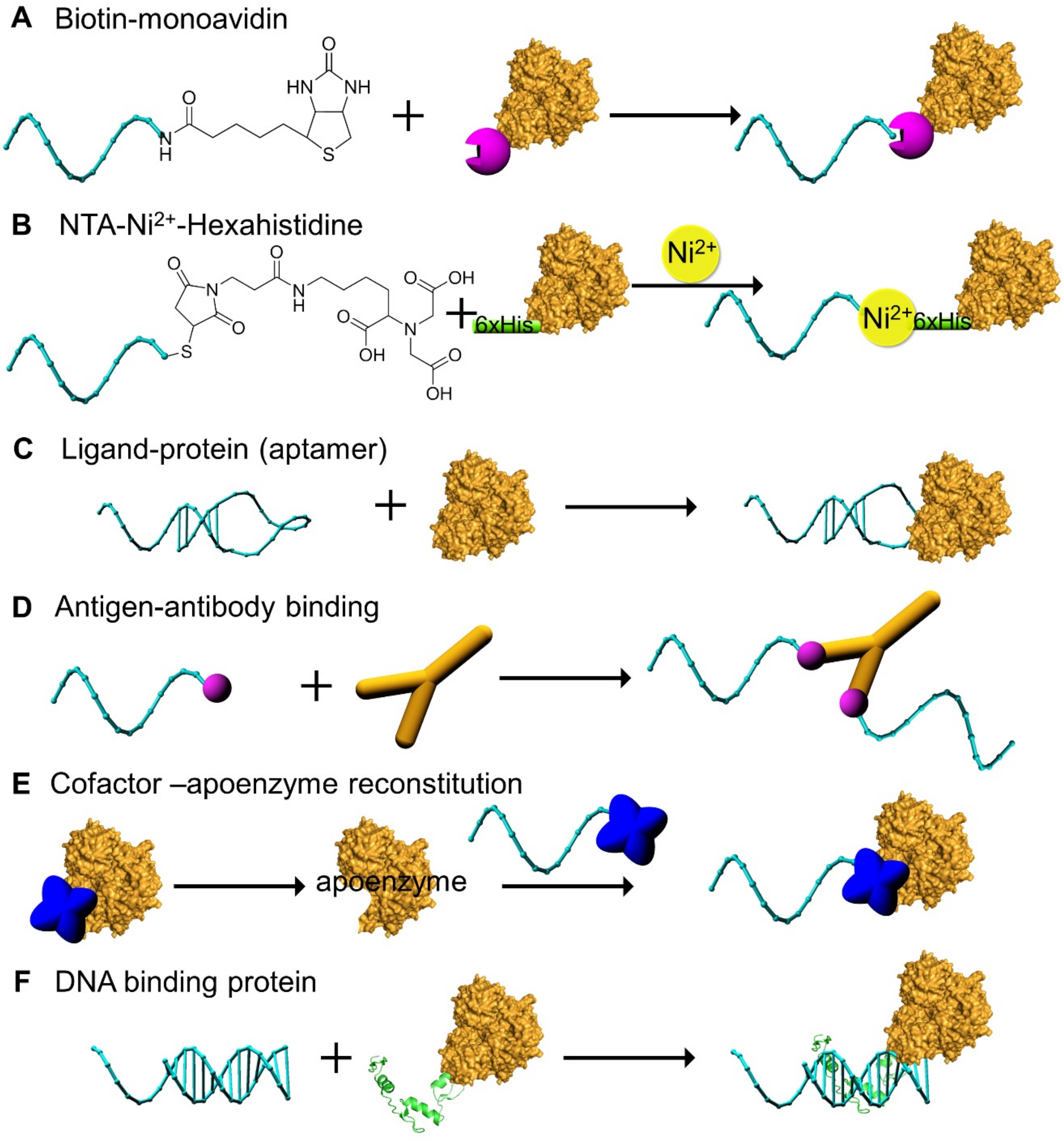

Scheme 1.1. Representative non-covalent protein-DNA conjugation methods through **(A)** biotin-monoavidin binding[38], **(B)** NTA-Ni^{2+}-Hexahistidine binding[39], **(C)** Ligand-protein binding (aptamer based)[45], **(D)** Antigen-antibody binding[47], **(E)** DNA-cofactor-apoenzyme reconstitution[49], and **(F)** DNA binding protein (Zinc finger protein)[55].

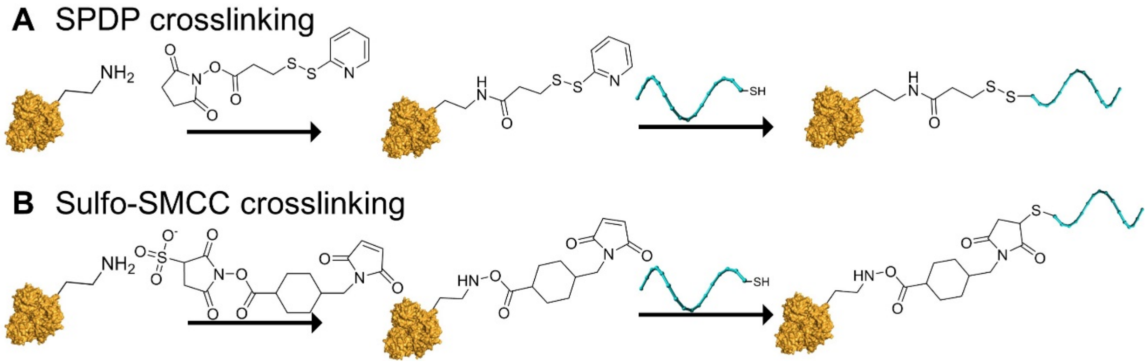

Scheme 1.2. Covalent non-site specific protein-DNA conjugation through **(A)** N-Succinimidyl 3-(2-pyridyldithio)-propionate (SPDP)[57] and **(B)** Sulfo-Succinimidyl-4-(N-maleimidomethyl)cyclohexane-1-carboxylate (Sulfo-SMCC)[58] crosslinkers. One end of the linker is covalently attached to the lysine side chains of protein and the other maleimide-functionalized end is subsequently coupled to thiolated DNA strands.

1.2.4 Covalent site-specific conjugation method

Site-specific DNA protein conjugation is typically achieved by expressing the protein of interest with a chemical handle that can subsequently react with functional groups on DNA at designed positions. These techniques require genetic manipulation to express the protein of interest with the desired mutations, which is challenging and has to be systematically optimized for any new proteins.

1.2.4.1 Azido-protein DNA conjugation

One commonly used site-specific protein-DNA ligation approach is based on azido-proteins. In this method, any protein of interest needs to be mutated with Azide first. One popular method is to incorporate unnatural amino-acids. A general strategy is to activate Azido-homoalanine by the methionyl-tRNA synthetase (MetRS) of Escherichia coli and replace methionine in proteins expressed in methionine-depleted bacterial cultures[60]. Another way is using protein farnesyltransferase (PFTase) to label protein containing a C-terminal tetrapeptide tag with an azide-modified isoprenoid diphosphate[61]. After labeling the protein site-specifically with azide, several reactions can be done to further modify the protein with ssDNA (**Scheme 1.3**). The Cu(I)-catalyzed 1,3-dipolar cycloaddition reaction which reacts with alkyne modified ssDNA has been a classic way for site-specific labeling[62]. However, this technique has drawbacks, including (1) toxicity of Cu(I) to cells, (2) enzyme activity loss by Cu(I) binding to the active site, and (3) reduced reaction rate by Cu(I) disproportionation in an aqueous environment. Therefore, interest is growing in methods involving Cu-free 1,3-dipolar cycloaddition reactions and Staudinger ligation reactions[63]. Cu-free method involves reaction with a dibenzocyclooctyne (DBCO) functional groups[62]. Staudinger ligation involves reaction between azide and phosphine-modified components, and has been used to label ssDNA on azido-functionalized glycoproteins on cell surface[64,65].

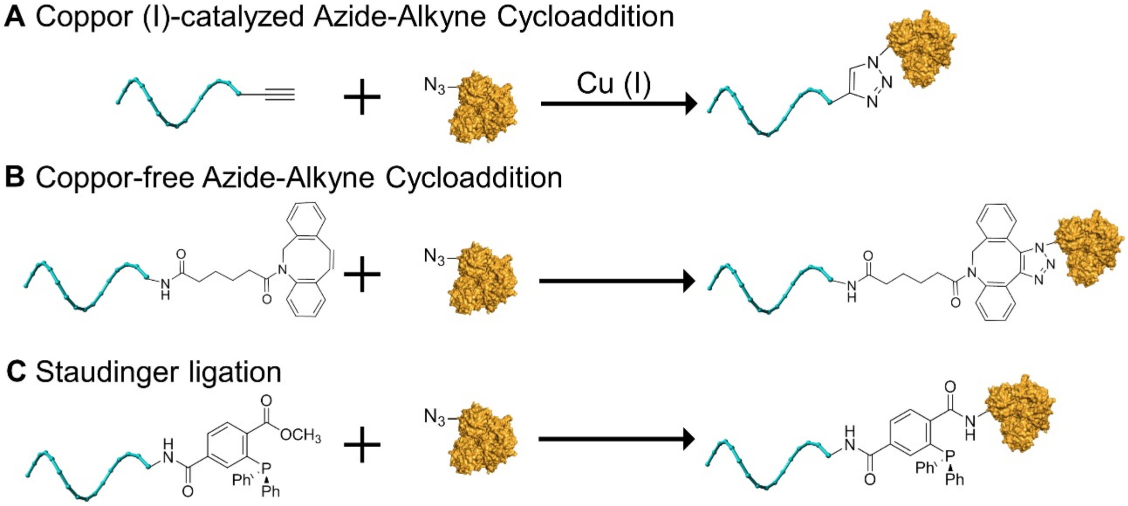

Scheme 1.3. Scheme of site-specific Azido-protein-DNA conjugation chemistry, including **(A)** Cu(I)-catalyzed 1,3-dipolar cycloaddition reaction[62], which reacts with terminal alkyne modified ssDNA; **(B)** Cu-free 1,3-dipolar cycloaddition reaction[62], which reacts with dibenzocyclooctyne (DBCO)-modfied ssDNA and **(C)** Staudinger ligation reaction[63-65], which reacts with phosphine-modified ssDNA.

1.2.4.2 Expressed protein ligation (EPL)

The expressed protein ligation method has been used to ligate both C-terminal[66] and N-terminal[67] intein-fused protein with peptide-modified ssDNA (**Scheme 1.4**). First, the target protein is fused to the construct of an intein, as well as an additional chitin binding domain (CBD) for the convenience of affinity purification using a chitin matrix. Then a thioester of the target protein is achieved by reacting with mercaptoethansulfonic acid (MESNA). This protein can be ligated to a Cysteine modified DNA. While having the advantage of the well-defined stoichiometric composition and site-specific linkage, this method has challenges regarding insoluble intein-fusions.

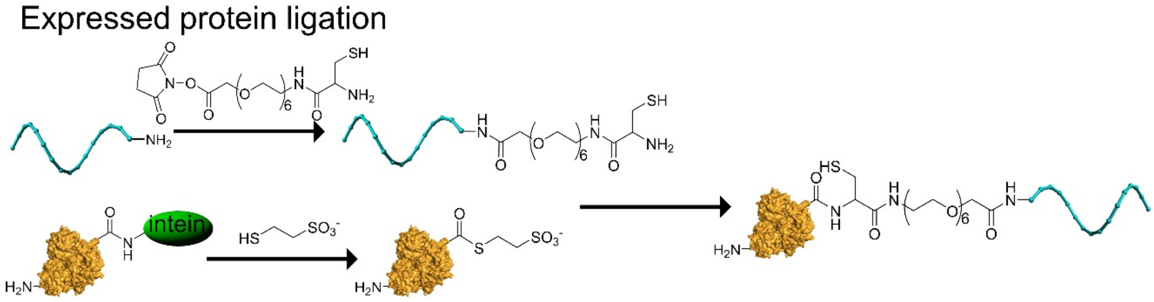

Scheme 1.4. Scheme of C-terminal fused intein protein-DNA conjugation by expressed protein ligation (EPL)[66]. The C-terminal intein fused protein reacts with mercaptoethansulfonic acid (MESNA) to generate thioester and then ligated to a Cysteine modified DNA.

1.2.4.3 Enzymatic ligation

High yield of Protein-DNA conjugation can be achieved by enzymatic ligation. For example, Microbial transglutaminase (MTG)[68] catalyzes an acyl transfer reaction between N-carbobenzyloxyglutaminylglycine (Z-QG) -DNA and short peptide tag (**Scheme 1.5A**). The targeted proteins can be fused through genetic modification with a short peptide tag (Met-Lys-His-Lys-Gly-Ser) containing the acyl-acceptor Lys residues to N or C terminals. The oligonucleotides are modified with short peptide Z-QG, which functions as the acyl donor. This method has been applied to alkaline phosphatase and enhanced green fluorescent protein (eGFP) and has been used in DNA directed immobilization[68].

Another method with a similar mechanism is the sortase-mediated protein-DNA conjugation[69,70]. The sortase enzyme catalyzes the formation of a covalent bond between two proteins by coupling two specific peptide sequences. Sortase first recognizes a C-terminal -LPETG- sequence, and then transposes the N-terminal-GGG sequence with the glycine from the –LPETGGG- sequence, resulting in a peptide bond between the two proteins (**Scheme 1.5B**). In detail, sortase cleaves the threonine-glycine bond via its active site cysteine residue and forms an acyl intermediate with threonine in the peptide, regenerating the active site cysteine on the sortase and conjugating the peptide-DNA to the N terminus of the protein. Note that at least one additional C-terminal amino acid is required for sortase to properly bind with the recognition sequence. Peptide-oligonucleotide conjugates can be prepared by automatic solid-phase synthesis[71].

There is another option for replacing DNA modification by using Terminal deoxynucleotidyl Transferase (TdT), which can ligate native DNA to proteins coupled with nucleotide triphosphates[72]. TdT can accept nucleoside triphosphates tethered to large biomolecules as substrates and direct the ligation of the biomolecules to the 3' end of any native oligodeoxynucleotides (**Scheme 1.5C**). The reaction is rapid and quantitative, while in mild and aqueous conditions. First, proteins are activated by NTP through a copper-free DBCO-mediated click reaction and then ligated to native DNA by TdT. The significant advantage of this method is the label-free ssDNA, allowing for batchwise functionalization of multiple staple strands that can be completed in one pot reaction. This leads to a high-throughput method for sensing purposes.

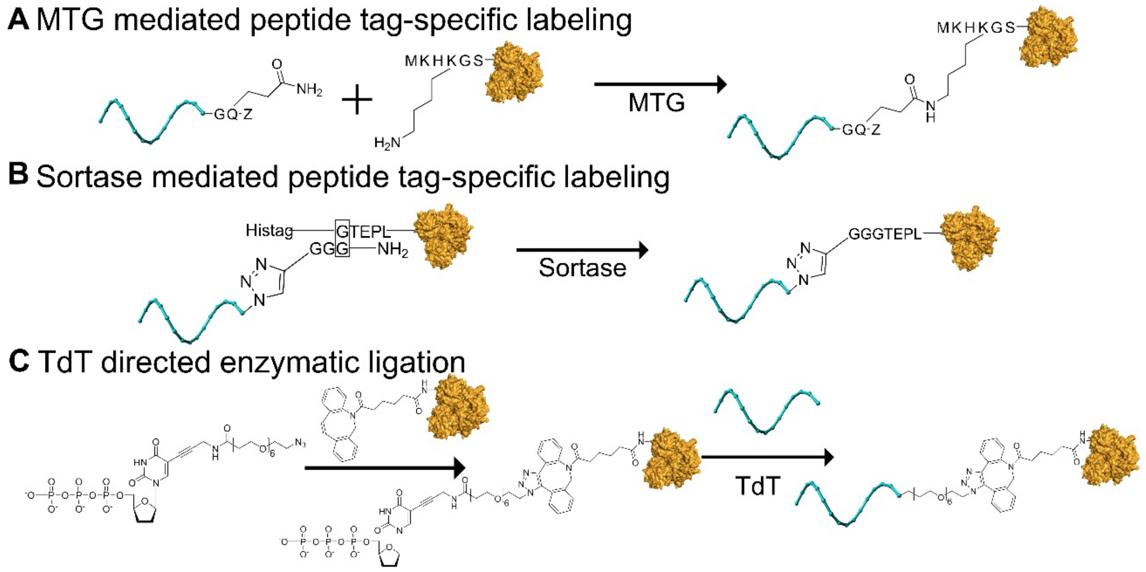

Scheme 1.5. Scheme of protein-DNA ligation mediated by pure enzyme system including **(A)** Microbial transglutaminase (MTG)[68], **(B)** Sortase[69,70], and **(C)** Terminal deoxynucleotidyl Transferase (TdT)[72]. **(A)** MTG catalyzes an acyl transfer reaction between N-carbobenzyloxyglutaminylglycine-DNA as the acyl-donor and a protein with short peptide tag containing the acyl-acceptor Lys residues (Met-Lys-His-Lys-Gly-Ser). **(B)** Sortase first recognizes a C-terminal -LPETG- sequence, and then transposes the N-terminal-GGG sequence with the glycine from the –LPETGGG- sequence, resulting in a peptide bond between protein and DNA. **(C)** TdT ligates the proteins that are activated by NTP through a copper-free DBCO-mediated click reaction to native DNA.

1.2.4.4 self-ligating protein tags

More recent site-specific protein-DNA conjugation techniques are based on the self-labeling protein tags which are fused by genetic modification to the targeted protein and catalyze the subsequent protein-DNA ligand reaction by themselves. The two popular examples are the human O6-alkylguanine-DNA-alkyltrans-ferase (hAGT, referred as 'SNAP-tag')[73,74], 20 kD and the haloalkane dehalogenase (referred as 'HALO-tag')[75,76], 34 kD. The reaction procedures are similar except that different self-labeling tags have their own substrates, therefore different functional groups need to be modified on ssDNA targets accordingly (**Scheme 1.6**). SNAP-tags can irreversibly transfer the alkyl group from its substrate, O_6-benzylguanine-DNA, to one of its cysteine residues, creating a thioether covalent bond with the maleimide-DNA moiety. With the Halo-tag, nucleophilic displacement of the terminal chloride with Asp residue leads to a covalent alkyl-enzyme intermediate. O6-benzylguanine and 5-chlorohexane modified ssDNA can be prepared through amino-reactive N-hydroxysuccinimide (NHS) derivatives[72]. The exact ratio of the ssDNA labeled on protein and the high yield of protein-DNA assembly can be achieved with mild protein reaction conditions. A considerable challenge for engineering artificial multienzyme systems *in vivo* is the stability of the protein-DNA complex. Compared to other protein tags, which form non-covalent linkage with DNA (i.e. His tag), the covalent linkage of protein-DNA appears to be much more stable in various buffers and potentially in blood circulation systems. Halo tag protein has also been used for *in vivo* cell labelling[71]. The high stability and specificity of this method make it a perfect candidate in therapeutic applications.

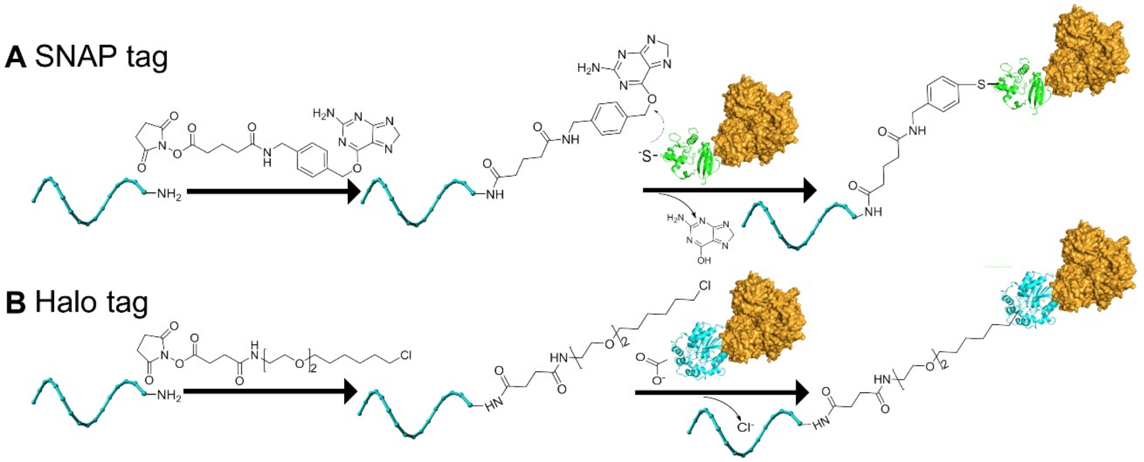

Scheme 1.6. Schemes of protein-DNA conjugation using self-labeling protein tags, including **(A)** human O6-alkylguanine-DNA-alkyltrans-ferase (SNAP) tagged protein-DNA conjugation[73,74] and **(B)** Reaction of haloalkane dehalogenase (HaloTag) ligand-DNA and Halotagged-protein conjugation[75]. SNAP-tags irreversibly transfer the alkyl group from its substrate, O$_6$-benzylguanine-DNA, to one of its cysteine residues, creating a thioether covalent bond with the maleimide-DNA moiety. With the Halo-tag, Nucleophilic displacement of the terminal chloride with Asp residue leads to a covalent alkyl-enzyme intermediate. O6-benzylguanine and 5-chlorohexane modified ssDNA can be prepared through amino-reactive N-hydroxysuccinimide (NHS) derivatives[76].

1.2.4.5 Template directed conjugation

To replace the complicated and problematic protein engineering process using protein tags, a novel and simpler way to create regio-selective DNA–protein conjugates has been developed[77]. This DNA-templated protein conjugation (DTPC) method is a combination of metal-affinity probes and DNA-templated synthesis. The method relies on three components: a protein to be labeled that possesses an affinity for a metal ions, a ssDNA modified with a ligand functionality, and a complementary strand that carries an activated ester capable of reacting with the surface amino acids. As shown in **Scheme 1.7**, a metal-binding ssDNA is introduced to bind with His_6-tagged or wild-type metal-binding proteins as a guide, which will hybridize with a second DNA strand and subsequently crosslink with surface lysines which are only close to a metal-binding site. This DNA-templated protein conjugation method provides an alternative way for regio-specific DNA conjugation in contrast to technically challenging protein engineering, however the site-specificity has not yet been realized.

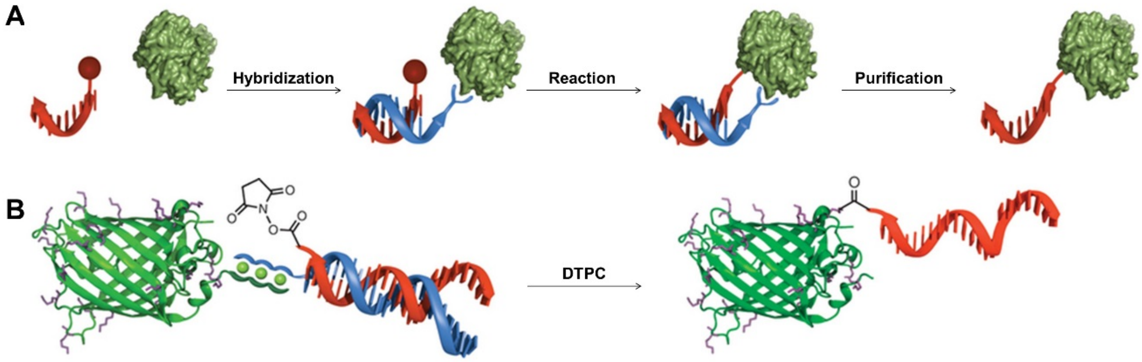

Scheme 1.7. Scheme and characterization of DNA-template protein conjugation (DTPC)[77]. (A) General procedure of regio-selective DNA-templated protein conjugation (DTPC) method. The guiding strand (blue waves) coordinates protein (green), and hybridize with the reacting strand (red waves), after the templated reaction of reacting strand and protein, the DNA–protein complex can be purified. **(B)** Detailed reaction scheme of the DTPC method: a Ni^{2+}-binding tris-(NTA)-ssDNA (blue) is introduced to bind with His_6-tagged protein as a guide, which will hybridize with a second DNA strand (red) and subsequently crosslink with lysine that are only close to the metal-binding site. Images reproduced with permission: ref 77, copyright (2014) Nature publishing group.

1.3 Applications

1.3.1 DNA machine/ responsive nanodevice

Other than simple switches based on dsDNA using modifications such as the photoisomerizable compounds[78], more complex DNA nanostructure-based switchable nanodevices can be easily constructed and manipulated using DNA strand hybridization and displacement principles. DNA tweezers became a popular design in switching distances of two components. DNA tweezers can switch between open and closed states for at least four cycles[79]. Initially, the two arms of the tweezer are in a 'closed' state, linked by a hairpin structure, and transferred to an 'open' state by adding a fuel strand, which hybridizes with the hairpin loop and forms a rigid duplex. The switchability and kinetics are characterized both by gel electrophoresis and Förster resonance energy transfer (FRET). DNA tweezers can be used to actuate enzyme and enzyme cascades. One example is the use of DNA tweezers to control GOx/HRP cascade system. Due to the differences of open and closed state of two arms, the cascade activity (H_2O_2 production) differs for ~2 fold[80]. Another example is to use DNA tweezers to control the binding and dissociation of enzymes and its co-factors, as demonstrated by attaching glucose-6-phosphate dehydrogenase (G6pDH) and Nicotinamide adenine dinucleotide (NAD^+)[81] to the two arms of the DNA tweezers (**Figure 1.2**) Since the enzyme is only active when directly 'touching' the cofactor, closed state revealed ~5 fold enhancement of enzyme activity compared to the open state and the 'on and off' state of enzyme activity can be reversibly regulated by adding fuel, and set DNA strands continuously.

1.3.2 Protein patterning for single molecule and structural analysis

One of the advantages of DNA origami is that it serves as an excellent template for single molecule visualization[82]. A DNA nanoarray is different from traditional microarrays generated by DNA-directed immobilization (DDI) method, with a higher order of spatial control. Because of this, DNA origami can be used as a molecular chip to display multiple probes for detection of various molecular interactions, i.e. RNA[83], DNA[84], distance-dependence of ligand-protein binding[85] and chemical reactions on a single molecule level[86-88]. In order to address multiple components, orthogonal binding sites are needed. Both spatially addressable multiprotein nanoarrays[46,89] and protein nanoarrays with orientation control[36, 90] have been built.

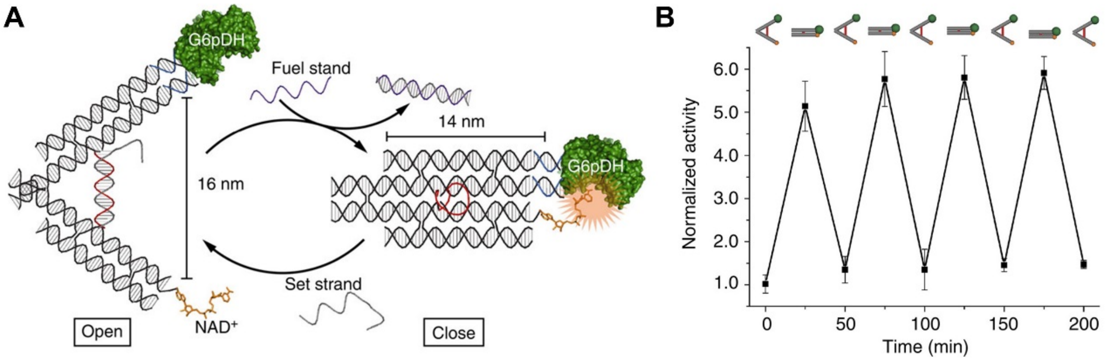

Figure 1.2. A enzyme-cofactor-DNA tweezer complex[81]. **(A)** Design of a tweezer complex using an enzyme-cofactor system including glucose-6-phosphate dehydrogenase (G6pDH) and nicotinamide adenine dinucleotide (NAD^+). The cofactor NAD^+ molecule is covalently linked to the end of one arm, while the enzyme is linked to the other. **(B)** Activity results showing that closed state revealed ~5 fold enhancement of enzyme activity compared to the open state, open and close states are reversible for at least 4 cycles. Images reproduced with permission: ref 81, copyright (2013) Nature publishing group

1.3.3 DNA scaffolded motor protein networks

Researchers have studied motor protein behaviors by assembling multiple motor proteins on DNA scaffold. 2D rectangular DNA origami scaffold has been used to pattern a combination of myosin V with rigid lever and myosin VI with flexible level, and study the role of intermotor interactions on collective functions[91] (**Figure 1.3A**). Results of movement trajectories on actin networks have shown that trajectory shape of multimotor scaffolds positively correlates with the stiffness of the myosin lever arm. Another study focused on kinesin and dynein motor proteins that transport cargo on microtubule tracks. Two motor proteins with opposite-polarity are organized on 12-helix bundle DNA origami with different stoichiometry (**Figure 1.3B**). A "tug-of-war" behavior of the two proteins was observed[92]. An artificial self-organized transport system based on motor protein-DNA complex has been developed (**Figure 1.3C**). With trigger molecules, assembly and disassembly of the network, as well as loading and unloading of cargos on the track network can be realized[93].

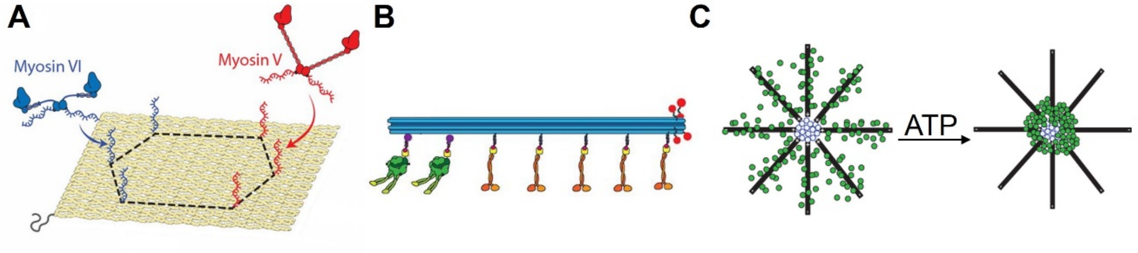

Figure 1.3. DNA nanostructure directed multiple motor proteins assembly. (A) Myosin lever arms with different stiffness organized on rectangular DNA origami that travel on a cellular actin network, Myosin V has more rigid lever and VI has more flexible

lever[91]. (**B**) Two motor proteins with opposite polarity assembled on a 12-helix bundle DNA origami structure, showing a tug-of war behavior[92]. (**C**) An artificial self-organized transport system based on microtubule motor protein-DNA complex that can assemble and disassemble with trigger molecules[93]. Images reproduced with permission: (A) ref 91, copyright (2014) Proceedings of the National Academy of Sciences; (B) ref 92, copyright (2012) American Association for the Advancement of Science (C) ref 93, copyright (2013) Nature publishing group.

1.3.4 Engineering enzymatic pathways

In living systems, multienzymatic pathways are often physically and spatially organized onto scaffolds, clusters, and into microcompartments. By careful control of enzyme positions, orientation and ratio, the efficiency and specificity of enzymatic pathways in nature is extremely high. Spatial organization helps substrates flow between interacting proteins, and increases yield of sequential metabolic reactions. By exploiting the programmability of DNA nanostructures, key parameters including position, stoichiometry, and inter-enzyme distance can be manipulated and tested for optimal activity.

In order to fully understand and further engineer enzymatic pathways with maximum efficiency and limited cross-talks between signaling pathways, artificial multienzyme complexes have been built to mimic intracellular biocatalytic processes. An artificial enzyme cascade formed by glucose oxidase (GOx) and horseradish peroxidases (HRP) has been studied extensively as a model system. An advantage of GOx/HRP cascade as model system is the convenience of the enzyme cascade assay. In this case the enzyme activity can be converted to optical signals with high sensitivity for detection[56]. In this review, studies of GOx and HRP using double-stranded DNA (dsDNA), 1D, 2D and origami as scaffolds are briefly summarized.

1D DNA scaffold

DsDNA has been used to bring two enzymes together to study the distance dependency[94,95] (**Figure 1.4A**). A 1D DNA nanowire[96,97] has been developed to attach tandem repeat units of GOx/HRP cascade, with the micrometer long ssDNA working as the wire synthesized by Rolling-Circle Amplification (RCA) process. The probes will hybridize with the enzyme conjugated complementary strand. The activation of an enzyme cascade by the spatial positioning of the two enzymes (GOx and HRP) on the DNA template has been observed by activity assay monitoring $ABTS^-$ formation.

2D DNA structure scaffold

Arranging multienzyme cascades on 2D complex geometric patterns was first studied by Willner[98]. In this work, GOx-HRP cascade was organized with a 2D hexagonal DNA array (**Figure 1.4B**). Two distances between GOx and HRP was designed by varying the probe strand positions. Enzymes organized on the two-hexagon strips (shorter distances) gives higher activity than the four-hexagon strips. With shorter distances, intermediate (H_2O_2) diffusion has higher efficiency, which therefore results in higher cascade efficiency.

DNA origami scaffold

More accurate distance control is realized using DNA origami as a scaffold[99]. Instead of only comparing the assembled system with the free system, distances varying from 10 nm, 20 nm, 40 nm, and 50 nm were systematically studied. Surprisingly, instead of a gradual decrease in cascade activity while increasing the interenzyme distances, a sharp transition was observed at 10 nm inter-enzyme distance, which was explained by hydration shell formation of the contacting proteins to facilitate the diffusion of H_2O_2 intermediate (**Figure 1.4C**). This mechanism is verified by constructing different sizes of protein bridges between GOx and HRP. The bridging protein changed the Brownian diffusion into a dimensional-limited diffusion through the hydration layer of the contacted enzymes. However, other than this specific GOx-HRP enzyme pair, more research is required for polar molecules other than H_2O_2 to fully understand the distance dependence of enzyme cascades. Recently, DNA origami nanostructures are also used to encapsulate GOx and HRP enzyme cascades into a confined environment with enhanced enzyme activity, although the mechanism of the caging effect remains to be further exploited[100].

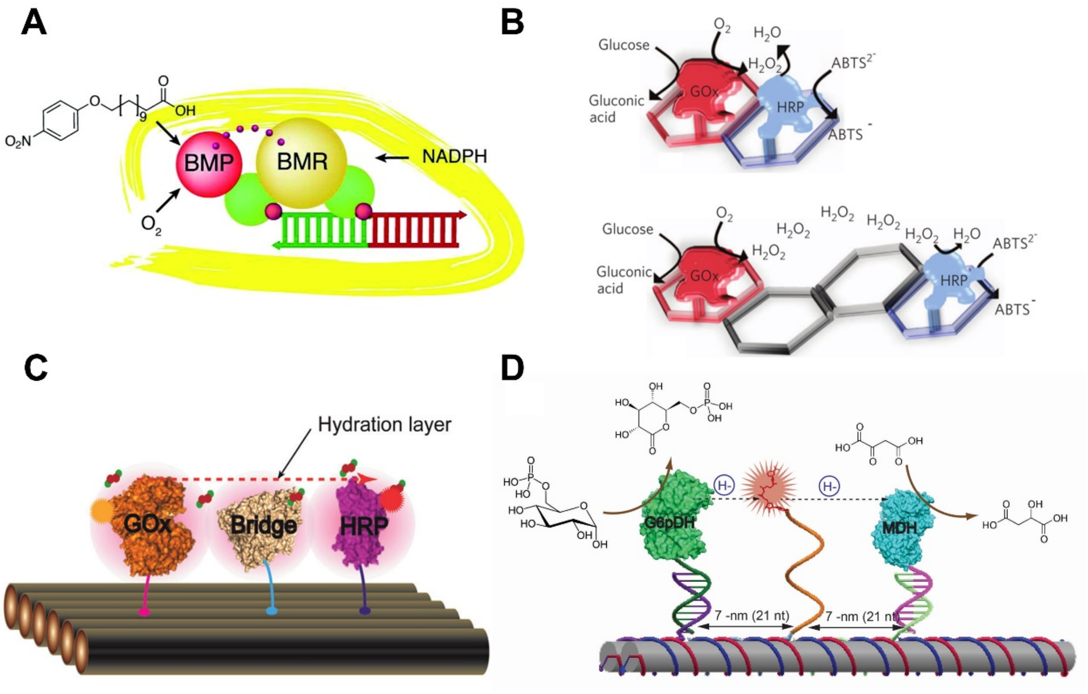

Figure 1.4. Artificial enzyme cascades organized by **(A)** double-stranded (ds) DNA[94], (**B**) 2D tile based DNA arrays[97], **(C)** rectangular DNA origami[99], and (**D**) DNA tile[57]. (**A**) Design of distance-dependence study of cytochrome P450 BM3 with organizing the BMR reductase domain and the BMP porphyrin domain on dsDNA scaffold. **(B)** Scheme of glucose oxidase (GOx) and horseradish peroxidases (HRP) cascade organized with two different distances between GOx and HRP on two-hexagon (top) and four-hexagon strips (bottom). **(C)** Scheme of the assembled GOx/HRP pair with a protein bridge working as a connected hydration layer to facilitate H2O2 diffusion. **(D)** An artificial swinging arm multi-enzyme complex consisting of glucose-6-phosphate dehydrogenase (G6pDH) and malic dehydrogenase (MDH) organized on a DNA DX tile, with a nicotinamide adenine dinucleotide (NAD^+)-modified ssDNA as the swinging arm, facilitating the transfer of hydrides. Images reproduced with permission: (A) ref 94, copyright (2011) American

Chemical Society; (B) ref 97, copyright (2009) Nature publishing group; (C) ref 99, copyright (2012) American Chemical Society; (D) ref 57, copyright (2014) Nature publishing group.

Directed substrate channeling with swinging arms

More complex enzymatic pathways have been explored by adding a swinging arm linked cofactor between two enzymes[55] to understand substrate channeling. Substrate channeling[101] is used by nature for direct transfer of intermediate from one enzyme to a proximal enzyme to facilitate cascade activity. In this work, a multi-enzyme complex has been created based on DNA scaffolding, with an artificial swinging arm positioned between two coupled dehydrogenases, glucose-6-phosphate dehydrogenase (G6pDH) and malic dehydrogenase (MDH) (**Figure 1.4D**). This arm can swing between two enzymes via a flexible linker (20T single-strand), allowing the direct transfer of substrate molecules between multiple active sites within the complex. By employing a DNA scaffold, precise control over the spatial parameters of the individual components within the assembled complex is realized. The swinging behavior of the covalently linked 'arm' is verified by single-molecule FRET experiment. Bulk activity results showed that the channeled NAD-protein complex has ~90 fold enhancement activity compared to free, and by changing the relative ratio of two enzymes, activity can be further increased.

1.3.5 Photosynthetic complexes/ light harvesting networks

People have been studying light harvesting systems for decades[102], and DNA nanostructures shed light on creating artificial photosynthetic complexes in order to understand the mechanism and modulate the energy transfer efficiency[102,103]. In a work using DNA nanostructures to study photosynthetic systems, an artificial light-harvesting antenna has been constructed by assembling donor-acceptors in ring-like structure on a 6-helix bundle DNA tile[104] (**Figure 1.5A**). More recently, an artificial photosynthetic complex has been created by site-specifically modifying a Y-shaped DNA nanostructure

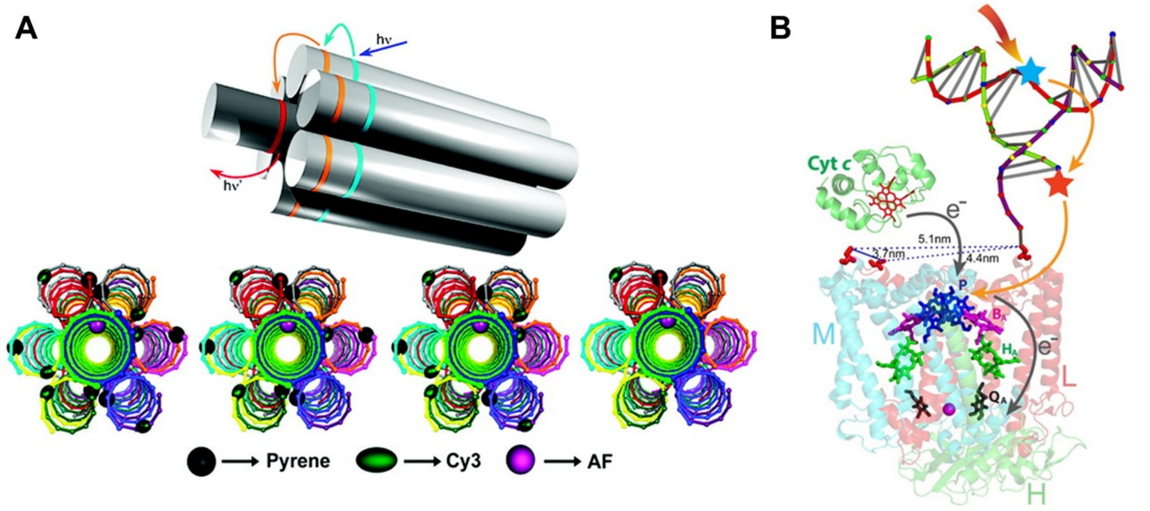

Figure 1.5. Artificial light-harvesting systems based on DNA nanostructures. **(A)** Artificial Light-Harvesting Antenna built with a 6-helix bundle DNA nanostructure[104]; **(B)** Scheme of a DNA-Directed Reaction Center System with expending light absorbing range by assembly of a Y-shapped DNA-dye complex on reaction center[105]. Images reproduced with permission: (A) ref 104, copyright (2011) American Chemical Society; (B) ref 105, copyright (2014) American Chemical Society.

with dyes for stepwise energy transfer to a reaction center protein[105] (**Figure 1.5B**). Experimental results showed that Cytochrome c oxidation (monitored at 550 nm) of DNA-dye-RC complex has dramatically increased comparing to wild-type RC with the excitation of Cy5 dye. The results indicate that the spectrum of the reaction center can be tuned and optimized by DNA directed artificial light harvesting systems.

1.3.6 *In vivo* regulation and sensing

DNA nanostructures as scaffolds to organize multi-enzyme pathways have largely remained limited to *in vitro* applications. In contrast, RNA can be produced via the transcription machinery and forms stable interactions *in vivo*[106]. The first breakthrough of *in vivo* cascading of two enzymes was realized using a self-assembled RNA scaffold inside of cells[107]. In this case, rationally designed RNA isothermal assemblies were successfully applied to form functional discrete, 1D, and 2D scaffolds *in vivo*. These RNA scaffolds were functionalized by capturing proteins with RNA aptamer domains (**Figure 1.6A**). The scaffolding effects led to improved hydrogen production after organization of hydrogen-producing biosynthetic pathways on RNA nanoscaffolds. At this stage, RNA nanostructures are still limited and only a handful rationally designed RNA 2D and 3D structures have been reported[108].

Another approach for *in vivo* regulation is assembling the structure *in vitro* and delivering the complex onto or into targeted cells. One successful example of this is the targeted delivery of a DNA nanobox for controlled drug release (in this case an antibody) with the ‘key’ molecules displayed on cell surface and the interactive ‘lock’ labeled on the DNA nanobox[109-111] (**Figure 1.6B**).

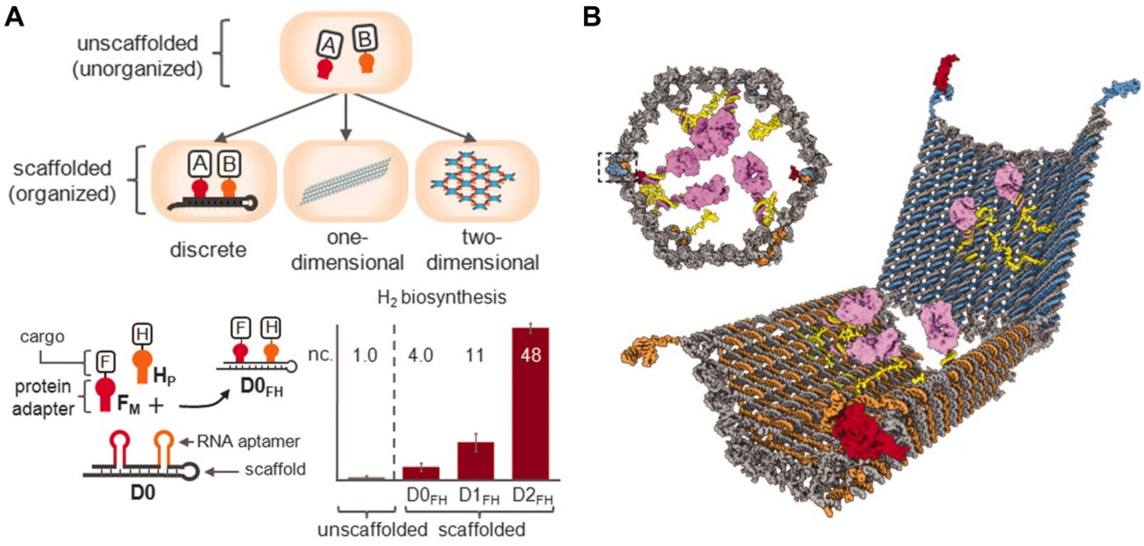

Figure 1.6. ***In vivo* assembly of enzyme cascade** by nucleic acid nanoscaffold. **(A)** Top: Scheme of two cascade proteins A and B scaffolded on discrete, 1D and 2D self-assembled RNA scaffold[107]. Bottom left: Design of hydrogen-producing biosynthetic pathways with Ferredoxin (F) and hydrogenase (H) enzyme cascade organized with RNA aptamer domains as probe. Bottom right: The scaffolding effects shown with hydrogen production enhancement after discrete, 1D and 2D organization of 2 enzymes. **(B)** Scheme of aptamer-gated DNA nanorobot loaded with a protein payload[110]. Two DNA-aptamer locks are used to control open and close of the device. Images reproduced with permission: (A) ref 107, copyright (2011) American Association for the Advancement of Science; (B) ref 110, copyright (2012) American Association for the Advancement of Science.

CHAPTER 2

METHODOLOGY DEVELOPMENT: DNA NANOSTRUCTURE-SCAFFOLDED ASSEMBLY OF MULTI-ENZYME COMPLEXES

Adapted with permission from Jinglin Fu, Yuhe Renee Yang, Soma Dhakal, Zhao Zhao, Minghui Liu , Ting Zhang, Nils G. Walter and Hao Yan. **DNA Nanostructure-Scaffolded Assembly of Multi-Enzyme Complexes** (manuscript under review).

Abstract

In nature, the catalytic efficiency of multi-enzyme complexes highly depends on their spatial organization in that the positions and orientations of the composite enzymes are often precisely controlled to facilitate substrate transport between them. Self-assembled DNA nanostructures hold great promise to organize biomolecules at the nanoscale. Here, we present detailed protocols for exploiting DNA nanostructures as assembly scaffolds that organize the spatial arrangements of multi-enzyme cascades with control over their relative distance, compartmentalization, and substrate diffusion paths. The architecture of assembled enzyme complexes is readily characterized using a broad selection of techniques from routine gel electrophoresis to advanced single-molecule imaging. We also describe methods to purify these nano-assemblies and test them with functional assays based on either bulk or single-molecule fluorescence measurements. The entire assembly and characterization of a multi-enzyme complex can be completed within one to two weeks.

2.1.Introduction

Biology has evolved complex, multi-step enzyme pathways to make molecules and derive energy that are vital to the metabolism and reproduction of living systems. The function of a pathway is critically dependent on the relative position, orientation, and quantity of the participating molecules[112,113]. The ability to exert control over these systems on the nanoscale will not only allow us to study the effects of spatial organization on the functions of biochemistry pathways, but also increase our ability to translate biochemical pathways to a variety of noncellular applications, such as production of high-value chemicals, smart materials, bio-diagnostics and drug delivery. Thus, it is imperative to develop assembly methods to engineer multi-enzyme systems, where their spatial parameters can be easily manipulated on the nanoscale. Over the past few decades, DNA based self-assembly has been exploited to construct various 1D, 2D and 3D nanostructures. The use of double helical DNA molecules for nanoscale engineering began with Seeman's construction of artificial "Holliday" junction tiles[1]. The further developments of double-crossover (DX) tiles and the sticky-end cohesion were used to create periodic nanostructures with distinct topological and geometric features[1,114,115]. Recent breakthroughs in scaffolded DNA origami[15] and single-stranded DNA bricks[28,116] have enabled the design and fabrication of spatially addressable 1D, 2D and 3D nanostructures[19,117], as well as structures with complex curvatures[18,21], polyhedral meshes[118,119] and DNA crystals[14,120]. Several computational tools including caDNAno[121], CanDo[122], and TIMAT[123] have been developed to facilitate the design of DNA nanostructures, making structural DNA nanotechnology more accessible to researchers from other fields.

DNA nanostructures have recently emerged as promising assembly templates to organize molecules on the nanoscale based on their programmable and sequence-driven self-assembly[115,124-128]. For example, multi-enzyme cascades can be positioned on the DNA nanostructures with precise control over the spatial distances to enhance the mass transport of substrates[94,98,99], the engineering of substrate channeling mechanisms[57], and the regulation of spatial interactions between enzyme pairs[80,81]. Self-assembled DNA nanoboxes and nanocages were demonstrated for the encapsulation of macromolecular payloads such as antibodies[17,110] and enzymes[129-131]. Tubular DNA nanostructures were also used to construct efficient enzyme cascade nanoreactors[100]. Here, we describe a protocol for the robust assembly, purification and characterization of multi-enzyme complexes organized by DNA nanoscaffolds. This protocol has been demonstrated to develop a series of artificial enzyme complexes with the functions of probing inter-enzyme substrate difusion[99], mimicking biocatalytic swinging arms[57], developing DNA nanocage compartmentalized enzymes[129] and the regulatory enzyme nanoreactors[81].

2.2.Protocol overview

The general strategy of assembling enzyme complexes on DNA nanostructures is illustrated in **Figure 2.1** as a flow chart. An enzyme is chemically conjugated to a single-stranded oligonucleotide, which serves as an anchor to hybridize with the corresponding complementary capture strand that is displayed on the surface of a DNA nanoscaffold. The entire protocol includes the following key steps: (1) the preparation of DNA-conjugated enzymes/cofactors and purification; (2) the assembly of enzyme complexes onto DNA nanostructures; (3) the characterization of the assembled enzyme complexes; (4) the purification of assembled enzyme complexes; and (5) the activity evaluation.

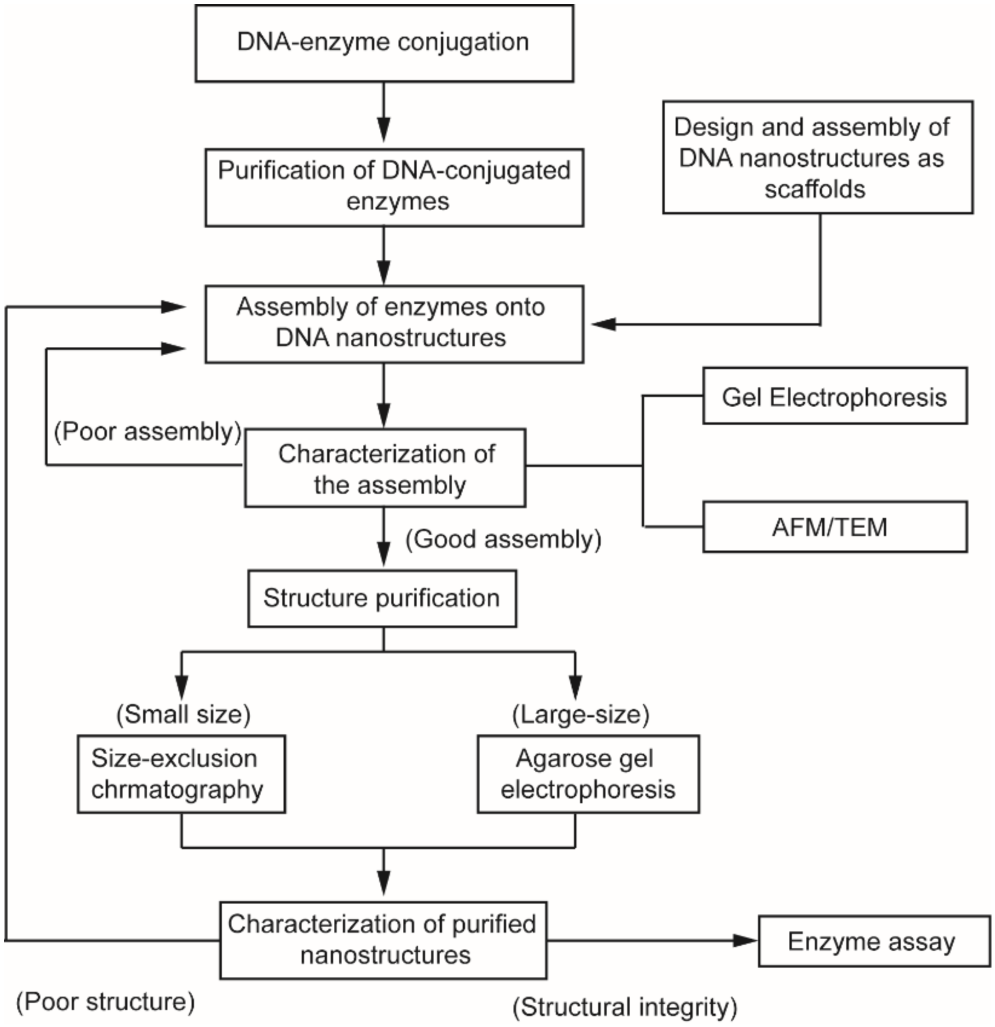

Figure 2.1 The protocol overview of the assembly, purification and characterization of multi-enzyme complexes organized by DNA nanoscaffolds.

2.2.1 DNA-enzyme/cofactor conjugation and purification

2.2.1.1 Non Site-specific bio-conjugation strategies for coupling DNA to protein enzymes

A variety of chemical methods has been developed to link a oligonucleotide with a protein[35], such as, aptamer-protein noncovalent interactions[46], N-terminal reaction[132], NTA–hexahistidine interactions[40], click chemistry[133], and disulfide[15] and maleimide coupling[99]. We use a simple SPDP (N-succinimidyl 3-(2-pyridyldithio) propionate) crosslinker to conjugate the primary amines of the lysine residues on the enzyme surface to a thiol-modified oligonucleotide (**Fig. 2.2a**). Enzyme solution is first incubated with the SPDP crosslinker, allowing amine-reactive N-hydroxysuccinimide (NHS) esters to react with the lysine residues on the enzyme surface. Next, the SPDP-modified enzyme is reacted with a thiol-modified oligonucleotide that undergoes a disulfide bond exchange of the activated pyridyldithiol group. The efficiency of the DNA-enzyme conjugation can be evaluated by the increased absorbance at 343 nm due to the release of pyridine-2-thione.

After the enzyme-DNA conjugation, it is important to completely remove the excess and unreacted DNA molecules. As a simple method, the centrifugal ultrafiltration is commonly used to filter out smaller DNA molecules from the solution of DNA-conjugated enzymes with a molecular weight cut-off filter (e.g. ~ 30 kDa cut-off)[81,98,99]. However, DNA molecules tend to nonspecifically bind to the protein surface due to the strong electrostatic interaction between the negatively charged phosphate backbones of DNA molecules and the positively charged residues (e.g. lysine and arginine) on the enzyme surface. Thus, a washing buffer containing a high concentration of NaCl (1.5 M) is used to disrupt this strong electrostatic interaction, and remove the smaller DNA molecules from the protein surface. As shown in **Table 2.1**, for a DNA-conjugated glucose-6-phosphate dehydrogenase (G6PDH-P1), the low-salt buffer of 10 mM sodium HEPES (pH 7.5) cannot remove the excess and unconjugated DNA molecules efficiently, where the DNA-to-enzyme ratio remains as high as 3.2 after three-time wash even though the average SPDP label ratio is only ~ 0.9. It indicates that there are excess DNA molecules nonspecifically binding to enzymes without covalent attachment. Conversely, a similar filtration process using a 10 mM HEPES buffer containing 1.5 M NaCl (pH 7.5) can reduce the DNA-to-protein ratio to ~ 0.7, suggesting that most of nonspecific DNA molecules are removed. Similarly, the DNA-to-enzyme ratio of a DNA-conjugated lactate dehydrogenase (LDH-P2) is reduced from ~ 2.7 to ~ 1.1 by increasing the NaCl concentration from ~ 10 mM to 1.5 M NaCl in the washing buffer. The addition of detergent such as P20 can further disrupt the strong noncovalent interaction between LDH and DNA molecules[134-137], reducing the DNA-to-protein ratio from 1.1 to 0.7 (SPDP label ratio for LDH is ~ 0.9.

Due to the presence of multiple lysine residues on the surface of enzymes, the collected solution from the centrifugal ultrafiltration is a mixture of enzymes labelled with different numbers of DNA molecules per protein. As shown in **Fig. 2.2b**, the anion-exchange fast-protein liquid chromatography (AE-FPLC) is used to isolate a homogeneous population of enzymes labelled with the identical number of oligonucleotides. Using a NaCl gradient increased from 20% to 55%, a DNA-conjugated G6PDH with an average DNA-to-enzyme ratio of ~ 1.5 is separated into five peaks of components, identified to be the unmodified G6PDH (~ 30% NaCl), G6PDH with 1 (~ 38-40% NaCl), 2 (~ 43-46% NaCl), 3 (~ 48-50% NaCl) and 4 DNA labels (~ 52% NaCl), respectively. The concentrations of identities of the distinct peaks are determined using the A260 and A280 absorbance as shown in **Table 2.2**. The activities of DNA-conjugated enzymes are measured as shown in **Fig. 2.2c**. The purified DNA-conjugated enzymes are further tested for the assembly onto DNA nanostructures. As shown in **Fig. 2.2d**, enzymes labeled with one DNA molecule may result in a lower assembly yield and formation of a secondary product with lower mobility in the gel, which is likely to consist of two enzymes bound to adjacent probes on the same DNA tile. Enzymes labeled with three or four DNA molecules produce aggregated, lower-mobility structures, possibly due to one enzyme bridging two or more DNA tiles. Based on the above studies, the purified enzyme possessing two identical anchor strands is chosen to assemble onto the DNA nanostructures, which has been proven to be the most efficient assembly components with high yield, as well as reducing the aggregated structures[57]. To achieve better separation, it is recommended to remove the excess DNA molecules by the centrifugal filtration before AE-FPLC.

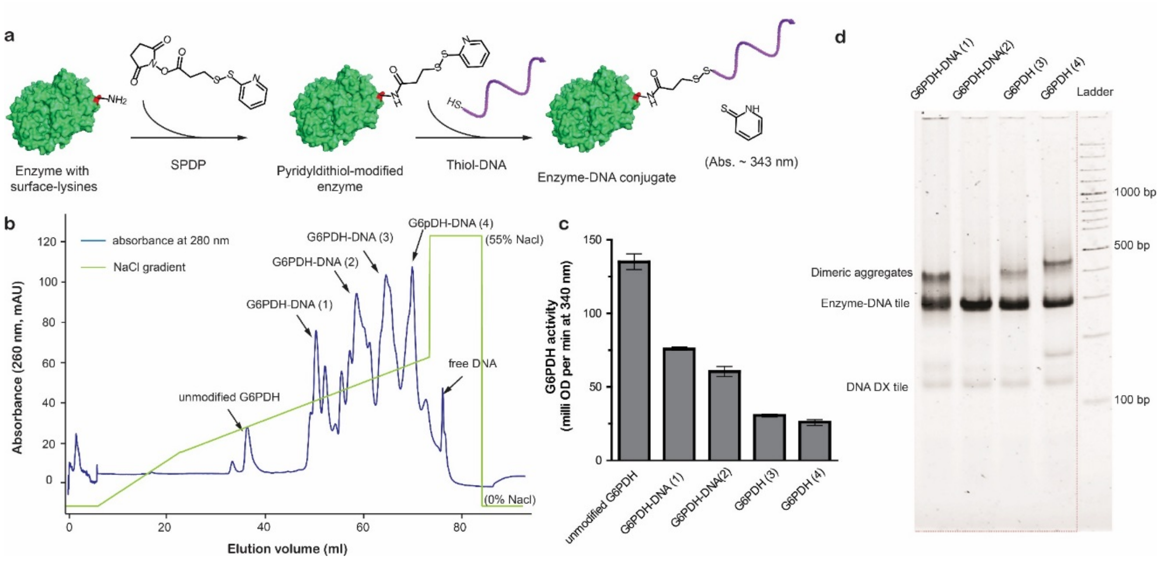

Figure 2.2. Conjugation and purification of protein-DNA using SPDP crosslinker. (a) A SPDP chemistry for crosslinking a thiol-modified oligonucleotide to the lysine group of an enzyme. **(b)** Anion-exchange FPLC to purify DNA conjugated proteins. The enzymes (G6PDH) labelled with different number of DNA are separated into distinct peaks that are collected in fractions. Condition: buffer A, 50 mM sodium phosphate (pH~7.5); buffer B, 50 mM sodium phosphate, 1 M NaCl (pH 7.5). The identities of the distinct peaks are assigned using the A260 and A280 absorbance as shown in **Table 2.4**. **(c)** DNA-conjugated G6PDH with the labelled DNA of 0, 1, 2, 3 and 4, collected from FPLC. Assay conditions: 2 nM enzyme is incubated with 1 mM G6P and 1 mM NAD^+ in 100 mM HEPES (pH 8).

Enzyme activity is measured by the initial velocity of increased absorbance at 340 nm due to the reduction of NAD^+ to NADH. **(d)** Native PAGE characterization of the assembly of a series of DNA-conjugated G6PDH onto a DX tile. A three-fold molar excess of enzyme is used for the assembly. The gels are stained with SYBR®Green to reveal the mobility of the assembled DNA structures.

Prior to the SPDP labelling, the enzyme solution must be exchanged into a non-amine buffer solution, such as HEPES or phosphate buffer. The presence of primary amines in the buffer (e.g. Tris) can react with SPDP, and decrease the labeling efficiency. The SPDP labelling reaction is also highly sensitive to the pH values of the reaction solution. For a neutral or acidic pH, the primary amine on the side chain of the lysine residue is protonated due to its high pKa of ~ 10.2, and thus reacting slowly with NHS group. The SPDP labelling reaction is kept at pH ~ 8.5 for deprotonating the primary amines. After the reaction, it is important to determine the labelling ratio of SPDP molecules per enzyme. The T-CEP (tris(2-carboxyethyl)phosphine) is added into the solution of SPDP-modified enzymes for reducing the disulfide bond to release pyridine-2-thione, resulting in an increased absorbance at 343 nm (extinction coefficient: 8080 $M^{-1}cm^{-1}$). The labelling ratio of SPDP molecules can be estimated using the equation as below:

$$SPDP\ labelling\ ratio = \frac{\frac{\Delta 343}{8080}}{[Enzyme]} \qquad (3)$$

As shown in **Fig. 2.3**, the activities of SPDP-labelled enzymes are tested depending on the labelling ratio of SPDP molecules per enzyme. Among the five tested enzymes, GOx is affected least upon SPDP labeling, maintaining ~ 80% activity of unmodified enzyme with even 6 labeled SPDP per enzyme on average. However, the activities of other enzymes are more seriously reduced when the labelled SPDP per protein is more than 2 or 3. These decreased activities may be attributed to the chemical neutralization of surface lysine residues (lysine is basic) with the SPDP labelling which makes enzymes to be more acidic pI values, or the partially structural denaturation during the chemical conjugation process. For maintaining the activity of enzymes, we generally label ~ 1 - 2 SPDP molecules per enzyme on average. Next, SPDP-modified enzyme is reacted with a thiol-modified oligonucleotide through a disulfide bond exchange of the activated pyridyldithiol group. The concentration of DNA-conjugated enzyme is estimated using the A260 and A280 absorbance as below:

$$A_{260} = \varepsilon_{260,enzyme} * Conc._{enzyme} + \varepsilon_{260,DNA} * Conc._{DNA} \tag{4}$$

$$A_{280} = \varepsilon_{280,enzyme} * Conc._{enzyme} + \varepsilon_{280,DNA} * Conc._{DNA} \tag{5}$$

$$Ratio \left(\frac{DNA}{enzyme}\right) = \frac{Conc._{DNA}}{Conc._{enzyme}} \tag{6}$$

The theoretical extinction coefficients of oligonucleotides are obtained from the IDT Biophysics (http://biophysics.idtdna.com/). For enzymes containing chromophores, such as HRP with heme cofactor ($\varepsilon_{405\ nm} \sim 100,000\ M^{-1}\ cm^{-1}$), the enzyme concentration can be determined by the absorbance of chromophores.

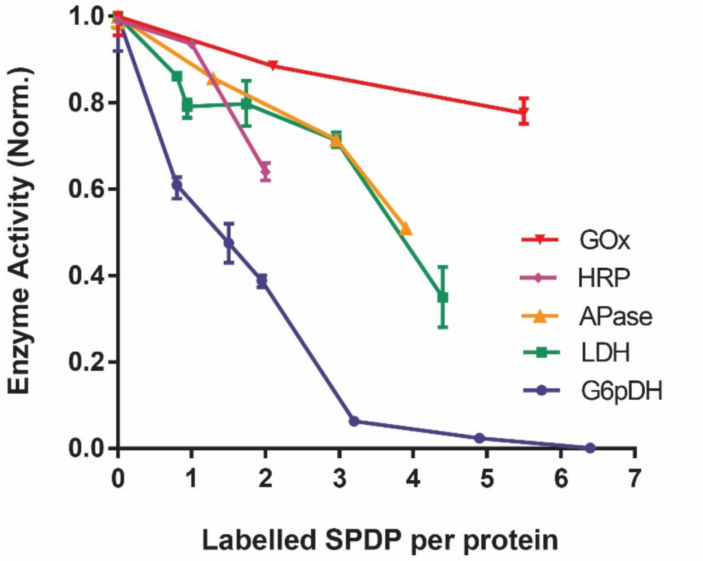

Figure 2.3 Enzyme activities vs labelled number of SPDP molecules. Assay conditions are described as: 1 nM GOx is measured with the addition of 1 mM glucose, 1 mM ABTS and 10 nM wildtype HRP in pH 7.5, 1×TBS buffer, with monitoring the increased absorbance at 420 nm. 1 nM HRP is measured with the addition of 1 mM glucose, 1 mM ABTS and 10 nM wildtype GOx in pH 7.5, 1×TBS buffer, with monitoring the increased absorbance at 420 nm. The activity of 20 nM APase is evaluated by adding 200 µM PNPP in 1×TBS buffer. 2 nM G6PDH is evaluated by adding 1 mM G6P and 1 mM NAD+ in pH 7.5, 1×TBS buffer, with monitoring the increased absorbance at 340 nm. 1 nM LDH is evaluated by adding 1 mM mM pyruvate and 1 mM NADH (LDH substrates) in pH 7.5, 1×TBS buffer, with monitoring the decreased absorbance at 340 nm. Error bars are calculated from the standard deviation of at least three replicates. All above results indicate that activity of enzymes may be significantly damaged with the SPDP label ratio > 2.

2.2.1.2 Site-specific bio-conjugation strategies for coupling DNA to protein enzymes

Gene cloning into Halo-tag vectors

Protein sequences of Glucose-6-phosphate dehydrogenase (G6pDH), Malate dehydrogenase (MDH), Alcohol dehydrogenase (ADH), Formaldehyde dehydrogenase (FALDH) and Formate dehydrogenase (FDH) were obtained from GenBank. DNA sequences encoding for these proteins were purchased from Genscript with codons optimized for E. coli expression. ADH, FALDH, FDH, G6pDH, and MDH genes were digested with the restriction enzymes PvuI and NotI (New England Biolabs) and cloned into pH6HTN vector (Promega) digested by the same enzymes. Ligation reactions were performed by mixing the digested gene and vector with a 3:1 molar ratio in 1X ligation buffer and 1U T4 DNA ligase (New England Biolabs) at room temperature for 2 hours. Ligation products were transformed into the NEB 5-alpha competent cells (New England Biolabs) and the correct clones were confirmed by DNA sequencing. The pH6HTN vector and gene plasmids maps were shown in **Figure 2.4**.

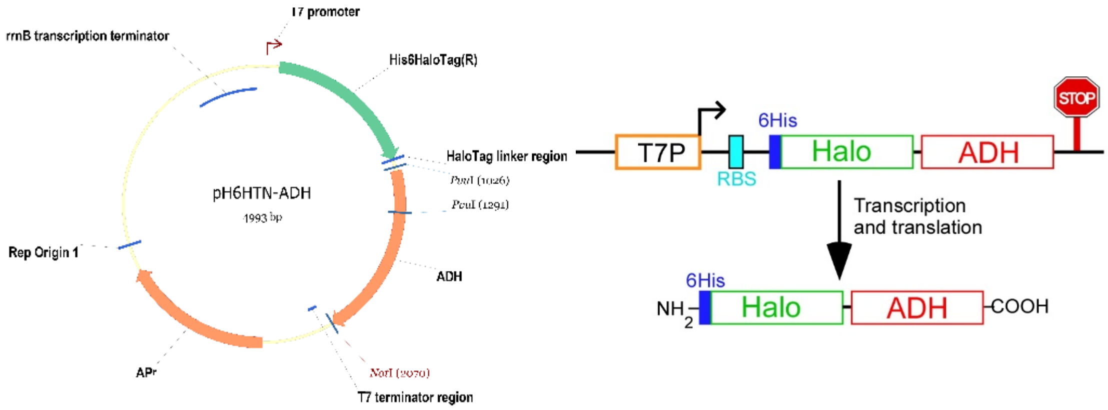

Figure 2.4. **An example plasmid schematic map and expression cassettes for Halo-ADH**. Transcription in *E. coli* is driven by T7 promoter, and a 6His tag was expressed at the N-terminal of Halo tag facilitating the protein purification by Histrap columns.

Halo-tagged enzyme expression and purification

Plasmids pH6HTN-protein were transformed into E. coli NEB T7 express LysY competent cells (New England Biolabs). A single colony was inoculated into 10 ml LB medium and grown at 37°C with constant shaking for overnight. The 10 ml overnight culture was then inoculated into 1 L LB medium and incubated in a 37°C shaking incubator. Isopropyl-β-D-thiogalactopyranoside (IPTG) was added to a final concentration of 0.5 mM after OD600 reached 0.6. E. coli cells were pelleted down 3 hours after IPTG induction by centrifugation at 7,000xg for 15 min. Cells were then resuspended in 20 ml of lysis buffer (20 mM Sodium Phosphate pH 7.5, 0.5 M NaCl, 20 mM imidazole and 0.3 mM TCEP supplemented with 1X Complete Protease Inhibitor Cocktails [Roche Diagnostics]) and lysed with sonication. The cell lysate was clarified by centrifugation at 20,000xg for 30 min at 4°C and the supernatant was filtered through a 0.22 μM membrane. The cell lysate containing 6XHis tagged Halo fusion proteins were loaded onto the Histrap HP chromatography (GE Healthcare) under the manufacturer's instructions (**Figure 2.5A**). The Histrap column was then washed with 10 ml buffer containing 70 mM imidazole in the lysis buffer and Halo tagged proteins were eluted with 10 ml 250 mM imidazole buffer. The purity of the three enzymes from the elution fractions were verified by 4-15% Mini-PROTEAN TGX Stain-free SDS-PAGE gel (**Figure 2.5B**). Different fractions containing the desired proteins were pooled and subjected for the DNA conjugation.

Conjugating DNA to Halo-tagged proteins

Previously, we developed SPDP (N-Succinimidyl 3-(2-pyridyldithio)-propionate) crosslinking chemistry for attaching oligonucleotides to Lysine residue on protein surface.

Due to presence of multiple lysine residues on the surface of dehydrogenases, the reaction products are mixtures of unique conjugates with different number of DNAs attached. To isolate enzymes modified with different numbers of DNA oligonucleotides, we developed purification method using anionic-exchange chromatography by AKTA fast-protein liquid chromatography (FPLC, GE Healthcare). It is important to be noted here after FPLC purification we got conjugates with the same average number of DNAs per protein, but the site of DNA labeling may vary. It was not a site-specific conjugation method.

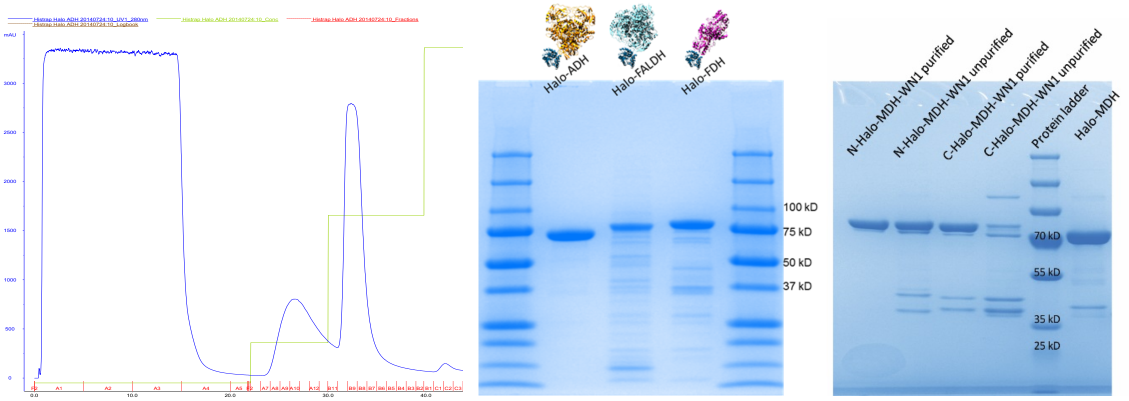

Figure 2.5 Halo-tag enzymes purification and charaterization. (**A**) Halo-ADH Histrap HP FPLC chromatography. (**B**) SDS-PAGE of three enzymes after Histrap purification. The theoretical molecular weight of these three enzymes are 73 kDa, 78 kDa and 80 kDa respectively. (C) SDS PAGE of wildtype Halo-MDH and N-terminal Halotagged MDH conjugated with WN1 (DNA strand) and C-terminal Halotagged MDH conjugated with WN1.

To achieve more accurate control over the orientation and decrease the activity lose after SPDP modification we developed a site-specific Halo-tagged protein-DNA conjugation method (**Figure 2.6**). First step, 100 µL of 10 mM HaloTag ® Succinimidyl Ester (O2) Ligand (purchased form Promega) was prepared in DMSO. 500 µL of 100 µM 5'amine-modified oligo was incubated with 20 fold excess Halo tag ligand in 100 mM NaHCO3 (pH 8.5) for 2h. After reaction, excess Halotag-ligand was removed by washing with Amicon, 3 kD cutoff filters. Halotag-ligand conjugated DNA was characterized by 14% denaturing gel as shown in **Figure 2.6B**. The reaction yield was estimated to be ~50% from the band intensity between ssDNA and ssDNA-ligand conjugates. Second step, 500 µL of 40 µM enzyme solution was incubated with DNA-ligand conjugates in 10 mM sodium HEPES (pH 8.5) at room temperature for one hour, allowing Halo tag ligand reacting with Halo-tagged protein forming a covalent linkage. For Halo-FDH-DNA conjugation, a 2-fold excess of ssDNA-ligand was used, while Halo-ADH/ FALDH-DNA conjugation used a 2-fold excess of ssDNA-ligand. For Halo-G6pDH-DNA conjugation, a 2-fold excess of ssDNA-ligand was used, while Halo-MDH-DNA conjugation used a 4-fold excess of ssDNA-ligand.

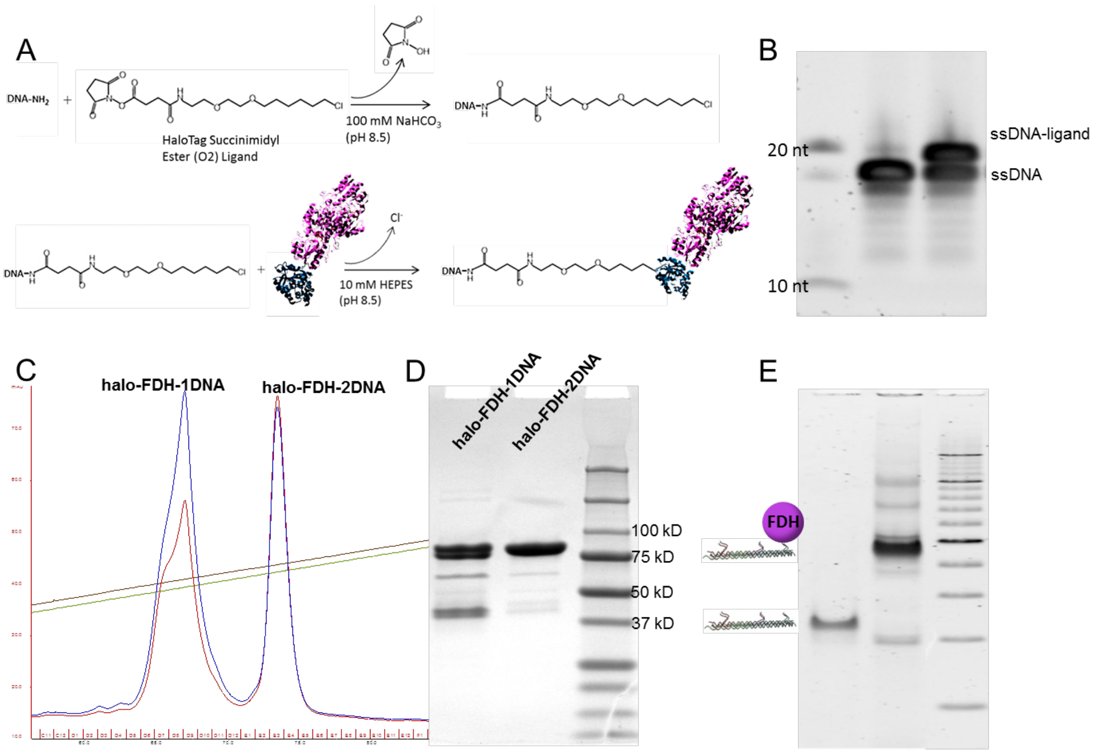

F

DNA	A260/A280	ε^{260} (M^{-1} cm^{-1})	ε^{280} (M^{-1} cm^{-1})	Protein	A260/A280	ε^{260} (M^{-1} cm^{-1})	ε^{280} (M^{-1} cm^{-1})	Conjugates	A260/A280	A260	A280	DNA - to- Protein Ratio	Protein Conc. (uM)
WN2	1.60	130100	81313	**halo-FDH**	0.63	147609	234300	**wildtype**	0.63	7.938	12.60	0.00	53.78
WN2	1.60	130100	81313	**halo-FDH**	0.63	147609	234300	**labeled with 2DNA**	0.97	3.8412	3.96	1.56	10.98

Figure 2.6. Site-specific Halo-tagged protein-DNA conjugation. (A) A schematic illustration of the conjugation process; (B) 14% denaturing gel of unmodified single-stranded DNA (ssDNA, lane 1) and ssDNA-ligand conjugates (lane 2), yield is estimated to be ~50% from band intensity; (C) Anion-exchange FPLC purification of Halo-Formate dehydrogenase (FDH)-DNA conjugates. Condition: buffer A, 50 mM sodium phosphate (pH7.5); buffer B, 50 mM sodium phosphate, 1 M NaCl (pH 7.5). (D) SDS PAGE of 1 DNA labeled Halo-FDH and 2 DNA labeled Halo-FDH; (E) 3% Native PAGE characterization of DNA tile-protein assembly. Lane 1: DNA tile, lane 2: tile assembled with with purified Halo-FDH labeled with 2 DNAs; (F) Quantification of a purified DNA-

conjugated Halo-FDH: an A260/A80 ratio of 1.6 corresponds to ~ 1.6 DNA per protein, with a DNA-conjugated protein concentration of ~ 11 μM.

To get enzyme modified with exact number of labeled oligonucleotides, the Halo-tagged protein-DNA conjugates obtained in the above procedures were then purified with anionic-exchange chromatography using ionic-exchanged FPLC as shown in **Figure 2.6C** (Same buffer and gradient as the purification method we used for SPDP conjugation). 2 peaks from the corresponding chromatogram were collected, including protein functionalized with 1 DNA and protein functionalized with 2 DNAs. The filtered protein-oligo solution was quantified by absorbance at 260 and 280 nm (**Figure 2.6F**).

SDS PAGE (**Figure 2.6D**) showed single band of Halo-FDH-2DNA since both two monomers has DNA conjugated on Halo tag, while Halo-FDH labeled with 1 DNA showed 2 bands, the higher one corresponds to DNA conjugated monomer and the lower band corresponds to monomer without DNA conjugation. Assembly of protein on DNA for Halo-FDH-DNA were evaluated by 3% native PAGE (**Figure 2.6E**). Halo-FDH labeled with two DNA molecules gave the correct assembly of one protein per DNA structures with more than 80% yield. Assembly of protein on DNA tiles depending on labeled DNA molecules per protein for Halo-G6pDH-WN1 and Halo-MDH-WN1 were evaluated by 3% native PAGE (**Figure 2.7**). Halo-G6pDH and Halo-MDH labeled with two DNA molecules gave the correct assembly of one protein per DNA structures with more than 90% yield. Protein labeled with one DNA molecules resulted in lower assembly yield and dimeric assembly.

Evaluating the enzymatic activity of Halo-tagged protein-DNA conjugates

The activities of purified Halo-protein-DNA were evaluated and compared with the activities of wild type Halo-proteins, as shown in **Figure 2.8**. The activity of all dehydrogenases (ADH, FALDH and FDH) was evaluated by the rate of reduction of NAD^+ to NADH as monitored by the change in absorbance at 340 nm (NADH production). Michaelis-Menten plot is analyzed to for determine the k_{cat} and K_m value of wild type Halo-tagged proteins and Halo-protein-DNA conjugates. For all 3 dehydrogenases, K_m value remains the same comparing before and after DNA conjugation: Halo-ADH (11.9 mM) and Halo-ADH-DNA (10.5 mM); Halo-FALDH (32.6 μM) and Halo-FALDH-DNA (35.2 μM); Halo-FDH (6.1 mM) and Halo-FDH-DNA (6.0 mM), which indicated that DNA labeling using Halo tag method doesn't inhibit or increase the binding affinity of substrate and 2 dehydrogenases. However, k_{cat} varied differently with different proteins (**Figure 2.8D**). For Halo-ADH, after DNA conjugation, the activity only remained ~ 30% of wild type. DNA labeling didn't change the activity at all. The reason of different activity change with different proteins is unknown for now. The activities of purified Halotagged protein conjugated with 1 and 2 DNAs were evaluated and compared with the activities of SPDP modified protein with 1 and 2 DNAs, as shown in **Figure 2.**8EF. Halo-G6pDH labeled by two DNA molecules has 1.5 fold activity of the SPDP-G6pDH, while Halo-G6pDH labeled by 1 DNA molecules has similar activity of the SPDP-G6pDH. N-terminal Halo-MDH labeled with 2 DNA has ~ 3 fold activity enhancement compared to SPDP labeled MDH. For both dehydrogenases we tested here, Halotagged dehydrogenases remains activity when labeled with multiple DNAs while SPDP method activity decreased significantly when labeled DNA molecules increases.

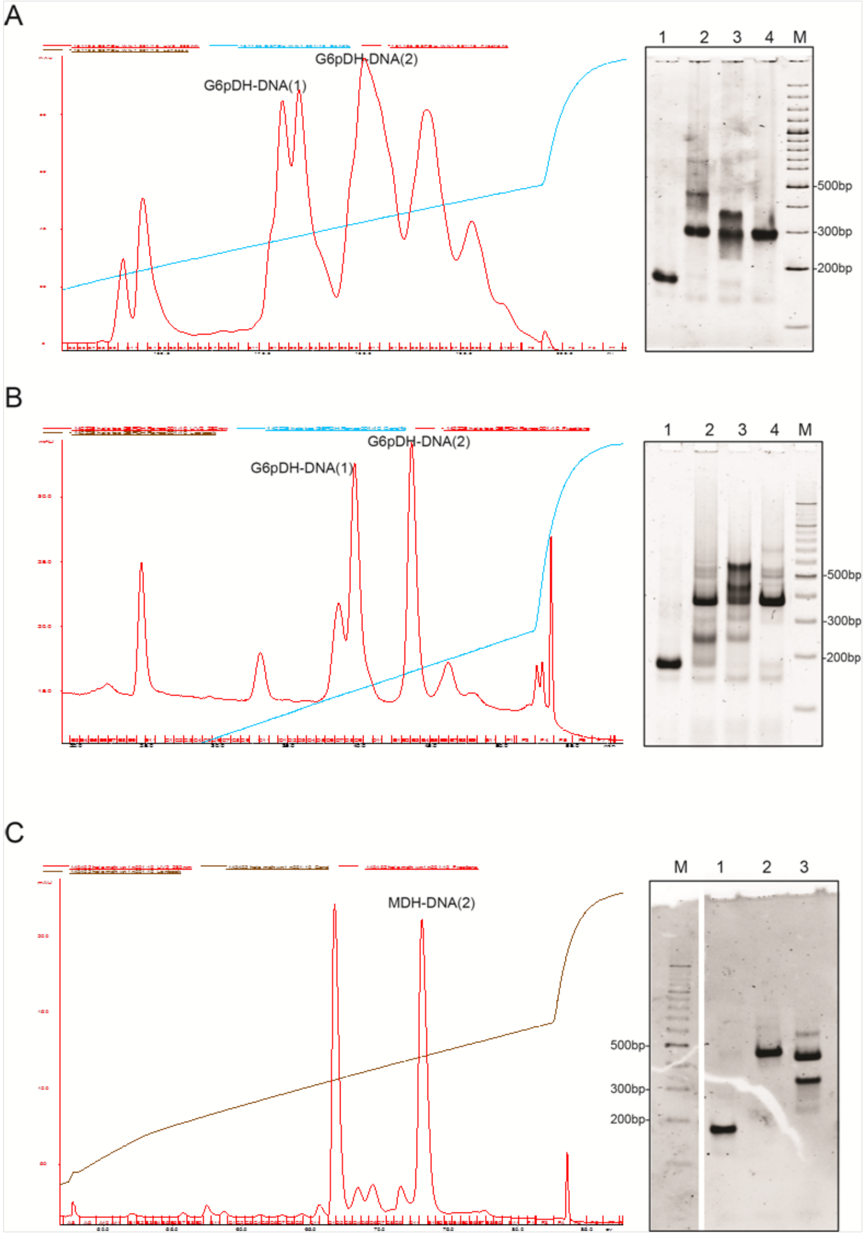

Figure 2.7 Structural comparison of SPDP crosslinking and halotag protein-DNA conjugation methods. Left, Anion-exchange FPLC chromatograph of G6pDH-DNA & MDH-DNA conjugates; right: native gel characterization of DNA tile-protein assembly. SPDP cross-linked G6pDH-DNA conjugates (A) and Halotagged G6pDH-DNA conjugates (B). Lane 1 to 4 of 3% native gel: DNA tile, tile assembled with unpurified G6pDH-DNA, tile assembled with purified G6pDH labeled with 1 DNA, and tile

assembled with purified G6pDH labeled with 2 DNA; (C) Halotagged MDH-DNA conjugates. Lane 1 to 3: DNA tile, tile assembled with purified N-Halo MDH labeled with 2 DNA and tile assembled with purified C-Halo MDH labeled with 2 DNA. Condition: buffer A, 50 mM sodium phosphate (pH7.5); buffer B, 50 mM sodium phosphate, 1 M NaCl (pH 7.5).

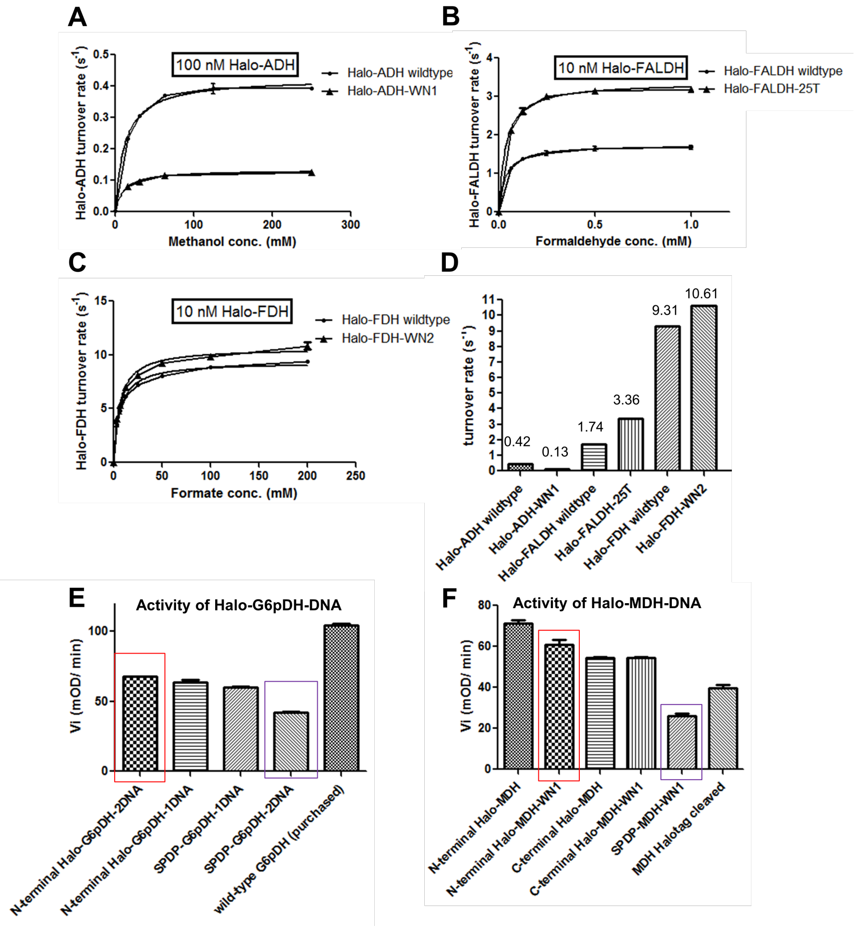

Figure 2.8 Michaelis-Menten plot of halotagged protein-DNA conjugates of alcohol dehydrogenase (ADH), Formaldehyde dehydrogenase (FALDH) and formate dehydrogenase (FDH). (A) Halo-ADH-DNA conjugates activity compared with wildtype

Halo-ADH with respect to methanol; (B) Halo-FALDH-DNA conjugates activity compared with wildtype Halo-FALDH with respect to formaldehyde; (C) Halo-FDH-DNA conjugates activity compared with wildtype Halo-FDH with respect to sodium formate; (D) turnover rates of all protein samples. Assay condition: 100 nM Halo-ADH-DNA conjugates with 15.6 - 250 mM of methanol and 1 mM NAD+ in 50 mM Sodium phosphate (pH 8.5); 10 nM Halo-FALDH-DNA with 0.0625 - 1 mM of formaldehyde and 1 mM NAD+ in 50 mM Sodium phosphate (pH 8.5); 10 nM Halo-FDH-DNA conjugates with 3.125 - 200 mM of sodium formate and 1 mM NAD+ in 50 mM Sodium phosphate (pH 8.5). (E) G6pDH-DNA conjugates activity compared with wildtype G6pDH purchased from Sigma. (F) MDH-DNA conjugates activity compared with wildtype MDH. Assay condition: 2 nM G6pDH-DNA conjugates with 1 mM G6p and 1 mM NAD+ in 100 mM HEPES (pH 8); 2 nM MDH-DNA conjugates with 1 mM OAA and 1 mM NADH in 100 mM HEPES (pH 8).

Cofactor-DNA conjugation

DNA molecules can also be modified with cofactors for controlling the catalytic functions[57,81]. As shown in **Fig. 2.9a**, an amino-modified NAD^+ analogue (enzyme cofactor) is conjugated to an amine-modified oligonucleotide using a disuccinimidyl suberate (DSS) linker on anion-exchange DEAE-Sepharose resins[57,81]. The NAD^+-modified DNA is purified using high pressure liquid chromatography (HPLC) and is characterized using mass spectrometry (**Fig. 2.9b**).

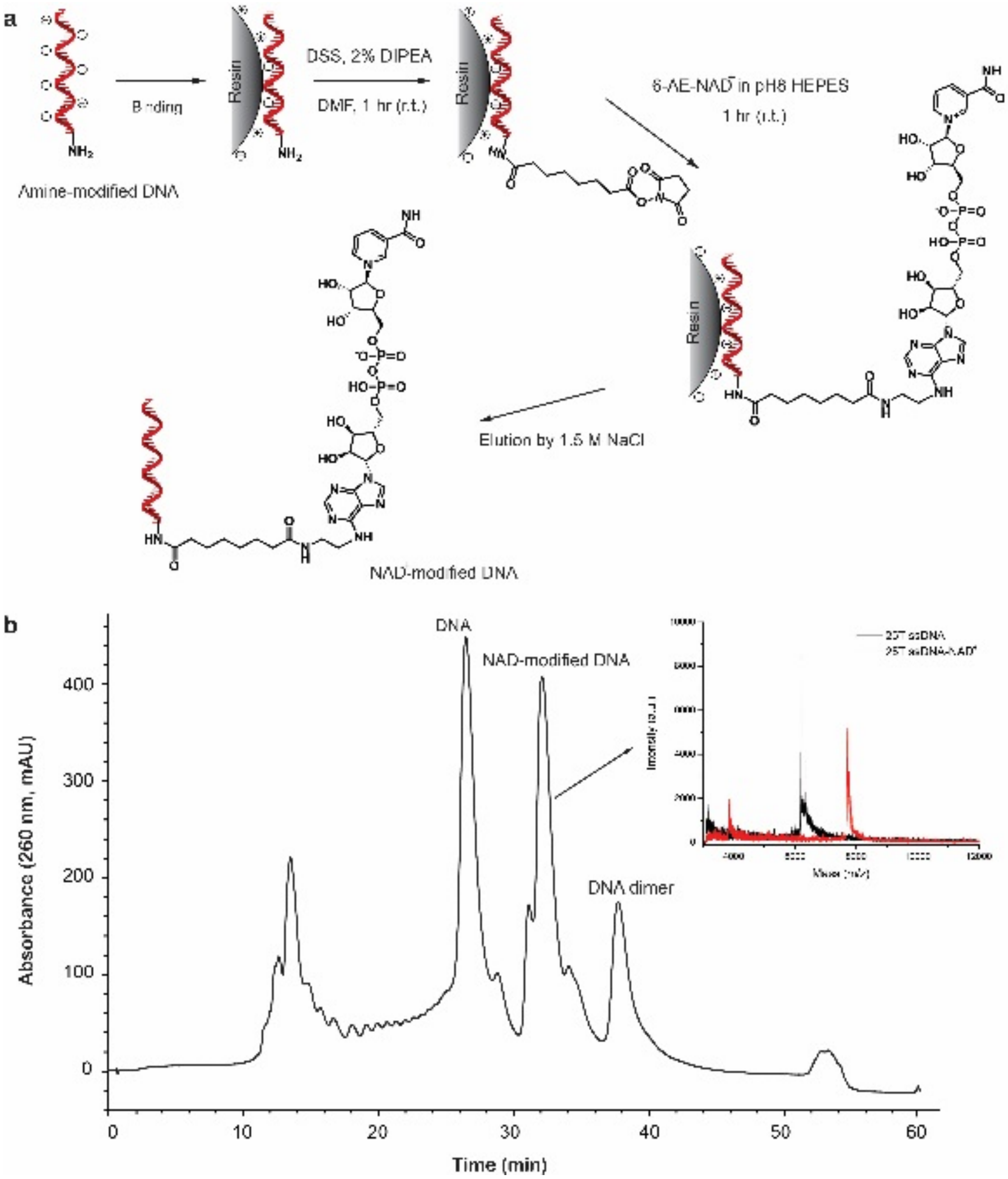

Figure 2.9 Chemical conjugation of oligonucleotides with cofactors. (a) Reaction pathway for conjugating an aminoethyl NAD$^+$ to a 5’ amine-modified DNA strands using the resin-based DSS crosslinking chemistry. **(b)** HPLC purification and MS characterization (inset, upper right) of NAD$^+$-modified oligonucleotides.

2.2.2 Assembly of enzyme complexes onto DNA nanostructures

Open-access softwares are available for designing DNA nanostructures, including Tiamat[138], CadNano[121] and NanoEngineer (Nanorex INC.)[57]. For the detailed methods, please see the previously published articles of designing DNA nanostructures[122,139]. As shown in **Table 2.3**, 2D DNA nanostructures are self-assembled by thermally incubating all the oligonucleotides together in 1×TAE-Mg^{2+} buffer (40 mM Tris, 20 mM acetic acid, 2 mM EDTA and 12.5 mM magnesium acetate, pH 8.0) under a temperature gradient from 90 ºC to 4 ºC[57,81,99,129]. For 3D DNA nanostructures like cages, a longer annealing program is used which slowly decreases temperature from 80°C to 4°C over 20 hours. The sequences design for the DNA nanostructures used in this protocol are available in **Supplementary Information**. After the assembly, the excess, and shorter staple strands can be removed by the centrifugal ultrafiltration with a 100 kDa M.W. cut-off filter.

To assemble enzymes onto the DNA nanostructures, two identical capture strands are displayed on the surface of the DNA scaffolds with a sequence complementary to the anchor strands conjugated to enzymes. The cooperative hybridization between the two capture strands and the two anchor strands can significantly increase the yield and stability of the assembled enzymes on the DNA nanostructures. Generally, excess enzymes (e.g. 3-fold molar excess) are incubated with DNA nanostructures in 1 × TAE-Mg^{2+} buffer (pH 7.5). The mixture is thermally incubated using a PCR thermocycler with a temperature gradient from 37°C to 10°C: 37°C for 5 min; 36 - 10°C, 2 min per degree decrease. The assembled sample is then kept at 4°C for storage.

2.2.3. Characterization of the assembled enzyme complexes

Multiple methods have been developed to analyze and visualize the assembled 2D and 3D enzyme complexes, including gel electrophoresis, AFM, and TEM (**Fig. 2.10**).

- **Gel electrophoresis**: For the smaller DNA tiles of a few hundred bps size (e.g. DNA double-crossover (DX) tiles), the native polyacrylamide gel electrophoresis (native PAGE, **Box 1**) is an efficient tool to characterize the assembled structures[57,81]. the addition of an enzyme onto a DNA tile results in a clear band shift with the slower mobility due to the increased mass and the change of the charge for the enzyme-assembled DNA nanostructure. To improve the imaging contrast, dual-color fluorescent gel imaging is used to confirm the co-assembly of dye-labelled enzymes onto the DNA nanostructures. The assembly yield of enzyme complexes can be approximately estimated by comparing the pixel intensity of a migrated band for an enzyme-assembled DNA structure with the pixel intensity of a migrated band only containing a DNA nanostructure.

  The assembly of large DNA nanostructures (e.g. DNA origami) can be characterized using agarose gel electrophoresis (AGE) (**Box 2**), such as the half DNA cage and the full DNA cage. Unlike native PAGE for characterizing small DNA tiles, the assembly of enzymes onto the DNA structures produces very small band shifts due to the almost ignorant mass of enzymes (a few hundred kDa) as compared with DNA origami structures (~ 4.7 million kDa). It is difficult to differentiate between the enzyme-assembled DNA structures and the DNA structures only using the band shifts of AGE. The assembly of enzymes onto the large nanostructures can be confirmed by using the fluorescently-labelled enzymes. However, the yield of the assembly cannot be accurately determined from the fluorescent gel.

- **AFM**: For the giant and planar DNA nanostructures, such as rectangular DNA origami, AFM (**Box 3**) is used to directly visualize the assembly of enzymes on the surface of the nanostructures, where the assembled enzymes result in brighter spots due to their increased heights on the surface of the DNA origami tile. With the AFM imaging, multiple spatial parameters of inter-enzyme distance, height and geometric arrangement can be accurately evaluated.
- **TEM**: For 3D DNA nanostructures, negative-staining TEM (**Box 3**) is used to visualize and characterize the assembly or encapsulation of enzymes on/within these 3D nanostructures. The encapsulation of two enzymes within a DNA nanocage is identified by TEM imaging, where the presence of the enzyme produces a brighter and lighter spot than DNA structures. This is due to the fact that the enzyme is negatively stained and absorbs fewer electrons (or more transmitted electrons) than the uranyl-stained DNA helices which absorb or scatter more electrons (less transmitted electrons). However, the negatively staining TEM generally produces a low-resolution image of enzyme complexes, which makes it difficult to quantitatively evaluate the encapsulated enzymes.

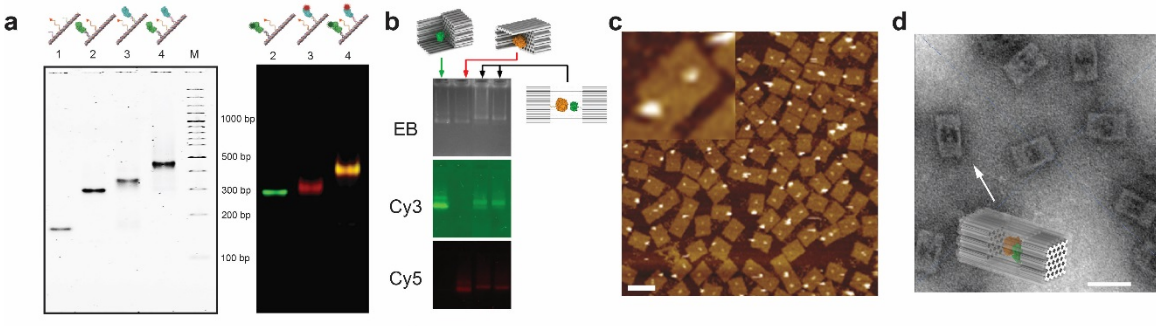

Figure 2.10 Characterization of enzyme-assembled DNA nanostructures. (a) Native PAGE (3%) characterization of a series of nanostructured complexes consisting of a pair of G6pDH/MDH. Left: SYBR Green-stained gel of (1) a DNA tile with a NAD$^+$-modified arm; (2) G6pDH-NAD$^+$ semi-structure; (3) MDH-NAD$^+$ semi-structure and (4) fully assembled G6pDH-NAD$^+$-MDH structure. Right: fluorescence gel image of an Alexa 555-labelled G6pDH-NAD$^+$ structure (lane 2), an Alexa 647-labelled MDH-NAD$^+$ structure (lane 3), and a dual color image of a G6pDH (AlexFluor 555 labelled)-NAD$^+$-MDH (AlexaFluor 647 labelled) structure (lane 4). M: double stranded DNA ladder[57]. (**b**) AGE characterization of a DNA nanocage encapsulating a GOx/HRP pair[129]: Lane 1 (from left), a half-cage encapsulated with a Cy3-labelled GOx; lane 2: a half-cage encapsulated with a Cy5-labelled HRP; lane 3 and 4: a full-cage (dimer of two half-cages) encapsulated with both GOx and HRP. The gel is visualized in three imaging channels: EB: visualization of ethidium bromide-stained DNA structures. Cy3: visualization of Cy3-labelled GOx. Cy5: visualization of Cy5-labelled HRP[129]. **(c)** AFM imaging of a pair of GOx/HRP assembled on a rectangular DNA origami tile, where the assembly of two enzymes results in the brighter spots due to the increased height than the surface of a DNA origami. Scale bar: 100 nm. **(d)** Negatively stained TEM images of DNA cages containing a pair of GOx and HRP (shown as less stained dots). Scale bar: 50 nm[129].

2.2.4. The purification of enzyme-assembled DNA nanostructures

To accurately analyze the function of the assembled enzyme complexes, it is necessary to remove the impurities of excess and free enzymes, oligonucleotides and aggregations. Two purification methods have been developed to purify the enzyme-assembled DNA nanostructures depending on their size. For smaller enzyme-DNA tiles less than 1000 kDa (e.g. DX tiles), size-exclusion (SE) chromatography is an efficient approach to separate the different assembly components based on their sizes. As shown in **Fig. 2.11a**, a DX tile-organized multienzyme complex is purified using SE-FPLC, where the large aggregates are eluted out first, followed by the assembled enzyme complex. The smaller and excess enzymes or DNA fragments are eluted out at last. These purified components are collected and characterized by native PAGE (**Fig. 2.11b**).

For larger nanostructures (e.g. DNA origami) that are beyond the separation range of size-exclusion chromatography, AGE (**Box 2**) is employed to purify the enzyme-assembled DNA structures and remove excess, free enzymes[140]. It is important to check the integrity of the purified nanostructures using native PAGE, AFM or TEM before evaluating the activities.

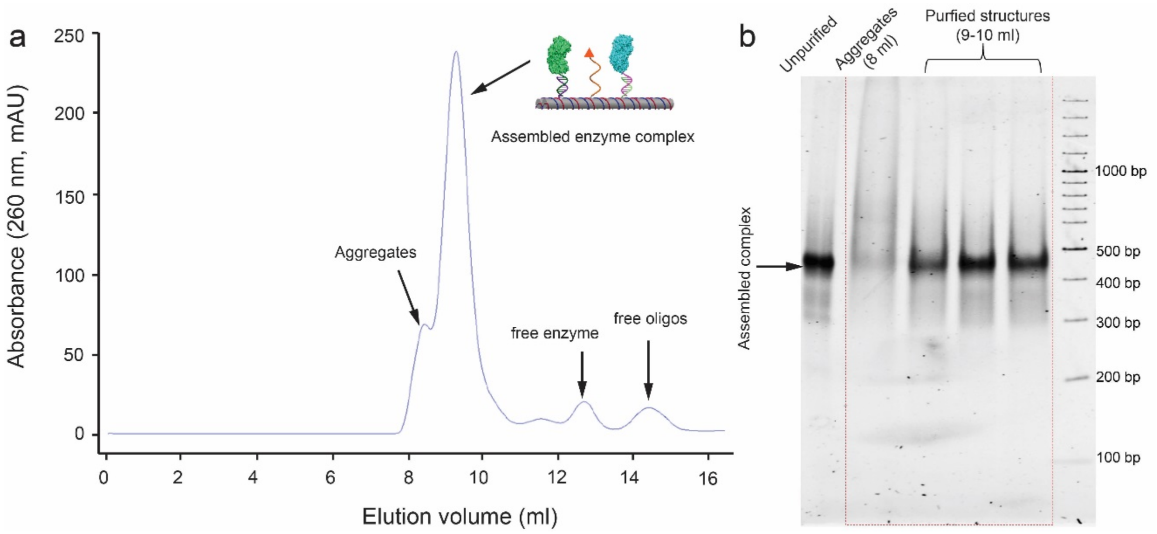

Figure 2.11 Purification and characterization of enzyme-DNA structure complex. (a) Size-exclusion FPLC purification of a fully assembled G6pDH-NAD$^+$-MDH structure to get rid of excess enzymes and free DNA oligoes. Running buffer: 100 mM HEPES (pH 8).

(b) 3% native PAGE characterization of the structures collected in size-exclusion FPLC: The faction 8-9 ml contains aggregated structures with smear bands. The fraction 9-10 ml is the fully assembled enzyme structures. Unpurified structure is also shown in the left lane as a control, which contains incomplete assemblies, aggregations and free proteins.

2.2.5. Activity evaluation of the assembled multienzyme complexes

Colorimetric or fluorescence assays are commonly used to evaluate enzyme activities in bulk solution, where the enzyme-catalyzed reactions produce a change in the absorbance of the solution or release fluorescence signals that are proportional to the generation of product molecules. The activity of a DNA nanocage-encapsulated G6PDH (cage-[G6PDH]) is evaluated by monitoring the increased absorbance at 340 nm due to the conversion of NAD^+ to NADH by the oxidation of glucose-6-phosphate. In a typical time-coursed assay, the fitted value of the initial slope is used to characterize the initial velocity of the enzyme-catalyzed reaction at the starting substrate concentration. Because the excess and free enzymes are removed from the solution of cage-[G6PDH], the activity enhancement of cage-[G6PDH] is estimated by directly comparing the initial velocity of the encapsulated enzyme with the value of the unencapsulaed one at the same enzyme concentration. Further, Michaelis–Menten kinetic analysis is performed by measuring the speed of the reactions depending on a series of substrate concentrations. The detailed kinetic analysis shows that the enhancement of a Cage-[G6PDH] is mainly attributed to the boosted turnover number of the enzyme (~ 5-fold k_{cat}) rather than the change of K_m.

2.2.6 Limitations

Although self-assembled DNA nanostructures have demonstrated great potentials for organizing multienzyme complexes with the precise control over several spatial parameters on the nanoscale, including distances and relative angles, as well as geometric arrangements, there are still limitations of the current technique that need to be realized or be improved for broader applications. First, DNA nanostructures organize multienzyme complex on nanometer precision (3-5 nm resolution), not angstrom precision. Thus, it is difficult to manipulate the molecule complex at the atomic-level, such as the arrangement of amino acids in the enzyme active sites. Second, the current protocol uses a traditional non-site specific chemistry (e.g. lysine conjugation via SPDP) to conjugate a DNA with an enzyme, which is unable to control the orientations of enzymes on the DNA scaffolds. To control the orientation, recent progresses of the site-specific protein conjugation chemistry[35,141] can be applied to labelling DNA molecules onto the protein surface. With the site-specific DNA-enzyme conjugation, the orientation of an enzyme may be more precisely controlled by using two or three capture strands to fix the enzyme on the DNA nanoscaffolds. Third, the current protocol was demonstrated successfully for assembling and characterizing the nanostructure complexes consisting of a few pairs of enzymes[57,81,99,129,142]. However, one should realize that the overall assembly yield may be reduced when increasing the size and the number of components in the assembled structures (e.g. protein arrays). This overall assembly yield can be estimated using the similar calculation as that is used for the peptide or nucleotide synthesis: $Y_{overall} \sim (p)^n$, where p is the average assembly yield for individual enzyme, n is the total number of assembled enzymes. The assembly yield also decreases for the crowded enzyme complexes due to the steric crowding between enzymes. For example, the assembly yield of a GOx/HRP pair on a DNA origami tile increases from ~ 50% for 10-nm spacing distance to > 90% for 45-nm spacing distance[99]. The stability of enzyme-assembled DNA nanostructures is another concern because of the possible degradation of DNA nanostructures under low Mg^{2+} concentration[143]. In our tests, the structures of assembled enzyme complexes were stable in a buffer (1 × TBS or 100 mM HEPES) containing 1 mM Mg^{2+} over a few days under the storage at 4 °C[57,81,99,129]. The assembled complexes also stay structurally intact and maintain integrity after enzyme reactions[57,99,129].

2.3.Procedure

DNA-enzyme conjugation and purification ● TIMING 6 - 8 hour

1| Enzymes are first pre-washed twice with 50 mM sodium HEPES buffer (pH 7.5) using an Amicon-30 kDa cutoff filter with the centrifuge at 10, 000 rpm for 15 min at 4 °C. The small impurities and primary amine contaminates are removed. The remaining enzyme solution in the filter is collected and quantified by UV-VIS absorbance using the Nanodrop.

! CAUTION Must wear gloves when handles the biochemical reagents.

▲CRITICAL STEP Prior to collect the enzyme solution, use a micropipette to blow up the solution a few times to re-suspend the accumulated enzymes in the bottom of the filter.

2| Prepare 20 mM SPDP stock solution in DMSO, and store on ice. Add appropriate amount of SPDP (2 – 20-fold excess depending on enzymes) into the enzyme solution For example, for a 5-fold excess SPDP, 5 μL SPDP stock solution is added into 500 μL of 40 μM enzyme solution. Then, 50 μL of 1 M $NaHCO_3$ is added to adjust the final pH value of the reaction solution to be ~ 8.5. The reaction solution is placed in the dark centrifuge tubes or is wrapped with aluminum foil, with the incubation on the rocker at room temperature for one hour.

▲CRITICAL STEP SPDP (NHS ester and pyridyldithiol) is not stable in water or DMSO. Prepare the fresh SPDP prior to the conjugation reaction. The control of pH (8-8.5) is critical for the SPDP modification. It is suggested to use pH paper (8-10) to test the pH value of the reaction mixture.

? TROUBLESHOOTING

3| After the first step of reaction, the excess SPDP is removed by the centrifugal filtration with 50 mM HEPES (pH 7.5) buffer using Amicon-30 kDa cutoff filters at 10, 000 rpm for 15 min at 4 °C, repeating three times. Collect the SPDP-modified enzymes and quantify the enzyme concentration with the Nanodrop. Also record the absorbance at 343 nm.

▲CRITICAL STEP SPDP-modified enzyme must be used for the DNA conjugation in the next a few hours. The modified SPDP group is not stable overnight.

4| Prepare a 20 mM T-CEP solution in 50 mM HEPES buffer, adjust pH to ~ 7.5. Add 1 μL of 20 mM T-CEP into 20 μL SPDP-modified enzyme solution, and incubated in dark at room temperature for half an hour. Quantify the labelled SPDP by reading the increased absorbance at 343 nm due to the release of pyridine-2-thione (extinction coefficient: 8080 $M^{-1}cm^{-1}$).

▲CRITICAL STEP The average labelled SPDP molecules per enzyme should be between 1 – 2 for maintaining the activity. If an enzyme is labeled for more than 3 SPDP molecules, the modified enzyme activity is significantly damaged. Some enzymes may have background absorbance at 343 nm (e.g. GOx or HRP), thus, the increased absorbance can be estimated by ΔA_{343} = A343 (SPDP-enzyme + T-CEP) – A343 (SPDP-enzyme).

5| The thiol-modified DNA purchased from IDT is protected by a disulfide-bond. Prior to use for conjugation, 20-fold excess T-CEP is added into the DNA solution and is incubated for one-hour to cleave the disulfide-bond. After the cleavage, the excess T-CEP is removed by the centrifugal filtration with water using a Amicon 3 kDa-cutoff filter at 10, 000 rpm for 15 min at 4 °C, repeated for three times. The successful cleavage can be characterized by MALDI-TOF. Collect the thiol-modified DNA and store at -20 °C.

6| The SPDP-modified enzyme solution is incubated with a 10-fold excess thiol-modified DNA solution in 50 mM sodium HEPES (pH 7.5) for one hour at room temperature in dark. The successful conjugation can be evaluated by measuring the increased absorbance at 343 nm.

? TROUBLESHOOTING

7| After the reaction, the excess DNA molecules are removed by the centrifugal filtration using Amicon cutoff filters (e.g. 30 kDa). For 500 µL DNA-conjugated enzyme solution, add 3500 µL of 50 mM HEPES (pH 7.5) containing 1.5 M NaCl to wash for one-time, followed by two-time wash with the regular 50 mM HEPES (pH 7.5).

8| The concentration of the DNA-conjugated enzyme and average DNA label ratio is quantified by UV-VIS absorbance of 260 nm and 280 nm as discussed in the Experiment Design.

▲CRITICAL STEP If the measured number of labelled DNA molecules per enzymes is still higher than the average number of labelled SPDP per enzyme, it indicates the presence of nonspecific and unconjugated DNA molecules in solution. The additional wash with 50 mM HEPES (pH 7.5) containing 0.05 % P20 is required to remove these nonspecific-bound DNA molecules.

■ **PAUSE POINT** The purified enzymes can be stored at 4 °C.

AE-FPLC purification of DNA-conjugated enzyme ● TIMING 3-5 hour

9| First spin down the solution of DNA-conjugated enzyme at 8000 rpm for 5 min at 4 °C to remove the insoluble aggregates. Load the supernatant enzyme solution into the FPLC with an anion-exchange column, and the separate the sample by using an elution gradient from 20% 50 mM sodium phosphate containing 1 M NaCl to 55% 50 mM sodium phosphate containing 1 M NaCl, with a flow rate of 1.0 mL/min. The elution gradient is shown in **Table 2.6**. After use, the FPLC system is cleaned by flowing with 30 mL deionized water, and stored in 20% ethanol-water solution.

▲**CRITICAL STEP** The sodium phosphate buffer must be pre-filtered with 0.22 μm filter in order to avoid any insoluble particles that may block the flow channel of the instrument.

10| Multiple peaks from the purification chromatogram are collected and concentrated to ~ 100 μL volume using an Amicon cutoff filter (e.g. 30 kDa). The DNA-conjugated enzyme is characterized by the UV-VIS absorbance for measuring the concentration and the labelled DNA ratio.

■ **PAUSE POINT** The purified enzymes can be stored at 4 °C.

DNA-NAD$^+$ conjugation ● TIMING ~ 4 hour

11| Prepare 10 mM amine-modified DNA and 50 mM AE-NAD$^+$ in deionized water. Prepare DNA-loading buffer and elution buffer for conjugation (**Fig. 2.9a**).

12| Shake the bottle of DEAE resin vigorously to emulsify resin solution. Add 200 μL resin into a Sigma Prep column, spin down at 3000 rpm for 30 s to remove solvent. Then wash the resin with 1 column-bed volume (500 μL) DNA loading buffer for 3 times.

13| 200 µL of 20 nmole DNA is prepared in DNA loading buffer (10 mM Acetate acid and 0.005% Triton X-100) by mixing 2 µL of 10 mM DNA stock with 198 µL loading buffer. Add DNA to resin and incubate DNA-resin mixture on shaker for 10 min, allowing DNA to bind to the resin. The suggested ratio of DNA-to-resin is ~ 1 nmole DNA/10 µL resin. After the incubation, excess solution is removed by spinning down at 3000 rpm for 30 s. DNA binding efficiency can be calculated by measuring the 260 nm absorbance of DNA solution before and after incubation with the resin : (Ab_{260} (before)-Ab_{260} (after))/ Ab_{260} (before). The DNA binding efficiency should be more than 90% for linear oligonucleotides.

▲ **CRITICAL STEP** The bottom of spin column must be capped with red rubber during the incubation.

? TROUBLESHOOTING

14| The resin is washed with 500 µL dry DMF for two times to remove extra water.

15| Prepare DSS linker in DMF with 2% DIPEA (v/v). For 20 nmole DNA, 200 µL of 150 mM DSS is needed. Add DSS linker to resin-bound DNA and incubate for 1 hour on shaker at room temperature.

! CAUTION DMF is flammable, toxic with skin and eye irritation. It is also known as a respiratory sensitization chemical. DIPEA is flammable, corrosive and toxic.

▲ **CRITICAL STEP** DSS linker is moisture sensitive. Store the DSS chemicals in a Dry Box. The DSS solution should be prepared just before the reaction. The bottom of spin column must be capped with red rubber during incubation.

16| The reactant is washed with 500 µL of dry DMF for 3 times to remove excess DSS liker. Then wash one-time with 500 µL DNA loading buffer to re-stabilize surface-bound DNA.

▲ **CRITICAL STEP** The resin-bound DNA must be re-stabilized by DNA loading buffer before the addition of AE-NAD$^+$.

17| A 10-fold excess AE-NAD$^+$ is added into the DSS-modified DNA. For 20 nmole DNA, 200 nmole NAD$^+$ is prepared by adding 4 μL of 50 mM NAD stock into 10 μL of 1 M HEPES (pH 8.0) and 186 μL water (Final reaction buffer contains 50 mM HEPES). The reaction is incubated on the shaker at room temperature for one hour.

▲**CRITICAL STEP** The pH of mixture solution must be controlled between 8 – 8.5 to improve the amine-NHS reaction efficiency. Avoid to add high concentration of NaCl (<100 mM) into the reaction buffer to prevent any ionic-elution of resin-bound DNA molecules. The bottom of spin column must be capped with red rubber during incubation.

■ **PAUSE POINT** The mixture can be stored at 4 °C for overnight.

18| Add 300 μL of DNA-loading buffer into the reaction mixture. Then incubate for 10 min to re-stabilize the DNA-bound resin.

▲ **CRITICAL STEP** The bottom of spin column must be capped with red rubber during incubation.

19| Remove red rubber cap and spin down the solution at 3000 rpm for 30 s to remove excess AE-NAD$^+$, then wash the resin with 200 μL elution buffer (50 mM HEPES (pH 7.5) and 1.5 M NaCl) for 3 times. Collect the filtrate.

■ **PAUSE POINT** The filtrate can be stored at 4 °C for overnight.

20| Wash and concentrate the eluted solution with deionized water using an Amicon 3kDa filter for 3 times. The washed solution is ready for HPLC purification.

■ **PAUSE POINT** The washed solution can be stored at 4 °C for several days.

HPLC purification of NAD$^+$-conjugated DNA ● TIMING 1-2 day

21| Setup the HPLC systems and running protocol as described in the Equipment Setup. Rinse the flow system with deionized water to remove the stored solvent.

22| Attach a MonoQ 4.6/100 PE anion-exchange column to the HPLC. Rinse the column with water for 10-column volumes at 1 mL/min to remove the stored solvent (e.g. 20% methanol). Then, switch the solvents to purge the pump A and the pump B with running buffer of TEAA and methanol, respectively, at a flow rate of 2 mL/min for 5 min. Switch the line to connect with the column to and equilibrate it with flowing 90 % TEAA and 10 % methanol for at least 10 column volumes at 1 mL/min.

! CAUTION TEAA may cause eye and skin irritation. Methanol is flammable, toxic and can cause respiratory sensitization.

▲CRITICAL STEP During the pump purge, make sure the column is disconnected from the flow lines. Make the flow pressure is stabilized during the column equilibration.

23| Inject 5 µL of DNA-NAD$^+$ conjugation mix for an analytical run. It is used to optimize the solvent gradient and sample collection in **Table 2.7**.

24| Inject no more than 50 – 100 µL sample and run the HPLC for separation and collection.

▲CRITICAL STEP For sample collection, it should be realized that there is a delay time between the detector and collector. Setup the appropriate delay for accurately collecting separated samples. The delay time can be estimated by injecting a dye solution into HPLC without column, observing the elution of the sample.

25| The collected samples are frozen at -80 °C for 1 hour, then transfer the sample solution into plastic tubes with a few holes on the cap, which are dried overnight using the lyophilizer. Lyophilized samples are re-dissolved in deionized water and are quantified for concentration with 260-nm absorbance.

■ **PAUSE POINT** The purified DNA solution can be stored at -20 °C for several weeks.

26| Use MALDI-TOF to characterize the purity and molecular weight of NAD$^+$-DNA sample (**Fig. 2.9b**).

Denaturing PAGE purification of the oligonucleotides ● TIMING 2 day

27| Prepare a gel mixture as suggested by **Table 2.5**, adding together solution (A) and solution (B) to a desired concentration.

! CAUTION Toxic PAGE solution. Acrylamide:bis-acrylamide solution is highly toxic and is a potential human carcinogen and teratogen. It is also known as a potent neurotoxin. Wear protective gloves and clothes. All the waste solution and pipettes must be collected in the special containers. It is recommended to assign a special lab space for operating PAGE gels and is labelled with “PAGE contamination area”.

28| The polymerization of the gel is imitated by adding 263 µL APS and 14.7 µL TEMED. 35 mL of the mixture solution is loaded into the gel cassette (SE 600 Vertical Unit, GE Healthcare) using a 50 mL transfer pipet carefully.

▲CRITICAL STEP Make sure that no air bubbles are trapped into the gel during pouring, to ensure a uniform electrical conductance.

29| Insert a comb with 15 wells. The gel casting assembly is left on the bench at room temperature for ~ 60-min for the gel to be polymerized. Then, remove the comb carefully and rinse the wells with deionized water.

? TROUBLESHOOTING

■ **PAUSE POINT** The gel can be stored at 4 °C for up to 1 month. To avoid drying, it is recommended to wrap them with plastic film.

30| Clamp the gel into the electrophoresis tank and carefully rinse the bottom of the wells carefully with 1 × TBE buffer using syringe.

▲**CRITICAL STEP** The bottom of gel wells must be cleaned with buffer to remove any precipitants such as urea crystals or gel aggregates, otherwise, DNA sample may not completely diffuse into the gels.

31| Prepare oligonucleotides in dI H_2O with a concentration of ~ 0.5 OD/μL. Add equal volume of 2 × denaturing tracking dyes (see reagent setup) of either bromphenol blue or xylene cynole FF or both. Vortex the mixture for 20 s, and spin down at 2000 rpm for 30 s. Heat up the mixture to 90 °C for 5 min.

▲**CRITICAL STEP** To improve the efficiency of PAGE purification, 5 OD of oligonucleotides is loaded into each well of the gel. When using the tracking dye, avoid the dye with mobility close to the oligonucleotides, otherwise, it may contaminate DNA sample. The mobility of tracking dyes is illustrated in **Table 2.5**.

32| Vortex the mixture for 10 s, and spin down at 2000 rpm for 30 s. Heat up the mixture to 90℃ for 5 min.

▲**CRITICAL STEP** Do no overheat the sample for higher temperature or longer time.

33| Load ~ 20 ul of the sample mixture into each well, with ~ 5 OD per lane.

34| Turn on the water circulating bath set the temperature at ~ 35 °C. Run the gel at a constant current of ~ 45 mA for ~1 hour. Use the tracking dyes to estimate the migration distance of sample.

! CAUTION High voltage.

35| After the electrophoresis, place the gel on a UV trans-illuminator in the dark room.

With 254 nm UV-light, the DNA band can be directly visualized without the addition of staining dyes (e.g. ethidium bromide). Cut the DNA band from the gel using a razor blade, followed by chopping down into small pieces.

▲**CRITICAL STEP** Prolonged UV illumination may damage the DNA, such as thymine dimerization.

? TROUBLESHOOTING

36| Collect the small pieces of DNA gel is by a centrifugal filter tube (Costar Spin X filter, 0.22 μm). Add 500 μL of denaturing PAGE elution buffer, and incubate on a shaker overnight.

■ **PAUSE POINT** The elution process can be prolonged for 3 day (e.g. over weekend).

37| Centrifuge the filter tube at 8000 rpm for 5 min at room temperature; discard the gel blocks on the top of the filter. Add 1000 μL ethanol into the filtrate solution and vortex to mix it. Incubate the mixture in -80 °C freezer for 1 hour.

▲**CRITICAL STEP** Shorter strands are harder to precipitate and need longer time for incubation.

38| Centrifuge the mixture at 13,000 rpm for 30 min at 4 °C. This step is to precipitate the DNA. Check whether there are white precipitants on the bottom of the tube. Carefully pour out the liquid, then add 1000 μL of ice-cold 70% ethanol into the precipitants, mix well and centrifuge again at 13, 000 rpm for 10 min at 4 °C. Pour out the solution.

39| Use a vacufuge to dry the DNA sample at 30 °C for 4-6 hour. Then, add in 50 μL dIH_2O to dissolve the DNA solid with vortexing the mixture for 1 min. The concentration of DNA is measured by absorbance at 260 nm using Nanodrop.

■ **PAUSE POINT** The DNA solutions (both purified and crude) can be stored at 4℃ for a few days. Preferably store at -20 °C for the long-period incubation (several months).

? TROUBLESHOOTING

Assembly of DNA nanostructures ● TIMING 2 – 24 hour

40| DNA Nanostructures are designed using open-access softwares of Tiamat[138] or CadNano.[121] The assembly and purification of DNA origami nanostructures are performed using the following procedures:

(A) Assembly of DX-DNA tiles:

(i) All oligonucleotides are purified using 8% denaturing PAGE as described above. 100 μL sample solution is prepared by mixing all oligonucleotides together with 1 μM of each strand in 1 × TAE-Mg^{2+} buffer (pH 8.0).

(ii) The DNA mixture is thermally annealed using PCR thermocycler (Eppendorf) from 90 ºC to 4 ºC with the temperature gradient as shown in **Table 2.3**.

▲CRITICAL STEP The volume of DNA solution cannot exceed 100 μL per PCR tube, otherwise the temperature is not precisely controlled during the thermal annealing process. Use ice to cool the cap of the PCR tube before taking the sample tube out of the PCR plate.

■ PAUSE POINT The assembled DNA structures can be stored at 4 ℃ for a few weeks.

? TROUBLESHOOTING (lost activity)

(B) Assembly of DNA origami structures:

(i) Single-stranded staples are ordered from IDT without further purification. The capture strands are purified using an 8% denaturing PAGE as described above.

▲CRITICAL STEP IDT provides staple strands (~ 100 - 200 stands) in 96-well plates with 100 μM in water. Prepare 1 μM core-solutions by mixing together all the staple strands in the same 96-well plate, and labeled as core-1, core-2 and core-3. The capture strands are excluded from the core-solutions.

(ii) 100 μL of 20 nM single-stranded M13mp18 DNA is mixed with a 5-fold molar excess of staple stands and a 10-fold molar excess of capture strands in 1 × TAE-Mg^{2+} buffer (pH 8.0).[99]

(iii) The DNA mixture is thermally annealed using PCR thermocycler (Eppendorf) from 90 ºC to 4 ºC with the temperature gradient as shown in **Table 2.3**.

▲CRITICAL STEP The assembly of 3D DNA origami structures require a longer and slower annealing program than the assembly of 2D DNA origami structures.

■ PAUSE POINT The assembled DNA origami structures can be stored at 4℃ for a few weeks. Do not remove the excess staple and capture strands for enhancing the stability of assembled structures.

(iv) The excess staple and capture strands are removed by the centrifugal filtration of the origami solution with a Amicon 100 kDa filter using 500 μL, 1 × TAE-Mg^{2+} buffer (pH 7.5), repeating three times. The concentration of DNA origami solution is quantified by 260-nm absorbance using an estimated extinction coefficient of ε_{260} = 109,119,009 $M^{-1}cm^{-1}$.

(v) The purity of the origami tiles is analyzed by agarose gel electrophoresis (2%) as shown in **Box 2**.

Assembly of Enzymes onto DNA nanostructures ● TIMING 2 hour

41| A 100 μL of DNA nanostructure solution is incubated with a 3-fold excess DNA-conjugated enzyme solution in 1 × TAE-Mg^{2+} buffer (pH 7.5). The mixture is thermally incubated within a PCR thermocycler with a temperature gradient from 37 °C to

10 °C[57,81,99,129]. The detailed temperature gradient is: 37 °C for 5 min; 36 – 10 °C, 2 min per degree decrease. The solution is then kept at 4 °C for storage. After the assembly, the enzymes-assembled DNA nanostructures are visualized and characterized using gel electrophoresis, AFM or TEM.

■ **PAUSE POINT** The assembled enzyme-DNA nanostructures can be stored at 4 °C for up to 2-3 weeks. However, it is highly recommended to use the sample within a week.

Gel electrophoresis characterization of enzyme-assembled DNA nanostructures ● TIMING 6-8 hour

42| For small DNA DX tiles, 3-5 % native PAGE is prepared and used to characterize the enzyme assemblies as described in **Box 1**. For DNA origami structures, 2% AGE is used to characterize the enzyme-assembled structures as shown in **Box 2**.

▲**CRITICAL STEP** For large DNA origami nanostructures, it is almost impossible to different the band shift between the DNA nanostructures and enzyme-assembled DNA nanostructures. Thus, fluorescently labelled enzymes and DNA nanostructures are used for dual-color gel imaging to confirm the assembly of enzymes onto the DNA structures as shown in **Fig. 2.10a-b**. The fluorescently (e.g. Cy3 or Cy5) labelled oligonucleotides can be purchased from IDT.

AFM/TEM characterization of enzyme-assembled DNA nanostructures ● TIMING 1-2 hour

43| For the direct observation of enzyme assembly on DNA nanostructures, AFM is used to visualize the small DNA DX tiles and 2D DNA origami structures; and TEM is used to image 3D DNA nanostructures as described in **Box 3**. The assembly yield is estimated by counting the enzyme-assembled DNA nanostructures and the DNA nanostructures containing no enzymes.

Size-exclusion purification of enzyme-assembled DNA nanostructures ● TIMING 4 hour

56| For a typical purification, ~ 500 µL, 750 nM enzyme-DNA assemblies are loaded onto the FPLC system and are eluted with 100 mM HEPES (pH 8) at a flow rate of 0.5 mL/min. An example chromatogram for purification of enzyme-assembled DNA DX tiles is shown in **Fig. 2.11a**.

▲**CRITICAL STEP** The size-exclusion column of Superdex 200 Increase 10/300 GL is a low-pressure column (Max. Pressure ~ 3 M Pa), adjust the flow rate to lower the pressure of the system.

57| The concentration of the purified enzyme-DNA tiles are estimated by 260-nm absorbance using an extinction coefficient that is equal to the ε_{260} sum of double-stranded DNA and enzymes.

AGE purification of enzyme-assembled DNA origami structures ● TIMING 4-6 hour

58| For enzyme-assembled DNA origami structures, excess and free enzymes are removed using AGE as described in **Box 2**. The concentration of purified structures are estimated using the extinction coefficient of DNA origami with ε_{260} = 109,119,009 $M^{-1}cm^{-1}$. The absorbance of individual enzymes is neglectable as compared with the large extinction coefficient of DNA origami.

Enzyme activity assay in bulk solution ● TIMING 2 hour

59| Enzyme assay is performed using 96-well microplate reader (e.g. Multimode from Moleclar Devices or BioTek Cytation 3). Set the instrument to be ready for kinetic measurements of absorbance or fluorescence.

60| For a typical assay, all substrates are prepared in 1 × TBS buffer (pH 7.5) with 1 mM $MgCl_2$, and are then transferred into a 96-well plate with 50 µL solution per well. To initiate the reaction, 50 µL of enzyme-DNA assemblies is added into each well, and start the reading immediately.

▲**CRITICAL STEP** It is highly recommended to use electronic multiple-channel pipettes to increase the pipetting accuracy between multiple samples. Enzyme assays are performed with at least three replicates.

61| Use the kintical software carried by the instrument, or other data-analyzing softwares (e.g. GraphPad Prism or Origin) to fit the initial velocity of enzyme-catalyzed reactions. Detailed kinetical analysis includes the measurement of Michaelis-Menten curves and standard curves of product molecules.

Box-1 | Native PAGE characterization of the enzyme assembly ● TIMING 6 - 8 hour

The native polyacrylamide gel electrophoresis (PAGE) is used to characterize the assembly of small DNA structures and the assembly of enzymes. The native PAGE separates DNA nanostructures depending on their structural size, shape and charges. The addition of an enzyme onto a DNA tile results in a clear band shift with the slower electrophoresis mobility due to the increased mass of the structure. The pixel intensity of the labelled bands (such as EB or SYBR dyes) can be used to estimate the assembly yield of the enzyme-DNA nanostructures, using the following equation:

$$Yield \sim \frac{Intensity_{enzyme-DNA\ complex}}{Intensity_{enzyme-DNA\ complex} + Intensity_{DNA\ structure\ alone}}$$

The native PAGE solutions (0% - 20%) are prepared by mixing 40% acrylamide solution and 1×TAE/Mg^{2+} buffer (**Table 2.4**). The percentage is decided by the size of the assembled structures. For DNA structures larger than 1000 bps, such as DNA origami, agarose gel electrophoresis with the bigger pore size is used to characterize the assembly of the structures.

Procedure

1| The 3% native PAGE is prepared by mixing together 3 mL of 40% acrylamide solution, 4 mL of 10 × TAE/Mg^{2+} and 33 mL of dIH_2O.

!CAUTION Toxic PAGE solution. Acrylamide:bis-acrylamide solution is highly toxic and is a potential human carcinogen, teratogen and neurotoxin. Wear protective gloves and clothes.

2| The polymerization of the gel is initiated by adding 263 µL APS and 14.7 µL TEMED into 35 mL of the gel solution. The mixture is immediately loaded into the gel cassette (SE 600 Vertical Unit, GE Healthcare) using a 50 mL transfer pipet.

▲**CRITICAL STEP** Make sure there is no air bubble being trapped inside the gel after loading into the gel cassette.

3| Insert a comb with 15 wells. The gel casting assembly is left on the bench at room temperature for ~ 3 h for the polymerization.

■ **PAUSE POINT** The polymerized gel can be stored at 4 °C for up to 1 month. It is recommended to wrap the gel cassette with plastic film to avoid dehydration.

? TROUBLESHOOTING

4| The gel cassette is placed into the electrophoresis tank that is filled with 1 × TAE/Mg^{2+}, set up the temperature of the water circulator at 15℃.

▲**CRITICAL STEP** Control of the temperature for PAGE is important for accurately analyzing the assembly of structures. A low temperature promotes the aggregation of the structures, while a temperature higher than the DNA melting point may induce the thermally dissociation of the structures.

5| Add 1.2 µL 10 × non-denaturing loading dye into 10 µL of DNA sample with the final concentration of DNA tiles ~ 50 – 200 nM. Load 10- 20 µL sample into each well.

Box-1 (continued)

6| The gel electrophoresis is run at a constant voltage of ~ 200 V for 2 – 3 hours depending on the size of DNA structures.
! CAUTION High voltage.
7| After the electrophoresis, the gel is stained in ~ 100 mL SYBR® Green/Gold solution (1: 10000 dilution) for 10 mins, followed by the rinse within ~ 200 mL dI H_2O for once.
▲CRITICAL STEP SYBR® Gold stains both single- and double-stranded DNA, as well as proteins. SYBR® Green preferentially stains double-stranded DNA.
8| Image the gel on UV-transilluminator with the selection of SYBR gold/green channel.
? TROUBLESHOOTING

Box-2 | AGE characterization and purification ● TIMING 4–6 hour

Unlike PAGE for small DNA nanostructures, the agarose gel electrophoresis (AGE) is used to characterize and purify large enzyme-assembled DNA nanostructures (e.g. DNA origami). Below, we describe a protocol for the characterization and purification of the enzyme-assembled DNA origami structures with ~15-25% recovery yield. The B2 Mini Gel Electrophoresis Systems is used to perform the AGE.

Procedure

Gel preparation

1| For the preparation of 120 mL, 2% agarose gel, 2.4 g of agarose is added into 120 mL of 1×TAE buffer in a 600 mL beaker.

2| Microwave the solution on high power for 3 min until bubbles start to appear. Gently swirling the solution to dissolve the solid. Then, microwave the solution again. Repeat these steps a few more times until all the agarose is fully dissolved in the buffer to form a clear solution.

! Caution Wear heat-insulating gloves to protect your hands from the boiling agarose solution and the hot bottle.

! Caution Avoid microwave longer than 3 min that may result in the bumping of the solution.

3| If a substantial amount of liquid has been evaporated, add water to a final volume of 120 mL.

4| Add 1 mL of 1.2 M $MgCl_2$ into the agarose solution with a final concentration of Mg^{2+} ~ 10 mM.

5| Add 12 µL of SYBR Safe (~ 1: 10000 dilution) into the agarose solution and swirling the solution gently until it is evenly distributed.

▲CRITICAL STEP Do not add staining dye directly into the very hot solution, but cool the solution on the lab bench for a few minutes before adding SYBR Safe.

! Caution Toxic SYBR Safe, wear gloves.

6| Pour the gel into the casting tray and insert a gel comb. Wait for one hour at the room temperature for the gel solidification.

Gel running

7| After the gel has solidified, assemble the casting tray into the gel box. Fill the gel box with 1× TAE buffer containing 10 mM $MgCl_2$.

▲CRITICAL STEP It is recommended to incubate the gel box in an ice-water bath to prevent the heat damage of gel and DNA structures during the electrophoresis.

8| Remove the comb carefully. Load ~ 150 µL of DNA nanostructure sample into each of the gel pockets.

9| Set a voltage of 60 V and run the gel for 2–4 h depending on the size of the structures.

10| After running the gel, the UV-VIS trans-illuminator is used to visualize the SYBR Safe-stained DNA nanostructures.

! Caution Wear goggles, gloves and lab coats with long sleeves to protect your skin and eyes from the harmful UV radiation.

Box-2 (continued)

The extraction of DNA nanostructures from the gel.

11| Under the UV illumination, use a razor blade to cut out the DNA band of interest, and further chop it into small pieces and transfer them into a Freeze ‘N Squeeze DNA gel extraction spin column.

▲CRITICAL STEP Cut out the DNA band of interest as much as possible to improve the recovery yield. It is also critical to cut it into very small pieces to facilitate the elution of DNA structures from the gel.

12| Freeze the spin column samples at −20 °C for 5 min and then centrifuge it at 10,000 g at 4 °C for 8 min. Discard the agarose debris remained on the top of the filter cup. The solution of DNA nanostructures is recovered at the bottom of the tube, and is stored at 4 °C.

? TROUBLESHOOTING

Box-3 | AFM/TEM imaging of enzyme assembly ● TIMING 1-2 hour

Gel electrophoresis gives the limited information about the sizes of nanostructures, without the further characterization of the structural conformation and integrity. For the direct observation of enzyme assembly on DNA nanostructures, two prominent techniques are used, including atomic force microscopy (AFM) and negatively staining transmission electron microscopy (TEM). AFM is particularly useful for imaging 2D DNA nanostructures. TEM can image 3D DNA nanostructures, as well as enzyme encapsulation within the DNA nanostructures.

AFM Imaging Procedure

AFM imaging is performed using the Multimode 8 (Bruker) instrument with the ScanAsyst module.

1| Turn on the AFM systems as described in the instrument setup.

! CAUTION Avoid the direct observation of laser beam with eyes.

2| Use a double-sided tape to glue on and tear off a few layers of mica in order to get a clean and flat surface. Deposit 2 μL of ~ 10 nM DNA origami sample (for small tiles, use ~ 200 nM) onto the center of a mica surface. Wait for 2 min and then add ~ 40 - 50 μL 1× TAE Mg^{2+} buffer (pH 8.0). The DNA nanostructures are tightly bound to the mica surface due to the electrostatic interaction. **Optional:** For enhancing the absorption of DNA nanostructures onto the mica surface, 2 μL of 100 mM $NiCl_2$ solution is added into DNA solution on the mica surface.

! CAUTION $NiCl_2$ is toxic and may cause respiratory sensitization, wear gloves.

▲CRITICAL STEP For imaging enzyme assembly in solution, do not dry the sample on the mica surface, but keep it in liquid.

? TROUBLESHOOTING

3| Assemble a ScanAsyst Fluid$^+$ AFM tip onto the liquid cell.

4| Transfer the sample disc onto AFM scanner and secure liquid cell on the top of sample disc.

▲CRITICAL STEP The scanner stage must be set at a low position. Carefully place the tip holder onto the top of sample solution without touching the mica surface. Avoid the leakage of solution into the AFM scanner.

5| Open the control software of ScanAsyst in Fluid, set the initial scan size for 2 μm, and the Samples/Line for 256 or higher. Then gradually reduce the peakforce set-point for decreasing the force applied onto the sample to avoid the damage of structures due to the tip scanning.

▲CRITICAL STEP Proteins may be torn off from the DNA nanostructures if too much force is applied for the scanning. Carefully adjust the peakforce set-point for

Box-3 (continued)

TEM Imaging Procedure

TEM imaging is performed using the JEM-1400 (JEOL), and images are analyzed using ImageJ software.

6| Open the raw image file in the NanoScope Analysis software.

7| Execute a Flatten function to correct image for tilt and bow.

8| The assembled enzymes typically result in brighter spots due to the increased height than the surface of the DNA structure.

Sample Preparation

9| Area of interests can be zoomed in for detailed analysis. Section function can be used to measure the parameters, such as height and distance.

10| Analyzed images are converted to JPEG or PNG formats for the future presentations.

11| Before depositing the sample, the EM grids should be negatively glow-discharged using Emitech K100× machine at 45 mA for 30 sec.

12| Deposit 2 μL of DNA sample solution onto a carbon-coated copper grid for 2 min, then remove the solution from the grid by absorbing it with a piece of filter paper at the edge of the grid.

! Caution Don't fully dry the grid, but leave a thin layer of solution.

13| Add 6 μL of the staining solution (1% (m/v) uranyl formate) onto the grid and incubate for 15 sec, then remove the solution using a piece of filter paper as described in the above step. Leave the grid in air for 30 min to dry completely.

14| Store the stained grid in a grid box and label it with the sample name.

TEM imaging

15| Insert the sample into the TEM and image at a working voltage of 80 kV.

▲CRITICAL STEP Cage DNA Origami, with enzyme encapsulated, can be observed in TEM images.

? TROUBLESHOOTING

Table 2.1 The effect of the salt and detergent concentration for removing nonspecific DNA molecules from DNA-conjugated enzyme solutions. Labelled DNA: P1, TTTTTCCCTCCCTCC; P2, TTTTTGGCTGGCTGG. 0.05% P20 is needed to disrupt the strong nonspecific binding of DNA with LDH[134-137].

DNA-conjugated enzyme	SPDP label ratio	DNA-to-enzyme ratio		
		10 mM HEPES (pH7.5)	10 mM HEPES + 1.5 M NaCl	10 mM HEPES +0.05% (v/v) P20
G6pDH-P1	0.9	3.2	0.7	-
LDH-P2	0.9	2.7	1.1	0.7

Table 2.2 Quantification of the concentration and DNA labeling ratio of the purified DNA-conjugated G6PDH by the absorbance at 260 nm and 280 nm using the equation (4) – (6). ε_{260} and ε_{280} are in M^{-1} cm^{-1}.

Peak	DNA (TTTTTCCCTCCCTCC)			Enzyme (G6PDH)			Measured absorbance			DNA-conjugated G6PDH	
	A260/A280	ε_{260}	ε_{280}	A260/A280	ε_{260}	ε_{280}	A260/A280	A260	A280	DNA - to-enzyme ratio	Enzyme conc. (μM)
G6PDH (1)	1.27	115200	90709	0.52	61594	118450	0.86	1.28	1.49	1.08	6.88
G6PDH (2)	1.27	115200	90709	0.52	61594	118450	0.96	6.651	6.90	1.89	23.80
G6PDH (3)	1.27	115200	90709	0.52	61594	118450	1.03	8.557	8.30	2.80	22.29
G6PDH (4)	1.27	115200	90709	0.52	61594	118450	1.08	6.855	6.34	3.88	13.47

Table 2.3 The temperature gradient program for assembling DNA tiles, 2D and 3D DNA origami structures in 1×TAE-Mg^{2+} buffer (40 mM Tris, 20 mM acetic acid, 2 mM EDTA and 12.5 mM magnesium acetate, pH 8.0).

DNA Tile/2D DNA origami (~ 10-hour)		3D DNA origami cage (~ 20-hour)	
Temperature	Gradient	Temperature	Gradient
90 ^{o}C	30 sec	80 ^{o}C	2 min
86-71 ^{o}C	1 min/step	65-25 ^{o}C	30 min/step
70-60 ^{o}C	10 min/step		
59-30 ^{o}C	15 min/step		
29-26 ^{o}C	10 min/step		
25 ^{o}C	25 min		
4 ^{o}C	hold	4 ^{o}C	hold

Table 2.4 The preparation of 40 mL of 3%-20% native PAGE with the suggested ranges of separation. Bromophenol blue is used as a high-mobility marker dye, and xylene cyanol is used as a low-mobility marker dye.

Gel percentage	3%	5%	8%	12%	15%	20%
40% acrylamide (mL)	3	5	8	12	15	20
10x TAE-Mg_2^+ (mL)	4	4	4	4	4	4
H_2O (mL)	33	31	28	24	21	16
Separation range (bp)	100-1000	75-500	50-400	35-250	20-150	5-100
Bromophenol blue (bp)	100	65	15	20	15	15
Xylene cyanol (bp)	460	260	60	70	60	45

Table 2.5 The preparation of 35 mL of 5%-20% denaturing PAGE with the suggested ranges of separation. Bromophenol blue is used as a high-mobility marker dye, and xylene cyanol is used as a low-mobility marker dye.

Gel percentage	5%	6%	8%	10%	12%	14%	20%
20% PAGE solution	8.75	10.5	14	17.5	21	24.5	35
0% PAGE solution	26.25	24.5	21	17.5	14	10.5	0
Separation range (nt)	70-300	45-70	35-45	25-35	<25		
Bromophenol Blue	35	26	19	12	8		
Xylene Cyanol	130	106	76	55	26		

Table 2.6 NaCl gradient for anionic-exchange FPLC of DNA-conjugated enzymes[57].

Step	Volume (mL)	% B (1 M NaCl)	Flow rate (mL/min)	Max. Press. (MPa)
1	0	0	1	3
2	5	0	1	3
3	20	20	1	3
4	70	55	1	3
5	75	100	1	3
6	85	100	1	3
7	90	0	1	3
8	100	0	1	3

Table 2.7 HPLC gradient for separating NAD$^+$-modified DNA molecules[57,81].

Step	Time (min)	% B (Methanol)	Flow rate (mL/min)	Max. Press. (bar)
1	0	10	1	400
2	10	25	1	400
3	50	35	1	400
4	53	100	1	400
5	58	100	1	400
6	60	10	1	400

Table 2.8 Troubleshooting

Step	Problem	Possible reasons	Solutions
DNA-enzyme conjugation			
2	Enzymes are labelled with very few SPDP molecules	Buffer contains amine contaminants, pH of the buffer is neutral or acidic, SPDP is hydrolyzed by moisture or is left too long on bench, very few available lysines on the enzyme surface	First wash enzyme solutions with non-amine buffers such as phosphates or HEPES. Adjust pH of reaction solution to be ~ 8 - 8.5. Prepare fresh SPDP in DMSO (anhydrous), and immediately add it into enzyme solutions. Check the enzyme structures under PDB, identify the surface lysines
6	Thiol-modified DNA poorly reacts with SPDP-modified enzymes	Disulfide-bond protection group is not fully cleaved, T-CEP is not fully removed from the DNA solution, SPDP-modified enzymes are stored for too long with broken pyridyldithio group	Cleave disulfide-bond protection group with T-CEP, completely remove T-CEP by centrifugal filtration with water or buffer for three times. Prepare fresh SPDP-modified enzymes, and use it immediately
NAD$^+$-DNA conjugation			
13	DNA binding efficiency is low	There are folded secondary structures which prevents DNA from binding to the resin.	Add 10% DMSO into the DNA loading buffer to open the folded structures
denaturing PAGE			

30	Gel is not completely solidified after 60 min.	APS loses activity during storage.	Make sure APS is kept at -20˚C and prepare fresh APS solution.
35	The sample band is very thick and wide (a round spot instead of a thin band).	Overly loaded DNA sample per well.	Collect the major band and repeat the gel purification with less amount of DNA per lane.
39	A_{260} is low for recovered DNA sample	Ethanol precipitation is not successful due to short freeze time (step 37) or the DNA sample is left too long at room temperature before pouring out the ethanol (step 38).	Collect the ethanol waste and repeat from step 37.
Assembly of DNA nanostructures			
40 A	Cofactor-modified DNA (e.g. NAD^+) loses activity after the thermally annealing process	Thermal damage and deactivation of cofactors	Decrease the maximal temperature of thermal annealing program, limit the thermal incubation above 70° C for < 10 min
Native PAGE			
42, **Box 1**, step 3	Gel is not completely solidified after 3 hour	low- percentage gel needs longer solidification time	Leave the gel overnight to solidify
42, **Box 1**, step 8	Gel staining is weak	Staining time is too short or sample concentration is low	Extend staining time to 20 min or increase the sample concentration
	DNA sample stays inside wells and does not run into gels	Acrylamide concentration of the gel is too high	Try to run the sample using another gel with a lower acrylamide concentration
	Unexpected upper bands appear	Aggregations of the DNA nanostructures	Decrease the sample concentration or increase the running temperature to reduce aggregations
	Unexpected lower bands appear	Partially assembled structures appear or the structures are dissociated during the electrophoresis	If the structures dissociate during the gel running, decrease running temperature. If partially assembled structures still exist, optimize the DNA folding strategy and sequences

42, **Box 2**, step12	Low recovery yield	The gel band of sample is not completely crushed into small pieces.	Cut the gel bands into small pieces, and crush completely before extraction
AFM characterization			
43, **Box 3**, step 2	The density of DNA nanostructures (e.g. origami) are too high on the mica surface under AFM imaging	The deposit concentration of DNA nanostructures is high	Decrease the deposit concertation (~ a few nM for DNA origami), do not add $NiCl_2$
	Very few DNA tiles are found on the mica surface	DNA tiles are not tightly bound to the mica surface, deposit concentration is low	Increase the deposit concentration of DNA tiles (~ 100 - 200 nM for DX tiles), add $NiCl_2$ to enhance the binding
TEM imaging			
43, **Box 3**, step 15	The contrasts of TEM image (very dark)is too low to observe enzymes	Sample is overstained	Try to stain sample with shorter time, e.g. 5 sec;
	Background is too dirty under TEM	Uranyl formate precipitates from solution	Prepare fresh uranyl formate solution

CHAPTER 3

AN ENGINEERED MULTI-ENZYME COMPLEX UTILIZING SUBSTRATE CHANNELING

Adapted with permission from Fu, J., & Yang, Y. R., Johnson-Buck, A., Liu, M., Liu, Y., Walter, N. G., & Yan, H. (2014). Multi-enzyme complexes on DNA scaffolds capable of substrate channeling with an artificial swinging arm. *Nature nanotechnology*,*9*(7), 531-536. Copyright (2014) Nature publishing group.

Abstract

Swinging arms are key functional components of multi-step, catalytic transformations in many multi-enzyme complexes. In such systems, these flexible prosthetic groups couple enzyme active sites via facilitated substrate channeling for high catalytic efficiency and specificity. Engineering systems with this kind of structural and mechanistic complexity is a grand challenge in the area of biomimetic nanotechnology. Here we report the design and assembly of a multi-enzyme complex based on a DNA nanostructure in which an artificial swinging arm is used to channel hydride transfer between two coupled dehydrogenase enzymes. By exploiting the programmability of DNA nanostructures, it was possible to optimize key parameters including orientation, stoichiometry and inter-enzyme distance for optimal activity.

3.1 Introduction

In many multi-functional biomolecular enzyme systems, a swinging arm is central to the mechanism of active-site coupling and substrate channeling. This arm is typically a prosthetic chemical group that is covalently attached to the enzyme complex via a flexible linker, allowing the direct transfer of substrate molecules between multiple active sites within the complex [144]. Examples include the lipoyl arm in pyruvate dehydrogenase complexes[145], the biotinyl-lysine arm in pyruvate carboxylase complexes[146], and acyl carrier proteins in polyketide synthases[147]. Mimicking this elegant method of substrate channeling outside of the cellular environment requires precise control over the spatial parameters of the individual components within the assembly complex. DNA nanostructures have recently emerged as promising materials to organize molecules on the nanoscale, enabling the fabrication of sophisticated 1D, 2D, and 3D complexes that exhibit spatial addressability for incorporating functional elements [115,124,125], as well as providing nano-mechanical control [17,81,148,149]. Protein-DNA assemblies [35] have been used to organize cascades of enzymatic reactions by controlling the relative distance and orientation of enzymatic components [94,98,99,107] or by facilitating the interface between enzymes and electrode surfaces [150,151]. Here, we present an artificial swinging arm-channeled multi-enzyme complex organized by a DNA nanoscaffold. In this system, a single-stranded DNA (ssDNA) arm, terminally modified with NAD^+, is attached half-way between two dehydrogenases positioned on the DNA scaffold such that it acts as swinging arm to facilitate the hydride transfer between the enzymes in a cascading pathway.

3.2 Design and assembly

The general design of the swinging arm nanostructure complex is shown in Fig. 1A, where a two-enzyme cascade consisting of glucose-6 phosphate dehydrogenase (G6pDH)[152] and malic dehydrogenase (MDH)[153] is displayed on a DNA double-crossover (DX) tile scaffold[114] (sequences design is shown in fig.S1-S6). G6pDH catalyzes the oxidation of glucose-6 phosphate and the reduction of NAD^+ to NADH. Subsequently, MDH catalyzes the reduction of oxaloacetate to malic acid using the NADH produced by G6pDH. To facilitate the efficient channeling of NADH between G6pDH and MDH, an NAD^+-functionalized poly $(T)_{20}$ oligonucleotide was attached to the DNA tile surface half-way between G6pDH and MDH (fig.S7-S19 for detailed conjugation and assembly). Fig. 1B shows a native polyacrylamide gel electrophoresis (PAGE) analysis of the assembled enzyme complex, together with various sub-complexes. Both the gel and size-exclusion chromatography (fig.S20) demonstrate assembly of the G6pDH-NAD^+-MDH swinging arm cascade with >80% yield. Assembly of the complete complex was also confirmed by atomic force microscopy (AFM) (Fig. 1C), where the presence of the enzymes is signified by differences in height (“brightness”) compared to the surface of the DNA tile (fig.S54 for more AFM images).

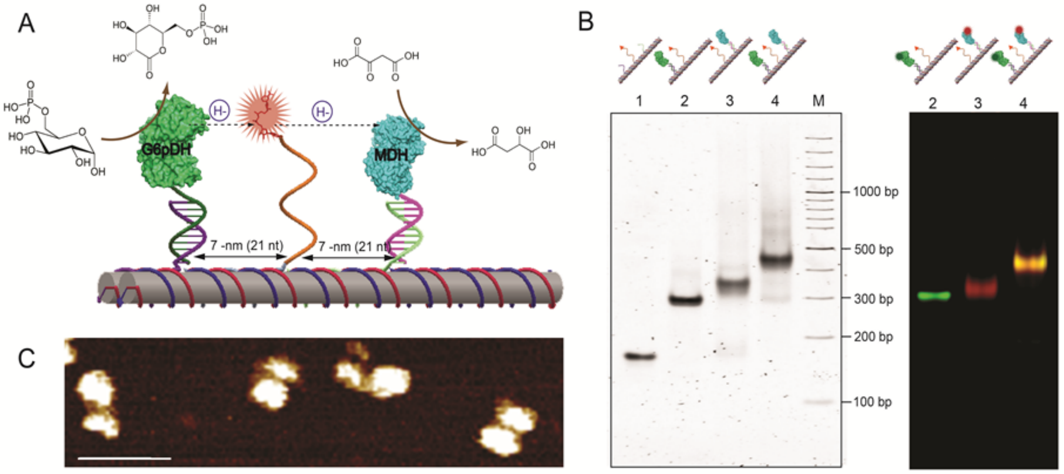

Fig. 3.1. Design and characterization of a NAD$^+$-modified swinging arm providing restricted diffusion of NAD$^+$/NADH between two dehydrogenases. (**A**) Schematic illustration of the nanostructure complex consisting of glucose-6 phosphate dehydrogenase (G6pDH) and malic dehydrogenase (MDH) organized on a DNA DX tile. The NAD$^+$-modified single-stranded poly(T)$_{20}$ is positioned half-way between the two enzymes, facilitating the transfer of hydrides. (**B**) Left: Native PAGE (3%) characterization of the assembled swinging arm enzyme complex: (1) a DNA tile with the NAD$^+$-modified arm; (2) G6pDH-NAD$^+$ complex; (3) MDH-NAD$^+$ complex; (4) fully assembled G6pDH-NAD$^+$-MDH swinging arm structure. Right: fluorescence gel image of an Alexa 555-labeled G6pDH-NAD$^+$ structure (lane 2), an Alexa 647-labeled MDH-NAD$^+$ structure (lane 3), and a dual color image of a G6pDH (AlexFluor 555 labeled)-NAD$^+$-MDH(AlexaFluor 647 labeled) swinging arm structure (lane 4). M: double stranded DNA ladder. (**C**) AFM imaging of the G6pDH-NAD$^+$-MDH swinging arm structures. Scale bar: 50 nm.

3.3 Single-molecule and half arm characterization

To optimize the design and understand the kinetics and mechanism of the restricted diffusive movement of the ssDNA-based swinging arm, we first developed a simplified model system. In this model, a Cy3 reporter dye takes the place of NAD^+ on the single-stranded poly$(T)_{20}$ arm, whereas a BHQ fluorescence quencher and a Cy5 energy transfer acceptor dye replace one or both enzymes on selected probe positions surrounding the swinging arm (Fig. 2A). To mimic the binding of NAD^+/NADH to the dehydrogenase enzymes, an oligonucleotide sequence (5'-ATA GTG AAA) was extended from the 5' end of the poly$(T)_{20}$ sequence, allowing the arm to transiently hybridize to the probes that each bear the complementary sequence (5'-TTT CAC TAT). The relative motion of the swinging arm was then monitored by single molecule fluorescence resonance energy transfer (smFRET) between its attached reporter and either the quencher (obliterating the reporter fluorescence) or the acceptor (yielding a distinct red acceptor signal) using the Total Internal Reflection Microscopy (TIRF) as previously described[154]. In Fig. 2A, the Cy3-labelled poly$(T)_{20}$ swinging arm is positioned halfway between the quencher and acceptor. In the resulting smFRET time traces, the fluorescence signal alternates between Cy3-BHQ quenching and Cy3-Cy5 energy transfer, indicating that the poly$(T)_{20}$ arm is swinging between the two probes and transiently hybridizing to them. The absence of observable low-FRET intermediates (Cy3 signal only) shows that the transient movement of the swinging arm between bound states occurs rapidly compared to the 100-ms time resolution of our single molecule measurement (fig.S21-S24 for more details). To characterize the distance dependence of the binding mediated by the swinging arm motion using smFRET, we chose a design in which a single Cy5-labeled probe was placed at one of three, topologically accessible, distances from the Cy3-labeled arm: 7 nm (21 base pairs), 14 nm (42 base pairs) and 21 nm (63 base pairs). As shown in Fig. 2B, the most efficient capture by the hybridization probe was observed at 7 nm, where ~94% of all individual swing arms were consistently associated with the Cy5 probe (leading to high FRET). As the distance increased, the efficiency of swinging arm capture decreased to ~58% of the sample at 14 nm and only ~10% at 21 nm, consistent with a theoretical considerations based on a recent coarse-grained model of the ssDNA poly$(T)_{20}$ arm (fig. S25). Titrating in free, unlabeled ssDNA to directly compete with the swinging arm for hybridization to the capture probe allowed us to also determine the effective local concentration of the swinging arm to be ~250 μM for the 7-nm design and ~1 μM for the 14 nm construct (fig. S27-S28), demonstrating a steep distance dependence. Based on these observations we predicted that the swinging arm enzyme complex should show the similar distance dependent activities.

Next, we evaluated the ability of an NAD^+-modified swinging arm to enhance dehydrogenase activity in the one enzyme-NAD^+ arm assembly (Fig. 2C and D). The activities of the two enzymes were measured individually in bulk solution for the three swinging arm-enzyme distances (7, 14 and 21 nm) using phenazine methosulfate (PMS) catalyzed resazurin fluorescence assays (fig. S29 and S32) [81,155]. As predicted, the 7-nm distance resulted in the highest activity for both G6pDH and MDH. At this distance from the NAD^+-modified swinging arm, G6pDH-NAD^+ assembly showed an activity enhancement of ~30-fold compared to an enzyme system with the same concentration of 100 nM freely diffusing NAD^+. Conversely, this enhanced activity by a swinging arm corresponds to the activity generated in the presence of ~5-10 μM freely diffusing NAD^+

(fig. S33-S34). Similarly, MDH-NAD$^+$ assembly exhibited a ~7-fold activity enhancement at 7 nm, corresponding to the activity at ~2.5-5 μM freely diffusing NAD$^+$ (fig. S35-S36). Notably, the effective local concentration of the NAD$^+$-coupled swinging arm determined by enzyme catalysis (~5 μM at 7 nm) is significantly lower than the swinging arm concentration estimated from competitive binding (~200 μM at 7 nm in Fig. 2B). We suggest that this difference may be due to the orientational and sterical constraints associated with the binding of the tethered NAD$^+$ to the active site of the enzymes and higher binding affinity of oligo-hybridization (~ 0.3 μM k_d) than NAD$^+$/dehydrogenase (> 10 μM k_d). In the further examination of the orientational effect, we varied the angle between the NAD$^+$-modified arm and the enzyme attachment site with keeping the similar distance of ~ 6-8 nm (Fig. 2E and F) and found the highest activity when the arm was attached to the top surface of the DNA nanostructure at an angle parallel to that of the enzyme (fig. S37-S40).

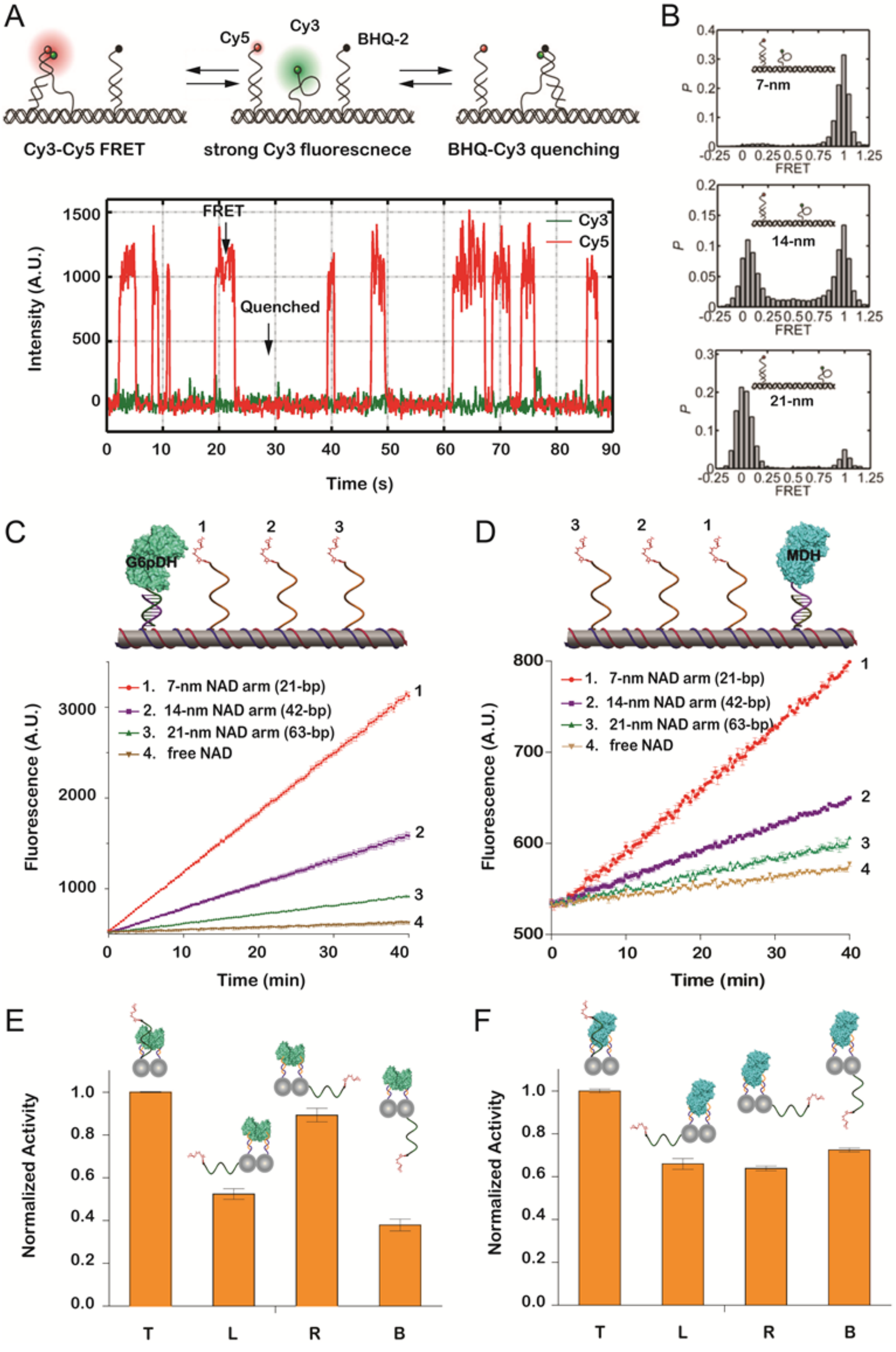
A
Cy5
Cy3
BHQ-2
Cy3-Cy5 FRET
strong Cy3 fluorescnece
BHQ-Cy3 quenching
FRET
Quenched
Cy3
Cy5
Intensity (A.U.)
1500
1000
500
0
0 10 20 30 40 50 60 70 80 90
Time (s)
B
P
7-nm
14-nm
21-nm
-0.25 0 0.25 0.5 0.75 1 1.25
FRET
C
G6pDH
1 2 3
1. 7-nm NAD arm (21-bp)
2. 14-nm NAD arm (42-bp)
3. 21-nm NAD arm (63-bp)
4. free NAD
Fluorescence (A.U.)
3000
2000
1000
0 10 20 30 40
Time (min)
D
MDH
3 2 1
1. 7-nm NAD arm (21-bp)
2. 14-nm NAD arm (42-bp)
3. 21-nm NAD arm (63-bp)
4. free NAD
Fluorescence (A.U.)
800
700
600
500
0 10 20 30 40
Time (min)
E
Normalized Activity
0.0 0.2 0.4 0.6 0.8 1.0
T L R B
F
Normalized Activity
0.0 0.2 0.4 0.6 0.8 1.0
T L R B

Fig. 3.2. Characterization of the NAD$^+$-modified swinging arm. (**A**) Single-molecule fluorescence resonance energy transfer (smFRET) characterization of the restricted diffusion of a single-stranded poly $(T)_{20}$- arm between two DNA probes anchored at either side of the structure. Top: Cy3-labeled poly$(T)_{20}$ with a 5' sticky end extension assembled between two capture probes that are modified with Cy5 (energy acceptor) and BHQ-2 (Black Hole Quencher®), respectively, with ~ 7nm distance from the anchor position of the arm. The Cy3-Cy5 FRET signal (red emission) is observed when the arm swings and binds to the Cy5-labeled capture probe, while a Cy3-BHQ interaction quenches the fluorescence when the arm swings and binds to the BHQ-labeled capture probe. Bottom: smFRET monitoring the swinging poly$(T)_{20}$ arm with alternating Cy3-BHQ quenching and Cy3-Cy5 FRET events. CCD integration time: 0.1 s. (**B**) smFRET characterization of the distance-dependent hybridization of the poly$(T)_{20}$ arm, with 7 nm (top), 14 nm (middle) and 21 nm (bottom) enzyme-NAD-modified arm distances. (**C & D**) Distance dependent enzyme activity for complexes in which the NAD$^+$-modified arm is coupled to either G6pDH (C) or MDH (D) with enzyme-NAD$^+$-modified arm distances of 7-nm, 14-nm and 21-nm. (**E & F**) Orientation dependent enzyme activity for complexes in which the NAD$^+$-modified arm is coupled to either G6pDH (E) or MDH (F) at various angles between the enzyme and arm attachment sites on the DNA scaffold. Angles of ~ parallel 0˚ (T), ~ left 90˚ (L), ~ right 90˚(R) and ~ bottom 180˚ (B) were investigated.

3.4 Full swinging arm characterization

Using the optimized distance and orientation parameters, a G6pDH-NAD$^+$-MDH swinging arm structure was constructed with the NAD$^+$-modified arm positioned centrally, 7 nm from either enzyme. In Fig. 3, the activity of this complete two-enzyme nanostructure is compared to that of the partially assembled structures including a G6pDH-MDH assembly with freely diffusing NAD$^+$, a G6pDH-NAD$^+$ arm assembly with freely diffusing MDH, and an MDH-NAD$^+$ arm assembly with freely diffusing G6pDH. For the same total NAD$^+$ and enzyme concentration (100 nM), the activity of the complete swinging arm structure is ~ 90-fold higher than that obtained with the similar two-enzyme assembly but freely diffusing NAD$^+$ system. Semi-assembled swinging arm complexes with only one enzyme attached (G6pDH-NAD$^+$ or MDH-NAD$^+$ structures) and the other enzyme freely diffusing in solution also resulted in higher activities than the enzyme complexes without NAD$^+$-modified arms (~14-fold for G6pDH-NAD$^+$, and ~4-fold for MDH-NAD$^+$), but were still considerably less active than the complete G6pDH-NAD$^+$-MDH enzyme cascade. The effective local NAD$^+$ concentration for G6pDH-NAD$^+$-MDH was determined to be ~20 μM, by titrating free NAD$^+$ to G6pDH-MDH assembly until the activity was equivalent to that of G6pDH-NAD$^+$-MDH assembly(Fig. 3B). See fig.S41-S44 for detailed raw data.

3.5 Stoichiometry analysis

In natural multi-enzyme complexes, the relative stoichiometry of the enzymes is optimized to maximize their catalytic efficiency. Toward this end, we investigated the dependence of enzymatic activity on the number of surrounding NAD^+-modified swinging arms on a DNA-scaffolded 4 × 4 tile (Fig. 3C)[4]. For the G6pDH-NAD^+ structure, the activity increased almost linearly as the number of NAD^+-modified arms increased from 1 to 4. By comparison, the enzymatic activity of the MDH-NAD^+ structure only improved 2-fold as the number of NAD^+-modified arms increased from 1 to 4 (fig. S45-S48). Kinetic measurements found ~10-fold higher turnover number (k_{cat}) for the isolated G6pDH than MDH, indicating that MDH is the rate-limiting enzyme in the G6pDH-MDH cascade (fig. S31). To optimize the catalytic efficiency we therefore engineered structures in which two MDH molecules surrounded a single G6pDH molecule, channeled by two NAD^+-modified arms (G6pDH-NAD^+_2-MDH_2) as shown in Fig. 3D. As expected, this enzyme complex exhibited an additional ~2-fold activity enhancement compared to G6pDH-NAD^+-MDH (fig. S49 and S52). Further, the assembly of four MDH surrounding a single G6pDH channeled by four NAD^+ arms (G6pDH-NAD^+_4-MDH_4) increased the activity to ~3-fold of G6pDH-NAD^+-MDH. The performance of G6pDH-NAD^+_4-MDH_4 complex is limited by the low yield (~ 50 - 60%) of the accurate assembly due to the highly crowded local proteins (fig. S50-S52).

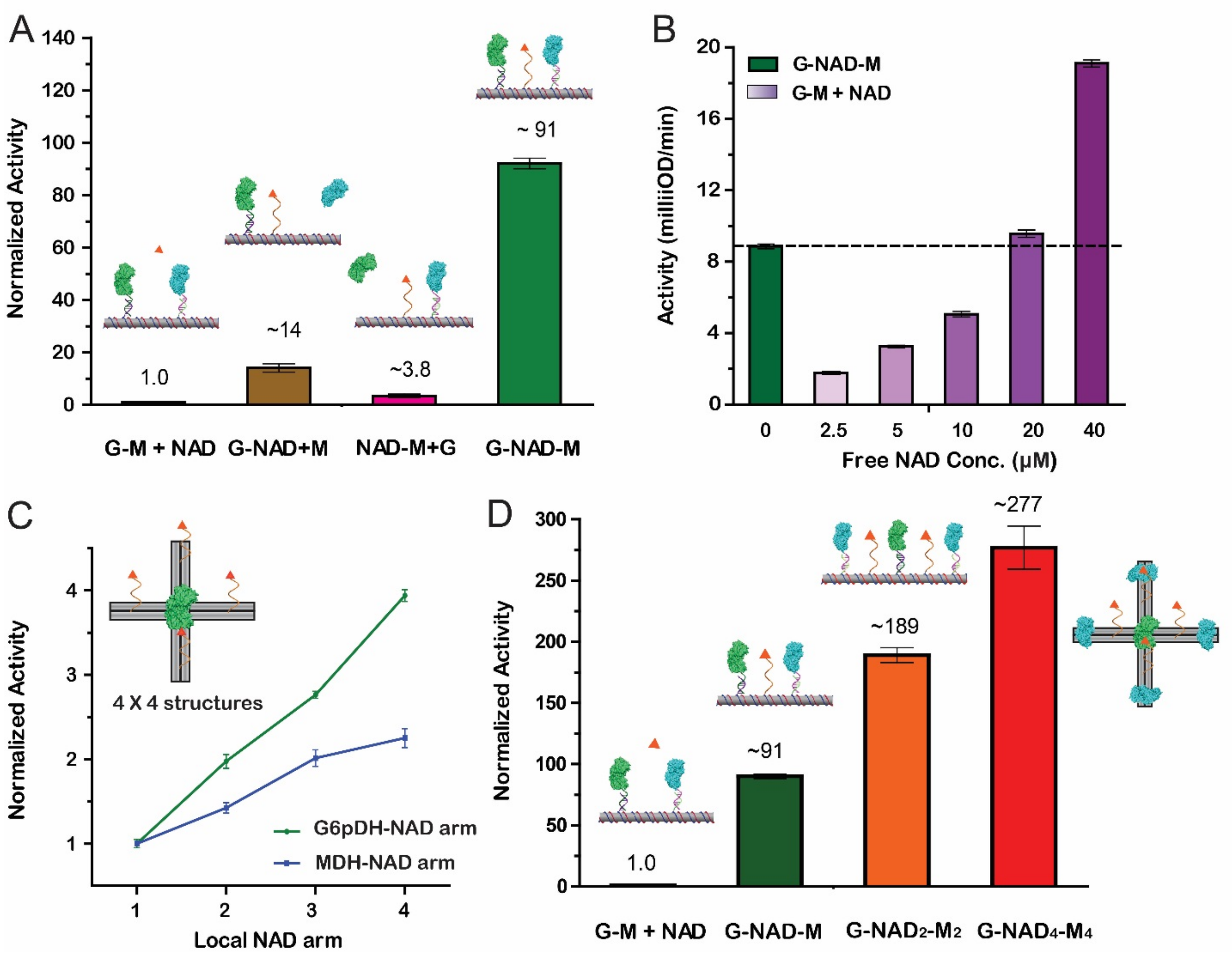

Fig. 3.3 Characterization of enzymatic activity in the G6pDH-NAD$^+$-MDH swinging arm structures. (**A**) Normalized overall pathway activities for G6pDH-MDH assembly with free NAD$^+$ (G-M + NAD, blue), G6pDH-NAD$^+$ semi-assembly with free MDH (G-NAD + M, brown), MDH-NAD$^+$ semi-assembly with free G6pDH (NAD-M + G, pink) and the fully assembled G6pDH-NAD$^+$-MDH swinging arm structure (G-NAD-M, green). Total enzyme structure and NAD$^+$ concentration: 100 nM. Substrate conditions: 1 mM glucose-6 phosphate and 1 mM oxaloacetic acid in 100 mM HEPES buffer (pH 8). (**B**) Titrating the effective concentration of freely diffusing NAD$^+$ into the G6pDH-MDH

assembly with equivalent activity to the swinging arm structure of G6pDH-NAD^+-MDH assembly: 100 nM G6pDH-MDH assemblies with free aminoethyl modified NAD^+ (AE-NAD) at 2.5, 5, 10, 20 and 40 μM. All NAD^+ used in the assay refers to aminoethyl modified NAD^+. (**C**) Relative stoichiometric dependence of enzyme activity as the number of NAD^+-modified arms on a 4 × 4 DNA tile increases from 1 to 4. (**D**) Improving the catalytic efficiency by adjusting the relative number of G6pDH and MDH molecules: G6pDH-MDH assembly with free NAD^+ (G-M + NAD, blue); G6pDH-NAD^+-MDH swinging arm structure (G-NAD-M, green); G6pDH-NAD_2^+-MDH_2 swinging arm structure (G-NAD_2-M_2, orange) and G6pDH-NAD_4^+-MDH_4 structure (G-NAD_4-M_4, red).

3.6 specificity analysis

Another important advantage of an enzyme cascade with a central swinging arm is the increased reaction specificity that results from restricting the diffusion of intermediates. To explore this notion, free lactate dehydrogenase (LDH) was added to compete for NADH with the malic dehydrogenase on the G6pDH-NAD^+-MDH nanostructure. The presence of LDH is expected to consume a fraction of the NADH generated by G6pDH and, thus, should interfere with the enzyme cascade, leading to decreased malic acid production (fig. S32). Fig. 4A shows the results of using various mixtures of G6pDH-MDH complexes, with and without the swinging arm, in competition with LDH for NADH. As expected, for the G6pDH-NAD^+ assembly with freely diffusing MDH and LDH, we found strong competition between the two free enzymes so that the coupled activity of the G6pDH-MDH pathway was very low. As the percentage of G6pDH-NAD^+-MDH increased in the mixture (keeping the total enzyme concentrations constant), the MDH activity increased accordingly, indicating that the fully assembled G6pDH-NAD$^+$-MDH complex was effectively channeling NADH from G6pDH to MDH, avoiding the competition from free LDH. The activity of LDH behaved in the opposite manner, exhibiting much lower activity as the amount of the fully assembled G6pDH-NAD$^+$-MDH increased (Fig. 4B). Fig. 4C presents the normalized activities of MDH and LDH against the fraction of assembled complexes.

3.7 Summary

In summary, we have designed and constructed artificial "swinging arm"-channeled multi-enzyme complexes with NAD$^+$-modified molecular arms to transfer hydrides between two dehydrogenase enzymes. The swinging arm not only significantly enhances enzymatic activity, but also affords high specificity in a complex environment. The concept of a flexible molecular arm-channeled reaction should be applicable to the design and assembly of other multi-enzyme systems. For example, a similar approach can be used to construct swinging arm enzyme cascades based on other reactive cofactors such as FAD, CoA, ATP, lipoic acid, biotin or pantetheine that are used in naturally occurring multi-enzyme complexes to carry intermediates. Artificial swinging arm structures may also lead to new approaches for regulating enzyme activities by incorporating mechanisms for controlling the diffusion and motion of the arm. In a simple demonstration, we exchanged a ssDNA arm for a double-stranded DNA-arm (dsDNA-arm) by introducing a poly(A)$_{22}$ oligonucleotide into solution to hybridize with the NAD$^+$-poly(T)$_{20}$ arm. We observed an almost 50% decrease in enzyme activity for the enzyme complex with the dsDNA-arm compared to the ssDNA-arm, likely due to the slower diffusion and increased structural rigidity of dsDNA (fig. S53). The underlying DNA nanostructure scaffolds provide programmable frameworks for creating more complex enzymatic circuitry, and will find utility in the development of functional catalytic systems for the synthesis of high-value chemicals, generation of energy, conversion of materials and bioenergy, and as regulatory biological circuits for diagnostic and therapeutic applications.

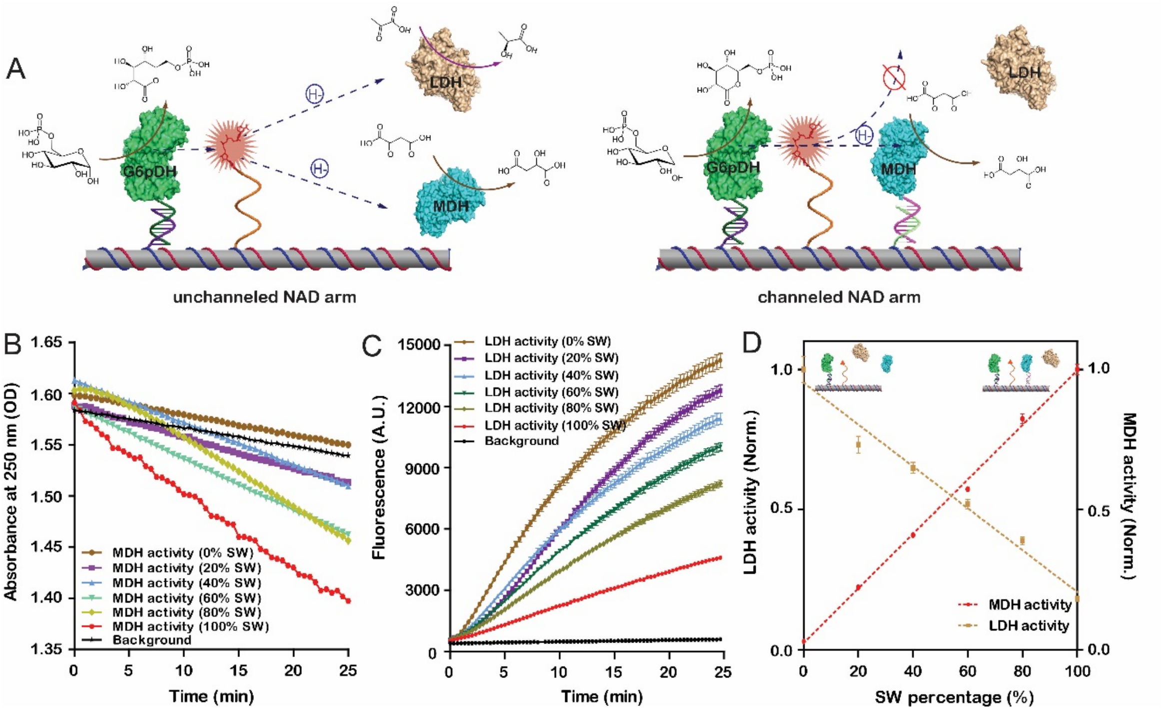

Fig. 3.4. Specificity of the G6pDH-NAD$^+$-MDH swinging arm structure when LDH is introduced to compete for the NADH produced by G6pDH. (**A**) Schematic illustration of LDH competition in G6pDH-NAD$^+$ swinging arm half structures with free MDH (left) and fully assembled G6pDH-NAD$^+$-MDH swinging arm structures (right). (**B**) MDH

activity vs. the fraction of fully assembled swinging arm complexes (SW). (**C**) LDH activity vs. the fraction of fully assembled swinging arm complexes. (**D**) Normalized LDH and MDH activities as a function of the fraction of assembled swinging arm complexes. Assay conditions: 100 nM G6pDH-NAD$^+$-MDH structures (total concentration including the half and fully assembled swinging arm structures); 100 nM LDH; 1 mM glucose-6 phosphate, 1 mM oxaloacetic acid, 1 mM sodium pyruvate in 100 mM HEPES buffer (pH8).

CHAPTER 4

AN ARTIFICIAL ENZYME 2D NETWORK USING DNA NANOSCAFFOLDS

Abstract

We have designed and constructed an artificial "swinging arm"-channeled multi-enzyme 2D network with NAD$^+$-modified molecular arms. Glucose-6-phosphate dehydrogenase (G6pDH)-NAD-Lactate dehydrogenase (LDH) swinging arm system was used as a model to study how an enzyme 2D network behaves compare to a single-particle system, which revealed how geometry affects the 2D enzyme network. A 5x5 square lattice like DNA origami has been used as the scaffold[119], on which 8 of each proteins are assembled alternatively at the junction points (shown in **Figure 4.1A**), NAD molecules are positioned between each pair of proteins, and therefore up to four NAD arms are surrounding each protein. The anchor point of NAD swinging arm to both proteins are ~10 nm. A DX DNA tile is used to assemble the single-particle swinging arm system as the control, in which one NAD arm is located between the two enzymes with the same distances between each components as that in the 2D system (**Figure 4.1B**). We compared the overall enzyme activities of the 2D network with that of the single particle. With same concentration of enzymes (8 nM), the 2D network showed about 4 fold activity enhancement compared to the single-particle assembly (**Figure 4.3**). The result indicates that the arranging the enzymes into a 2D network enhances the overall efficiency of the enzyme cascade pathway, presumably due to the enhanced accessibility of multiple swinging arms and availability of the downstream enzymes in a close distance compared to the single-particle system.

4.1 Introduction

Natural system gives us big inspiration. Cell membrane consists of the phospholipid bilayer with embedded proteins which works like a huge 2D platform packed with carefully organized functional enzymes achieving a variety of cellular processes such as cell adhesion, ion conductivity and cell signaling, etc.

One of the presentative examples is the structure of ATP synthase to facilitate the synthesis of ATP through chemiosmosis in photosynthetic membrane. Recent studies by cryoelectron microscopy and tomography have shown that this large complex forms a unique 2 row of dimers along the cristae ridges instead of distributed randomly in the membrane[156,157]. The arrangement is proposed to contribute to functionality: i.e. partly responsible for shaping the cristae[156].

Another example is the carefully arranged photosynthetic membrane[158]. In photosynthesis, the harvesting of solar energy and its subsequent conversion into a stable charge separation are dependent upon an interconnected macromolecular network of membrane-associated chlorophyll–protein complexes. The size, relative positions and associations of the photosynthetic complexes reveals crucial new features of the organization of the network. It has been reported that the membrane is divided into specialized domains each with a different network. The light-capture LH2 domains form linear arrays and The LH1 complex is ideally positioned to function as an energy collection hub, which are often only separated by narrow ‘energy conduits’ of LH2 just two or three complexes wide.

In order to better understand 2D enzymatic networks in nature. We use the artificial distance sensitive swinging arm system[57] has a model to study how enzyme 2D network behaves compare to single-particle system, how does geometry affect the 2D enzyme network. Scaling up of the engineered multi-enzyme complexes better mimics the cell organization of multi-enzyme network.

4.2 Design and assembly of Swinging arm channeled 2D protein array

To mimic the multi-enzyme network in nature, here we use a 5 x 5 square lattice like DNA origami as a scaffold[119], 8 of each protein are assembled on the structure, NAD molecules are positioned between each protein, therefore 4 NAD arms are surrounding one protein instead of one in the single tile swinging arm design (**Figure 4.1A**). The anchor point of NAD swinging arm to both proteins are designed to be 10 nm. This origami with finite size is applied to mimic the infinite 2D array, but with better quantitate control. A double crossover (DX) DNA tile is used to assemble the single-particle swinging arm system, with the same distances between each component in the 2D system (**Figure 4.1B**). The complex consists of equal number of two types of enzymes: glucose-6 phosphate dehydrogenase (G6pDH) and lactate dehydrogenase (LDH), and a NAD^+-modified double-stranded poly$(A)_{30}$-$(T)_{25}$ swing arm is positioned half-way between the pair of enzymes, facilitating the transfer of hydrides, enabling continued enzyme cascade.

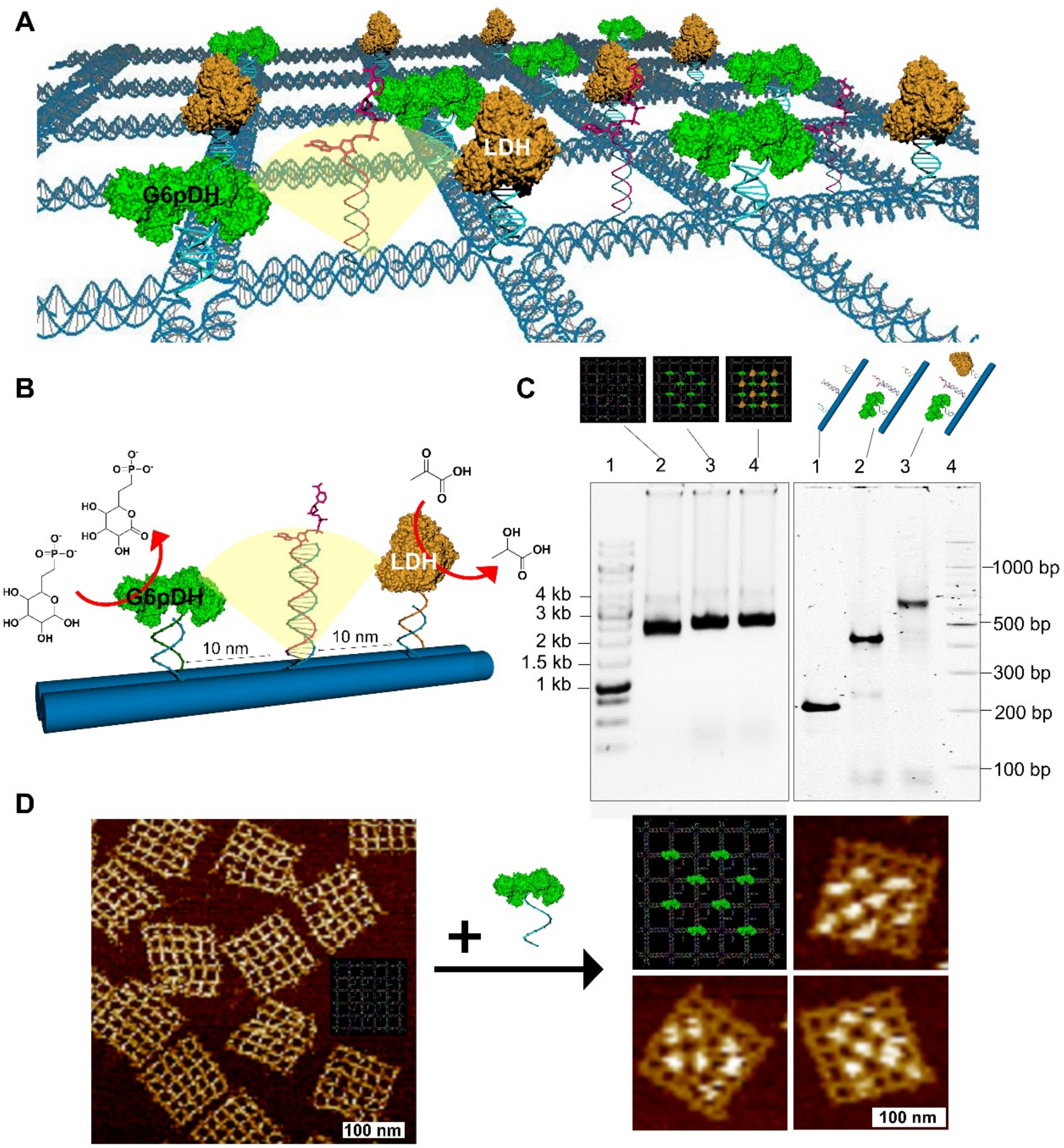

Figure 4.1. Design and characterization of a NAD$^+$-modified swinging arm 2D array and single particle swinging arm. Schematic illustration of the design of a **(A)** swinging arm array on a 5 × 5 lattice DNA origami and **(B)** a single-particle swinging arm organized on a DX DNA tile. The complex consists of equal number of two types of enzymes: glucose-6 phosphate dehydrogenase (G6pDH) and lactate dehydrogenase (LDH), and a NAD$^+$-modified double-stranded poly(A)$_{30}$-(T)$_{25}$ swing arm is positioned half-way

between the pair of enzymes, facilitating the transfer of hydrides, enabling continued enzyme cascade. **(C)** (left) Agarose gel (0.75%) characterization of the origami-enzyme complex and (right) native PAGE characterization (3%) of the DX tile-enzyme complex: lane 1, 1 kb DNA ladder; lane 2, origami; lane 3, origami-G6PDH$_8$-NAD$_8$ complex, lane 4, origami-G6PDH$_8$-NAD$_8$-LDH$_8$ complex, lane 5, DX tile; lane 6, DX tile-G6pDH-NAD complex, lane 7, DX tile-G6pDH-NAD-LDH complex, lane 8, 100 bp DNA ladder. **(D)** Representative AFM images of the origami-enzyme complexes. Scale bar: 100 nm.

To avoid the heterogeneity generated by multiple NAD-ssDNA conjugation, a double-stranded swinging arm is used with 30T hybridized with 25A, 5 A is used as ssDNA linker to give enough flexibility. Experimental results showed that the activity of the G6pDH-NAD$^+$ semi-swinging arm is enhanced after adding a poly(A)$_{15}$ strand to hybridize with the NAD$^+$-poly(T)$_{20}$ arm, so dsDNA swinging arm won't restrict the swinging.

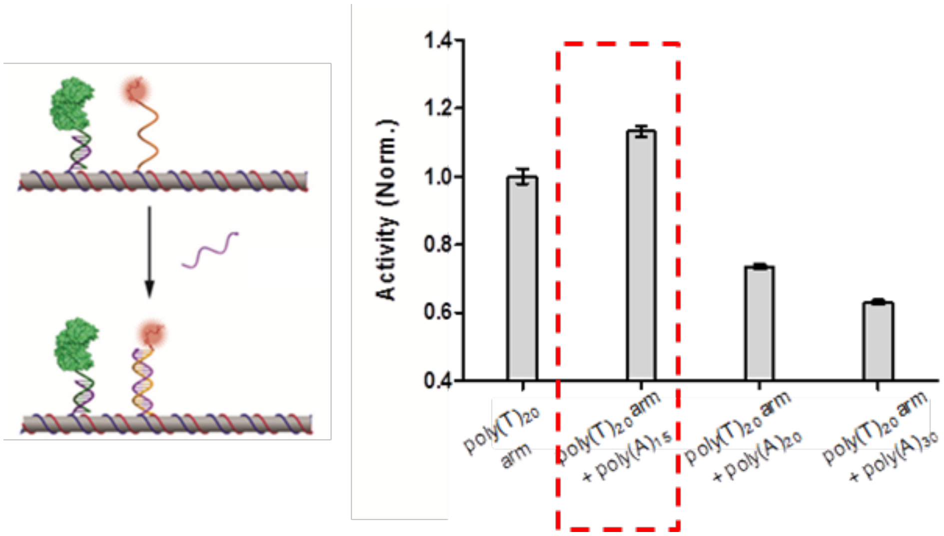

Figure 4.2. Activity comparison of double-stranded (dsDNA) swinging arm vs. single-stranded (ssDNA) swinging arm. Poly(T)$_{20}$-poly(A)$_{15}$ double-stranded swinging arm showed higher activity compared to ssDNA swinging arm poly(T)$_{20}$.

To assemble the proteins, we used a site-specific Halo-tagged protein-DNA conjugation illustrated in chapter 2. **Figure 2.6A** is a schematic illustration of the conjugation process. The assembly yield of origami-enzyme-NAD complex is characterized by both agarose gel and AFM imaging. The origami is purified to remove extra helper and then react with 5 fold excess enzymes and poly(T)$_{25}$-NAD annealed at 37℃ for 30 mins. From the gel, different mobility clearly showed the difference between origami, origami with G6pDH only, and origami with both G6pDH and LDH (**Figure 4.3A**). Although the number of each enzyme on one origami scaffold is hard to quantify from the gel. Number of enzymes can be calculated from AFM imaging comparing origami with proteins, in average 7 to 8 enzymes are assembled on the scaffold (**Figure 4.3C**). The tile-enzyme-NAD complex is characterized with 3% native PAGE as previously described (**Figure 4.3B**).

4.3 Activity of Swinging arm channeled 2D protein array compare to single particle system

First, we evaluated the length dependency of both the 2D array system and single-tile system. The activities of the two designs were measured individually in bulk solution for three swinging arm lengths (polyA$_{20}$-T$_{15}$, polyA$_{30}$-T$_{25}$, polyA$_{40}$-T$_{35}$) using phenazine methosulfate (PMS) catalyzed resazurin fluorescence assays (**Figure 4.4AB**). As predicted, the arm with poly(A)$_{30}$ resulted in the highest activity for both origami and tile, because the length matches the distance between enzymes and swinging arm (10 nm). With the optimal arm length, NAD^{+}-modified swinging arm, origami-G6pDH-NAD^{+} assembly showed an activity enhancement of ~4-fold compared to tile-G6pDH-NAD^{+} with the same concentration of enzymes at 8 nM (**Figure 4.4CD**). The control samples with freely diffusing NAD$^+$ shows little activity (almost same as substrate autocatalysis).

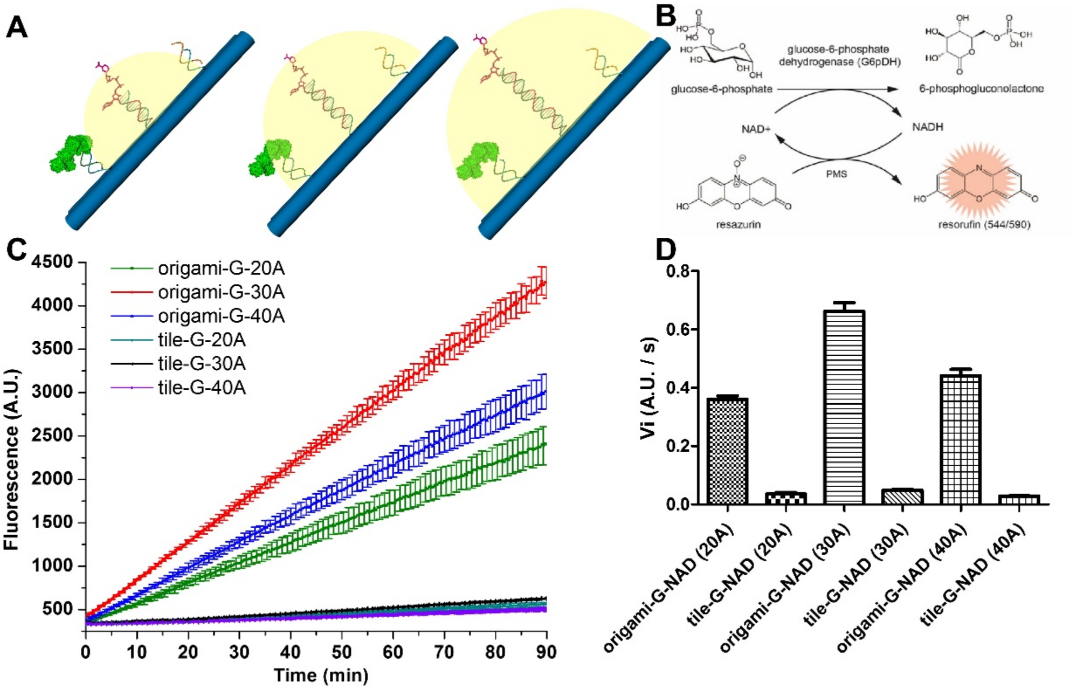

Figure 4.3. Optimization of the length of the double-stranded NAD$^+$-swinging arm. (**A**) Schematic illustration of design of polyA$_{(20)}$ -T$_{(15),}$ polyA$_{(30)}$ -T$_{(25),}$ and polyA$_{(40)}$ -T$_{(35).}$ Five single stranded T bases were left unpaired at the connection point to the DNA tile to allow enough flexibility of the swing. The double stranded body of the swing arm allows a better distance control then a single stranded swing arm. (**B**) The coupled fluorescence assay for activity test. (**C & D**) Activity of polyA$_{(20)}$ -T$_{(15),}$ polyA$_{(30)}$ -T$_{(25),}$ to polyA$_{(40)}$ -T$_{(35)}$ double-stranded swinging arm both on origami and DX tile scaffold. On both scaffolds, the A$_{30}$-T$_{25}$ swinging arm show higher activities.

Next, using the optimized distance and parameters, a G6pDH-NAD$^+$-LDH swinging arm structure was constructed. The activity of this complete two-enzyme nanostructure is compared to that of the partially assembled structures including a G6pDH-LDH assembly with freely diffusing NAD$^+$, a G6pDH-NAD$^+$ arm assembly with freely diffusing LDH (**Figure 4.4A**). For the same total NAD$^+$ and enzyme concentration (8 nM), the activity of the complete swinging arm structure is ~ 50-fold higher than Semi-assembled swinging arm complexes with G6pDH-NAD$^+$ attached and the LDH freely diffusing in solution, confirming the LDH harm arm also works. Kinetic measurements found ~5-fold higher turnover number (k_{cat}) for the isolated G6pDH than LDH, indicating that LDH is the rate-limiting enzyme in the G6pDH-LDH cascade (**Figure 4.4B**).

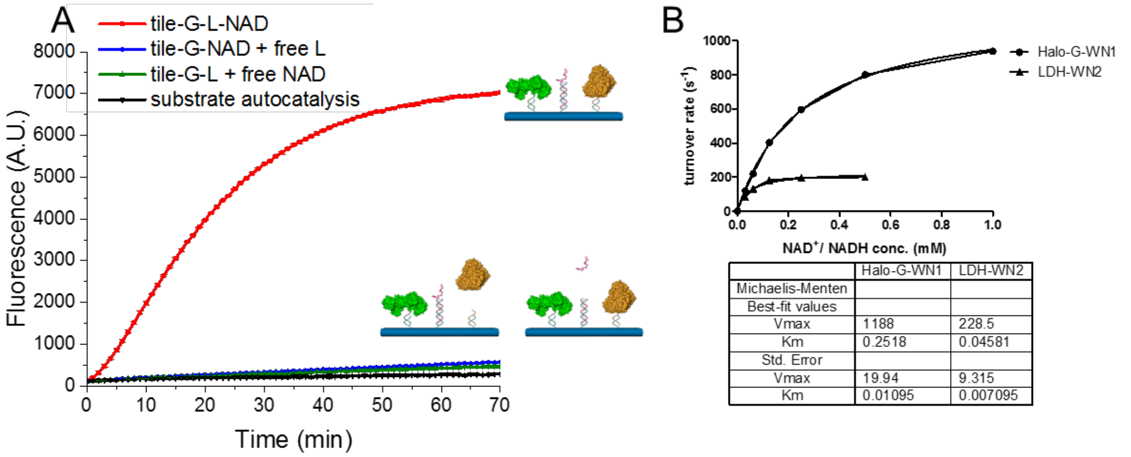

	Halo-G-WN1	LDH-WN2
Michaelis-Menten		
Best-fit values		
Vmax	1188	228.5
Km	0.2518	0.04581
Std. Error		
Vmax	19.94	9.315
Km	0.01095	0.007095

Figure 4.4 Activity characterization of LDH- half arm. (**A**) G6pDH-NAD$^+$-LDH swinging arm activity compare to that of the partially assembled structure G6pDH-NAD$^+$ arm assembly with freely diffusing LDH. (**B**) Michaelis-Menten plot for G6pDH and LDH activity (turnover rate) *vs.* NAD$^+$ concentration. Kcat of G6pDH is roughly 5 fold higher than the LDH.

We compared the 2D network with single particle of the complete origami/ tile-G6pDH-LDH-NAD complex. Overall pathway activities for origami-G6pDH-LDH-NAD compared to tile-G6pDH-LDH-NAD, with same concentration of enzymes (8 nM), showed about 4 fold activity enhancement. Indicating the network effect of enzyme cascades do benefit the overall pathway efficiency, potentially due to the accessibility of multiple swinging arms and downstream enzymes in a close distance compared to single-particle systems (**Figure 4.5CD**).

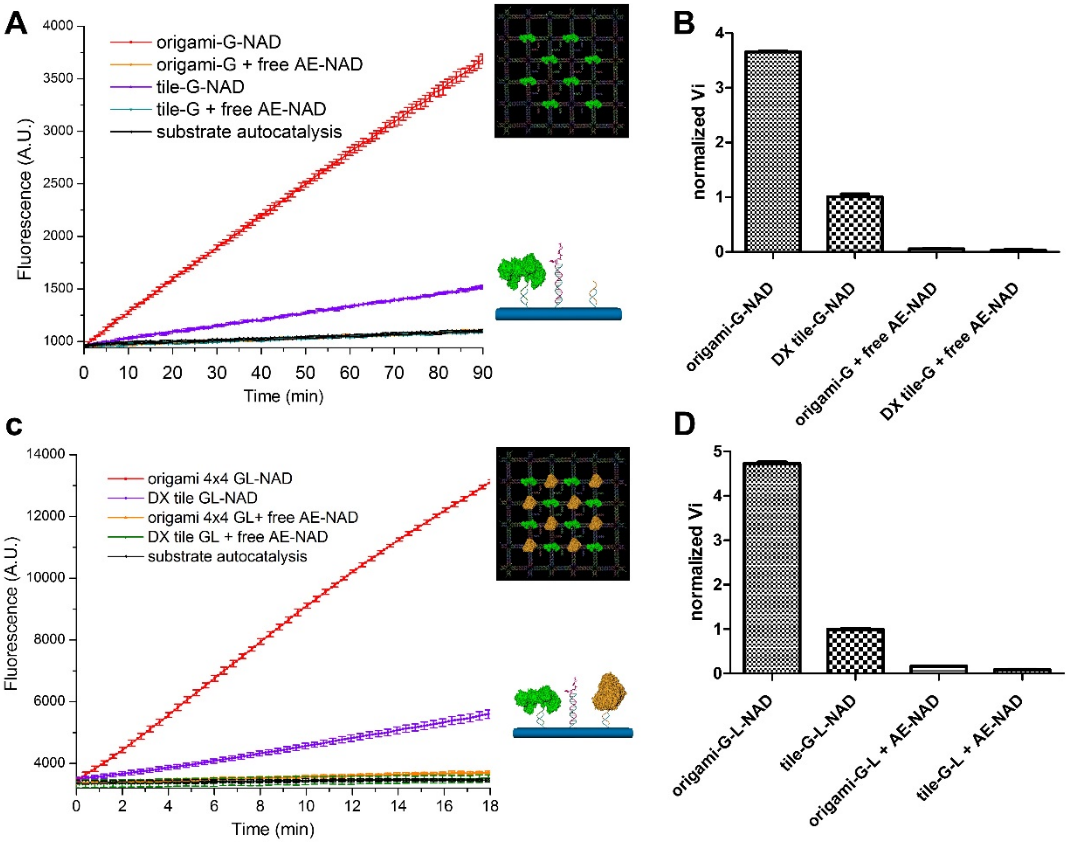

Figure 4.5. Characterization of enzymatic activity comparing the Origami- G_8-NAD^+_8-L_8 array and DX tile-G-NAD^+-L swinging arm structures. (A) Activity of Origami-G_8-NAD^+_8 (red), Origami-G_8 with free AE-NAD (orange, hidden in the back of

green and black), DX tile-G-NAD$^+$ (purple), DX tile-G with free AE-NAD (green), and substrate autocatalysis (black). (**B**) Overall pathway activities for Origami-G$_8$-NAD$^+_8$–L$_8$ (red), Origami-G$_8$–L$_8$ with free AE-NAD (orange), DX tile-G-NAD$^+$–L (purple), DX tile-G–L with free AE-NAD (green), and substrate autocatalysis (black).

4.4 Stoichiometry analysis

To understand the correlation of enhancement fold of activity and geometry. We investigate the dependence of enzymatic activity on the number of surrounding NAD$^+$-modified swinging arms on a DNA-scaffolded 4 × 4 tile [4]**.** Since in the 2D network, for each enzyme, there is 4 arms and 4 enzymes around it locally. Titration from 1 to 4 G6pDH around one LDH, and 1 to 4 LDH around one G6pDH has be tested. The stepwise assembly of 4 x 4 tile-enzymes has been characterized by agarose gel (**Figure 4.6**). Higher mobility has been observed with more enzyme assembled.

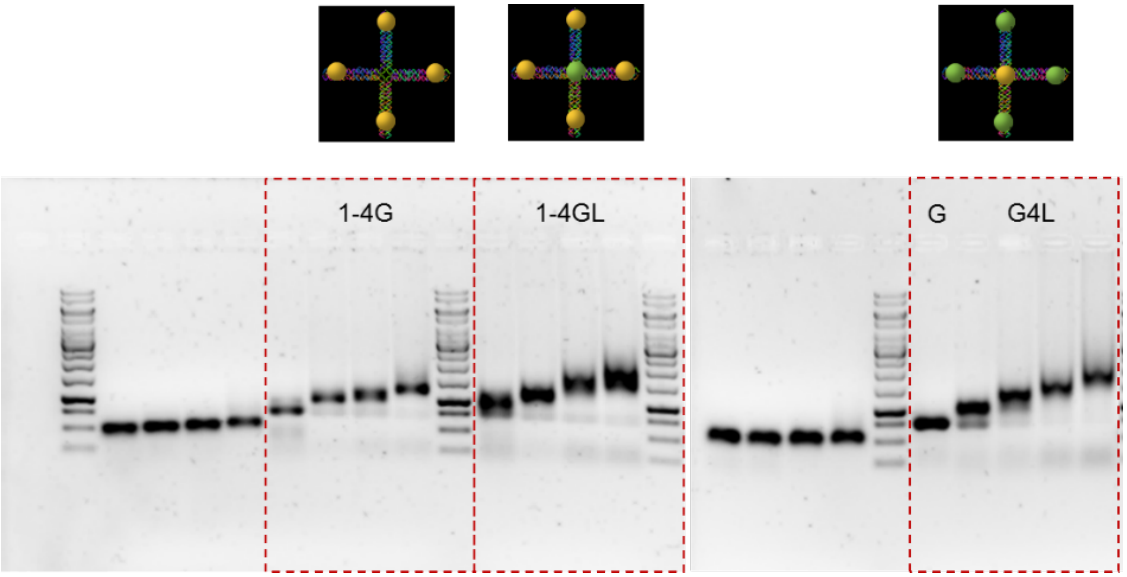

Figure 4.6. Agarose gel (0.75%) characterization of the tile-enzyme complex: lane 1,10,15,20, 1 kb DNA ladder; lane 2-5, 4x4 tiles; lane 6-9,16-19, 4x4 tile-G6PDH$_{1-4}$-NAD$_{1-4}$ complex; lane 11-14, 4x4 tile-G6PDH$_{1-4}$-NAD$_{1-4}$-LDH complex; lane 21, 4x4 tile-G6PDH-NAD; lane 22-25, 4x4 tile-G6PDH$_1$-NAD$_{1-4}$-LDH$_{1-4}$ complex.

The activity of different stoichiometry of G6pDH, NAD, and LDH has been investigated. For group one, LDH is assembled at the center, from one to four NAD-LDH has been assembled in different samples (**Figure 4.7A).** A linear increase of activity has been observed when increasing the ratio G to L from 1 to 4. in the design. The activity of network system has comparable activity as the 4x4 tile-G6pDH$_4$-NAD$^+_4$-LDH, indicating the LDH in network system is reacting with 4 G around it locally at the same time and saving extra 3 fold of G6pDH. (in the network system, we only have 1 to 1 ratio of G:L, while in the tile we have 4:1 ratio of G:L). For group two, we are measuring the LDH activity increase while increasing the number of LDH around one G6pDH. The activity in 2D system is between ratio of 3 and 4 which indicates the G in network is a little less activite than the 4:1 L:G ratio, but still ~ 4 fold faster than equal number of enzymes in tile system due to more accessibility to the other enzymes.

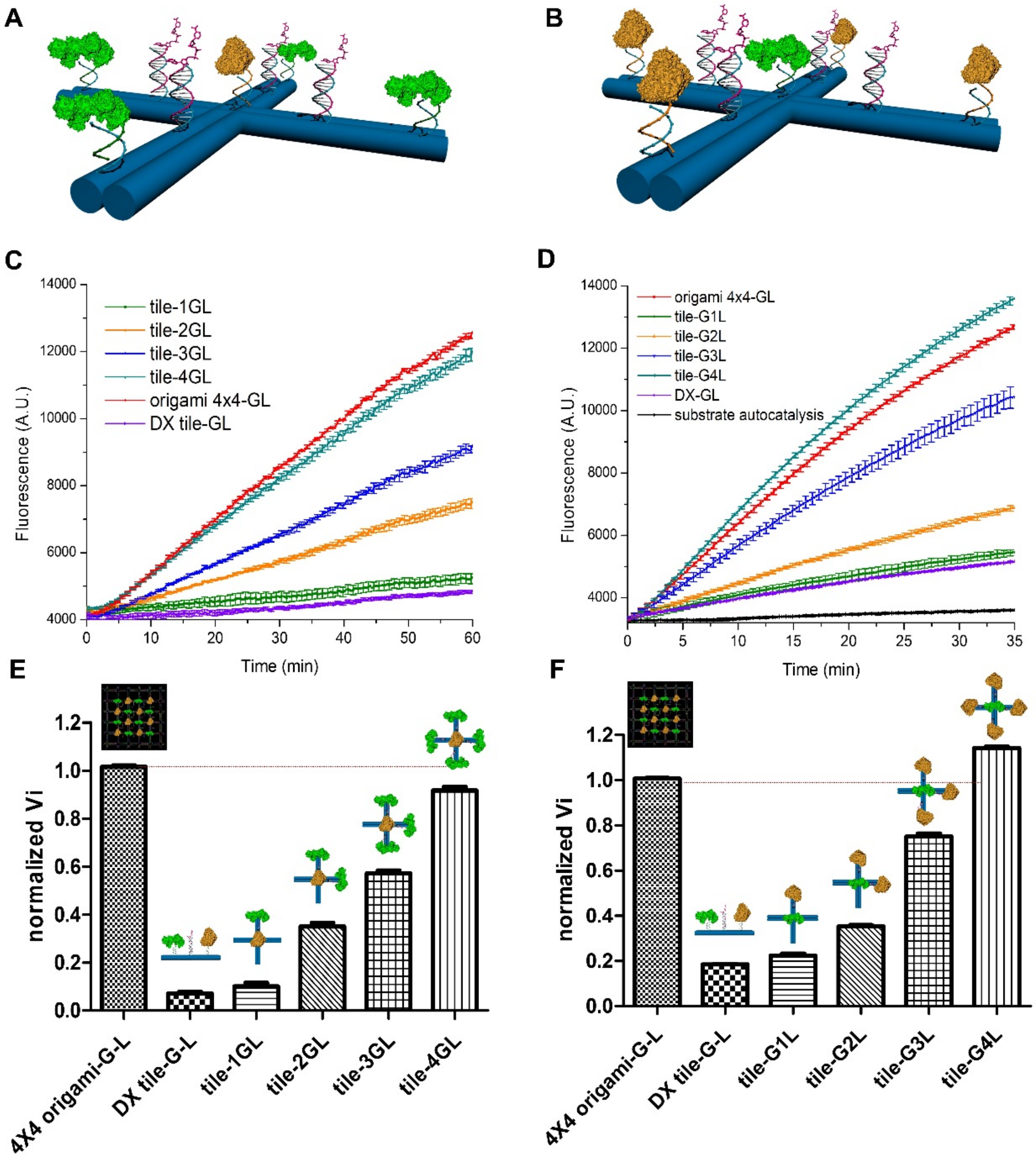

Figure 4.7. Comparison of enzymatic activity on the 2D array structure of an origami with the G6pDH-NAD^+_n-LDH$_n$/ G6pDH$_n$-NAD^+_n-LDH (n = 1, 2, 3, 4) swinging arm structures on a 4x4 tile or a DX tile**.** (**A & B**). Schematic figures of the control samples to test the relative stoichiometric dependence of enzyme activity with G6pDH or LDH at

center of a 4 × 4 DNA tile and the numbers of NAD^+-modified arms and LDH or G6pDH increases from 1 to 4, respectively. (**C&D**) Activity results for Origami-$G6pDH_8$-NAD^+_{24}-LDH_8 construct compared to small tile based G6pDH-NAD^+_n-LDH_n (n = 1, 2, 3, 4): Origami-G_8-NAD^+_{24}-L_8 (red); 4x4 tile-G6pDH-NAD^+_1-LDH_1 (green), 4x4 tile-G6pDH-NAD^+_2-LDH_2 (orange), 4x4 tile-G6pDH-NAD^+_3-LDH_3 (blue), 4x4 tile-G6pDH-NAD^+_4-LDH_4 (canyon), and DX tile-G6pDH-NAD^+-LDH (purple). (**E&F**) Activity results for Origami-$G6pDH_8$-NAD^+_{24}-LDH_8 construct comparing to $G6pDH_n$-NAD^+_n-LDH (n = 1, 2, 3, 4): Origami-G_8-NAD^+_{24}-L_8 (red); 4x4 tile-$G6pDH_1$-NAD^+_1-LDH (green), 4x4 tile-$G6pDH_2$-NAD^+_2-LDH (orange), 4x4 tile-$G6pDH_3$-NAD^+_3-LDH (blue), 4x4 tile-$G6pDH_4$-NAD^+_4-LDH (canyon), and DX tile-G6pDH-NAD^+-LDH (purple).

4.5 Summary

In summary, we designed and constructed artificial “swinging arm”-channeled multi-enzyme 2D network with NAD^+-modified molecular arms and compared to the previously developed single particle swinging arm. The benefits of enzyme networks have been discovered. To further study the geometry effects of network on enzyme activities, more pattern needs to be explored. Organizing enzyme cascades in a 3D scaffold, e.g. hosted in DNA 3D crystals is a promising direction in the future.

REFERENCES

1 Seeman, N. C. Nucleic acid junctions and lattices. *Journal of Theoretical Biology* **99**, 237-247, doi:http://dx.doi.org/10.1016/0022-5193(82)90002-9 (1982).

2 Seeman, N. C. DNA in a material world. *Nature* **421**, 427-431 (2003).

3 LaBean, T. H. *et al.* Construction, Analysis, Ligation, and Self-Assembly of DNA Triple Crossover Complexes. *Journal of the American Chemical Society* **122**, 1848-1860, doi:10.1021/ja993393e (2000).

4 Yan, H., Park, S. H., Finkelstein, G., Reif, J. H. & LaBean, T. H. DNA-Templated Self-Assembly of Protein Arrays and Highly Conductive Nanowires. *Science* **301**, 1882-1884, doi:10.1126/science.1089389 (2003).

5 He, Y. *et al.* Hierarchical self-assembly of DNA into symmetric supramolecular polyhedra. *Nature* **452**, 198-201, doi:http://www.nature.com/nature/journal/v452/n7184/suppinfo/nature06597_S1.html (2008).

6 Lund, K., Liu, Y., Lindsay, S. & Yan, H. Self-Assembling a Molecular Pegboard. *Journal of the American Chemical Society* **127**, 17606-17607, doi:10.1021/ja0568446 (2005).

7 Liu, Y., Ke, Y. & Yan, H. Self-Assembly of Symmetric Finite-Size DNA Nanoarrays. *Journal of the American Chemical Society* **127**, 17140-17141, doi:10.1021/ja055614o (2005).

8 He, Y., Chen, Y., Liu, H., Ribbe, A. E. & Mao, C. Self-Assembly of Hexagonal DNA Two-Dimensional (2D) Arrays. *Journal of the American Chemical Society* **127**, 12202-12203, doi:10.1021/ja0541938 (2005).

9 Mitchell, J. C., Harris, J. R., Malo, J., Bath, J. & Turberfield, A. J. Self-Assembly of Chiral DNA Nanotubes. *Journal of the American Chemical Society* **126**, 16342-16343, doi:10.1021/ja043890h (2004).

10 Wilner, O. I. *et al.* Self-assembly of DNA nanotubes with controllable diameters. *Nat Commun* **2**, 540, doi:http://www.nature.com/ncomms/journal/v2/n11/suppinfo/ncomms1535_S1.html (2011).

11 Goodman, R. P. *et al.* Rapid Chiral Assembly of Rigid DNA Building Blocks for Molecular Nanofabrication. *Science* **310**, 1661-1665, doi:10.1126/science.1120367 (2005).

12 Aldaye, F. A. & Sleiman, H. F. Modular Access to Structurally Switchable 3D Discrete DNA Assemblies. *Journal of the American Chemical Society* **129**, 13376-13377, doi:10.1021/ja075966q (2007).

13 Erben, C. M., Goodman, R. P. & Turberfield, A. J. A Self-Assembled DNA Bipyramid. *Journal of the American Chemical Society* **129**, 6992-6993, doi:10.1021/ja071493b (2007).

14 Zheng, J. *et al.* From molecular to macroscopic via the rational design of a self-assembled 3D DNA crystal. *Nature* **461**, 74-77, doi:http://www.nature.com/nature/journal/v461/n7260/suppinfo/nature08274_S1.html (2009).

15 Rothemund, P. W. K. Folding DNA to create nanoscale shapes and patterns. *Nature* **440**, 297-302, doi:http://www.nature.com/nature/journal/v440/n7082/suppinfo/nature04586_S1.html (2006).

16 Douglas, S. M. *et al.* Rapid prototyping of 3D DNA-origami shapes with caDNAno. *Nucleic Acids Research*, doi:10.1093/nar/gkp436 (2009).

17 Andersen, E. S. *et al.* Self-assembly of a nanoscale DNA box with a controllable lid. *Nature* **459**, 73-76, doi:http://www.nature.com/nature/journal/v459/n7243/suppinfo/nature07971_S1.html (2009).

18 Dietz, H., Douglas, S. M. & Shih, W. M. Folding DNA into Twisted and Curved Nanoscale Shapes. *Science* **325**, 725-730, doi:10.1126/science.1174251 (2009).

19 Douglas, S. M. *et al.* Self-assembly of DNA into nanoscale three-dimensional shapes. *Nature* **459**, 414-418, doi:http://www.nature.com/nature/journal/v459/n7245/suppinfo/nature08016_S1.html (2009).

20 Ke, Y. *et al.* Multilayer DNA Origami Packed on a Square Lattice. *Journal of the American Chemical Society* **131**, 15903-15908, doi:10.1021/ja906381y (2009).

21 Han, D. *et al.* DNA Origami with Complex Curvatures in Three-Dimensional Space. *Science* **332**, 342-346, doi:10.1126/science.1202998 (2011).

22 Han, D. *et al.* DNA Gridiron Nanostructures Based on Four-Arm Junctions. *Science* **339**, 1412-1415, doi:10.1126/science.1232252 (2013).

23 Kato, T., Goodman, R. P., Erben, C. M., Turberfield, A. J. & Namba, K. High-Resolution Structural Analysis of a DNA Nanostructure by cryoEM. *Nano Letters* **9**, 2747-2750, doi:10.1021/nl901265n (2009).

24 Birkedal, V. *et al.* Single molecule microscopy methods for the study of DNA origami structures. *Microscopy Research and Technique* **74**, 688-698, doi:10.1002/jemt.20962 (2011).

25 Bai, X.-c., Martin, T. G., Scheres, S. H. & Dietz, H. Cryo-EM structure of a 3D DNA-origami object. *Proceedings of the National Academy of Sciences* **109**, 20012-20017 (2012).

26 Opherden, L., Oertel, J., Barkleit, A., Fahmy, K. & Keller, A. Paramagnetic Decoration of DNA Origami Nanostructures by Eu3+ Coordination. *Langmuir* **30**, 8152-8159, doi:10.1021/la501112a (2014).

27 Pan, K. *et al.* Lattice-free prediction of three-dimensional structure of programmed DNA assemblies. *Nat Commun* **5**, doi:10.1038/ncomms6578 (2014).

28 Ke, Y., Ong, L. L., Shih, W. M. & Yin, P. Three-Dimensional Structures Self-Assembled from DNA Bricks. *Science* **338**, 1177-1183, doi:10.1126/science.1227268 (2012).

29 Ke, Y. *et al.* DNA brick crystals with prescribed depths. *Nat Chem* **advance online publication**, doi:10.1038/nchem.2083 http://www.nature.com/nchem/journal/vaop/ncurrent/abs/nchem.2083.html#supplementary-information (2014).

30 Williams, B. A. R., Lund, K., Liu, Y., Yan, H. & Chaput, J. C. Self-Assembled Peptide Nanoarrays: An Approach to Studying Protein – Protein Interactions. *Angewandte Chemie* **119**, 3111-3114, doi:10.1002/ange.200603919 (2007).

31 Kuzyk, A., Laitinen, K. T. & Törmä, P. DNA origami as a nanoscale template for protein assembly. *Nanotechnology* **20**, 235305 (2009).

32 Goodchild, J. Conjugates of oligonucleotides and modified oligonucleotides: a review of their synthesis and properties. *Bioconjugate Chemistry* **1**, 165-187, doi:10.1021/bc00003a001 (1990).

33 Meyer, R., Giselbrecht, S., Rapp, B. E., Hirtz, M. & Niemeyer, C. M. Advances in DNA-directed immobilization. *Current Opinion in Chemical Biology* **18**, 8-15, doi:http://dx.doi.org/10.1016/j.cbpa.2013.10.023 (2014).

34 Stephanopoulos, N. & Francis, M. B. Choosing an effective protein bioconjugation strategy. *Nat Chem Biol* **7**, 876-884 (2011).

35 Niemeyer, C. M. Semisynthetic DNA – Protein Conjugates for Biosensing and Nanofabrication. *Angewandte Chemie International Edition* **49**, 1200-1216, doi:10.1002/anie.200904930 (2010).

36 Li, H., Park, S. H., Reif, J. H., LaBean, T. H. & Yan, H. DNA-Templated Self-Assembly of Protein and Nanoparticle Linear Arrays. *Journal of the American Chemical Society* **126**, 418-419, doi:10.1021/ja0383367 (2003).

37 Kuzuya, A. *et al.* Precisely Programmed and Robust 2D Streptavidin Nanoarrays by Using Periodical Nanometer-Scale Wells Embedded in DNA Origami Assembly. *ChemBioChem* **10**, 1811-1815, doi:10.1002/cbic.200900229 (2009).

38 Howarth, M. *et al.* A monovalent streptavidin with a single femtomolar biotin binding site. *Nature methods* **3**, 267-273 (2006).

39 Hochuli, E., Döbeli, H. & Schacher, A. New metal chelate adsorbent selective for proteins and peptides containing neighbouring histidine residues. *Journal of Chromatography A* **411**, 177-184, doi:http://dx.doi.org/10.1016/S0021-9673(00)93969-4 (1987).

40 Shen, W., Zhong, H., Neff, D. & Norton, M. L. NTA Directed Protein Nanopatterning on DNA Origami Nanoconstructs. *Journal of the American Chemical Society* **131**, 6660-6661, doi:10.1021/ja901407j (2009).

41 Shimada, J. *et al.* Conjugation of DNA with protein using His-tag chemistry and its application to the aptamer-based detection system. *Biotechnology letters* **30**, 2001-2006 (2008).

42 Kapanidis, A. N., Ebright, Y. W. & Ebright, R. H. Site-Specific Incorporation of Fluorescent Probes into Protein: Hexahistidine-Tag-Mediated Fluorescent Labeling with (Ni2+:Nitrilotriacetic Acid)n−Fluorochrome Conjugates. *Journal of the American Chemical Society* **123**, 12123-12125, doi:10.1021/ja017074a (2001).

43 Goodman, R. P. *et al.* A Facile Method for Reversibly Linking a Recombinant Protein to DNA. *ChemBioChem* **10**, 1551-1557, doi:10.1002/cbic.200900165 (2009).

44 Wegner, S. V. & Spatz, J. P. Cobalt(III) as a Stable and Inert Mediator Ion between NTA and His6-Tagged Proteins. *Angewandte Chemie International Edition* **52**, 7593-7596, doi:10.1002/anie.201210317 (2013).

45 Williams, B. A. R. *et al.* Creating Protein Affinity Reagents by Combining Peptide Ligands on Synthetic DNA Scaffolds. *Journal of the American Chemical Society* **131**, 17233-17241, doi:10.1021/ja9051735 (2009).

46 Chhabra, R. *et al.* Spatially Addressable Multiprotein Nanoarrays Templated by Aptamer-Tagged DNA Nanoarchitectures. *Journal of the American Chemical Society* **129**, 10304-10305, doi:10.1021/ja072410u (2007).

47 Voss, E. W. & Lopatin, D. E. Fluorescein. Hapten and antibody active-site probe. *Biochemistry* **10**, 208-213, doi:10.1021/bi00778a003 (1971).

48 He, Y., Tian, Y., Ribbe, A. E. & Mao, C. Antibody Nanoarrays with a Pitch of ~20 Nanometers. *Journal of the American Chemical Society* **128**, 12664-12665, doi:10.1021/ja065467 (2006).

49 Fruk, L., Kuo, C.-H., Torres, E. & Niemeyer, C. M. Apoenzyme Reconstitution as a Chemical Tool for Structural Enzymology and Biotechnology. *Angewandte Chemie International Edition* **48**, 1550-1574, doi:10.1002/anie.200803098 (2009).

50 Fruk, L. & Niemeyer, C. M. Covalent Hemin – DNA Adducts for Generating a Novel Class of Artificial Heme Enzymes. *Angewandte Chemie International Edition* **44**, 2603-2606, doi:10.1002/anie.200462567 (2005).

51 Fruk, L., Müller, J. & Niemeyer, C. M. Kinetic Analysis of Semisynthetic Peroxidase Enzymes Containing a Covalent DNA – Heme Adduct as the Cofactor. *Chemistry – A European Journal* **12**, 7448-7457, doi:10.1002/chem.200501613 (2006).

52 Fruk, L. *et al.* DNA-Directed Immobilization of Horseradish Peroxidase – DNA Conjugates on Microelectrode Arrays: Towards Electrochemical Screening of Enzyme Libraries. *Chemistry – A European Journal* **13**, 5223-5231, doi:10.1002/chem.200601793 (2007).

53 Simon, P., Dueymes, C., Fontecave, M. & Décout, J.-L. DNA Detection through Signal Amplification by Using NADH:Flavin Oxidoreductase and Oligonucleotide – Flavin Conjugates as Cofactors. *Angewandte Chemie International Edition* **44**, 2764-2767, doi:10.1002/anie.200461145 (2005).

54 Gianneschi, N. C. & Ghadiri, M. R. Design of Molecular Logic Devices Based on a Programmable DNA-Regulated Semisynthetic Enzyme. *Angewandte Chemie* **119**, 4029-4032, doi:10.1002/ange.200700047 (2007).

55 Klug, A. & Schwabe, J. W. Protein motifs 5. Zinc fingers. *The FASEB Journal* **9**, 597-604 (1995).

56 JH, L., BM, L. & PE, W. Zinc finger proteins: new insights into structural and functional diversity. *Curr. Opin. Struct. Biol.* **11**, 39 (2001).

57 Fu, J. *et al.* Multi-enzyme complexes on DNA scaffolds capable of substrate channelling with an artificial swinging arm. *Nat Nano* **9**, 531-536, doi:10.1038/nnano.2014.100 http://www.nature.com/nnano/journal/v9/n7/abs/nnano.2014.100.html#supplementary-information (2014).

58 Erben, C. M., Goodman, R. P. & Turberfield, A. J. Single-Molecule Protein Encapsulation in a Rigid DNA Cage. *Angewandte Chemie* **118**, 7574-7577, doi:10.1002/ange.200603392 (2006).

59 Cecconi, C., Shank, E., Dahlquist, F., Marqusee, S. & Bustamante, C. Protein-DNA chimeras for single molecule mechanical folding studies with the optical tweezers. *Eur Biophys J* **37**, 729-738, doi:10.1007/s00249-007-0247-y (2008).

60 Kiick, K. L., Saxon, E., Tirrell, D. A. & Bertozzi, C. R. Incorporation of azides into recombinant proteins for chemoselective modification by the Staudinger ligation. *Proceedings of the National Academy of Sciences* **99**, 19-24, doi:10.1073/pnas.012583299 (2002).

61 Duckworth, B. P. *et al.* A Universal Method for the Preparation of Covalent Protein − DNA Conjugates for Use in Creating Protein Nanostructures. *Angewandte Chemie* **119**, 8975-8978, doi:10.1002/ange.200701942 (2007).

62 ά van Berkel, S. S., Floris, P., ά van Hest, J. C. & ά van Delft, F. L. Aza-dibenzocyclooctynes for fast and efficient enzyme PEGylation via copper-free (3+2) cycloaddition. *Chemical Communications* **46**, 97-99 (2010).

63 Köhn, M. & Breinbauer, R. The Staudinger Ligation—A Gift to Chemical Biology. *Angewandte Chemie International Edition* **43**, 3106-3116, doi:10.1002/anie.200401744 (2004).

64 Chandra, R. A., Douglas, E. S., Mathies, R. A., Bertozzi, C. R. & Francis, M. B. Programmable Cell Adhesion Encoded by DNA Hybridization. *Angewandte Chemie* **118**, 910-915, doi:10.1002/ange.200502421 (2006).

65 Douglas, E. S., Chandra, R. A., Bertozzi, C. R., Mathies, R. A. & Francis, M. B. Self-assembled cellular microarrays patterned using DNA barcodes. *Lab on a Chip* **7**, 1442-1448 (2007).

66 Takeda, S., Tsukiji, S. & Nagamune, T. Site-specific conjugation of oligonucleotides to the C-terminus of recombinant protein by expressed protein ligation. *Bioorganic & Medicinal Chemistry Letters* **14**, 2407-2410, doi:http://dx.doi.org/10.1016/j.bmcl.2004.03.023 (2004).

67 Takeda, S., Tsukiji, S., Ueda, H. & Nagamune, T. Covalent split protein fragment-DNA hybrids generated through N-terminus-specific modification of proteins by oligonucleotides. *Organic & Biomolecular Chemistry* **6**, 2187-2194, doi:10.1039/B720013G (2008).

68 Tominaga, J. *et al.* An enzymatic method for site-specific labeling of recombinant proteins with oligonucleotides. *Chemical Communications*, 401-403, doi:10.1039/B613793H (2007).

69 Theile, C. S. *et al.* Site-specific N-terminal labeling of proteins using sortase-mediated reactions. *Nat. Protocols* **8**, 1800-1807, doi:10.1038/nprot.2013.102 (2013).

70 Koussa, M. A., Sotomayor, M. & Wong, W. P. Protocol for sortase-mediated construction of DNA – protein hybrids and functional nanostructures. *Methods* **67**, 134-141, doi:http://dx.doi.org/10.1016/j.ymeth.2014.02.020 (2014).

71 Venkatesan, N. & Kim, B. H. Peptide conjugates of oligonucleotides: synthesis and applications. *Chemical Reviews* **106**, 3712-3761 (2006).

72 Sørensen, R. S. *et al.* Enzymatic Ligation of Large Biomolecules to DNA. *ACS Nano* **7**, 8098-8104, doi:10.1021/nn403386f (2013).

73 Keppler, A. *et al.* A general method for the covalent labeling of fusion proteins with small molecules in vivo. *Nat Biotech* **21**, 86-89, doi:http://www.nature.com/nbt/journal/v21/n1/suppinfo/nbt765_S1.html (2003).

74 Jongsma, M. A. & Litjens, R. H. G. M. Self-assembling protein arrays on DNA chips by auto-labeling fusion proteins with a single DNA address. *PROTEOMICS* **6**, 2650-2655, doi:10.1002/pmic.200500654 (2006).

75 Los, G. V. *et al.* HaloTag: A Novel Protein Labeling Technology for Cell Imaging and Protein Analysis. *ACS Chemical Biology* **3**, 373-382, doi:10.1021/cb800025k (2008).

76 Saccà, B. *et al.* Orthogonal Protein Decoration of DNA Origami. *Angewandte Chemie International Edition* **49**, 9378-9383, doi:10.1002/anie.201005931 (2010).

77 Rosen, C. B. *et al.* Template-directed covalent conjugation of DNA to native antibodies, transferrin and other metal-binding proteins. *Nat Chem* **6**, 804-809, doi:10.1038/nchem.2003 http://www.nature.com/nchem/journal/v6/n9/abs/nchem.2003.html#supplementary-information (2014).

78 You, M. *et al.* Photon-Regulated DNA-Enzymatic Nanostructures by Molecular Assembly. *ACS Nano* **5**, 10090-10095, doi:10.1021/nn204007y (2011).

79 Zhou, C., Yang, Z. & Liu, D. Reversible Regulation of Protein Binding Affinity by a DNA Machine. *Journal of the American Chemical Society* **134**, 1416-1418, doi:10.1021/ja209590u (2012).

80 Xin, L., Zhou, C., Yang, Z. & Liu, D. Regulation of an Enzyme Cascade Reaction by a DNA Machine. *Small* **9**, 3088-3091, doi:10.1002/smll.201300019 (2013).

81 Liu, M. *et al.* A DNA tweezer-actuated enzyme nanoreactor. *Nat Commun* **4**, doi:10.1038/ncomms3127 (2013).

82 Rajendran, A., Endo, M. & Sugiyama, H. Single-Molecule Analysis Using DNA Origami. *Angewandte Chemie International Edition* **51**, 874-890, doi:10.1002/anie.201102113 (2012).

83 Ke, Y., Lindsay, S., Chang, Y., Liu, Y. & Yan, H. Self-Assembled Water-Soluble Nucleic Acid Probe Tiles for Label-Free RNA Hybridization Assays. *Science* **319**, 180-183, doi:10.1126/science.1150082 (2008).

84 Subramanian, H. K. K., Chakraborty, B., Sha, R. & Seeman, N. C. The Label-Free Unambiguous Detection and Symbolic Display of Single Nucleotide Polymorphisms on DNA Origami. *Nano Letters* **11**, 910-913, doi:10.1021/nl104555t (2011).

85 Eberhard, H., Diezmann, F. & Seitz, O. DNA as a Molecular Ruler: Interrogation of a Tandem SH2 Domain with Self-Assembled, Bivalent DNA – Peptide Complexes. *Angewandte Chemie* **123**, 4232-4236, doi:10.1002/ange.201007593 (2011).

86 Tørring, T., Helmig, S., Ogilby, P. R. & Gothelf, K. V. Singlet Oxygen in DNA Nanotechnology. *Accounts of Chemical Research* **47**, 1799-1806, doi:10.1021/ar500034y (2014).

87 Keller, A. *et al.* Probing Electron-Induced Bond Cleavage at the Single-Molecule Level Using DNA Origami Templates. *ACS Nano* **6**, 4392-4399, doi:10.1021/nn3010747 (2012).

88 Voigt, N. V. *et al.* Single-molecule chemical reactions on DNA origami. *Nat Nano* **5**, 200-203, doi:http://www.nature.com/nnano/journal/v5/n3/suppinfo/nnano.2010.5_S1.html (2010).

89 Cohen, J. D., Sadowski, J. P. & Dervan, P. B. Programming Multiple Protein Patterns on a Single DNA Nanostructure. *Journal of the American Chemical Society* **130**, 402-403, doi:10.1021/ja0772400 (2007).

90 Kuzuya, A., Numajiri, K. & Komiyama, M. Accommodation of a Single Protein Guest in Nanometer-Scale Wells Embedded in a “DNA Nanotape”. *Angewandte Chemie International Edition* **47**, 3400-3402, doi:10.1002/anie.200800028 (2008).

91 Hariadi, R. F., Cale, M. & Sivaramakrishnan, S. Myosin lever arm directs collective motion on cellular actin network. *Proceedings of the National Academy of Sciences* **111**, 4091-4096, doi:10.1073/pnas.1315923111 (2014).

92 Derr, N. D. *et al.* Tug-of-War in Motor Protein Ensembles Revealed with a Programmable DNA Origami Scaffold. *Science* **338**, 662-665, doi:10.1126/science.1226734 (2012).

93 Wollman, A. J. M., Sanchez-Cano, C., Carstairs, H. M. J., Cross, R. A. & Turberfield, A. J. Transport and self-organization across different length scales powered by motor proteins and programmed by DNA. *Nat Nano* **9**, 44-47, doi:10.1038/nnano.2013.230 http://www.nature.com/nnano/journal/v9/n1/abs/nnano.2013.230.html#supplementary-information (2014).

94 Erkelenz, M., Kuo, C.-H. & Niemeyer, C. M. DNA-Mediated Assembly of Cytochrome P450 BM3 Subdomains. *Journal of the American Chemical Society* **133**, 16111-16118, doi:10.1021/ja204993s (2011).

95 Niemeyer, C. M., Koehler, J. & Wuerdemann, C. DNA-Directed Assembly of Bienzymic Complexes from In Vivo Biotinylated NAD(P)H:FMN Oxidoreductase and Luciferase. *ChemBioChem* **3**, 242-245, doi:10.1002/1439-7633(20020301)3:2/3<242::AID-CBIC242>3.0.CO;2-F (2002).

96 Wang, Z.-G., Wilner, O. I. & Willner, I. Self-Assembly of Aptamer−Circular DNA Nanostructures for Controlled Biocatalysis. *Nano Letters* **9**, 4098-4102, doi:10.1021/nl902317p (2009).

97 Wilner, O. I., Shimron, S., Weizmann, Y., Wang, Z.-G. & Willner, I. Self-Assembly of Enzymes on DNA Scaffolds: En Route to Biocatalytic Cascades and the Synthesis of Metallic Nanowires. *Nano Letters* **9**, 2040-2043, doi:10.1021/nl900302z (2009).

98 Wilner, O. I. *et al.* Enzyme cascades activated on topologically programmed DNA scaffolds. *Nat Nano* **4**, 249-254, doi:http://www.nature.com/nnano/journal/v4/n4/suppinfo/nnano.2009.50_S1.html (2009).

99 Fu, J., Liu, M., Liu, Y., Woodbury, N. W. & Yan, H. Interenzyme substrate diffusion for an enzyme cascade organized on spatially addressable DNA nanostructures. *Journal of the American Chemical Society* **134**, 5516-5519 (2012).

100 Fu, Y. *et al.* Single-Step Rapid Assembly of DNA Origami Nanostructures for Addressable Nanoscale Bioreactors. *Journal of the American Chemical Society* **135**, 696-702, doi:10.1021/ja3076692 (2013).

101 Miles, E. W., Rhee, S. & Davies, D. R. The Molecular Basis of Substrate Channeling. *Journal of Biological Chemistry* **274**, 12193-12196, doi:10.1074/jbc.274.18.12193 (1999).

102 Frischmann, P. D., Mahata, K. & Würthner, F. Powering the future of molecular artificial photosynthesis with light-harvesting metallosupramolecular dye assemblies. *Chemical Society Reviews* **42**, 1847-1870 (2013).

103 Pullerits, T. & Sundström, V. Photosynthetic light-harvesting pigment-protein complexes: toward understanding how and why. *Accounts of chemical research* **29**, 381-389 (1996).

104 Dutta, P. K. *et al.* DNA-Directed Artificial Light-Harvesting Antenna. *Journal of the American Chemical Society* **133**, 11985-11993, doi:10.1021/ja1115138 (2011).

105 Dutta, P. K. *et al.* A DNA-Directed Light-Harvesting/Reaction Center System. *Journal of the American Chemical Society*, doi:10.1021/ja509018g (2014).

106 Delebecque, C. J., Silver, P. A. & Lindner, A. B. Designing and using RNA scaffolds to assemble proteins in vivo. *Nat. Protocols* **7**, 1797-1807 (2012).

107 Delebecque, C. J., Lindner, A. B., Silver, P. A. & Aldaye, F. A. Organization of Intracellular Reactions with Rationally Designed RNA Assemblies. *Science* **333**, 470-474, doi:10.1126/science.1206938 (2011).

108 Guo, P. The emerging field of RNA nanotechnology. *Nat Nano* **5**, 833-842 (2010).

109 Fu, J. & Yan, H. Controlled drug release by a nanorobot. *Nat Biotech* **30**, 407-408, doi:10.1038/nbt.2206 (2012).

110 Douglas, S. M., Bachelet, I. & Church, G. M. A Logic-Gated Nanorobot for Targeted Transport of Molecular Payloads. *Science* **335**, 831-834, doi:10.1126/science.1214081 (2012).

111 Elbaz, J. & Willner, I. DNA origami: Nanorobots grab cellular control. *Nat Mater* **11**, 276-277 (2012).

112 Savage, D. F., Afonso, B., Chen, A. H. & Silver, P. A. Spatially Ordered Dynamics of the Bacterial Carbon Fixation Machinery. *Science* **327**, 1258-1261, doi:10.1126/science.1186090 (2010).

113 Srere, P. A. & Mosbach, K. Metabolic Compartmentation: Symbiotic, Organellar, Multienzymic, and Microenvironmental. *Annual Review of Microbiology* **28**, 61-84, doi:doi:10.1146/annurev.mi.28.100174.000425 (1974).

114 Fu, T. J. & Seeman, N. C. DNA double-crossover molecules. *Biochemistry* **32**, 3211-3220, doi:10.1021/bi00064a003 (1993).

115 Seeman, N. C. Nanomaterials Based on DNA. *Annual Review of Biochemistry* **79**, 65-87, doi:doi:10.1146/annurev-biochem-060308-102244 (2010).

116 Wei, B., Dai, M. & Yin, P. Complex shapes self-assembled from single-stranded DNA tiles. *Nature* **485**, 623-626, doi:http://www.nature.com/nature/journal/v485/n7400/abs/nature11075.html#supplementary-information (2012).

117 Zhang, F., Nangreave, J., Liu, Y. & Yan, H. Structural DNA Nanotechnology: State of the Art and Future Perspective. *Journal of the American Chemical Society* **136**, 11198-11211, doi:10.1021/ja505101a (2014).

118 Benson, E. *et al.* DNA rendering of polyhedral meshes at the nanoscale. *Nature* **523**, 441-444, doi:10.1038/nature14586 http://www.nature.com/nature/journal/v523/n7561/abs/nature14586.html#supplementary-information (2015).

119 Zhang, F. *et al.* Complex wireframe DNA origami nanostructures with multi-arm junction vertices. *Nat Nano* **10**, 779-784, doi:10.1038/nnano.2015.162 http://www.nature.com/nnano/journal/v10/n9/abs/nnano.2015.162.html#supplementary-information (2015).

120 Ke, Y. *et al.* DNA brick crystals with prescribed depths. *Nat Chem* **6**, 994-1002, doi:10.1038/nchem.2083 http://www.nature.com/nchem/journal/v6/n11/abs/nchem.2083.html#supplementary-information (2014).

121 Douglas, S. M. *et al.* Rapid prototyping of 3D DNA-origami shapes with caDNAno. *Nucleic Acids Research* **37**, 5001-5006, doi:10.1093/nar/gkp436 (2009).

122 Castro, C. E. *et al.* A primer to scaffolded DNA origami. *Nat Meth* **8**, 221-229, doi:http://www.nature.com/nmeth/journal/v8/n3/abs/nmeth.1570.html#supplementary-information (2011).

123 Williams, S. *et al.* in *DNA Computing: 14th International Meeting on DNA Computing, DNA 14, Prague, Czech Republic, June 2-9, 2008. Revised Selected Papers* (eds Ashish Goel, Friedrich C. Simmel, & Petr Sosík) 90-101 (Springer Berlin Heidelberg, 2009).

124 Fu, J., Liu, M., Liu, Y. & Yan, H. Spatially-Interactive Biomolecular Networks Organized by Nucleic Acid Nanostructures. *Accounts of Chemical Research* **45**, 1215-1226, doi:10.1021/ar200295q (2012).

125 Pinheiro, A. V., Han, D., Shih, W. M. & Yan, H. Challenges and opportunities for structural DNA nanotechnology. *Nat Nano* **6**, 763-772 (2011).

126 Zhang, T., Collins, J., Arbuckle-Keil, G. A. & Fu, J. DNA-Directed Assembly of Conductive Nanomaterials. *Advanced Science, Engineering and Medicine* **7**, 1019-1032 (2015).

127 Zhang, T., Collins, J. & Fu, J. Single-Molecule Sensing of Biomolecular Interactions on DNA Nanostructures. *Current Nanoscience* **11**, 722-735 (2015).

128 Yang, Y. R., Liu, Y. & Yan, H. DNA Nanostructures as Programmable Biomolecular Scaffolds. *Bioconjugate Chemistry* **26**, 1381-1395, doi:10.1021/acs.bioconjchem.5b00194 (2015).

129 Zhao, Z. *et al.* Nanocaged enzymes with enhanced catalytic activity and increased stability against protease digestion. *Nat Commun* **7**, doi:10.1038/ncomms10619 (2016).

130 Juul, S. *et al.* Temperature-Controlled Encapsulation and Release of an Active Enzyme in the Cavity of a Self-Assembled DNA Nanocage. *ACS Nano* **7**, 9724-9734, doi:10.1021/nn4030543 (2013).

131 Linko, V., Eerikainen, M. & Kostiainen, M. A. A modular DNA origami-based enzyme cascade nanoreactor. *Chemical Communications* **51**, 5351-5354, doi:10.1039/C4CC08472A (2015).

132 Witus, L. S. & Francis, M. in *Current Protocols in Chemical Biology* (John Wiley & Sons, Inc., 2009).

133 Duckworth, B. P. *et al.* A Universal Method for the Preparation of Covalent Protein – DNA Conjugates for Use in Creating Protein Nanostructures.

Angewandte Chemie International Edition **46**, 8819-8822, doi:10.1002/anie.200701942 (2007).

134 Fang, X., Li, J. J. & Tan, W. Using Molecular Beacons To Probe Molecular Interactions between Lactate Dehydrogenase and Single-Stranded DNA. *Analytical Chemistry* **72**, 3280-3285, doi:10.1021/ac991434j (2000).

135 Cattaneo, A., Biocca, S., Corvaja, N. & Calissano, P. Nuclear localization of a lactic dehydrogenase with single-stranded DNA-binding properties. *Experimental Cell Research* **161**, 130-140, doi:http://dx.doi.org/10.1016/0014-4827(85)90497-5 (1985).

136 Kaiserman, H. B., Odenwald, W. F., Stowers, D. J., Poll, E. H. & Benbow, R. M. A major single-stranded DNA binding protein from ovaries of the frog, Xenopus laevis, is lactate dehydrogenase. *Biochimica et Biophysica Acta (BBA)-Gene Structure and Expression* **1008**, 23-30 (1989).

137 Fiume, L. *et al.* Galloflavin prevents the binding of lactate dehydrogenase A to single stranded DNA and inhibits RNA synthesis in cultured cells. *Biochemical and Biophysical Research Communications* **430**, 466-469, doi:http://dx.doi.org/10.1016/j.bbrc.2012.12.013 (2013).

138 Williams, S. *et al.* in *DNA Computing* Vol. 5347 *Lecture Notes in Computer Science* (eds Ashish Goel, FriedrichC Simmel, & Petr Sosík) Ch. 8, 90-101 (Springer Berlin Heidelberg, 2009).

139 Schmied, J. J. *et al.* DNA origami ‐ based standards for quantitative fluorescence microscopy. *Nat. Protocols* **9**, 1367-1391, doi:10.1038/nprot.2014.079 http://www.nature.com/nprot/journal/v9/n6/abs/nprot.2014.079.html#supplementary-information (2014).

140 Bellot, G., McClintock, M. A., Lin, C. & Shih, W. M. Recovery of intact DNA nanostructures after agarose gel-based separation. *Nat Meth* **8**, 192-194, doi:http://www.nature.com/nmeth/journal/v8/n3/abs/nmeth0311-192.html#supplementary-information (2011).

141 ElSohly, A. M. & Francis, M. B. Development of Oxidative Coupling Strategies for Site-Selective Protein Modification. *Accounts of Chemical Research* **48**, 1971-1978, doi:10.1021/acs.accounts.5b00139 (2015).

142 Dhakal, S. *et al.* Rational design of DNA-actuated enzyme nanoreactors guided by single molecule analysis. *Nanoscale* **8**, 3125-3137, doi:10.1039/C5NR07263H (2016).

143 Hahn, J., Wickham, S. F. J., Shih, W. M. & Perrault, S. D. Addressing the Instability of DNA Nanostructures in Tissue Culture. *ACS Nano* **8**, 8765-8775, doi:10.1021/nn503513p (2014).

144 Perham, R. N. SWINGING ARMS AND SWINGING DOMAINS IN MULTIFUNCTIONAL ENZYMES: Catalytic Machines for Multistep Reactions. *Annual Review of Biochemistry* **69**, 961-1004, doi:doi:10.1146/annurev.biochem.69.1.961 (2000).

145 Mattevi, A. *et al.* Atomic structure of the cubic core of the pyruvate dehydrogenase multienzyme complex. *Science* **255**, 1544-1550, doi:10.1126/science.1549782 (1992).

146 Jitrapakdee, S. *et al.* Structure, Mechanism and Regulation of Pyruvate Carboxylase. *Biochem J.* **413**, 369-387, doi:10.1042/BJ20080709 (2008).

147 Zhou, P., Florova, G. & Reynolds, K. A. Polyketide synthase acyl carrier protein (ACP) as a substrate and a catalyst for malonyl ACP biosynthesis. *Chemistry & biology* **6**, 577-584 (1999).

148 Liedl, T., Hogberg, B., Tytell, J., Ingber, D. E. & Shih, W. M. Self-assembly of three-dimensional prestressed tensegrity structures from DNA. *Nat Nano* **5**, 520-524, doi:http://www.nature.com/nnano/journal/v5/n7/abs/nnano.2010.107.html#supplementary-information (2010).

149 Gu, H., Chao, J., Xiao, S.-J. & Seeman, N. C. A proximity-based programmable DNA nanoscale assembly line. *Nature* **465**, 202-205, doi:http://www.nature.com/nature/journal/v465/n7295/suppinfo/nature09026_S1.html (2010).

150 Teller, C. & Willner, I. Organizing protein – DNA hybrids as nanostructures with programmed functionalities. *Trends in Biotechnology* **28**, 619-628, doi:http://dx.doi.org/10.1016/j.tibtech.2010.09.005 (2010).

151 Piperberg, G., Wilner, O. I., Yehezkeli, O., Tel-Vered, R. & Willner, I. Control of Bioelectrocatalytic Transformations on DNA Scaffolds. *Journal of the American Chemical Society* **131**, 8724-8725, doi:10.1021/ja900718m (2009).

152 Rowland, P., Basak, A. K., Gover, S., Levy, H. R. & Adams, M. J. The three – dimensional structure of glucose 6 – phosphate dehydrogenase from Leuconostoc mesenteroides refined at 2.0 Å resolution. *Structure* **2**, 1073-1087, doi:http://dx.doi.org/10.1016/S0969-2126(94)00110-3 (1994).

153 Chapman, A. D. M., Cortés, A., Dafforn, T. R., Clarke, A. R. & Brady, R. L. Structural basis of substrate specificity in malate dehydrogenases: crystal structure of a ternary complex of porcine cytoplasmic malate dehydrogenase, α - Ketomalonate and TetrahydoNAD. *Journal of Molecular Biology* **285**, 703-712, doi:http://dx.doi.org/10.1006/jmbi.1998.2357 (1999).

154 Johnson-Buck, A., Nangreave, J., Jiang, S., Yan, H. & Walter, N. G. Multifactorial Modulation of Binding and Dissociation Kinetics on Two-Dimensional DNA Nanostructures. *Nano Letters* **13**, 2754-2759, doi:10.1021/nl400976s (2013).

155 P. Candeias, L. *et al.* The catalysed NADH reduction of resazurin to resorufin. *Journal of the Chemical Society, Perkin Transactions 2* **0**, 2333-2334, doi:10.1039/a806431h (1998).

156 Strauss, M., Hofhaus, G., Schröder, R. R. & Kühlbrandt, W. Dimer ribbons of ATP synthase shape the inner mitochondrial membrane. *The EMBO Journal* **27**, 1154-1160, doi:10.1038/emboj.2008.35 (2008).

157 Buzhynskyy, N., Sens, P., Prima, V., Sturgis, J. N. & Scheuring, S. Rows of ATP Synthase Dimers in Native Mitochondrial Inner Membranes. *Biophysical Journal* **93**, 2870-2876, doi:http://dx.doi.org/10.1529/biophysj.107.109728 (2007).

158 Bahatyrova, S. *et al.* The native architecture of a photosynthetic membrane. *Nature* **430**, 1058-1062, doi:http://www.nature.com/nature/journal/v430/n7003/suppinfo/nature02823_S1.html (2004).

APPENDIX A

SUPPLEMENTAL INFORMATION FOR CHAPTER 2

Supplemental Information

REAGENTS

!CAUTION ALL REAGENTS ARE POTENTIALLY DANGEROUS. THEY SHOULD ONLY BE HANDLED BY SPECIALLY TRAINED PERSONNEL.

- Trizma base (Sigma-Aldrich, ≥ 99.9% (titration), crystalline, cat. no. T1503)
- Acetic Acid (Sigma-Aldrich, ≥ 99.7%, cat. no. 695092)
- Ethylenediaminetetraacetic acid (Sigma-Aldrich, ACS reagent, 99.4-100.6%, powder, cat. no. E9884)
- Urea (Sigma-Aldrich, cat. no. U6504)
- Formamide (Sigma-Aldrich, ACS reagent, ≥ 99.5%, cat. no. 221198)
- Xylene Cyanole FF (Sigma-Aldrich, Dye content 75 %, cat. no. 335940)
- Bromophenol Blue (Sigma-Aldrich, cat. no. B0126)
- Glycerol (Sigma-Aldrich, ≥ 99.5%, cat. no. G9012)
- Ammonium Acetate (Sigma-Aldrich, for molecular biology, ≥ 98%, cat. no. A1542)
- Magnesium acetate tetrahydrate (Sigma-Aldrich, for molecular biology, ≥ 99%, cat. no. M5661)
- Sodium hydroxide (Sigma-Aldrich, reagent grade, ≥ 98%, pellets (anhydrous) cat. no. S5881)
- Boric acid (Sigma-Aldrich, for electrophoresis, ≥ 99.5% cat. no. B7901)
- 40% acrylamide stock solution (19:1 Acrylamide:bis-acrylamide) (Bio-Rad, cat. no. 1610154) **! CAUTION** Highly toxic at skin contact; known as a potent neurotoxin. Handling within the organic hood. Store at 4 °C
- Tetramethylethylendiamine (TEMED; Merck, cat. no. 1.10732.0100-100 ml) **!CAUTION** Toxic, can cause skin and eye irritation.
- Ammonium persulfate (APS) **!CAUTION** Harmful if swallowed. Oxidizing. m CRITICAL Store as 0.3 ml aliquotes of 10% (wt/wt) water solution and freeze at -20℃ till use.
- SYBR® Green I Nucleic Acid Gel Stain, 10,000X concentrate in DMSO (Thermo Fisher Scientific, cat. no. S-7585)
- SYBR® Gold Nucleic Acid Gel Stain, 10,000X concentrate in DMSO (Thermo Fisher Scientific, cat. no. S-11494)
- Agarose (Thermo Fisher Scientific, cat. no. 16500-100 g)
- Uranyl formate (Electron Microscopy Sciences, cat. no. 22450-1 g) **!CAUTION** It is toxic by ingestion and if inhaled as dust. Wear protective clothing and use it in a fume hood.

- Deionized water (dI H2O, 18.2 MΩ• cm at 25°C)
- Glucose-6-phosphate Dehydrogenase (G6PDH) (Sigma-Aldrich, from Leuconostoc mesenteroides lyophilized powder, 550-1,100 units/mg protein (biuret), cat. no. G8529)
- L-Lactic Dehydrogenase from rabbit muscle (800-1,200 units/mg protein, Sigma-Aldrich, cat. no. L2500)
- Alkaline Phosphatase (APase, from bovine intestinal mucosa, Sigma-Aldrich, cat. no. P5521).
- Glucose oxidase (GOx, from Aspergillus Niger, Sigma-Aldrich, cat. no. G7141).
- Horseradish peroxidase (HRP), (Sigma-Aldrich, Peroxidase from horseradish, Type VI, essentially salt-free, lyophilized powder, 250-330 units/mg solid, cat. no. P8375)
- Tris Buffered Saline (TBS), (Sigma-Aldrich, pH 8.0, powder cat. no. T6664)
- Dimethyl sulfoxide (DMSO) (Sigma-Aldrich, for molecular biology, cat. no. D8418)
- T-CEP (Tris-(2-carboxyethyl)-phosphine hydrochloride), (Sigma-Aldrich, powder, ≥ 98% cat. no. C4706)
- ABTS (2,2'-Azinobis [3-ethylbenzothiazoline-6-sulfonic acid] -diammonium salt) (Sigma-Aldrich, ≥ 98%, cat. no. A1888)
- SPDP (N-Succinimidyl 3-(2-pyridyldithio)-propionate) (Pierce™ Premium Grade SPDP, cat. no. PG82087)
- DSS (Disuccinimidyl suberate) (Sigma, cat. no. S1885-1G)
- 6AE-NAD$^+$ (BioLog, cat. no. N 013)
- DEAE-Sepharose resin (Sigma, cat. no. DFF100)
- N,N-Dimethylformamide (DMF, anhydrous) (Sigma, cat. no. 227056-100ML)
- N,N-Diisopropylethylamine (DIPEA) (Sigma, cat. no. 387649-100ML)
- Amplex® UltraRed Reagent (Thermofisher Scientific. cat. no. A36006)
- Potassium hydroxide (KOH) pellets (Fisher, cat. no. P250-1)
- Ammonium hydroxide, 28-30 wt. % solution of NH3 in Water (Fisher, cat. no. 29130)
- Hydrogen peroxide, 35 wt. % solution in water (Fisher, cat. no. AC20246-0010)
- Resazurin sodium salt (Fisher, cat. no. 50-700-7914)
- Phenazine methosulfate (Fisher, cat. no. AC130160010)
- D(+)-glucose-6-phosphate sodium salt (Fisher, cat. no. AC446980010)
- Biotin-PEG-SVA (MW 5,000, Laysan Bio Inc, cat. no. Biotin-PEG-SVA-5000-500 mg)

- mPEG-Succinimidyl Valerate (MW 5,000, Laysan Bio Inc, cat. no. MPEG-SVA-5000-1g)
- Disulfosuccinimidyl tartrate (Soltec Ventures, cat. no. CL107)
- Streptavidin (Invitrogen, cat. no. S-888)
- (3-Aminopropyl)triethoxysilane, APTES (Fisher, cat. no. BP 179-25)
- Biotinylated bovine serum albumin (ImmunoPure, ThermoFisher, cat. no. 29130)
- Methanol (HPLC grade, Fisher, cat. no. A452-4)
- Acetone (HPLC grade, Fisher, cat. no. A949-4)
- Alconox (Fisher, cat. no. 50821294)
- Trolox (Fisher, cat. no. 218940050)
- Immersion oil (Low fluorescence, Olympus, cat. no. Z-81225)
- Denaturing gel tracking dye (see reagent setup)
- Non-denaturing (or native) tracking dye (see reagent setup)
- 10 × TBE (see reagent setup)
- 10 × TAE-Mg^{2+} (see reagent setup)
- M13mp18 single-stranded DNA (Affymetrix, cat. No. 71706)
- Crude oligonucleotides (25-100 nmole) are ordered from Integrated DNA Technology (IDT). The oligonucleotides are further purified using denaturing PAGE as described in the Experiment design. Oligonucleotides with terminus (5’ or 3’) modified amines (Amino Modifier C6) or thiols (Thiol Modifier C6 S-S) are ordered at the 1 μmole scale from IDT.

EQUIPMENT

- Water circulating bath (VWR, mod. 1160S, cat. no. 13721-082)
- Vertical electrophoresis system (GE Healthcare Life Sciences, mod. SE 600 Ruby, cat. no. 80-6479-57)
- Electrophoresis power supply (Fisher Scientific, cat. no. FB1000)
- Molecular weight cut-off filters (EMD Millipore, Amicon Ultra-4 Centrifugal Filters, 30 kDa, cat. no. UFC803096)
- Standard heat block (VWR, cat. no. 13259-030)
- Agarose gel electrophoresis system, Owl™ EasyCast™ B2 Mini Gel Electrophoresis Systems, (Thermo Scientific, cat. No. 09528110B)
- Freeze 'N Squeeze spin columns (Bio-Rad, cat. no. 732-6165)
- SigmaPrep™ spin column (Sigma, cat. no. SC1000-1KT)

- Refrigerated centrifuge (Eppendorf, mod. 5804R, 15 amp version)
- Hand-held UV lamp (UVP, mod. UVGL-58, 254/365 nm)
- Vacufuge (Eppendorf Vacufuge plus, mod. 5305)
- Thermocycler (Eppendorf Mastercycler Pro with vapo. Protect technology, mod. 6321)
- Gel imager (Bio-Rad, Molecular Imager Gel Doc XR$^+$ System, cat. no. 1708195)
- Typhoon TRIO plus variable mode imager (GE Healthcare, Mod. 63-0055-86) equipped with excitations at 532, 633 and 488 nm and emissions at 520, 580, 610 and 670 nm.
- Freezer at -20 ºC (Fisher Scientific Isotemp General-Purpose Freezer, cat. no. 13986148).
- Freezer at -80 ºC (VWR Signature Ultra-Low Temperature Upright Freezer, -86 to - 50 ºC, mod. 5604)
- Lyophilizer (Labconco FreeZone 2.5plus Freezer Dry System, cat. no. 7420020)
- Vortex mixer (Fisher Scientific Analog Vortex Mixer, cat. no. 02215365)
- Nanodrop 2000 (Thermo Scientific, S06497)
- HPLC system (Agilent Technologies, 1200 series, equipped with G1379B degasser, G1312A binary pump, G1329A autosampler, G1316A thermostatted column, G1321A fluorescence detector, G1315C DAD SL and G1364B preparative scale fraction) with OpenLAB Control Panel Software (version A.01.05).
- HPLC column: Clarity 3µ Oligo-RP column (Phenomenex, 50 × 4.6 mm, cat no. 00B-4441-E0, stored in 20% methanol).
- Thin layer chromatography (TLC) silica gel aluminium sheet (Millipore, F_{254}; 20 × 20 cm, cat. no. M1055540001)
- AKTA purifier 10 FPLC system (Glocal Medical Instrumentation, cat. no. 28-4062-64), equipped with pump P-900, monitor pH/C-900, Box-900, injection valve INV-907, PV-908, mixer M-925, fraction collector Frac-950, Unicorn 5.11 workstation
- MonoQ 4.6/100 PE anion-exchange column (GE Healthcare Life Sciences, cat. no. 17-5179-01)
- Superdex 200 Increase 10/300 GL size exclusion chromatography column (GE Healthcare Life Sciences, cat. no. 28990944)
- AFM (Bruker, Multimode 8 with Nanoscope V controller)
- ScanAsyst-Fluid+ AFM probes (Bruker, k ~0.7 N/m, tip radius < 10 nm)

- Software for designing DNA nanostructures (Tiamat, http://yanlab.asu.edu/Resources.html); CadNano (http://cadnano.org/) and Nanorex (http://nanorex-inc.software.informer.com/).
- Transmission electron microscope (JEOL; JEM-1400)
- Copper mesh grids (Electron Microscopy Sciences, cat. no. FCF400-CU-50)
- Parafilm M (Electron Microscopy Sciences, cat. no. 70990)
- Fine pointed tweezers (Dumont, cat. no. 72870-DZ)

REAGENT SETUP

All buffer solutions are prepared in deionized water (dI H2O, 18.2 MΩ• cm at 25°C) and are stocked at 4 °C in dark.

The 50 × TAE stock solution contains 2 M Trizma base, 1 M acetic acid and 0.1 M EDTA. 1000 mL stock solution is prepared by adding 242.2 g of Trizma Base, 57.1 mL of acetic acid and 37.2 g of EDTA.Na_2•$12H_2O$ into dI H_2O for the total volume of 1000 mL.

The 10 × TAE-Mg^{2+} stock solution contains 0.4 M Trizma and 125 mM Mg^{2+}, which is prepared by adding 200 mL of 50 × TAE stock and 26.8 g of $(CH_3COO)_2Mg$•$4H_2O$ (Sigma, 99%) into dI H_2O for the total volume of 1000 mL. The pH value is adjusted to 8 using NaOH or acetic acid.

The 1 × TAE-Mg^{2+} buffer solution is diluted from 10 × TAE-Mg^{2+} with the final concentration of 0.04 M Trizma and 12.5 mM Mg^{2+}.

The 10 × TBE stock solution is prepared by adding 108 g of Trizma Base, 55 g of boric acid (Sigma) and 40 mL of 0.5 M EDTA into dI H_2O for the total volume of 1000 mL, with the final concentration of 0.89 M Trizma, 0.89 M boric acid and 20 mM EDTA.

The 20% denaturing PAGE gel mix (A) is prepared by adding 500 mL of 40% acrylamide solution (19:1 for Ac/Bis, BioRad), 100 mL 10 × TBE, 500 g of urea (OmniPur, EMD Millipore) into dI H_2O for a total volume of 1000 mL, with the final concentration of 20% acrylamide, 8.3 M urea and 1 × TBE.

The 0% denaturing PAGE gel mix (B) is prepared by adding 500 g of urea and 100 mL 10 × TBE into dI H_2O for a total volume of 1000 mL, with the final concentration of 8.3 M urea and 1 × TBE.

2 × denaturing tracking dye buffer Xylene Cyanole FF (Heavy one) 100 ml is prepared by mixing 90 ml Formamide, 37mg EDTA.Na_2.$2H_2O$, 40 mg NaOH, and 0.1 g Xylene Cyanole FF dye to get 0.10% dye concentration.

2 × denaturing tracking dye buffer Bromophenol Blue (Light one) 100 ml is prepared by mixing 90 ml Formamide, 37mg EDTA.Na_2.$2H_2O$, 40 mg NaOH, and 0.1 g Bromophenol Blue dye to get 0.10% dye concentration.

Denaturing PAGE elution buffer contains 500 mM CH_3COONH_4, 10 mM $(CH_3COO)_2Mg$ and 2 mM EDTA), which is prepared by adding 19.3 gram of ammonium acetate, 1.07 gram of magnesium acetate and 2 mL of 0.5 M EDTA to dI H_2O for the total volume of 500 mL with the pH ~ 8.

10 × native tracking Dye 100 ml is prepared by adding 0.20g Bromophenol Blue dye, 0.20g Xylene Cyanole FF dye, 50 ml Glycerol, 10 ml 10 x TAE/ Mg^{2+} , and 40 ml dIH_20.

DNA-loading buffer for NAD^+-DNA conjugation contains 10 mM Acetate acid and 0.005% Triton X-100.

DNA elution buffer NAD^+-DNA conjugation contains 50 mM HEPES (pH 7.5) and 1.5 M NaCl.

Preparation of Buffer for FPLC: (A) 50 mM sodium phosphate (pH7.5), (B) 50 mM sodium phosphate (pH7.5) + 1 M NaCl. 1L of the stock solution of 1M sodium phosphate (pH=7.5) is prepared by mixing 106.8 g (774 mM) $Na_2HPO_4.H_2O$ and 32.08 g (226 mM) NaH_2PO_4 , add dIH2O to 1 L. All buffer solutions needs to be filtered with 0.22 μm filter prior to use.

10 × T50 buffer (pH8) contains 0.1M Tris, 0.5 M NaCl, 10 mM EDTA.

EQUIPMENT SETUP

Polyacrylamide gel electrophoresis setup The Vertical electrophoresis system (SE 600 Ruby) is used for the denaturing PAGE purification of oligonucleotides and the native PAGE characterization of DNA nanostructures. The sandwiched gel is assembled by two glass plates, 2 spacers on the sides and one spacer mate sheet in the middle. The sandwich is then secured with clamps and set upright on the gel casting stand and well-sealed. Spacer mate will be removed before gel casting. The gel casting assembly is left on the bench at room temperature for around 30 minutes for the gel to polymerize. Upper buffer chamber is firstly attached to the gel assembly and filled with running buffer. Buffer in the lower chamber should be the same as used in upper chamber and can be stirred. Lower buffer chamber will be maintained at a certain temperature by water tubes which connect to water circulating bath. Power supply leads are connected to a safety lid which covers the gel box. A constant current 40 mA per gel and 40 °C water bath for denaturing PAGE gel is generally used. For Native PAGE gel, a constant voltage 200 V and 15 °C water bath is recommended.

FPLC setup Methods can be created, viewed and edited in the Unicorn workstation software. A flow rate of 1.0 ml/min is used for anion-exchange chromatography and 0.5 ml/min is used for size-exclusion chromatography. The pump pressure limit is set at 3 -4 MPa for the protection of separation columns. An appropriate elution gradient is loaded into the system as shown in **Table 7**. The flow system and the separation columns are stored in 20% ethanol if they are not used.

HPLC setup The HPLC (Agilent 1200 series) is used for purifying NAD^+-modified oligonucleotides with an elution gradient from 25% methanol/100 mM Triethylammonium acetate (TEAA) to 35% methanol/100 mM TEAA as shown in **Fig.10b**. The flow rate is set at 1.0 ml/min. The Pressure limit is set at 400 bar. The flow system of the HPLC and the separation column are stored in 20% methanol if they are not used.

AFM setup Assembled DNA Origami sample with enzymes can be visualized and characterized using Bruker Multimode 8 system with Nanoscope V controller in a ScanAsyst in Fluid mode which can be selected in Nanoscope 8 software. ScanAsyst self-optimizing AFM technique and ScanAsyst-Fluid+ AFM probes are equipped. Samples were deposited on freshly peeled mica surface and incubated with 1 × TAE Mg^{2+} buffer (pH 8.0). 1 mM $NiCl_2$ buffer can be used to enhance the adsorption of DNA nanostructures on mica surface. To manually adjust the peakforce setpoint, auto scanning mode must be switched off first. Images can be viewed and processed offline in Nanoscope Analysis software.

APPENDIX B

SUPPLEMENTAL INFORMATION FOR CHAPTER 3

Supporting Information

Multi-enzyme complexes on DNA scaffolds capable of substrate channeling with an artificial swinging arm

Jinglin Fu, Yuhe Yang, Alexander Johnson-Buck, Minghui Liu, Yan Liu, Nils G. Walter, Neal W. Woodbury and Hao Yan

Table of contents:

Section 1: Materials

Enzymes: Glucose-6-phosphate dehydrogenase (G6pDH, *Leuconostoc mesenteroides*), malic dehydrogenase (MDH, *porcine heart*), lactate dehydrogenase (LDH, *rabbit muscle*), oxaloacetate decarboxylase (OAD, *Pseudomonas sp.*), lactate oxidase (LOX, *Pediococcus sp.*) and horseradish peroxidase (HRP) were purchased from Sigma (St. Louis, MO).

DNA strands: Single-stranded oligonucleotides, Cy3-, Cy5- and BHQ-2-labeled oligonucleotides, and 5'-amino- and 5'-thiol (C6 S-S)-modified oligonucleotides were purchased from IDT DNA (Integrated DNA Technologies, INC.). Dye-labeled oligonucleotides were HPLC-purified by the manufacturer.

Crosslinking reagents: *N*-Succinimidyl 3-(2-pyridyldithio)-propionate (SPDP) was ordered from Pierce. Disuccinimidyl suberate (DSS), N,N-Diisopropylethylamine (DIPEA), and Dimethyl sulfoxide (DMSO) were purchased from Sigma.

NAD^+: β-Nicotinamide-N6-(2-aminoethyl) adenine dinucleotide (6AE-NAD^+ or AE-NAD^+) was ordered from BIOLOG (Bremen, Germany). Unmodified NAD^+ was ordered from Sigma.

Substrates and activity assay reagents: Glucose-6-phosphate (G6p), sodium pyruvate, oxaloacetic acid (OAA), resazurin (RESA), and phenazine methosulfate (PMS) were purchased from Sigma. Amplex® Red for assaying peroxidase activity was purchased from Life Technologies.

Buffers: Phosphate buffered saline (PBS), HEPES sodium salt, Tris buffered saline (TBS), Tris base, acetic acid, EDTA, and magnesium acetate were also purchased from Sigma.

Dye-labeling reagents for proteins: AlexaFluor®555 and AlexaFluor®647 amine reactive dyes were ordered from Life Technologies.

Section 2: Design, assembly, and characterization of DNA nanostructures

1. DNA nanostructure design: The detailed sequence designs of the DNA double-crossover (DX) nanostructures are shown in Figures S1-S7. The computer programs of Tiamat, Cadnano and NanoEngineer (version 1.1.1, Nanorex INC.) were used to facilitate the structure design. To improve the assembly efficiency of protein onto the DNA tiles, two identical capture probes were displayed on the DNA scaffolds with a sequence complementary to the DNA strands conjugated to proteins.

2. Denaturing PAGE purification of oligonucleotides: Oligonucleotides purchased from IDT (Integrated DNA Technologies, INC.) were purified using denaturing polyacrylamide gel electrophoresis (PAGE). Denaturing (6–8 %) PAGE gels (8.3 M urea) were prepared at room temperature. The crude DNA strands were loaded in the wells and run for 1 to 1.5 hours at 35 ℃ at a constant current of 90 mA and subsequently stained with ethidium bromide (EB). The bands corresponding to the correct strand length were cut from the gel, chopped into small pieces, and incubated for 1 hour in elution buffer (500 mM ammonium acetate, 10 mM magnesium acetate, 2 mM sodium ethylenediaminetetraacetic acid, pH 8.0). The DNA strands were extracted from the gel pieces by centrifugation using a Costar Spin X filtration device (Corning, cellulose acetate membrane with 0.22 μm size). The filtrate was subjected to butanol extraction to remove the EB stain, then the DNA was ethanol precipitated, washed by ethanol and vacuum dried. The DNA strands were dissolved in nanopure water and the concentrations of the individual purified strands were measured by UV absorbance at 260 nm using the extinction coefficient provided by the manufacturer.

3. DNA nanostructure assembly: The DNA strands constituting each DNA structure were mixed in 1×TAE/Mg^{2+} buffer (40 mM Tris, 20 mM acetic acid, 2 mM EDTA and 12.5 mM magnesium acetate, pH 8.0) to reach a final concentration of 1 μM per strand, except for the NAD^{+}-conjugated DNA strands, which were added to the mixture at a final concentration of 1.5 μM (with 50% excess to ensure efficient incorporation of the NAD^{+}-labeled strand in the DX tile). All samples were annealed using an Eppendorf Mastercycler using the annealing protocol shown in Table S1, with the temperature decreasing from 90 ℃ to 72 ℃ over 10 min (a relatively steep gradient to avoid thermal damage to NAD^{+}), decreasing from 68 ℃ to 24 ℃ over 60 min, and finally holding at 15 ℃. The formation of the DNA structures was characterized by native PAGE. Excess NAD$^+$-conjugated DNA strands were removed by size-exclusion chromatography as described in Section 5.

4. Native PAGE characterization of DNA structures: 3% Native PAGE gels were prepared at room temperature and run for 2.5 to 3.5 hours at a constant voltage of 200V and subsequently stained with SYBR® Green.

5. Quantifying the concentration of the purified DX tiles and the yield of protein-DNA tile assembly: The concentrations of the purified DX tiles were measured using OD_{260} based on the extinction coefficients of the DX tile estimated by summing the extinction coefficients of all the DNA strands involved (dsDNA value). The measured concentrations of the DX tiles were within 5% of the theoretical concentration, as shown in Table S2.

Table S2 also shows the estimated extinction coefficients for the different protein-DNA tile assemblies. The theoretical extinction coefficients of ssDNA and dsDNA were obtained from the web site IDT Biophysics-DNA Thermodynamics & Hybridization (http://biophysics.idtdna.com/UVSpectrum.html)

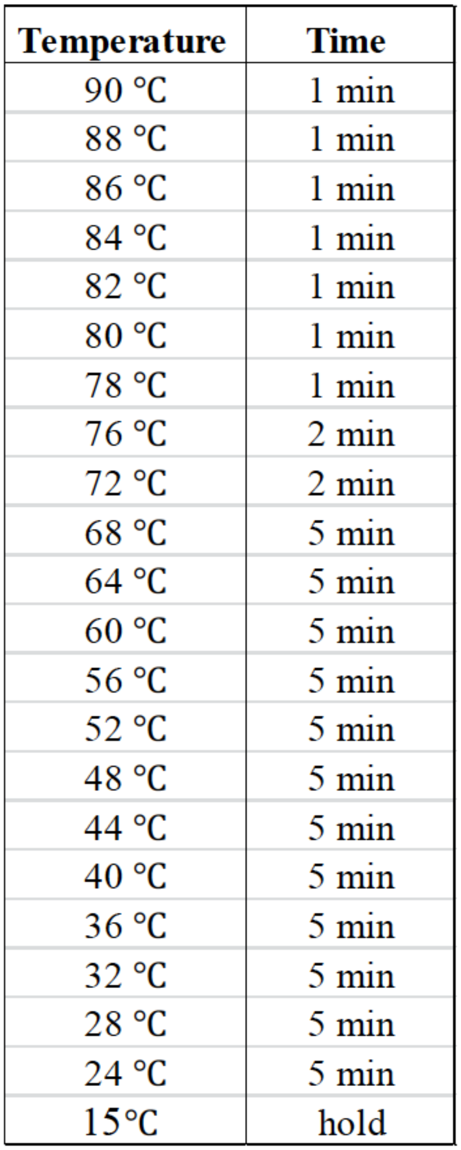

Temperature	Time
90 °C	1 min
88 °C	1 min
86 °C	1 min
84 °C	1 min
82 °C	1 min
80 °C	1 min
78 °C	1 min
76 °C	2 min
72 °C	2 min
68 °C	5 min
64 °C	5 min
60 °C	5 min
56 °C	5 min
52 °C	5 min
48 °C	5 min
44 °C	5 min
40 °C	5 min
36 °C	5 min
32 °C	5 min
28 °C	5 min
24 °C	5 min
15°C	hold

Table S1. Thermal annealing program for assembling all DNA nanostructures. Note: Fast process from 90˚C – 72˚C is performed to avoid thermal damage of NAD+.

Structures	Theoretical ε_{260} (M^{-1} cm^{-1})	Prepared Conc.(nM)	Measured A_{260}	Calculated conc. (nM)	Error (%)
7-nm MDH-NAD$^+$ semi-swinging arm	3735503	200	0.778	208	+ 4.1
14-nm MDH-NAD$^+$ semi-swinging arm	3735503	200	0.773	207	+ 3.5
21-nm MDH-NAD$^+$ semi-swinging arm	3735503	200	0.783	210	+ 4.8
DNA tile	3187221.6	1000	3.15	988	-1.2

Structure	Theoretical ε_{260} (M^{-1} cm^{-1})
NAD$^+$ -DNA tile structure in Figure S1 without assembled protein	3187221.6
MDH-NAD$^+$ semi arm structure in Figure S2 with assembled MDH	3735503.2
MDH-DNA tile (structure similar to Figure S2 without NAD arm) + free NAD$^+$	3554526.8
G6pDH-NAD$^+$ semi-swinging arm structure in Figure S1 with assembled G6pDH	3785354.2
G6pDH-DNA tile (structure similar to Figure S2 but without NAD arm) + free NAD$^+$	3604377.8
G6pDH-NAD$^+$-MDH full swinging arm in Figure S3 with assembled G6pDH and MDH	3799466.2
G6pDH-MDH assembly (structure similar to Figure S3 but without NAD arm) + free NAD$^+$	3618489.8
G6pDH-NAD$^+_2$-MDH$_2$ in Figure S5 with assembled G6pDH and MDH	4398701
G6pDH-NAD$^+_4$-MDH$_4$ in Figure S7 with assembled G6pDH and MDH	5695362

Table S2. Theoretical vs. measured concentrations and extinction coefficients of all structures used in enzyme studies. The theoretical extinction coefficients were obtained by summing the extinction coefficients of all the DNA strands involved (dsDNA value) and protein/NAD$^+$ components. G6pDH: $\varepsilon_{260} \sim 61594\ M^{-1}cm^{-1}$; MDH: $\varepsilon_{260} \sim 14112\ M^{-1}cm^{-1}$; 6AE-NAD$^+$: $\varepsilon_{260} \sim 21000\ M^{-1}cm^{-1}$ (provided by Biolog).

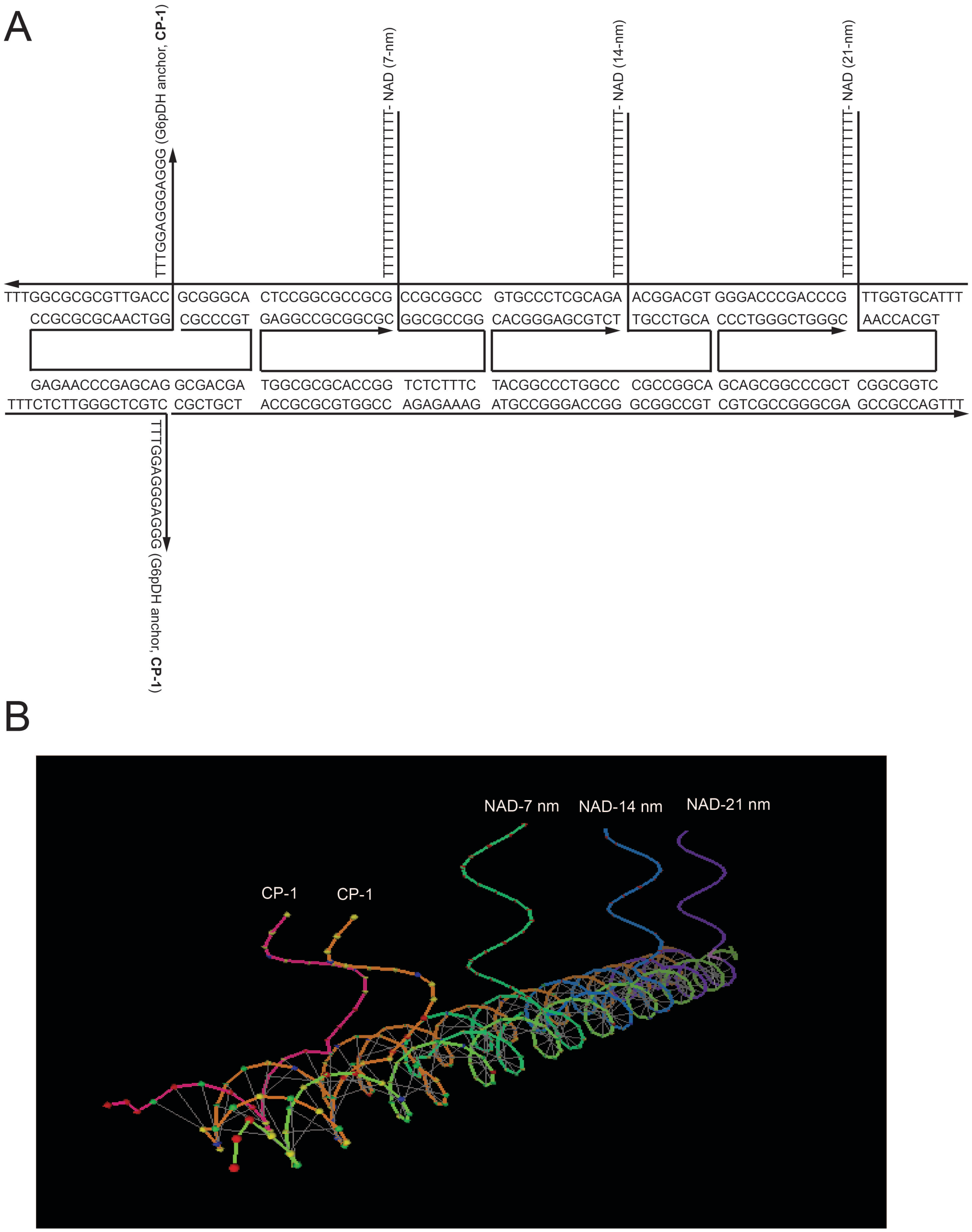
A
TTTGGAGGGAGGG (G6pDH anchor, CP-1)
TTTTTTTTTTTTTTTTTTT- NAD (7-nm)
TTTTTTTTTTTTTTTTTTT- NAD (14-nm)
TTTTTTTTTTTTTTTTTTT- NAD (21-nm)
TTTGGCGCGCGTTGACC GCGGGCA CTCCGGCGCCGCG CCGCGGCC GTGCCCTCGCAGA ACGGACGT GGGACCCGACCCG TTGGTGCATTT
CCGCGCGCAACTGG CGCCCGT GAGGCCGCGGCGC GGCGCCGG CACGGGAGCGTCT TGCCTGCA CCCTGGGCTGGGC AACCACGT
GAGAACCCGAGCAG GCGACGA TGGCGCGCACCGG TCTCTTTC TACGGCCCTGGCC CGCCGGCA GCAGCGGCCCGCT CGGCGGTC
TTTCTCTTGGGCTCGTC CGCTGCT ACCGCGCGTGGCC AGAGAAAG ATGCCGGGACCGG GCGGCCGT CGTCGCCGGGCGA GCCGCCAGTTT
TTTGGAGGGAGGG (G6pDH anchor, CP-1)
B
NAD-7 nm
NAD-14 nm
NAD-21 nm
CP-1
CP-1

Figure S1. **DNA sequence design for characterizing the distance-dependent activity of the G6pDH-NAD$^+$ semi-swinging arm.** (**A**) The structure incorporates two identical capture probes (CP) with the sequence **CP-1** (5'-TTTGGAGGGAGGG), which are extended from 3'-ends of the respective stands and 7 bps from the nearest crossover on the helics. The theoretical angle between the anchor point of the CP-1 probes and the surface of the DNA scaffolds is ~ 240°(34.5°×7), facing to the top of the surface of the DNA scaffolds. The pair of CPs are expected to cooperatively recruit one G6pDH that is labeled with two DNA molecules with the sequence **P-1** (5'-TTTTTCCCTCCCTCC). For each experiment, only one of the three positions, 21, 42 or 63 bp away from the protein anchor position, is extended with the NAD$^+$-modified poly(T)$_{20}$, which acts as the swinging arm at a distance of 7 nm, 14 nm or 21 nm from the anchor site of the enzyme. The CP-1 and poly(T)$_{20}$ strands are all designed to project from the same side of the DX tile. (**B**) Computer modeling (Tiamat) of DNA nanostructures: two capture probes (CP-1) and NAD$^+$ arms are all facing to the same side of the structure.

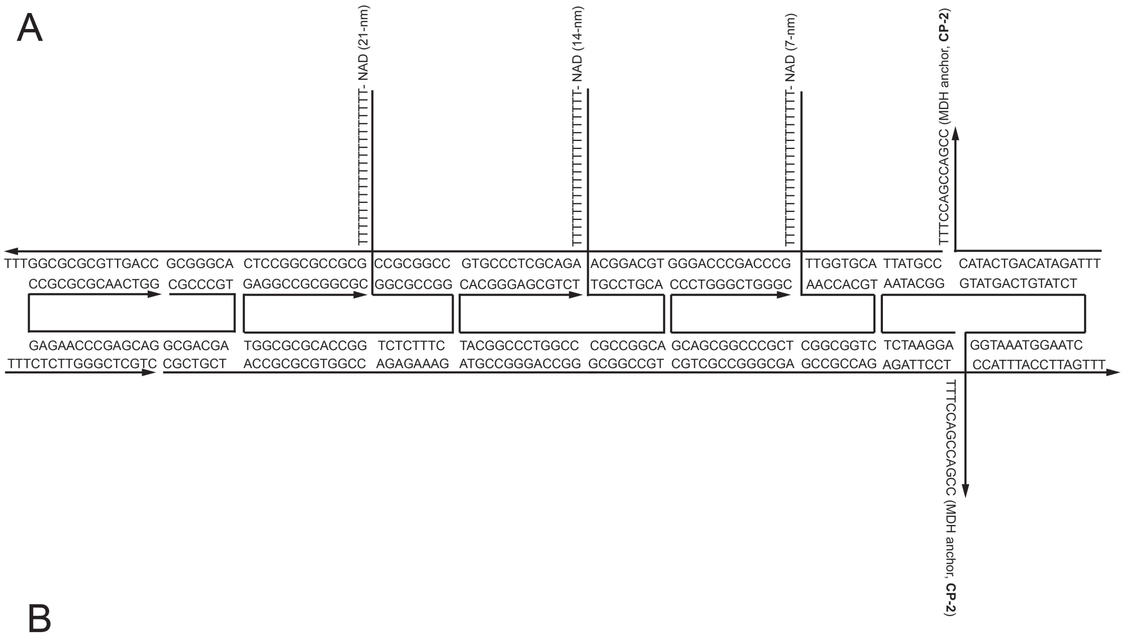
A
TTTTTTTTTTTTTTTTTTTT- NAD (21-nm)
TTTTTTTTTTTTTTTTTTTT- NAD (14-nm)
TTTTTTTTTTTTTTTTTTTT- NAD (7-nm)
TTTCCAGCCAGCC (MDH anchor, **CP-2**)
TTTGGCGCGCGTTGACC GCGGGCA CTCCGGCGCCGCG CCGCGGCC GTGCCCTCGCAGA ACGGACGT GGGACCCGACCCG TTGGTGCA TTATGCC CATACTGACATAGATTT
CCGCGCGCAACTGG CGCCCGT GAGGCCGCGGCGC GGCGCCGG CACGGGAGCGTCT TGCCTGCA CCCTGGGCTGGGC AACCACGT AATACGG GTATGACTGTATCT
GAGAACCCGAGCAG GCGACGA TGGCGCGCACCGG TCTCTTTC TACGGCCCTGGCC CGCCGGCA GCAGCGGCCCGCT CGGCGGTC TCTAAGGA GGTAAATGGAATC
TTTCTCTTGGGCTCGTC CGCTGCT ACCGCGCGTGGCC AGAGAAAG ATGCCGGGACCGG GCGGCCGT CGTCGCCGGGCGA GCCGCCAG AGATTCCT CCATTTACCTTAGTTT
TTTCCAGCCAGCC (MDH anchor, **CP-2**)

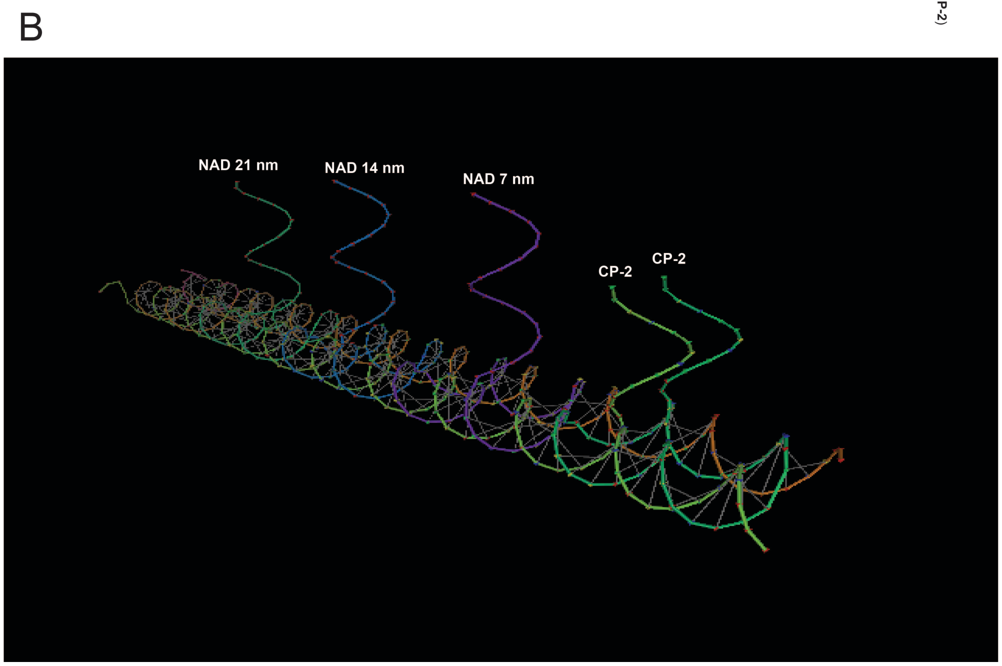
B
NAD 21 nm
NAD 14 nm
NAD 7 nm
CP-2
CP-2

Figure S2. **DNA sequence design for characterizing the distance-dependent activity of an MDH-NAD$^+$ semi-swinging arm structure.** (**A**) The structure incorporates two identical capture probes with the sequence **CP-2** (5'-TTTCCAGCCAGCC), which are extended from 3'-ends of the respective stands and 7 bps from the nearest crossover on the helics. The theoretical angle between the anchor point of the CP-2 probes and the surface of the DNA scaffolds is ~ 240˚(34.5˚×7), facing to the top of the surface of the DNA scaffolds. The two CP-2 probes are expected to cooperatively recruit one MDH that is labeled with two DNA molecules with the sequence **P-2** (5'-TTTTTGGCTGGCTGG). For each experiment, only one of the three positions, 21, 42 or 63 bp away from the MDH anchor position, is extended with the NAD$^+$-modified poly(T)$_{20}$, which acts as the swinging arm at a distance of 7 nm, 14 nm or 21 nm away from the anchor site of the enzyme. The CP-2 and poly(T)$_{20}$ strands are all designed to project from the same side of the DX tile. (**B**) Computer modeling (Tiamat) of DNA nanostructures: two capture probes (CP-2) and NAD$^+$ arms are all facing to the same side of the structure.

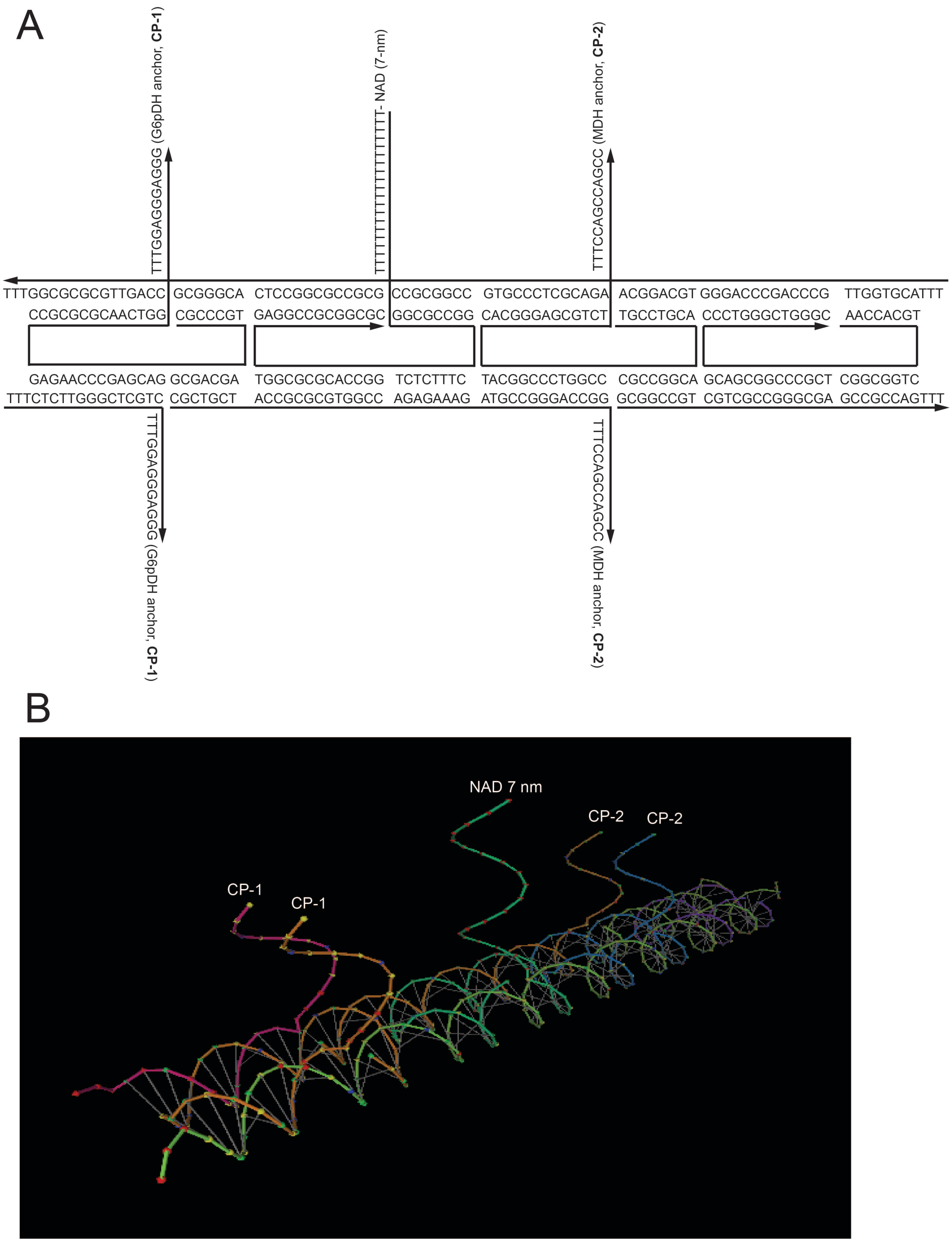
A
TTTGGAGGGAGGG (G6pDH anchor, CP-1)
TTTTTTTTTTTTTTTTTTT- NAD (7-nm)
TTTCCAGCCAGCC (MDH anchor, CP-2)
TTTGGCGCGCGTTGACC GCGGGCA CTCCGGCGCCGCG CCGCGGCC GTGCCCTCGCAGA ACGGACGT GGGACCCGACCCG TTGGTGCATTT
CCGCGCGCAACTGG CGCCCGT GAGGCCGCGGCGC GGCGCCGG CACGGGAGCGTCT TGCCTGCA CCCTGGGCTGGGC AACCACGT
GAGAACCCGAGCAG GCGACGA TGGCGCGCACCGG TCTCTTTC TACGGCCCTGGCC CGCCGGCA GCAGCGGCCCGCT CGGCGGTC
TTTCTCTTGGGCTCGTC CGCTGCT ACCGCGCGTGGCC AGAGAAAG ATGCCGGGACCGG GCGGCCGT CGTCGCCGGGCGA GCCGCCAGTTT
TTTGGAGGGAGGG (G6pDH anchor, CP-1)
TTTCCAGCCAGCC (MDH anchor, CP-2)
B
NAD 7 nm
CP-2
CP-2
CP-1
CP-1

Figure S3. **DNA sequence design for the G6pDH-NAD$^+$-MDH swinging arm structure.** (**A**) The structure incorporates one pair of each of the capture probes **CP-1** (TTTGGAGGGAGGG) and **CP-2** (TTTCCACCAGCC), which serve as anchors for G6pDH and MDH, respectively. The NAD$^+$-modified poly(T)$_{20}$ swinging arm is located in the middle and designed to be anchored 7 nm away from the anchoring points of either enzyme. All the probes and poly(T)$_{20}$ strand are designed to project from the same face of the tile. (**B**) Computer modeling (Tiamat) of DNA nanostructures: capture probes (CP-1 and CP-2) and NAD$^+$ arms are all facing to the same side of the structure.

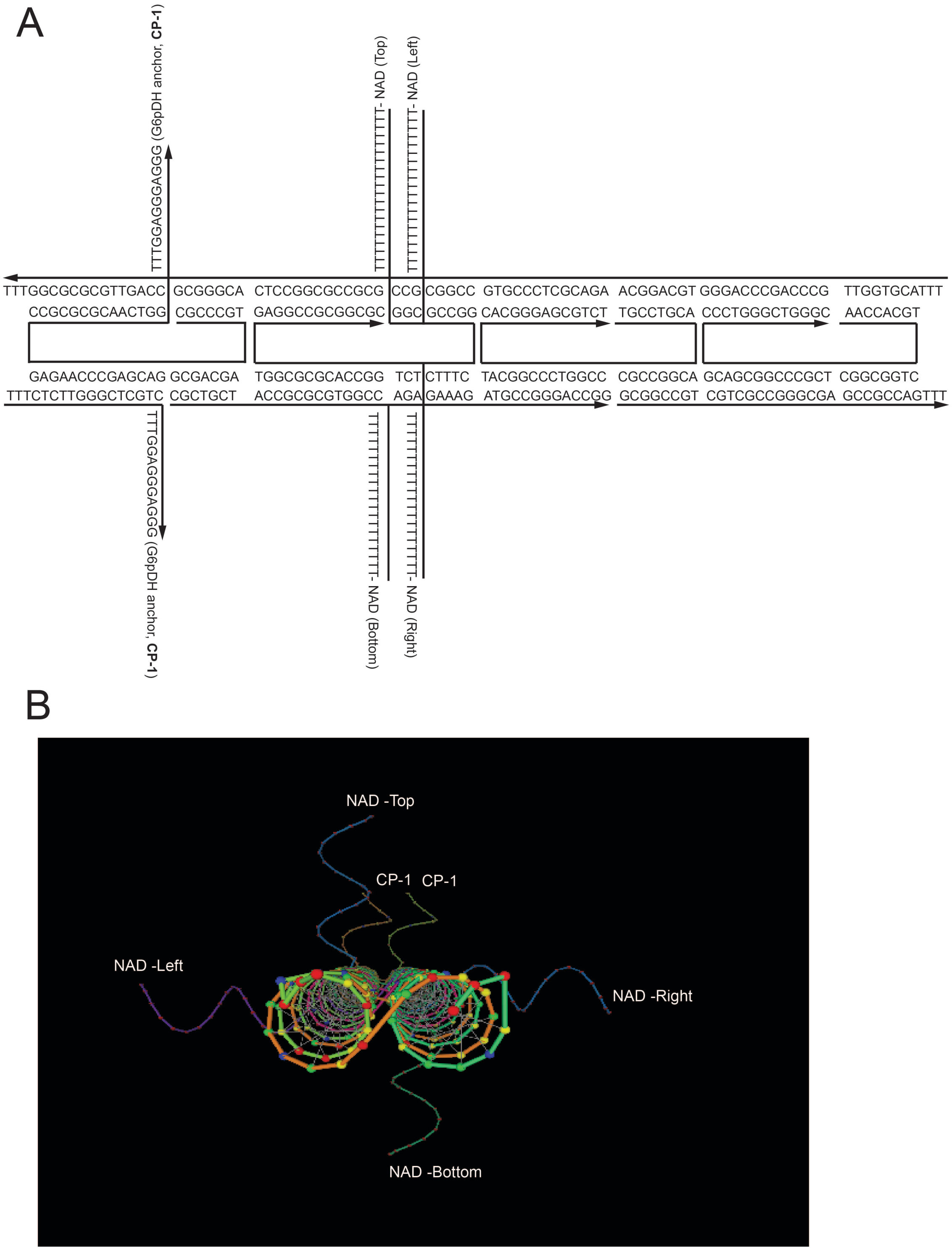
A
TTTGGAGGGAGGG (G6pDH anchor, **CP-1**)
TTTTTTTTTTTTTTTTTTTT- NAD (Top)
TTTTTTTTTTTTTTTTTTTT- NAD (Left)
TTTGGCGCGCGTTGACC
CCGCGCGCAACTGG
GCGGGCA
CGCCCGT
CTCCGGCGCCGCG
GAGGCCGCGGCGC
CCG
GGC
CGGCC
GCCGG
GTGCCCTCGCAGA
CACGGGAGCGTCT
ACGGACGT
TGCCTGCA
GGGACCCGACCCG
CCCTGGGCTGGGC
TTGGTGCATTT
AACCACGT
GAGAACCCGAGCAG
TTTCTCTTGGGCTCGTC
GCGACGA
CGCTGCT
TGGCGCGCACCGG
ACCGCGCGTGGCC
TCT
AGA
CTTTC
GAAAG
TACGGCCCTGGCC
ATGCCGGGACCGG
CGCCGGCA
GCGGCCGT
GCAGCGGCCCGCT
CGTCGCCGGGCGA
CGGCGGTC
GCCGCCAGTTT
TTTGGAGGGAGGG (G6pDH anchor, **CP-1**)
TTTTTTTTTTTTTTTTTTTT- NAD (Bottom)
TTTTTTTTTTTTTTTTTTTT- NAD (Right)
B
NAD -Top
CP-1
CP-1
NAD -Left
NAD -Right
NAD -Bottom

Figure S4. DNA sequence design for Orientation dependent enzyme-NAD$^+$ arm activity for complexes. (**A**) The structure incorporates one pair of the capture probes **CP-1** (TTTGGAGGGAGGG), which serve as anchors for G6pDH and MDH, respectively. The NAD$^+$-modified poly(T)$_{20}$ swinging arms are located at four different positions: **NAD-Top**, 21 bps (~ 7 nm) from CP-1 probes on the same helix, and 8 bps from the nearest crossover position. The theoretical angle between the anchor point of the NAD-Top probe and the surface of the DNA scaffolds is ~ 270˚(34.5˚×8), facing to the top side of the DNA scaffolds. **NAD-Left**, 24 bps (~ 8 nm) from CP-1 probes on the same helix, and 5 bps from the nearest crossover position. The theoretical angle between the anchor point of the NAD-Top probe and the surface of the DNA scaffolds is ~ 172˚(34.5˚×5), facing to the left side of the DNA scaffolds. **NAD-Right**, 24 bps (~ 8 nm) from CP-1 probes on the same helix, and 5 bps from the nearest crossover position. The theoretical angle between the anchor point of the NAD-Right probe and the surface of the DNA scaffolds is ~ -172˚(-34.5˚×5), facing to the right side of the DNA scaffolds. **NAD-Bottom**, 21 bps (~ 7 nm) from CP-1 probes on the same helix, and 8 bps from the nearest crossover position. The theoretical angle between the anchor point of the NAD-Bottom probe and the surface of the DNA scaffolds is ~ -240˚(-34.5˚×7), facing to the bottom side of the DNA scaffolds. (**B**) Computer modeling (Tiamat) of DNA nanostructures.

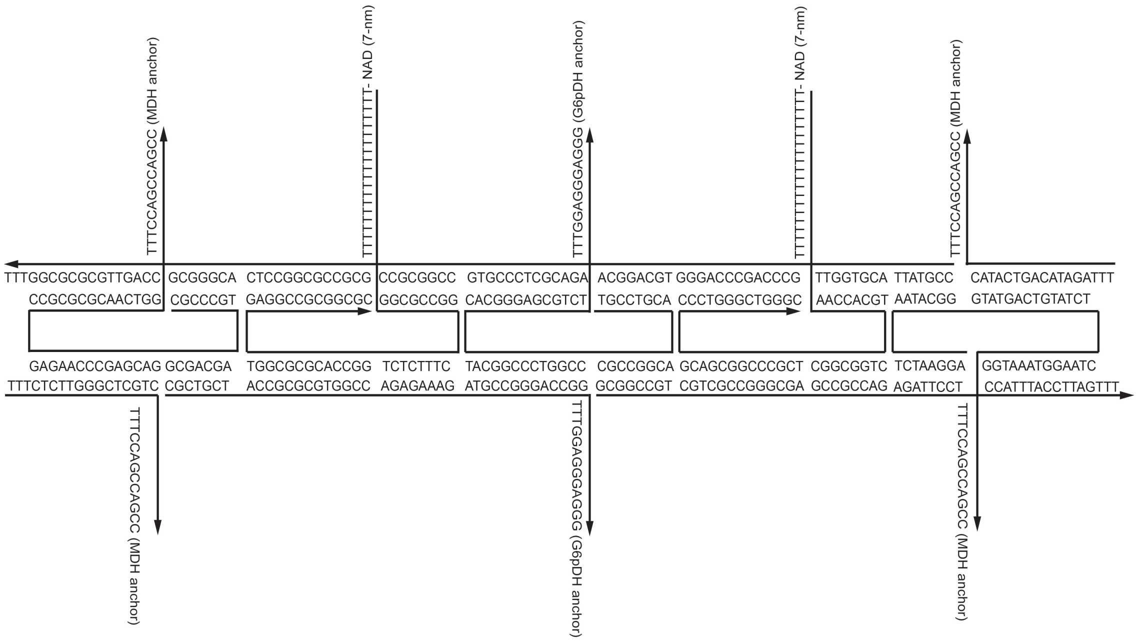

Figure S5. **The DNA sequence design for the G6pDH-NAD$^{+}_{2}$-MDH$_2$ swinging arm structure.** The structure incorporates one pair of CP-1 strands to anchor G6pDH, two pairs of CP2 probes to anchor MDH, and two NAD$^+$-modified poly(T)$_{20}$ swinging arms located in between the G6pDH and MDH anchor sites. The anchoring points of the swinging arms are designed to be 7 nm from the nearest molecules of G6pDH and MDH. All the probes and poly(T)$_{20}$ strand are designed to project from the same face of the tile.

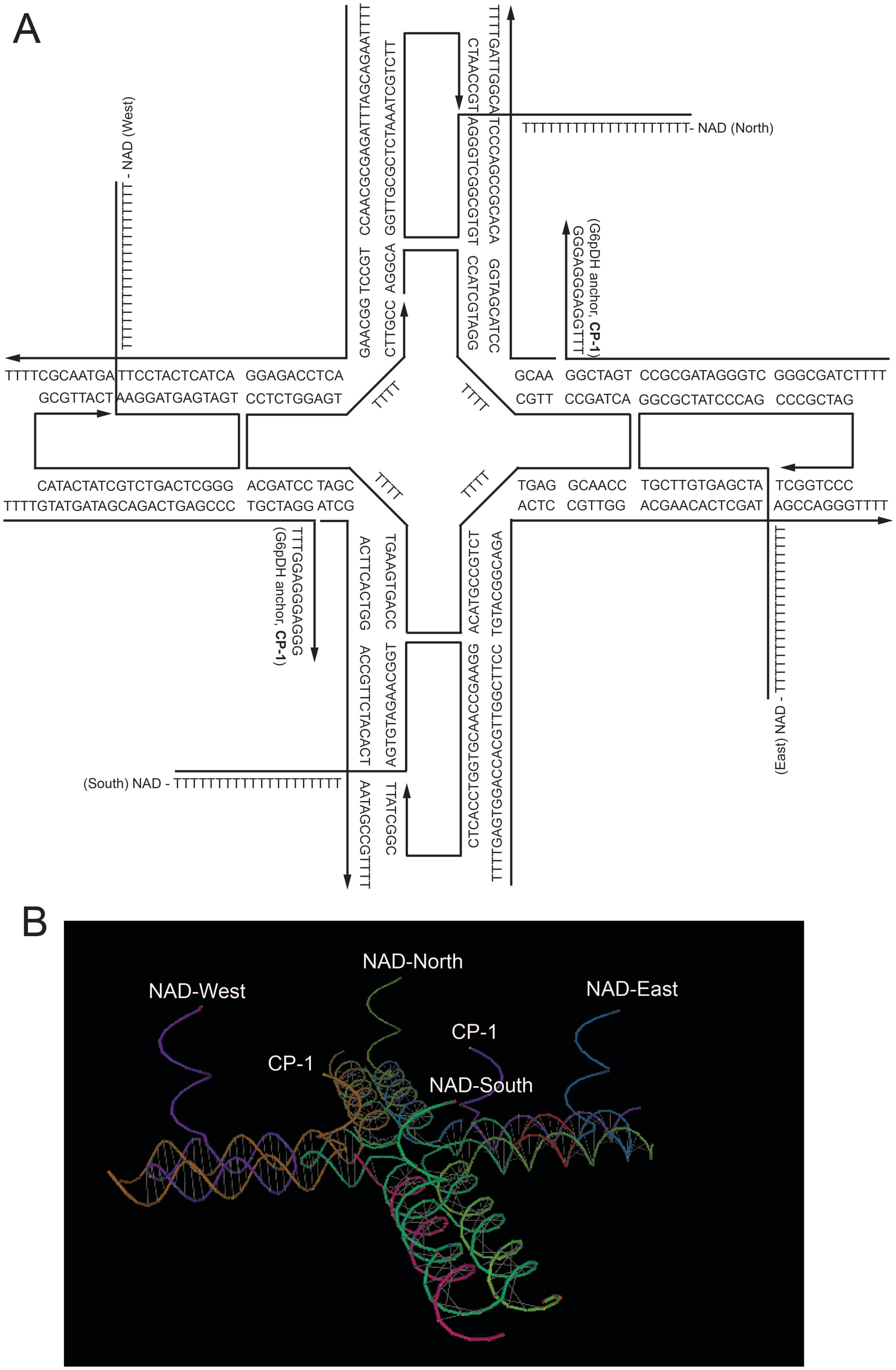
A
TTTTTTTTTTTTTTTTTTTT - NAD (West)
GAACGG TCCGT CCAACGCGAGATTTAGCAGAATTTT
CTTGCC AGGCA GGTTGCGCTCTAAATCGTCTT
CTAACCGT AGGGTCGGCGTGT CCATCGTAGG
TTTTGATTGGCA TCCCAGCCGCACA GGTAGCATCC
TTTTTTTTTTTTTTTTTTTT- NAD (North)
(G6pDH anchor, CP-1)
GGGAGGGAGGTTT
TTTTCGCAATGA TTCCTACTCATCA GGAGACCTCA
GCGTTACT AAGGATGAGTAGT CCTCTGGAGT
TTTT
TTTT
GCAA GGCTAGT CCGCGATAGGGTC GGGCGATCTTTT
CGTT CCGATCA GGCGCTATCCCAG CCCGCTAG
CATACTATCGTCTGACTCGGG ACGATCC TAGC
TTTTGTATGATAGCAGACTGAGCCC TGCTAGG ATCG
TTTT
TTTT
TGAG GCAACC TGCTTGTGAGCTA TCGGTCCC
ACTC CGTTGG ACGAACACTCGAT AGCCAGGGTTTT
TTTGGAGGGAGGG
(G6pDH anchor, CP-1)
ACTTCACTGG ACCGTTCTACACT AATAGCCGTTTT
TGAAGTGACC AGTGTAGAACGGT TTATCGGC
ACATGCCGTCT CTCACCTGGTGCAACCGAAGG
TGTACGGCAGA TTTTGAGTGGACCACGTTGGCTTCC
(East) NAD - TTTTTTTTTTTTTTTTTTTT
(South) NAD - TTTTTTTTTTTTTTTTTTTT
B
NAD-West
NAD-North
NAD-East
CP-1
CP-1
NAD-South

Figure S6. **DNA sequence design for the G6pDH–NAD$^+_4$ swinging arm structure based on the 4×4 tile design.** The structure incorporates two CP-1 strands that anchor G6pDH near the center of the tile, and four NAD$^+$ modified poly(T)$_{20}$ located on the four arms of the tile (North, East, South, and West) are the swinging arms. All the probes and poly(T)$_{20}$ strands are designed to project from the same face of the 4×4 tile, with approximately 7-8 nm between the swinging arms and the enzyme at the center of the tile. (**B**) Computer modeling (Tiamat) of DNA nanostructures.

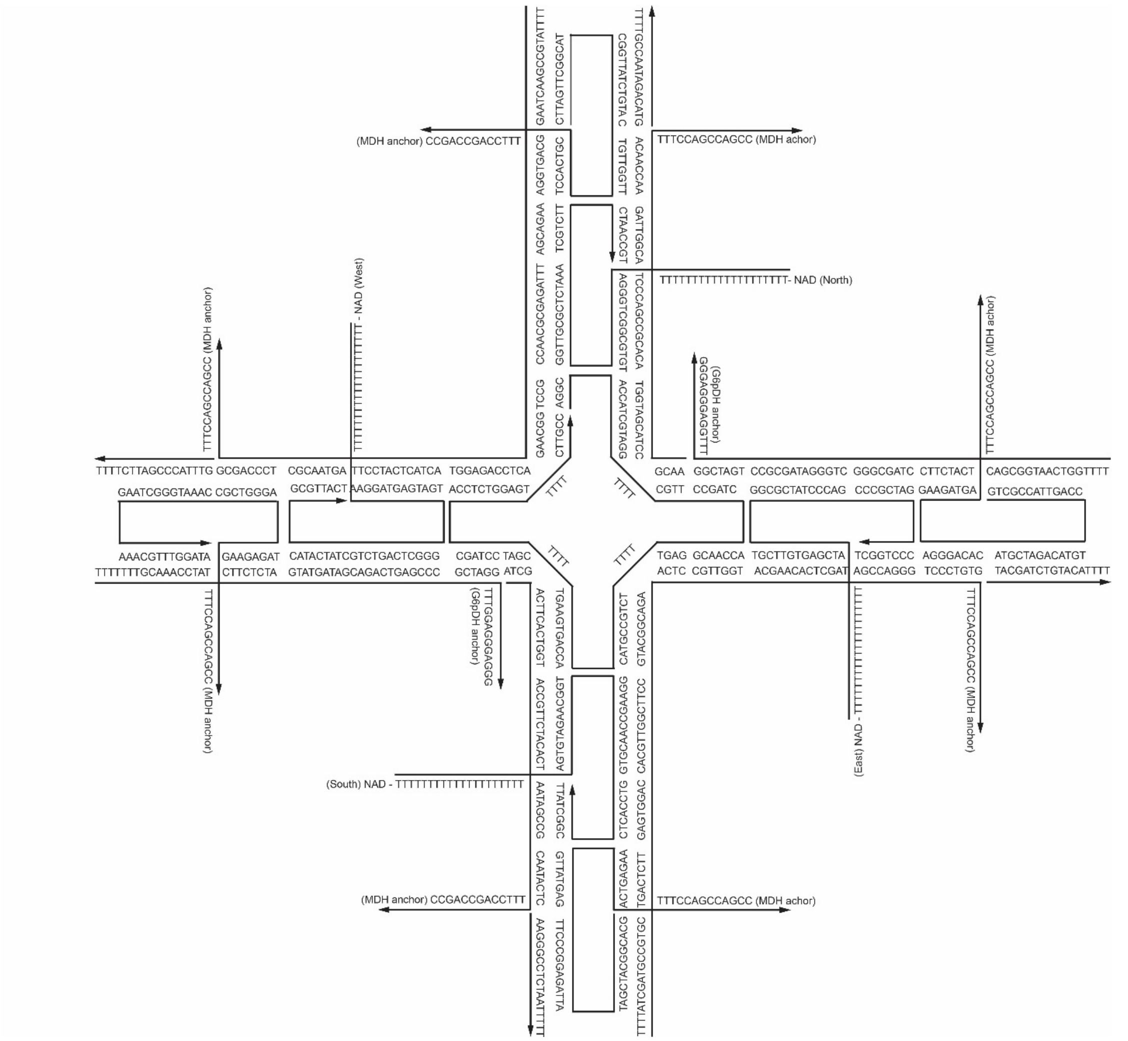

Figure S7. **The DNA sequence design for the G6pDH–NAD$^+_4$ –MDH$_4$ swinging arm structure based on the 4×4 tile design.** The structure incorporates two CP-1 strands to assemble a single molecule of G6pDH near the center of the tile, four pairs of CP-2 strands to anchor MDH near the end of each of the four arms, and one NAD$^+$-modified poly(T)$_{20}$ in the middle of each arm, ~5-8 nm away from each enzyme. All the probes are designed to project from the same face of the 4×4 tile.

Section 3: Preparation, purification, and characterization of protein-DNA conjugates

1. Protein-DNA conjugation

A. Pretreatment of proteins before conjugation to DNA: G6pDH (dimeric, ~ 100 kDa) ordered from Sigma (*1*) was washed with 10 mM sodium HEPES buffer (pH 7.4) using an Amicon-30 kD cutoff filter to get rid of small-molecular weight impurities. The crude MDH received from Sigma was found to form large protein aggregates. To reduce these aggregates, MDH was first washed with 10 mM sodium HEPES buffer (pH 7.4) using an Amicon-100 kD cutoff filter to remove impurities larger than 100 kD. Then the filtrate was concentrated with an Amicon-30 kD cutoff filter to collect the dimeric MDH (~ 70 kD) (*2*). The concentration of the enzymes was measured using UV absorbance at 280 nm and their respective extinction coefficients provided by the company (115200 $M^{-1}cm^{-1}$ for G6pDH and 19600 $M^{-1}cm^{-1}$ for MDH).

B. DNA-protein conjugation reactions: The method used to link the enzyme to single-stranded oligonucleotides is similar to that described in a previous study (*3*). As shown in Figure S8A, SPDP was used to crosslink G6pDH to a 5' thiol-modified oligo (**P-1**: 5'-HS-TTT TTC CCT CCC TCC), and MDH (dimeric, ~ 70 kD) with another 5' thiol-modified oligo (**P-2**: 5'-HS-TTT TTG GCT GGC TGG). The conjugation reaction occurs in two steps, followed by multiple purification steps:

a. First, 1000 μL of 40 μM enzyme solution was reacted with SPDP in 10 mM sodium HEPES (pH 8-8.5) for one hour, allowing amine-reactive N-hydroxysuccinimide (NHS) esters to react with the lysine residues on the protein surface. For G6pDH-SPDP conjugation, a 2-fold excess of SPDP was used, while for MDH-SPDP conjugation a 3.5-fold excess of SPDP was used. The optimal fold excess of SPDP was chosen by titrating varied ratios of SPDP to protein with the aim to label ~ 1-2 SPDP per protein on average. The SPDP label number determines the maximum number of DNA oligos that can be linked to the protein.

b. Excess SPDP was removed by washing with 10 mM HEPES buffer using Amicon-30 kD cutoff filters. The SPDP coupling efficiency was evaluated by monitoring the increase in absorbance at 343 nm due to the release of pyridine-2-thione (extinction coefficient: 8080 $M^{-1}cm^{-1}$). Quantification of MDH-SPDP and G6pDH-SPDP modification *via* absorbance spectra is shown in Figure S8B and C).

c. Next, the SPDP-modified protein was conjugated to a thiol-modified oligo ((P-1 for G6pDH and P-2 for MDH, 8-fold excess) through a disulfide bond exchange of the activated pyridyldithiol group. The reaction mixture was incubated in 10 mM sodium HEPES with 150 mM NaCl (pH 8-8.5) for one hour. The probability of SPDP reacting with cysteine on the protein surface is very low due to the very few available reduced cysteine on the protein surfaces, much more slow reaction diffusion of larger proteins as compared to smaller, and linear DNA molecules and over excess of DNA molecules over proteins in the solution.

d. The excess oligo was removed by the filtration using Amicon-30 kD cutoff filters and washing one time with 100 mM HEPES (pH 7.4) containing 1 M NaCl, and three times with 1×PBS (pH 7.4). The high salt concentration in the first washing buffer helps to remove nonspecifically bound DNA from the surface of the protein due to electrostatic interactions. MDH-oligo conjugates were washed one extra time with 10 mM HEPES containing 150 mM NaCl and 0.05% (v/v) P-20 detergent to remove additional nonspecifically bound DNA.

2. FPLC purification of DNA-protein conjugates: Due to the presence of multiple lysine residues on the surface of both proteins, the reaction product is a mixture of protein-DNA conjugates with different numbers of DNA oligos per protein (and even for the conjugates with the same DNA labeling ratio, the labeling sites on the protein may also vary). To isolate a homogeneous population of enzymes modified with the same number of oligonucleotides, the DNA-conjugated proteins obtained in the above procedures were then purified by anion-exchange chromatography using AKTA fast-protein liquid chromatography (FPLC, GE Healthcare). For a typical purification, ~ 500 µL 50 µM G6pDH-P1 solution with an average labeling ratio of ~ 1.5 DNA molecules per protein was loaded into FPLC with an anion exchange column (MonoQ 4.6/100 PE, GE Healthcare) using an elution gradient (Figure S9) from 20% 50 mM sodium phosphate, 1 M NaCl to

55% 50 mM sodium phosphate, 1 M NaCl, with a flow rate of 1.5 mL/min. Multiple peaks from the purification chromatogram were collected and were identified respectively to be the unmodified protein, proteins with 1, 2, 3 and 4 DNA labels, and free DNA molecules which are determined by the UV-absorbance measurement (Figure S10 and Table S3). The collected fractions were concentrated using Amicon-30 kD cutoff filters. After use, the FPLC system was cleaned by flowing with 30 mL pure water, and stored in 20% ethanol-water solution.

3. Characterization of the activity of DNA–protein conjugates:

A. Method for concentration measurements: The concentration of the DNA-conjugated protein in fractions collected during FPLC purification was quantified by absorbance at 260 and 280 nm (Table S3).

B. Activity assay: Activity of the purified DNA-labeled dehydrogenases was measured as dependent function of the number of DNA labels, as shown in Figure S11. Enzyme activities are evaluated by the rate of reduction of NAD^+ to NADH (for G6pDH) or oxidation of NADH to NAD^+ (for MDH) with absorbance change at 340 nm. The assay was performed with 1 mM glucose-6 phosphate or pyruvate (for MDH), 1 mM NAD^+ or NADH(for MDH) in pH 8 HEPES buffer. G6pDH labeled with two DNA molecules maintained ~ 40% activity of the wild type, while labeling with 3 or 4 DNA molecules diminished activity further. In contrast, MDH is less sensitive to DNA labeling: MDH labeled with two DNA molecules maintained ~80% activity of the wild type.

4. Characterization of the assembly efficiency of DNA-protein conjugates on DNA nanostructures: The DNA-conjugated proteins with different DNA labeling ratios were tested for their efficiency of assembly on the DNA tiles, as shown in Figure S12. Both G6pDH and MDH labeled with two DNA molecules gave the highest proportion of the predominant product, presumably representing one protein per DX tile, with >80% yield.

5. Alexa dye labeling of DNA-conjugated proteins: The DNA-conjugated proteins were further labeled with spectrally distinct fluorescent dye molecules, which allow us to use native gel electrophoresis to unambiguously confirm the correct assembly of both proteins on the DNA tiles (Figure 1B in the main text). For a typical reaction, ~100 µL of 20 µM DNA-conjugated protein was incubated with a 10-fold molar excess of AlexaFluor 555 or AlexaFluor 647 in 1× PBS buffer for one hour in the dark (the AlexaFluor dyes are activated with an NHS ester, and react with lysine residues on the protein surface). 10 µL of 1 M sodium bicarbonate was added into the solution to adjust the pH between 8–8.5. After incubation, the extra unreacted dye molecules were removed by washing the protein solution with 1× PBS buffer three times using an Amicon-30 kD cutoff filter, spun at 4,000 rpm (rcf would be more universal than rpm) for 10 minutes at 4˚C. The UV-Vis absorbance spectra of the purified dye-labeled proteins are shown in Figure S13, and were used to quantify the concentration and labeling ratio of the dye-labeled proteins together with the extinction coefficients of the dye (150,000 M^{-1} cm^{-1} for Alexa555 at 546 nm; 250,000 M^{-1} cm^{-1} for Alexa647 at 647 nm) and the protein-DNA conjugates (quantification is similar to that shown in Table S3).

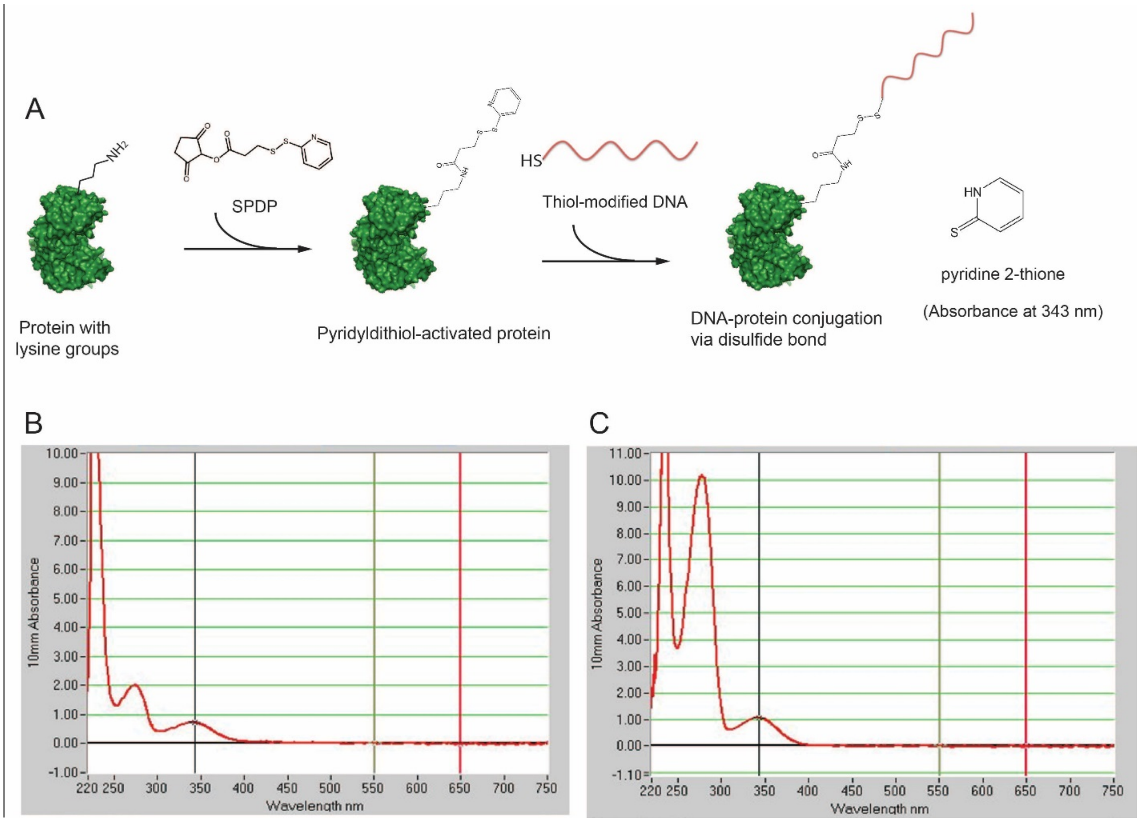

Figure S8. Protein-DNA conjugation using a SPDP cross-linker. (**A**) A schematic illustration of the conjugation chemistry. First, SPDP is coupled to the primary amine groups of the lysine residues at the protein surface; then, it is further reacted with thiol-modified DNA to couple the DNA to the protein. The reaction side product 2-thiopyridine has an absorbance at 343 nm with an extinction coefficient 8080 M^{-1} cm^{-1} which can be used to quantify the number of SPDP labeled per protein(*4*). (**B**) Quantification of MDH-SPDP modification by absorbance spectrum. ΔA343 upon SPDP conjugation and T-CEP treatment is ~ 0.72, corresponding to ~ 90 μM SPDP coupled to 70 μM MDH (ε=19600 M^{-1} cm^{-1} at 280 nm for MDH) (**C**) Quantification of G6pDH-SPDP modification by absorbance spectrum. ΔA343 upon SPDP conjugation is ~ 1.07, corresponding to ~ 130 μM SPDP coupled with 90 μM G6pDH (ε=115200 M^{-1} cm^{-1} at 280 nm for G6pDH). The SPDP labeling ratio was determined by adding 1 μL of 20 mM T-CEP (pH 7.4) to 20 μL SPDP-labeled protein in 10 mM sodium HEPES buffer (pH 7.4). T-CEP cleaves the disulfide bond and releases pyridine 2-thione with strong absorbance at 343 nm. T-CEP cleavage causes a slight absorbance increase at 280 nm, so it is necessary to record the protein concentration before performing the cleavage.

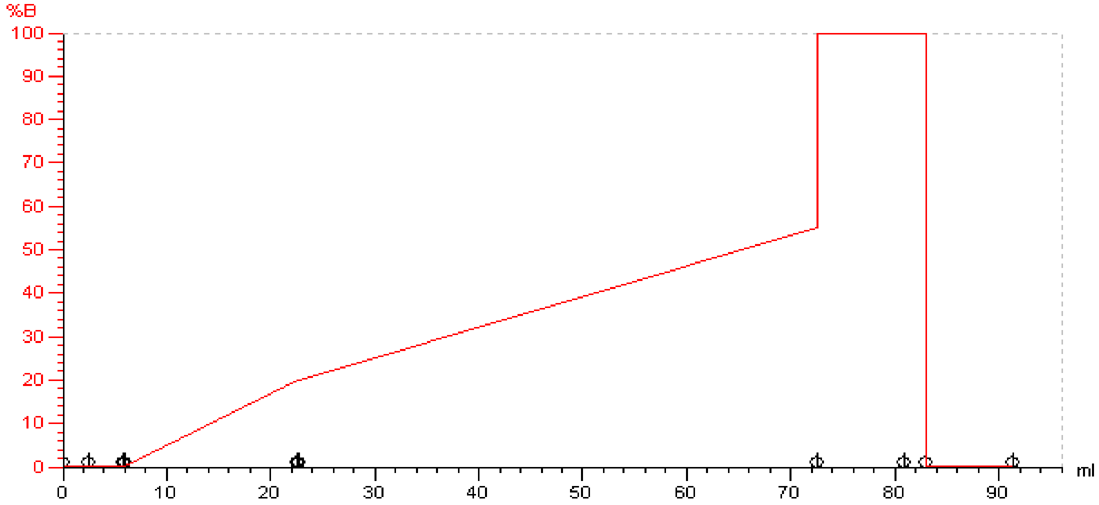

Figure S9. Elution gradient for anion-exchange chromatography. Buffer A: 50 mM sodium phosphate (pH 7.5); buffer B: 50 mM sodium phosphate and 1 M NaCl (pH 7.5).

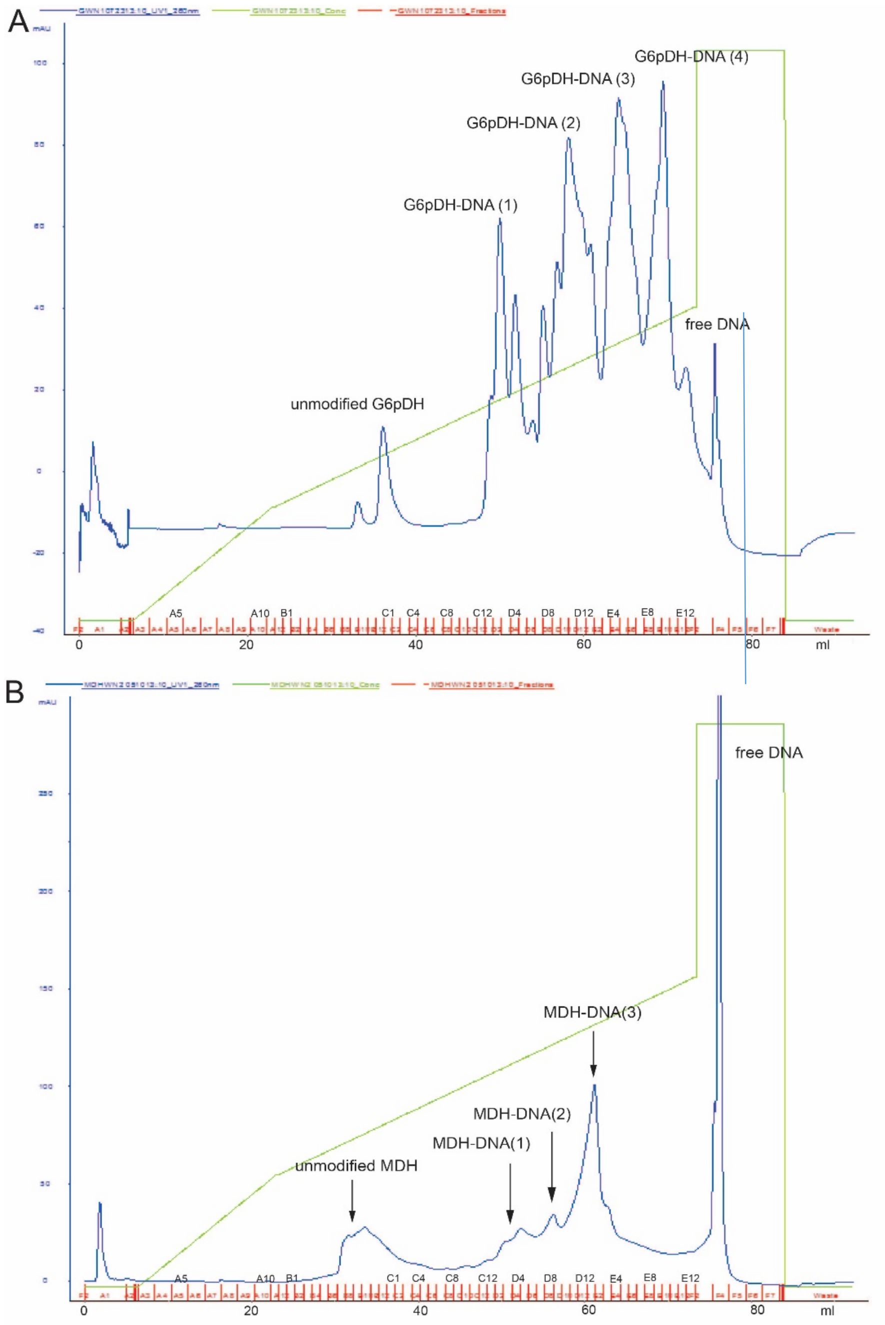

Figure S10. Anion-exchange FPLC to purify DNA conjugated proteins. (A) G6pDH-DNA conjugates, and (B) MDH-DNA conjugates. The proteins with different DNA label ratios were separated into distinct peaks that were collected in fractions. Condition: buffer A, 50 mM sodium phosphate (pH7.5); buffer B, 50 mM sodium phosphate, 1 M NaCl (pH 7.5). The identities of the distinct peaks were assigned using the A260 and A280 data (Table S3).

DNA	A260/A280	ε_{260} (M^{-1} cm^{-1})	ε_{280} (M^{-1} cm^{-1})	Protein	A260/A280	ε_{260} (M^{-1} cm^{-1})	ε_{280} (M^{-1} cm^{-1})	FPLC Fractions	A260/A280	A260	A280	DNA - to-Protein Ratio	Protein Conc. (uM)
P-1	1.27	115200	90709	**G6pDH**	0.52	61594	118450	D1-D5	0.86	1.28	1.49	1.08	6.88
P-1	1.27	115200	90709	**G6pDH**	0.52	61594	118450	D9-E2	0.96	6.651	6.90	1.89	23.80
P-1	1.27	115200	90709	**G6pDH**	0.52	61594	118450	E3-E7	1.03	8.557	8.30	2.80	22.29
P-1	1.27	115200	90709	**G6pDH**	0.52	61594	118450	E8-E11	1.08	6.855	6.34	3.88	13.47
P-2	1.60	130100	81313	**MDH**	0.72	14112	19600	D2-D6	1.42	1.73	1.22	0.92	12.87
P-2	1.60	130100	81313	**MDH**	0.72	14112	19600	D7-D10	1.50	2.05	1.37	1.81	8.23
P-2	1.60	130100	81313	**MDH**	0.72	14112	19600	E1-E4	1.53	6.16	4.014	2.97	15.39

Table S3. Quantification of the concentration and DNA labeling ratio of the purified G6pDH-DNA (P-1) and MDH-DNA (P-2) conjugates by measuring the absorbance at 260 and 280 nm, and using the following equations:

$$A_{260}(DNA - protein) = \varepsilon_{260}(protein) * Conc.(protein) + \varepsilon_{260}\ (DNA) * Conc.(DNA)$$

$$A_{280}(DNA - protein) = \varepsilon_{280}(protein) * Conc.(protein) + \varepsilon_{280}\ (DNA) * Conc.(DNA)$$

$$Ratio\left(\frac{DNA}{protein}\right) = \frac{Conc.(DNA)}{Conc.(protein)}$$

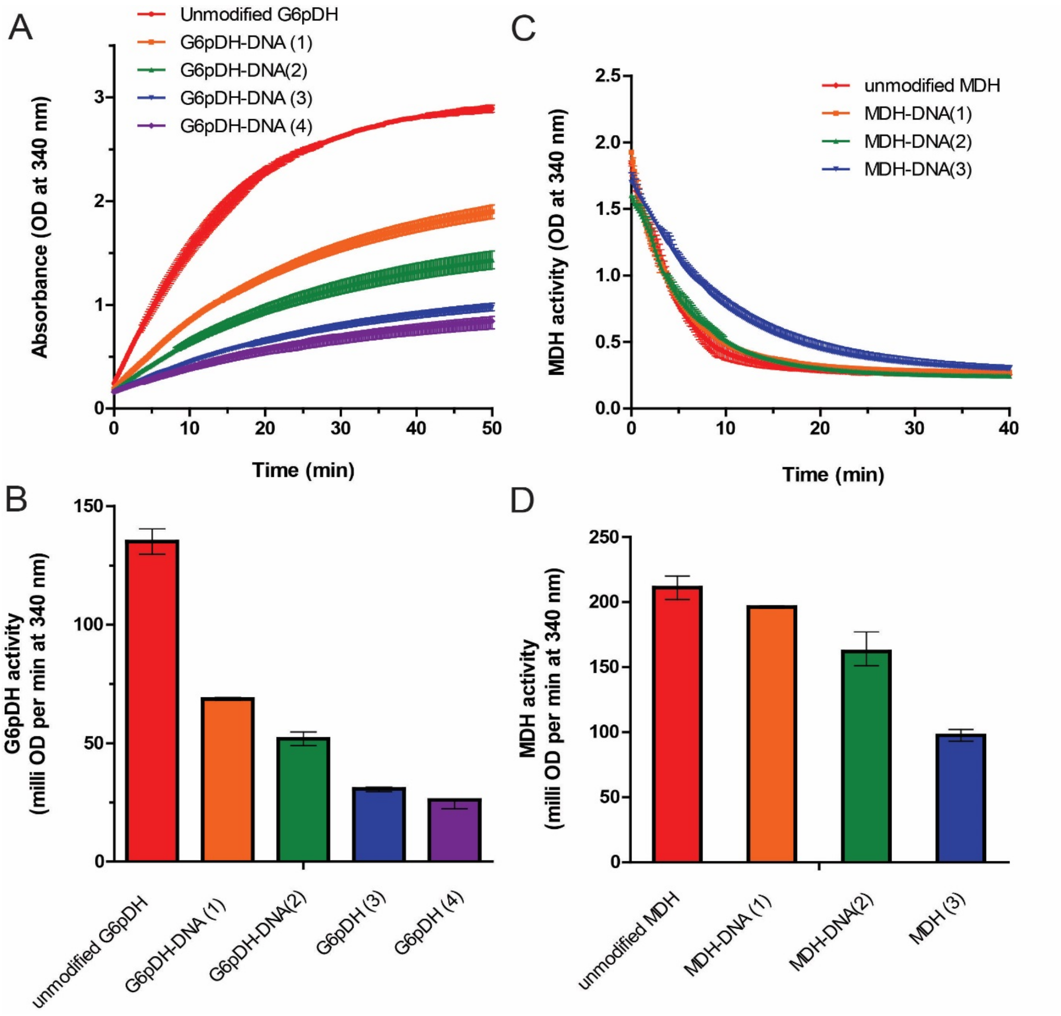

Figure S11. Dependence of the activity of the DNA-conjugated dehydrogenases on the DNA:protein labeling ratio. (**A-B**) G6pDH-DNA conjugates with DNA:protein labeling ratios of 0, 1, 2, 3 and 4, collected from FPLC in Figure S10A. Assay conditions: 2 nM G6pDH-DNA conjugate with 1 mM G6p and 1 mM NAD$^+$ in 100 mM HEPES (pH 8). Enzyme activity is measured by the initial velocity of OD increase in absorbance at 340 nm due to the reduction of NAD$^+$ to NADH. (**C-D**) MDH-DNA conjugates with DNA:protein labeling ratios of 0, 1, 2 and 3, collected from FPLC in Figure S10B. Assay conditions: 20 nM MDH-DNA conjugate with 1 mM oxaloacetic acid and 1 mM NADH in 100 mM HEPES (pH 8). Enzyme activity is measured by the initial velocity of OD decrease in absorbance at 340 nm due to the oxidation of NADH to NAD$^+$. The details of the assay are in supplemental section 7.

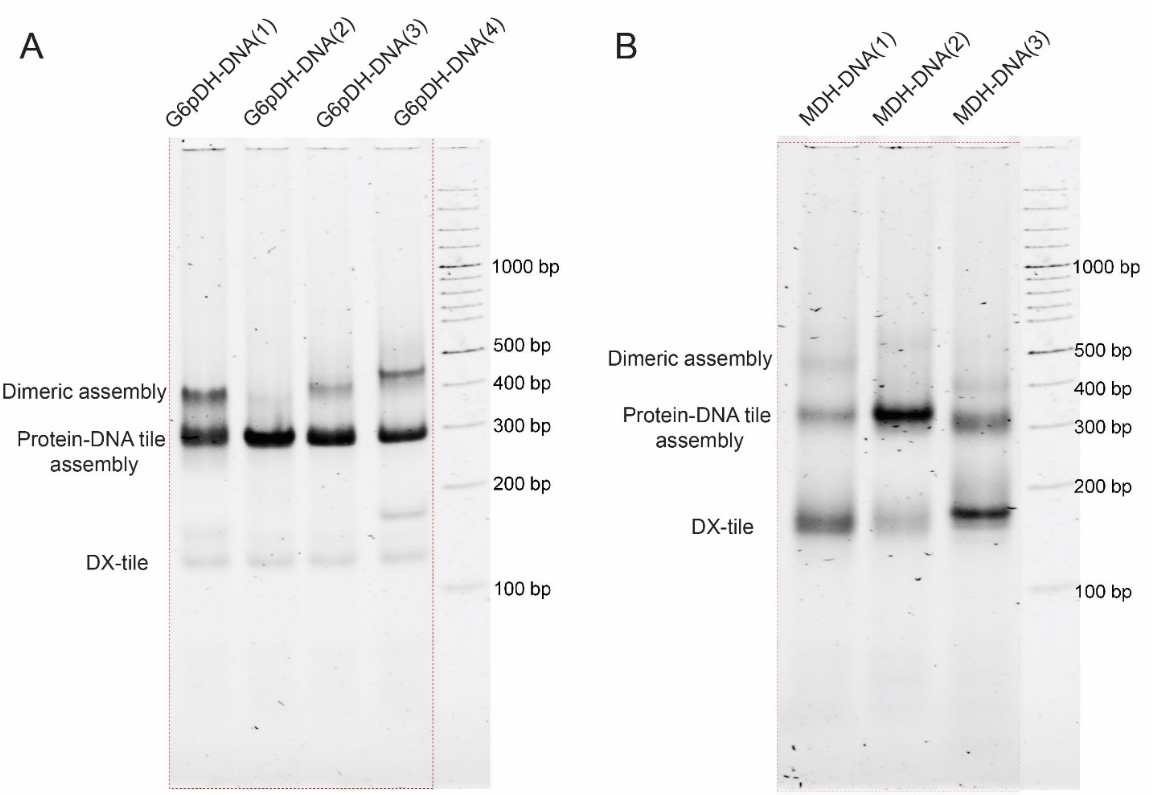

Figure S12. Native gel assay of the DNA labeling ratio on the assembly efficiency of the DNA-conjugated proteins on the DNA tile. (**A**) G6pDH-DNA conjugates and (**B**) MDH-DNA conjugates. DNA-conjugated proteins were purified using FPLC as shown in Figure S10. A twofold molar excess of protein-DNA conjugates was used for the assembly. The gels were stained with SYBR®Green to reveal the mobility of the assembled DNA structures. DX tile structures were similar as shown in Figure S1 and S2.

Discussion: For both G6pDH and MDH, the FPLC fractions labeled with two DNA molecules per protein gave the highest proportion of the predominant product, presumably representing one protein per DX tile, with >80% yield. Proteins labeled with one DNA molecule resulted in lower assembly yield and formation of a secondary product with lower mobility in the gel, which is likely to consist of two proteins bound to adjacent probes on the same DNA tile. Proteins labeled with three or four DNA molecules also resulted in aggregated, lower-mobility structures, possibly due to one protein molecule bridging two or more DNA tiles.

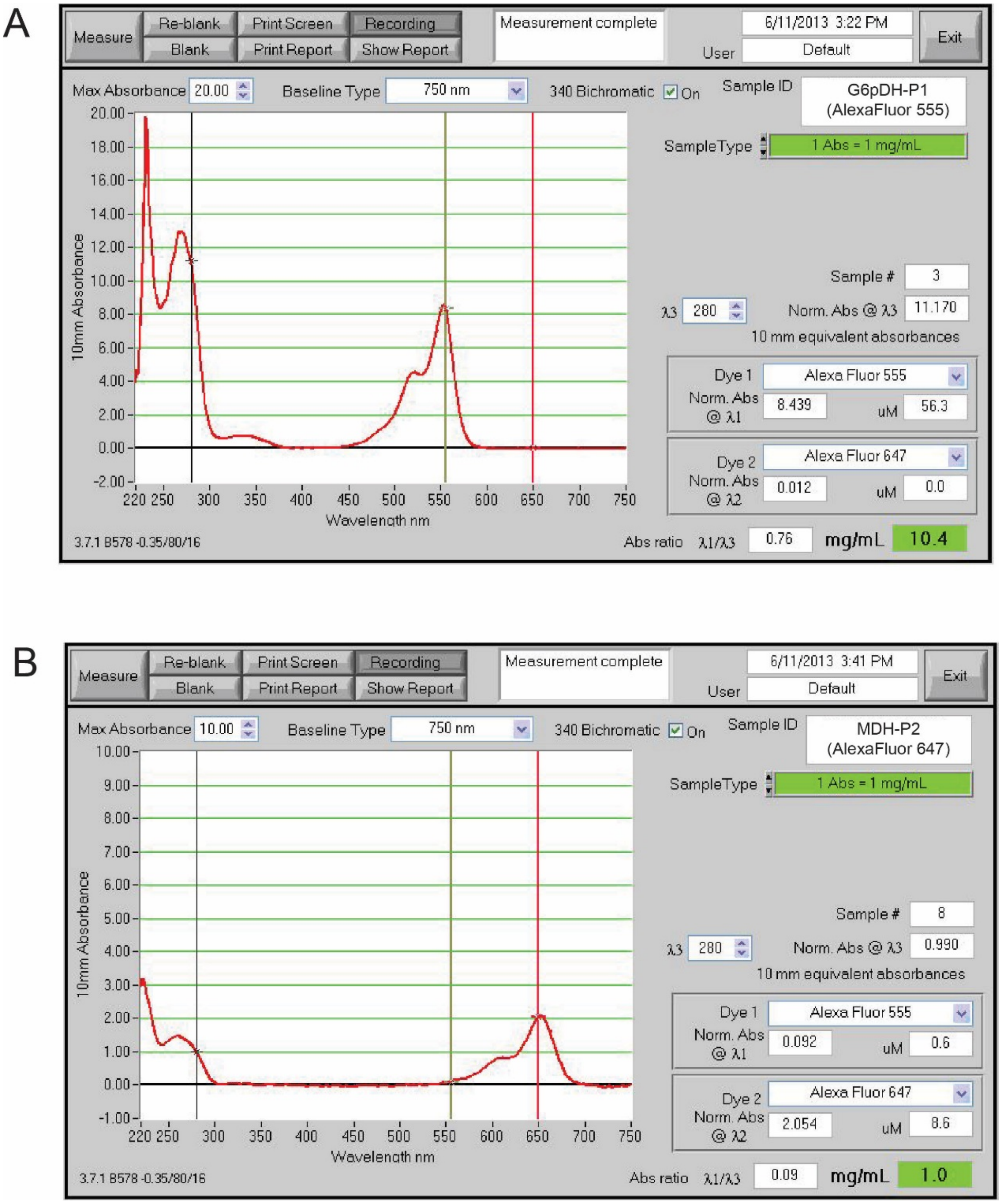

A

Measurement complete
6/11/2013 3:22 PM
User Default
Max Absorbance 20.00
Baseline Type 750 nm
340 Bichromatic ☑ On
Sample ID G6pDH-P1 (AlexaFluor 555)
SampleType 1 Abs = 1 mg/mL
Sample # 3
λ3 280
Norm. Abs @ λ3 11.170
10 mm equivalent absorbances
Dye 1 Alexa Fluor 555
Norm. Abs @ λ1 8.439
uM 56.3
Dye 2 Alexa Fluor 647
Norm. Abs @ λ2 0.012
uM 0.0
3.7.1 B578 -0.35/80/16
Abs ratio λ1/λ3 0.76
mg/mL 10.4

B

Measurement complete
6/11/2013 3:41 PM
User Default
Max Absorbance 10.00
Baseline Type 750 nm
340 Bichromatic ☑ On
Sample ID MDH-P2 (AlexaFluor 647)
SampleType 1 Abs = 1 mg/mL
Sample # 8
λ3 280
Norm. Abs @ λ3 0.990
10 mm equivalent absorbances
Dye 1 Alexa Fluor 555
Norm. Abs @ λ1 0.092
uM 0.6
Dye 2 Alexa Fluor 647
Norm. Abs @ λ2 2.054
uM 8.6
3.7.1 B578 -0.35/80/16
Abs ratio λ1/λ3 0.09
mg/mL 1.0

Figure S13. Quantification of fluorescent dye-labeled enzyme-DNA conjugates using UV-Vis absorbance spectroscopy. (**A**) AlexaFluor 555-labeled G6pDH-P1 with dye:protein labeling ratio about 2:1. (**B**) AlexaFluor 647-labeled MDH-P2 with dye:protein labeling ratio about 1.4:1.

Section 4: Preparation, purification, and characterization of NAD$^+$-DNA conjugates

1) NAD$^+$-DNA conjugation: The method for the conjugation approach is similar to that reported in a previous publication (*4*). Figure S14 shows the detailed reaction pathway of the conjugation of Aminoethyl NAD$^+$ (AE-NAD$^+$) to a 5'-amine-modified single-stranded oligonucleotide. A 200-µL sample of 100 µM 5'-amine-modified oligo was first immobilized onto 200 µL anion-exchange DEAE-Sepharose resin (Sigma) by charge adsorption. Unbound oligo and water were removed by washing with DMF and filtering the resin in a Sigma Prep Spin column (pore size 7-30 µm). A 200-µL portion of 150 mM DSS was prepared in DMF with 2% (v/v) DIPEA. The oligo-bound resin was incubated with DSS for one hour. Excess DSS crosslinker was removed by washing the resin with DMF. To couple NAD$^+$ to an oligo, a 10- fold excess of AE-NAD$^+$ was incubated with the oligo-bound resin in 1 M HEPES, pH 8 for one hour. After the reaction, the oligo-bound resin was spun down at 3000 rpm to remove any unreacted AE-NAD$^+$. To elute DNA molecules from the resin, DNA-bound resin was incubated with 50 mM HEPES containing 1.5 M NaCl (pH 8) for 10 min and spun down to collect the filtrate. AE-NAD$^+$ was purified from the filtrate using HPLC (Agilent 1200) with an elution gradient of 25% methanol, 100 mM TEAA to 35% methanol, 100 mM TEAA (Figure S15A). Purified NAD$^+$ conjugated DNA was characterized by MALDI-TOF Mass Spectrometry as shown in Figure S15B-D.

2) Characterization of the activity of the NAD$^+$-DNA conjugates: Since the NAD$^+$-modified DNA must undergo thermal annealing to form DNA nanostructures, the thermal stability of the NAD$^+$-coupled oligo was measured by incubating them at varied temperatures (25-95°C) for different times (0-60 min) and then measuring the dehydrogenase activity using G6pDH/NAD$^+$ catalyzed reactions, as shown in Figure S16. AE-NAD$^+$ activity was evaluated via the reduction of NAD$^+$ to NADH by G6pDH, followed by a coupled PMS-catalyzed resazurin reaction as described in Figure S30A. The relative enzyme activity was calculated by analyzing the slopes of the product vs. time traces, which were obtained by fitting the raw time traces in (Figure S16b-d) with a linear regression. Assay conditions: 50 nM G6pDH, 50 µM AE-NAD$^+$, 1 mM glucose-6-

phosphate, 200 µM PMS and 400 µM resazurin in 1×TBS with 1 mM $MgCl_2$ at pH 7.5, at room temperature. The results indicate that NAD^+ maintains most of its activity after incubation at temperatures < 75˚C, but is dramatically inactivated by incubation at temperatures higher than 85˚C for even a short time (10 min).

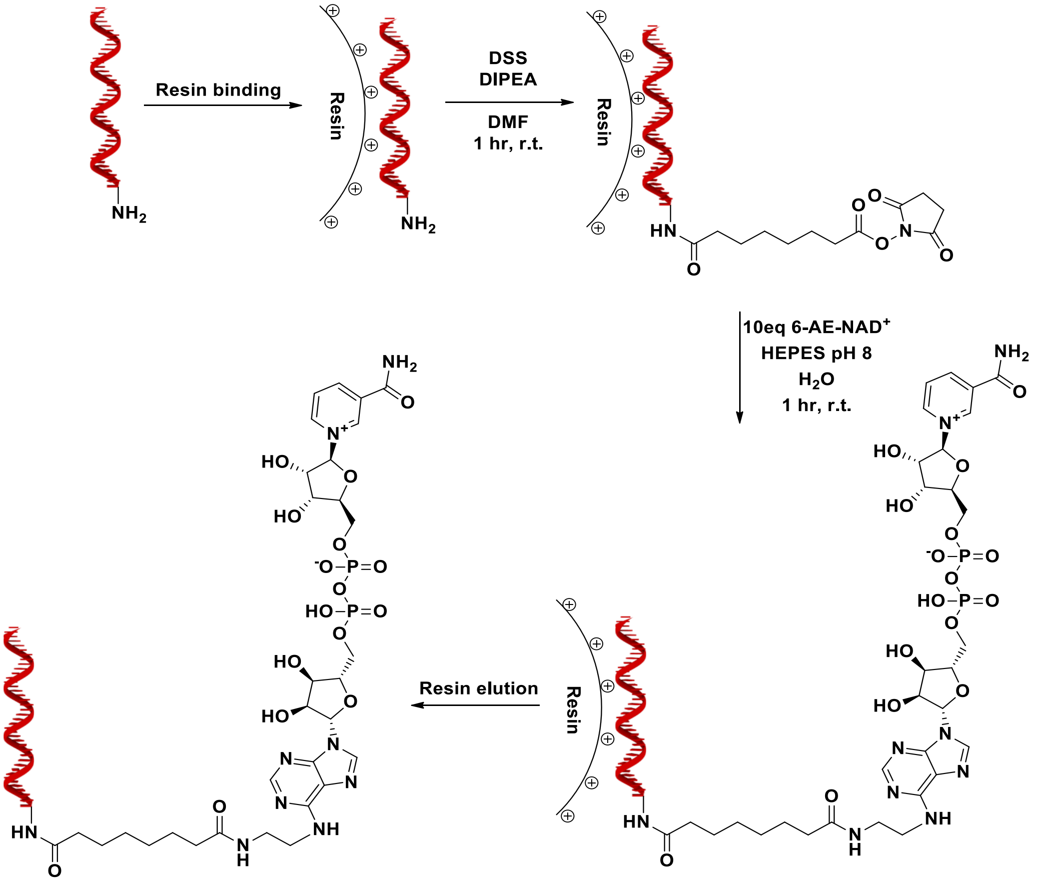

Figure S14. Reaction pathway for the conjugation of aminoethyl NAD^+ to 5' amine-modified DNA strands using resin-based DSS crosslinking chemistry. First the 5'-amine-modified DNA strand is adsorbed on the surface of positively charged resin by electrostatic interactions. A solution of DSS and DIPEA in DMF is added to the resin for 1 hour to activate the amine group on DNA. The excess DSS and DIPEA are removed by washing the resin with DMF. 10 equivalents of 6-AE-NAD^+ in HEPES buffer (pH 8) are added to the resin and incubated for 1 hour, coupling the NAD^+ to the DNA. The NAD^+-DNA is eluted from the resin with 50 mM HEPES containing 1.5 M NaCl, then further purified by HPLC and characterized by MALDI-MS (Figure S15) (*4*).

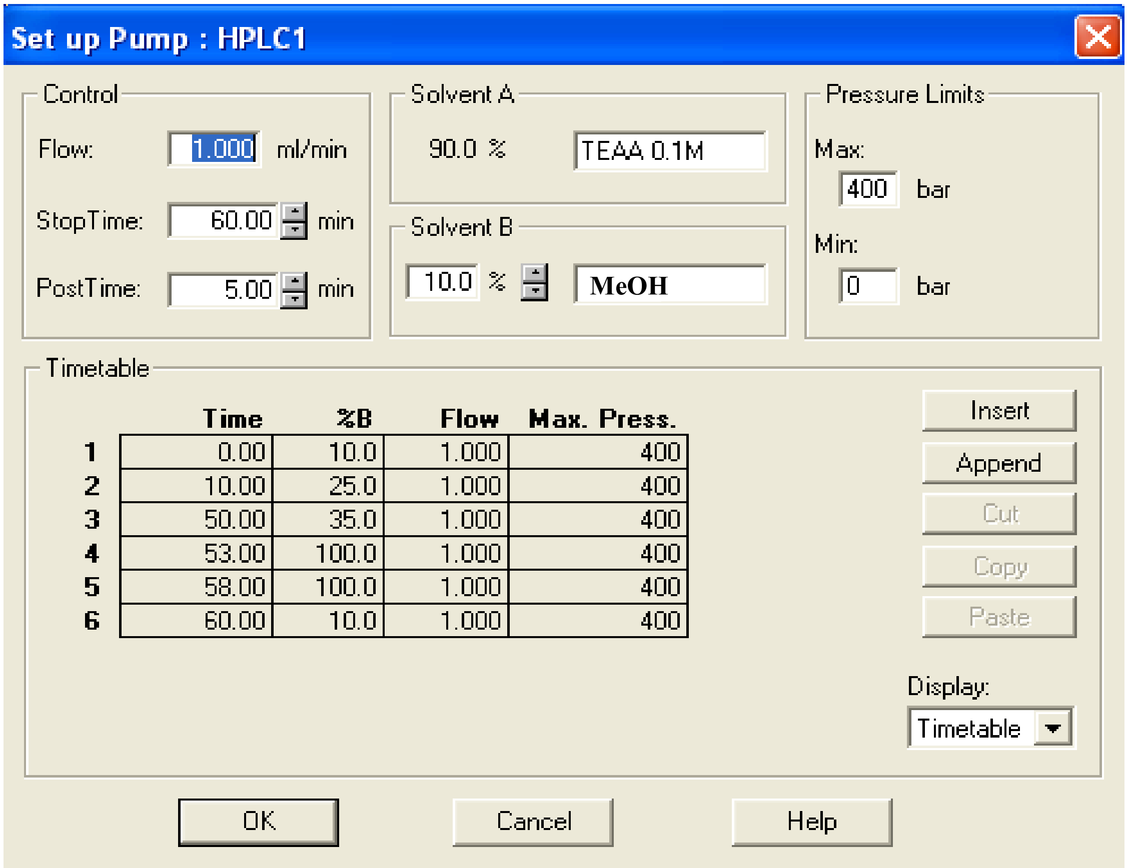
Set up Pump : HPLC1

Control
Flow: 1.000 ml/min
StopTime: 60.00 min
PostTime: 5.00 min

Solvent A
90.0 % TEAA 0.1M

Solvent B
10.0 % MeOH

Pressure Limits
Max: 400 bar
Min: 0 bar

Timetable

	Time	%B	Flow	Max. Press.
1	0.00	10.0	1.000	400
2	10.00	25.0	1.000	400
3	50.00	35.0	1.000	400
4	53.00	100.0	1.000	400
5	58.00	100.0	1.000	400
6	60.00	10.0	1.000	400

Display: Timetable

Figure S15 A. HPLC elution gradient for purifying DNA-NAD$^+$ conjugates. Buffer A: 100 mM Triethylammonium acetate (TEAA); Buffer B: Methanol.

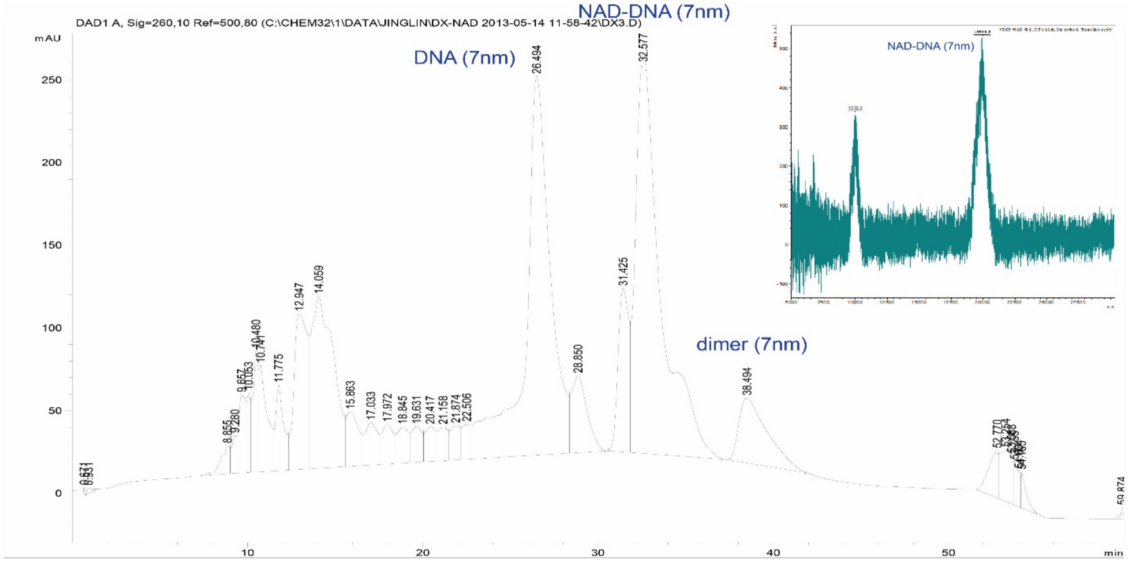
DAD1 A, Sig=260,10 Ref=500,80 (C:\CHEM32\1\DATA\JINGLIN\DX-NAD 2013-05-14 11-58-42\DX3.D)
mAU
250
200
150
100
50
0
10
20
30
40
50
min
NAD-DNA (7nm)
DNA (7nm)
dimer (7nm)
26.494
32.577
31.425
28.850
38.494
12.947
14.059
10.480
10.741
10.053
9.657
9.280
8.855
11.775
15.863
17.033
17.972
18.845
19.631
20.417
21.158
21.874
22.506
52.770
59.874
NAD-DNA (7nm)

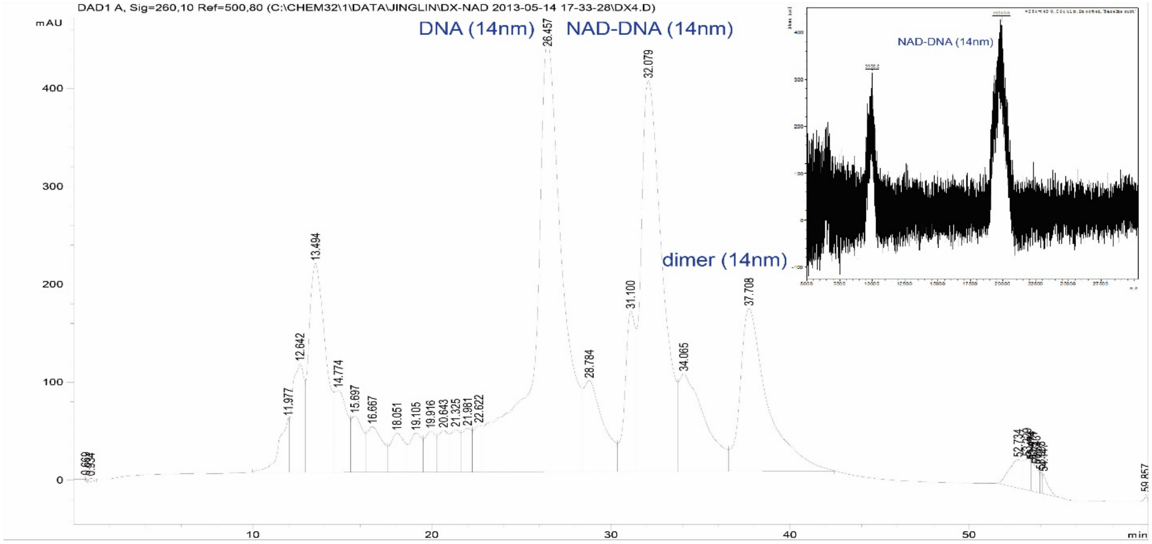
DAD1 A, Sig=260,10 Ref=500,80 (C:\CHEM32\1\DATA\JINGLIN\DX-NAD 2013-05-14 17-33-28\DX4.D)
mAU
400
300
200
100
0
10
20
30
40
50
min
DNA (14nm)
NAD-DNA (14nm)
dimer (14nm)
26.457
32.079
31.100
37.708
34.065
28.784
13.494
12.642
11.977
14.774
15.697
16.667
18.051
19.105
19.916
20.643
21.325
21.981
22.622
52.734
59.857
NAD-DNA (14nm)

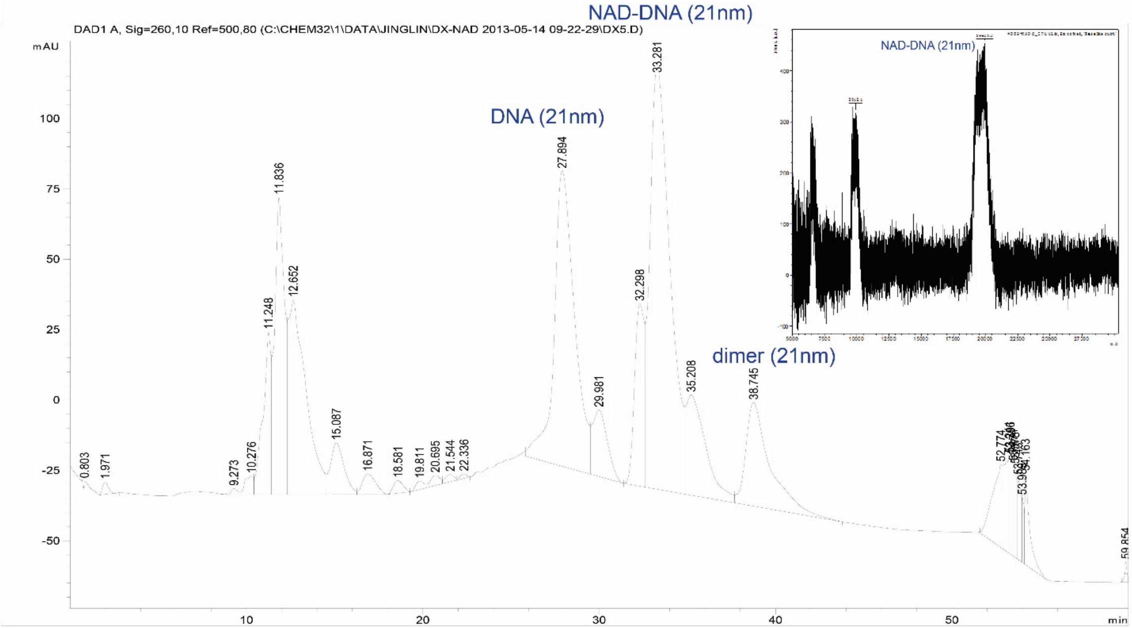

Figure S15 B. HPLC purification and MS characterization (inset, upper right) of NAD$^+$-modified poly(T)$_{20}$ oligos that are designed to be anchored 7-nm, 14-nm and 21-nm away from G6pDH as shown in Figure S1 and Figure 2C and D in the main text. The MALDI-MS characterization of the HPLC-purified sample shows peaks for product carrying both one and two positive charges, the latter appearing at half the molecular weight of the former.

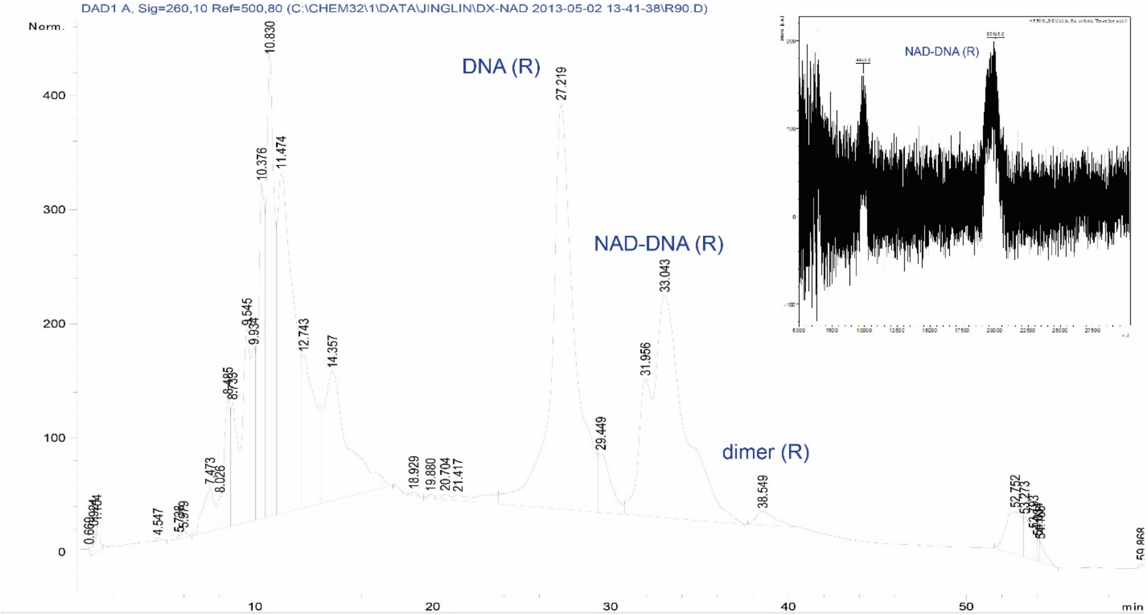
DAD1 A, Sig=260,10 Ref=500,80 (C:\CHEM32\1\DATA\JINGLIN\DX-NAD 2013-05-02 13-41-38\R90.D)
Norm.
DNA (R)
NAD-DNA (R)
dimer (R)
NAD-DNA (R)
10.830
27.219
10.376
11.474
33.043
9.545
9.934
12.743
14.357
31.956
29.449
38.549
min

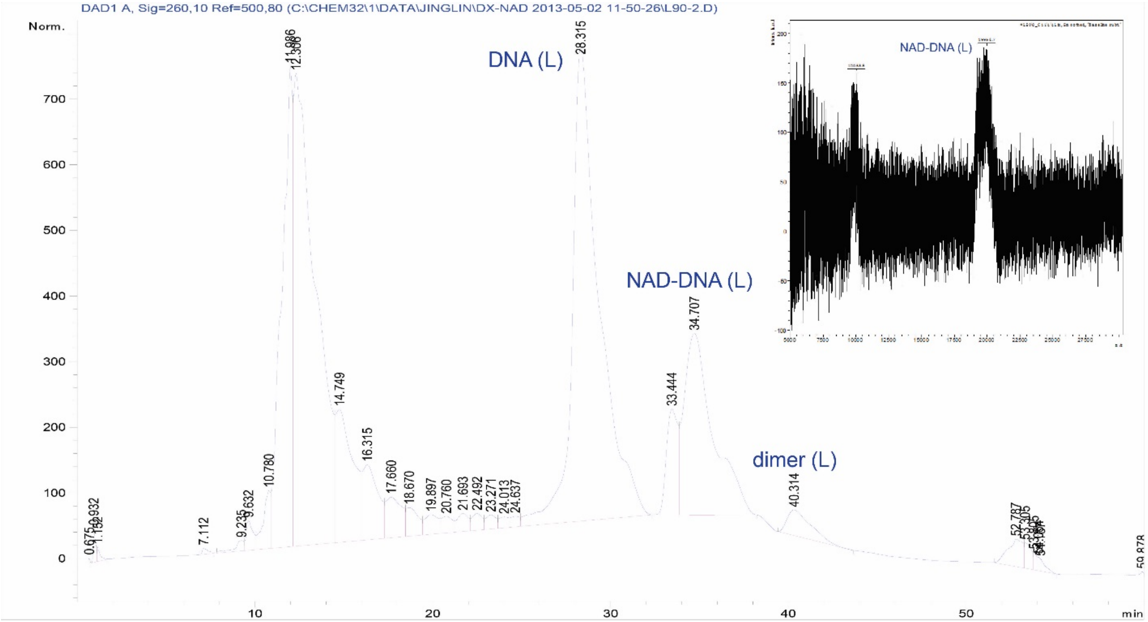
DAD1 A, Sig=260,10 Ref=500,80 (C:\CHEM32\1\DATA\JINGLIN\DX-NAD 2013-05-02 11-50-26\L90-2.D)
Norm.
DNA (L)
NAD-DNA (L)
dimer (L)
NAD-DNA (L)
11.986
28.315
34.707
33.444
14.749
16.315
10.780
40.314
min

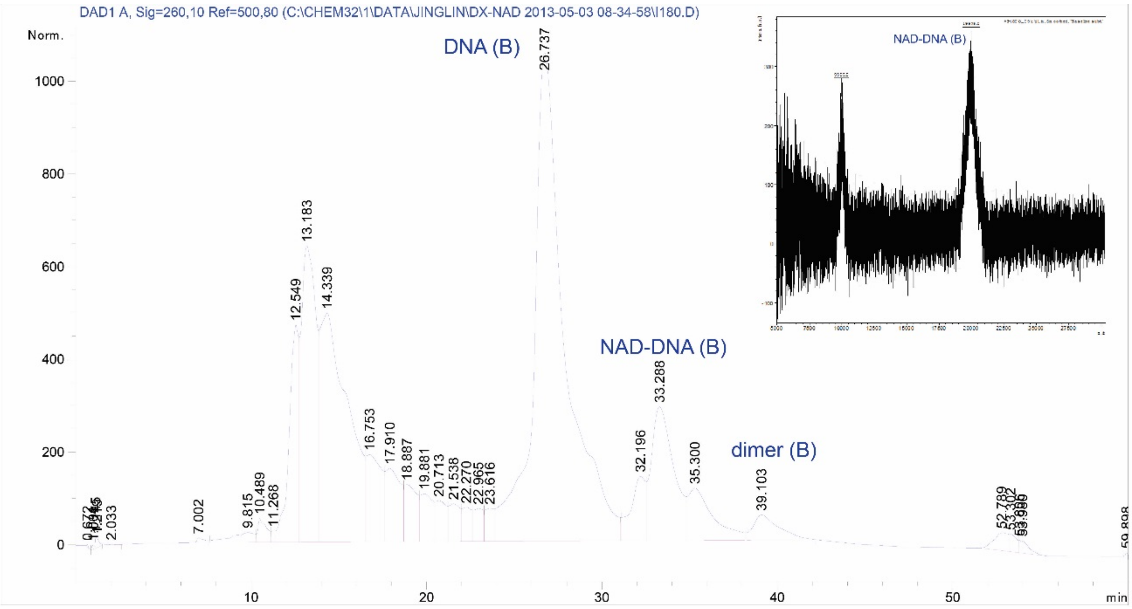

Figure S15 C. HPLC purification and MS characterization of NAD$^+$-modified poly(T)$_{20}$ strands that are designed to be anchored at the left, right and bottom relative to the anchoring position of the enzymes as shown in Figure 2E and F in the main text and Figure S4. The MALDI-MS characterization of the HPLC-purified sample shows peaks for product carrying both one and two positive charges, the latter appearing at half the molecular weight of the former.

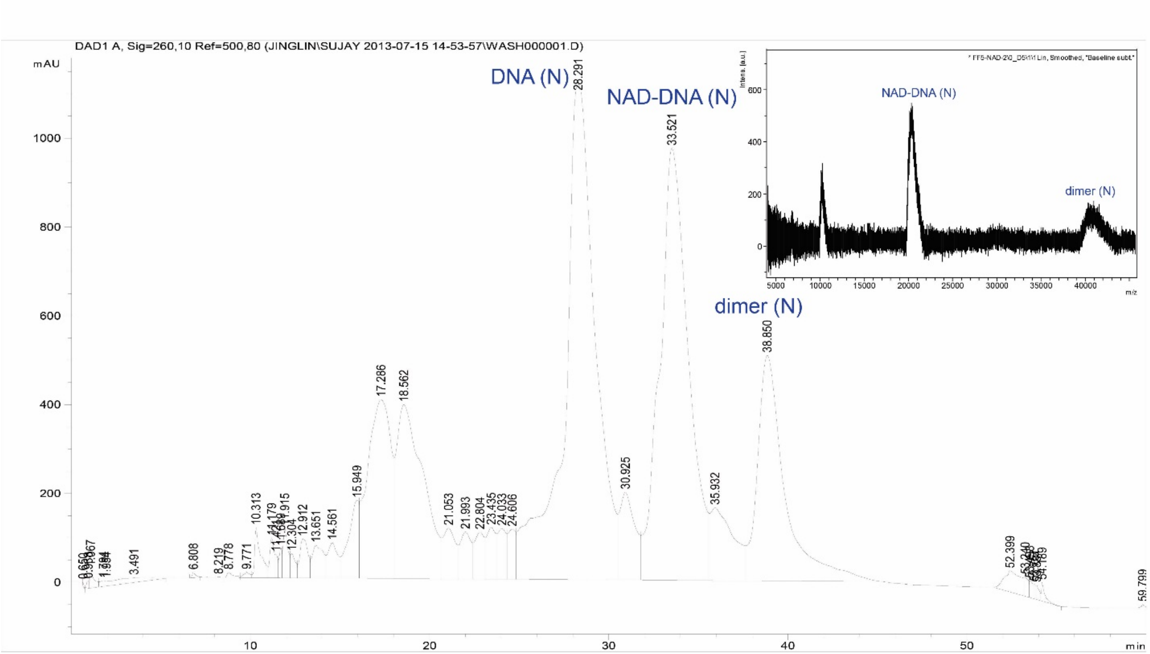
DAD1 A, Sig=260,10 Ref=500,80 (JINGLIN\SUJAY 2013-07-15 14-53-57\WASH000001.D)
mAU
DNA (N)
28.291
NAD-DNA (N)
33.521
dimer (N)
38.850
17.286
18.562
30.925
35.932
15.949
52.399
59.799
1000
800
600
400
200
0
10
20
30
40
50
min
Intens. [a.u.]
NAD-DNA (N)
dimer (N)
m/z

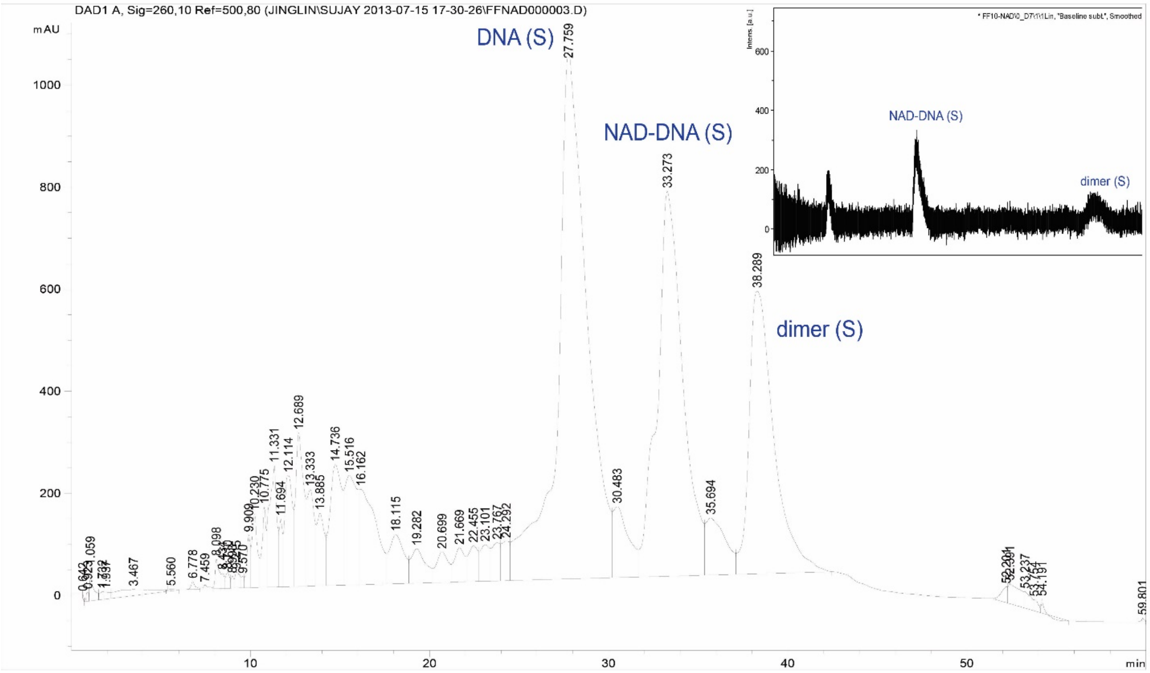
DAD1 A, Sig=260,10 Ref=500,80 (JINGLIN\SUJAY 2013-07-15 17-30-26\FFNAD000003.D)
mAU
DNA (S)
27.759
NAD-DNA (S)
33.273
dimer (S)
38.289
12.689
14.736
15.516
16.162
30.483
35.694
59.801
1000
800
600
400
200
0
10
20
30
40
50
min
Intens. [a.u.]
NAD-DNA (S)
dimer (S)

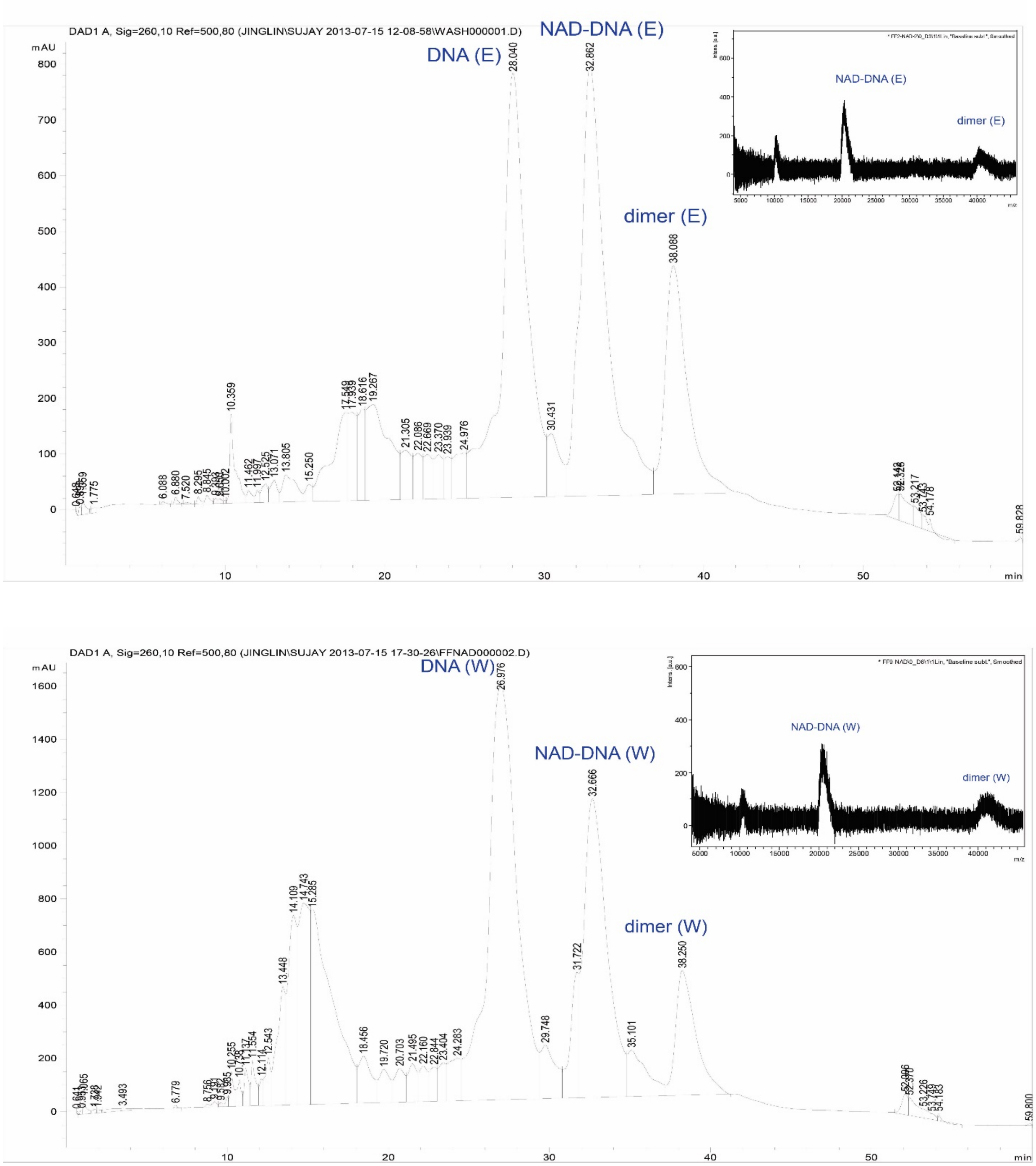

Figure S15 D. HPLC purification and MS characterization of NAD$^+$-modified poly(T)$_{20}$ strands that are designed to be anchored on the 4x4 tile as shown in Figure S6 and S7. (N), (S), (E), (W) indicate the strands located on the North, South, East and West arms of the 4x4 tile, respectively. The observed mass of each of the NAD$^+$-DNA conjugates matches the expected mass well.

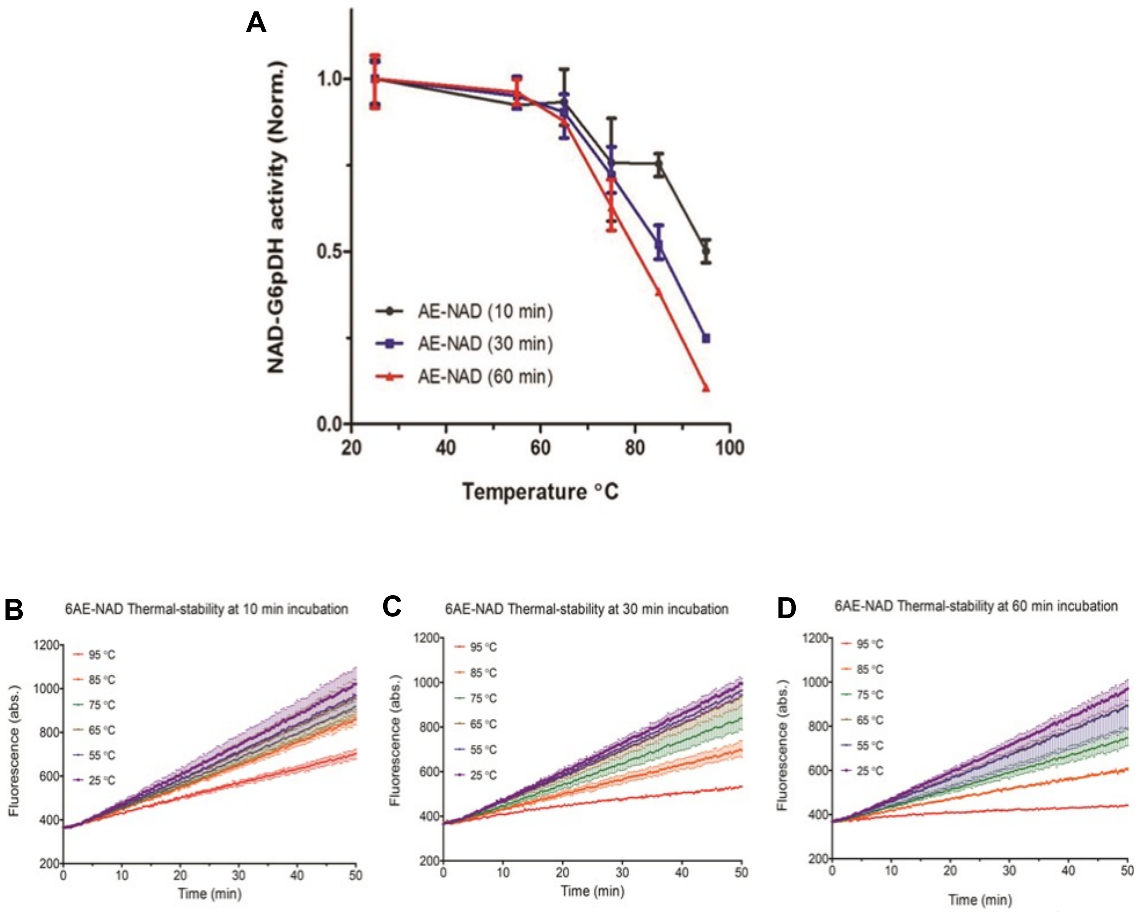

Figure S16. Evaluation of the thermal stability of aminoethyl-modified NAD$^+$ (AE-NAD$^+$). (**A**) Normalized G6pDH/AE-NAD$^+$ activity after incubating the AE-NAD$^+$ at various temperatures then adding it to the enzyme-substrate reaction mixture. AE-NAD$^+$ was incubated at a series of temperatures ranging from 25 to 95˚C for 10 min (black), 30 min (blue) and 60 min (red), respectively. Activity under all conditions was normalized to that of the sample incubated at 25˚C. (**B-D**) Raw activity traces for G6pDH/AE-NAD$^+$ after AE-NAD$^+$ was pre-incubated at various temperatures for 10, 30 and 60 min, respectively (*4*).

Discussion: The activity of AE-NAD$^+$ is significantly diminished after incubation at temperatures higher than 70˚C, even briefly (10 minutes). Incubation at temperatures up to 60˚C for 1 hour did not cause significant reduction of NAD$^+$ activity. In order to assemble the DNA nanostructures, a thermal annealing process is required which involved an increase of the temperature and then slowly cool down. Based on the thermal stability studies here, a modification of the annealing program with a very quick temperature drop in the high temperature range (Table S1) is necessary to avoid losing the activity of NAD$^+$ carried on the DNA structure.

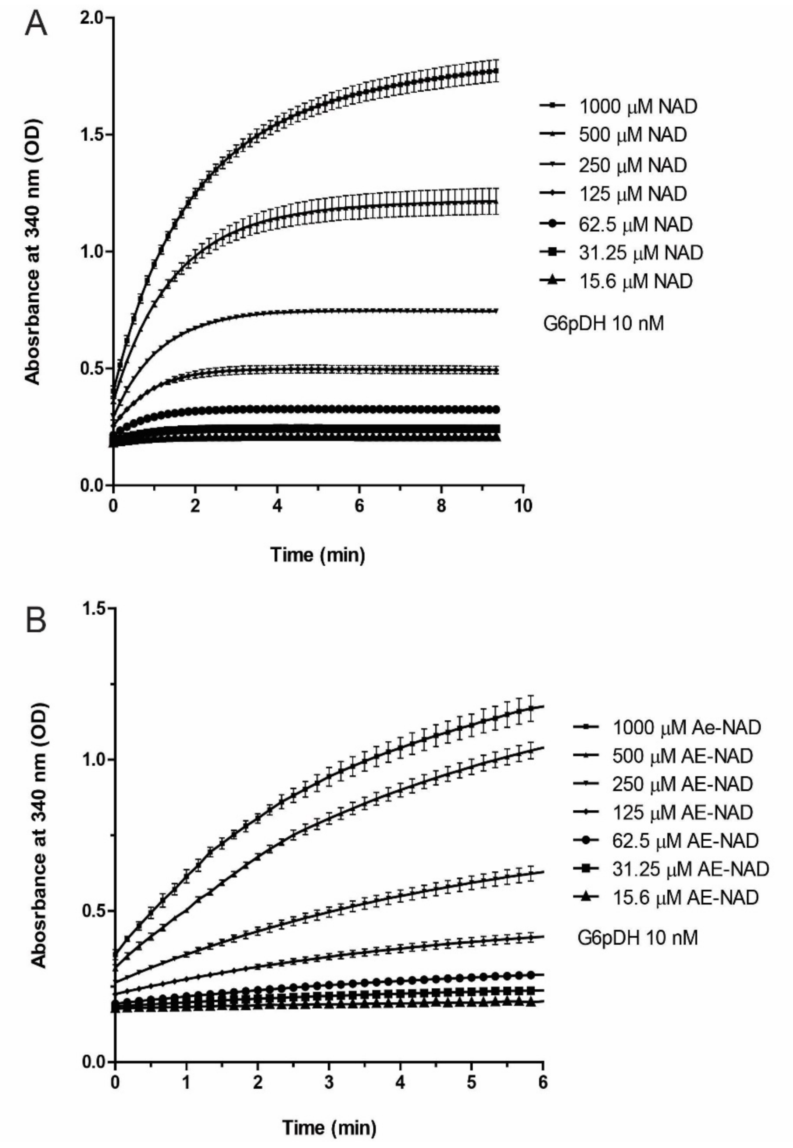

Figure S17. Raw data showing the dependence of G6pDH activity on cofactor concentration. Time traces are shown for the (**A**) G6pDH/NAD$^+$ pair and (**B**) G6pDH/AE-NAD$^+$ pair. Assay conditions: 10 nM G6pDH (unmodified), 1 mM G6p, 15.6-1000 µM NAD$^+$ or AE-NAD$^+$ in 100 mM HEPES (pH 8). The production of NADH was monitored by following absorbance at 340 nm over time.

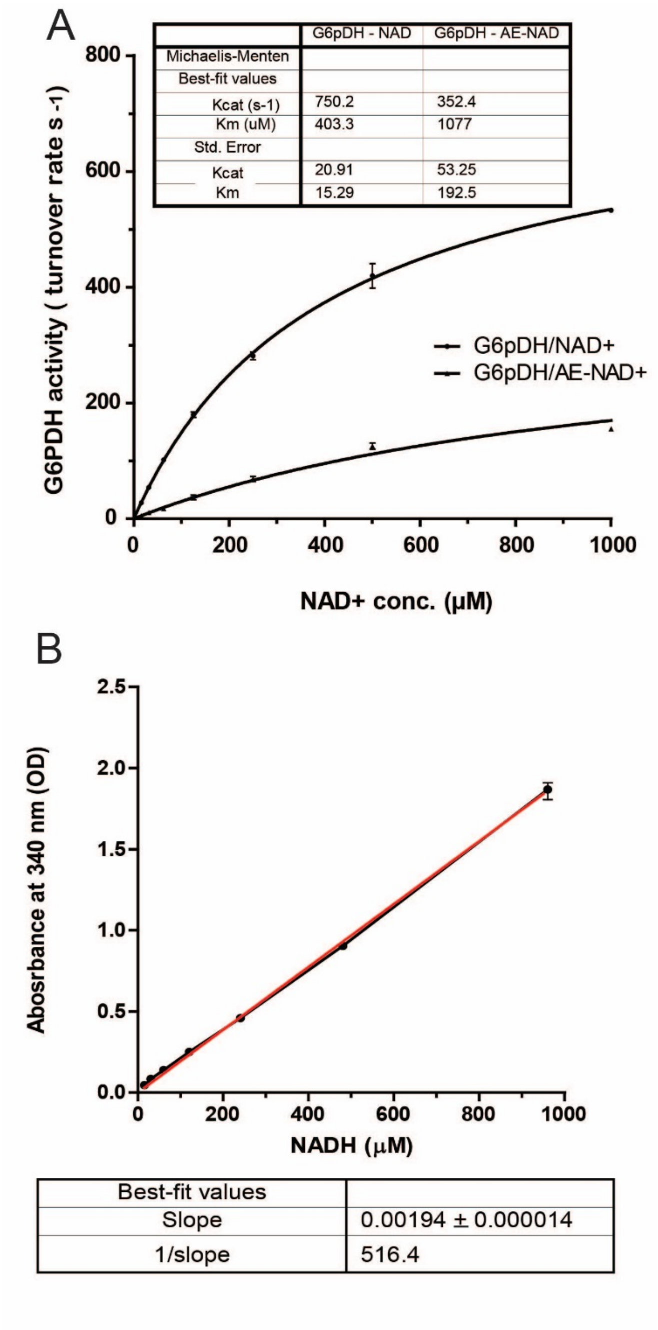

	G6pDH - NAD	G6pDH - AE-NAD
Michaelis-Menten		
Best-fit values		
Kcat (s-1)	750.2	352.4
Km (uM)	403.3	1077
Std. Error		
Kcat	20.91	53.25
Km	15.29	192.5

Best-fit values	
Slope	0.00194 ± 0.000014
1/slope	516.4

Figure S18. (**A**) Michaelis-Menten plot for G6pDH activity (turnover rate) *vs.* NAD^+ and AE-NAD^+ concentration. Enzyme turnover rate was calculated by fitting the initial velocity (linear activity range) of raw activity traces in Figure S17 to a straight line. (**B**) Standard curve of Absorbance vs. NADH concentration for converting the OD value to the molar concentration of NADH produced by G6pDH. The standard curve fitting sets the condition of X=0, Y=0. GraphPad Prism 6 is used for the Michaelis-Menten fitting. All the tests were performed with free enzymes and free NAD^+ molecules.

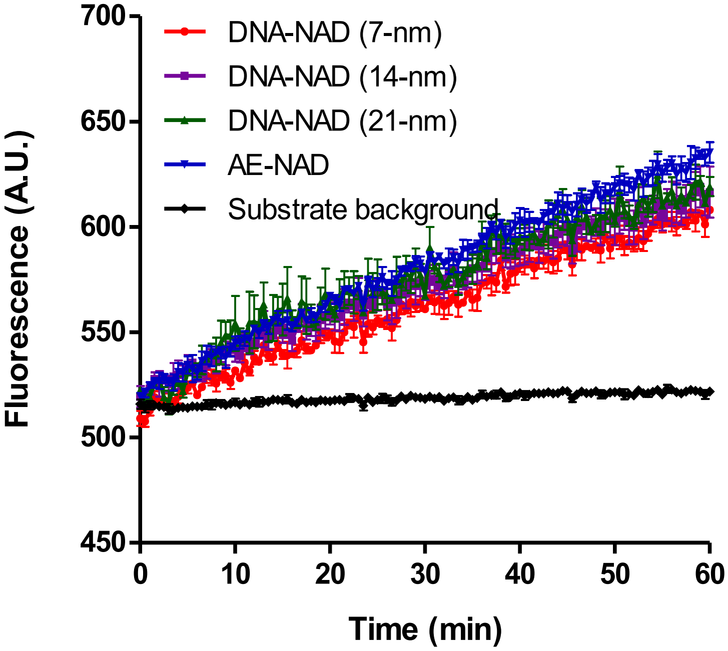

Figure S19. Comparison of the activity of DNA-NAD^+-conjugates with that of AE-NAD^+. All three DNA- NAD^+ conjugates with different sequences (for the 7-nm, 14-nm and 21-nm swinging arms, as shown in Figure S1 have similar activities. AE-NAD^+ shows comparable activity with those of the DNA-NAD^+ conjugates – only slightly (10%-20%) higher. Conditions: 100 nM G6pDH and 100 nM DNA-NAD^+-conjugate or AE-NAD^+ assayed with 1 mM G6p and 500 µM PMS/resazurin in 1×TBS buffer (pH 7.5). The reaction is monitored by the fluorescence increase of PMS/resazurin at 590 nm with excitation at 544 nm.

Discussion: The activity of DNA-NAD^+ conjugates was compared with those of AE-NAD^+ and unmodified NAD^+ by a G6pDH-catalyzed reaction. Figures S16 and S17 show that the G6pDH/AE-NAD^+ pair maintains ~ 20% catalytic efficiency (k_{cat}/K_m) of the G6pDH/NAD^+ pair. The NAD^+-DNA conjugates exhibit slightly lower activity (~10–20%

less active) than that of AE-NAD$^+$, as shown in Figure S19. The activity of NAD$^+$-DNA conjugates with different DNA sequences of the same length (for the 7, 14 and 21-nm distances) is similar, indicating that the activity of NAD$^+$-DNA conjugates is independent of the sequence of the attached DNA.

Section 5: Assembly, purification, and characterization of proteins on DNA nanostructures

1) DNA tile assembly was described in section 2 and used the thermal annealing program shown in Table S1.

2) Protein-DNA tile Assembly: The assembly of protein-DNA nanostructures was optimized by combining the DNA tiles with a one-, two-, or threefold molar excess of protein as shown in Figure S20. An optimal assembly yield of more than 80% was achieved with a twofold molar excess of DNA-conjugated G6pDH or MDH; a threefold excess gave no significant improvement. Proteins were assembled onto DNA structures using a one-hour annealing program in which the temperature was first held at 37 ℃ for 5 min and then decreased from 36 ℃ to 16 ℃ at 2 min/ ℃ and finally held at 15 ℃.

3) Size-exclusion purification of protein-DNA tile assemblies: After assembly, excess proteins and aggregates were removed by size-exclusion chromatography using a Superdex 200 HR 10/30 column (GE Healthcare) and a fast protein liquid chromatograph (FPLC) system (AKATA, GE Healthcare). For a typical purification, ~ 500 µL, 750 nM protein-DNA tile assemblies were loaded onto the FPLC column and eluted with 100 mM HEPES containing 100 mM NaCl (pH 8) at a flow rate of 0.25 mL/min. An example chromatogram from the purification of G6pDH-NAD$^+$-MDH swinging arm structures is shown in Figure S21.

4) Native gel characterization of the purified assembly: The fractions collected from the FPLC column were characterized with native PAGE to identify assembled structures based on comparison with an unpurified sample. The purified protein-DNA tile structures were quantified by absorbance at 260 nm (see data in Table S2).

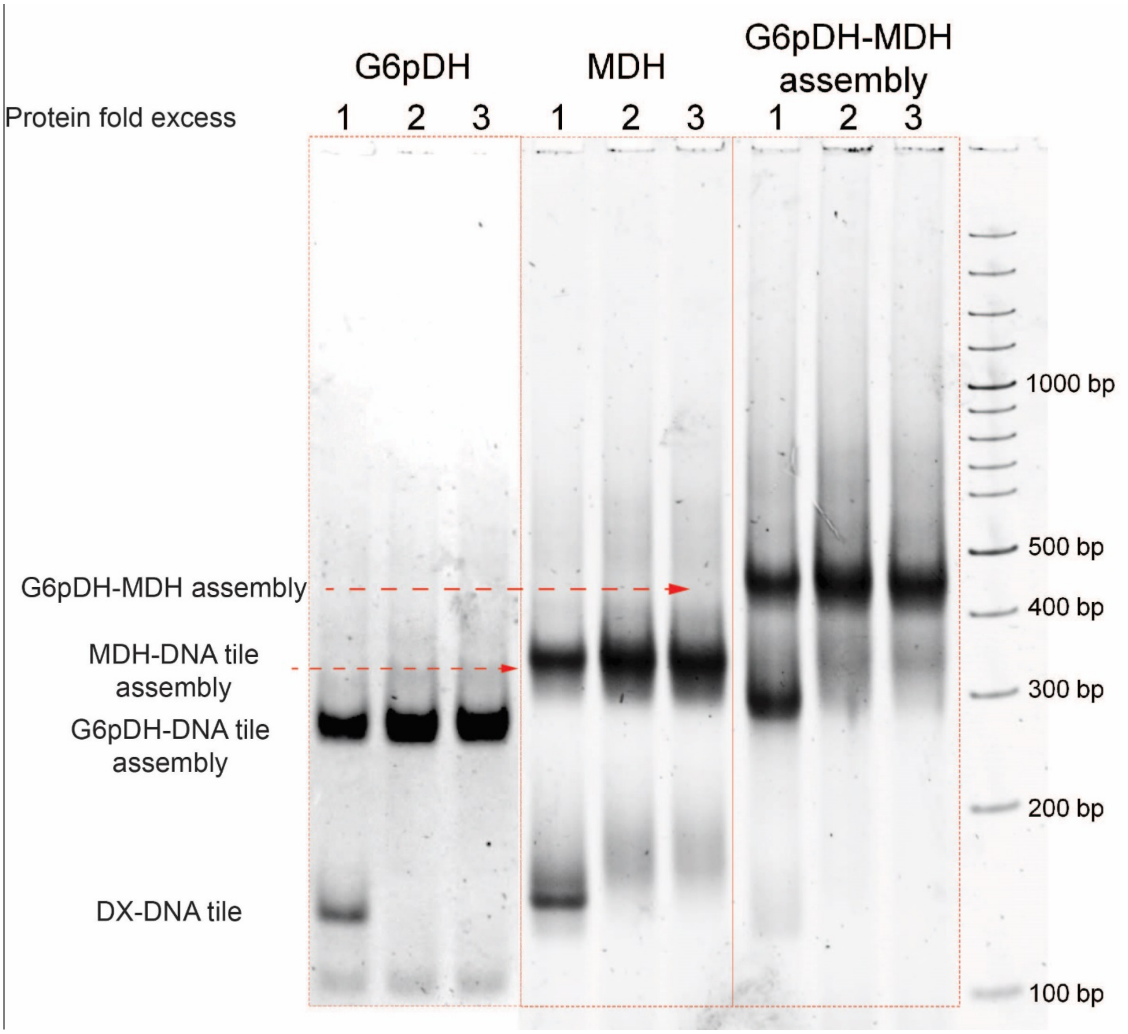

Figure S20. **Native 3% PAGE characterization of the assembly of protein-DNA conjugates with DNA tiles.** Each assembly is carried out with a protein:DNA tile molar ratio of 1:1, 2:1 and 3:1. The DNA-conjugated G6pDH and MDH possess ~2 DNA labels per protein and have been purified using anion exchange chromatography as shown in Figure S10 A&B. A twofold molar excess of DNA-conjugated G6pDH and/or MDH gave the high assembly yield of more than 80% according to the gel results (product band intensity divided by the intensity of the entire lane) and FPLC.

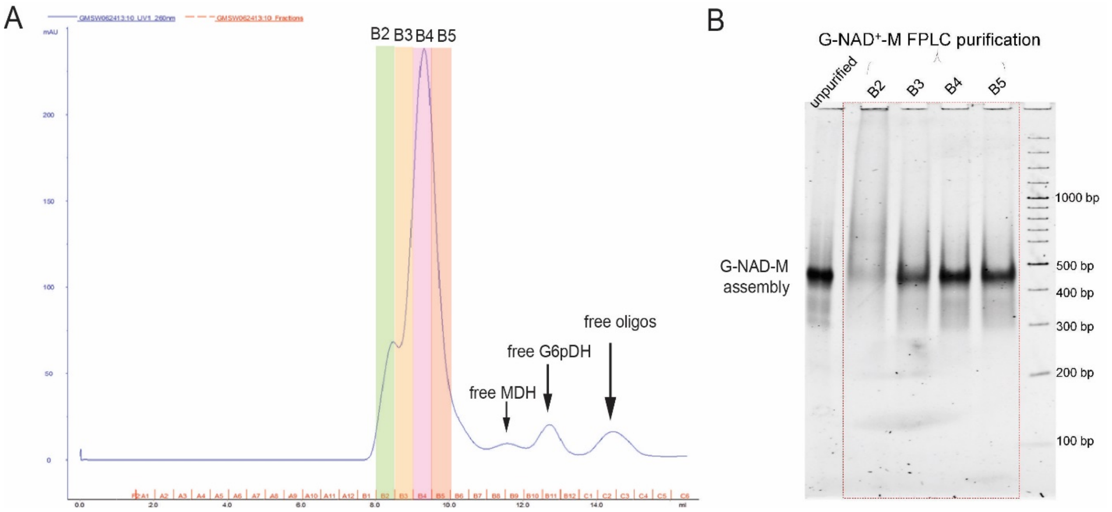

Figure S21. **Purification of G6pDH-NAD$^+$-MDH swinging arm structures.** (**A**) Chromatogram from size-exclusion FPLC purification of assembled G6pDH-NAD$^+$-MDH swinging arm structures to remove excess enzymes and free DNA oligoes. Fractions B2-B5 were collected, representing the fully assembled structure incorporating both the enzymes and the NAD$^+$-labeled poly(T)$_{20}$. (**B**) Native 3% PAGE characterization the fractions collected in size-exclusion FPLC; faction B2 contains a large proportion of aggregated structures (smear band). Fractions B3 to B5 consist primarily of fully assembled swinging arm structures. Unpurified swinging arm structure is also shown in the left lane as a control.

Section 6: Single-molecule FRET (smFRET) characterization of swinging arm dynamics

1. Design of DNA nanostructures. The designs of the DNA-only models of the swinging arm system for single-molecule FRET experiments are shown in Figure S22. These include (a) a full swinging arm system with 7 nm between the anchoring points of the Cy3-labeled swinging arm and each of two probes, labeled with Cy5 or BHQ-2; and (b) a semi-swinging arm system with varying distance (7, 14, or 21 nm) between the anchoring points of a Cy5-labeled probe and the Cy3-labeled swinging arm. The DNA tiles are also biotinylated to allow immobilization on a streptavidin-coated microscope slide.

2. Instrument and methods. Single-molecule FRET experiments were carried out on an inverted total internal reflection fluorescence (TIRF) microscope with a 1.2 NA 60· water-immersion objective (IX71, Olympus) in a darkened room at an environmentally controlled temperature of 20 ± 3 °C. Fluorescence excitation was provided by a 532-nm green laser (CrystaLaser CL532-050-L, 50 mW, attenuated and focused to give an illumination intensity of ~100 W/cm^2 in the sample plane); presence of an active FRET acceptor was confirmed at the beginning and end of each experiment by brief excitation with a 640-nm red laser (Coherent CUBE 635-25C, 25 mW). The Cy3 and Cy5 emission signals were separated by a dichroic mirror with a cutoff wavelength of 610 nm (Chroma) and projected side-by-side onto an ICCD camera chip (iPentamax HQ Gen III, Roper Scientific, Inc.) with a full-frame acquisition rate of 10 Hz. The Cy3 channel image was passed through a bandpass filter (HQ580/60m, Chroma) and the Cy5 channel was passed through a long-pass filter (HQ655LP, Chroma). A Newport ST-UT2 vibration isolation table was used in all experiments to reduce instrument interference. In all smFRET measurements, an oxygen scavenger system (OSS ≡ 5 mM 3,4-dihydroxybenzoic acid, Sigma P5630; 2 mM Trolox, Acros 218940050; and 50 nM protocatechuate dioxygenase, Sigma-Aldrich P8279) was included in the imaging buffer to retard photobleaching (*5*).

3. Sample preparation for smFRET experiments. Microscope slides were constructed with flow channels and coated with biotinylated BSA and streptavidin as described previously (*6*) to permit surface immobilization of biotinylated DX tiles bearing the swinging arm and complementary probe(s). A solution containing 20 nM of a DX tile and either 0.2 µM (in the case of half-arm structures) or 2 µM (in the case of the full swinging arm structure) of **P*-1** (5'-CCC TCC CTC CTT TAT AGT GAA ATT), **Cy5-P*-1** (5'-CCC TCC CTC CTT TAT AGT GAA ATT-Cy5), **P*-2** (5'-GGC TGG CTG GTT TAT AGT GAA ATT), and/or **BHQ2-P*-2** (5'-GGC TGG CTG GTT TAT AGT GAA ATT-BHQ2) strands was incubated for 30 min at 37 °C in the presence of 1×TAE-Mg^{2+} (see Figure S22 for DNA sequence design). The sample was kept on ice in the dark until use. About 10 min prior to each experiment, a portion of the sample was diluted to a DX tile concentration of ~200 pM in 1×TAE-Mg^{2+} buffer. Then, the sample was immobilized on a streptavidin-coated microscope slide, and the excess sample flushed away with 1×TAE-Mg^{2+} buffer, followed by imaging buffer. In the case of single-molecule competition experiments, the buffer was supplemented with 0.5-320 µM of inhibitor DNA molecule ***I*** (5′-AAT TTC ACT ATT TTT TTT TTT TTT TTT TTT TTT T). The inhibitor contains a stretch of 11 bases (labeled in red) complementary to the (5′-AT AGT GAA ATT) probe sequence of **Cy5-P*-1,** and was designed to compete with the Cy3-labeled swinging arm for hybridization to **Cy5-P*-1**.

4. Data analysis for smFRET: Figure S24 shows CCD images of representative fields of view from smFRET measurements. Analysis of single-molecule FRET trajectories and inhibition experiments was performed with custom-written IDL and MATLAB scripts as previously described (*7*). A given smFRET trajectory was used in subsequent analysis only if it (1) exhibited total fluorescence of Cy3 and Cy5 exceeding 500 counts/frame; (2) showed clear evidence of both Cy3 + Cy5; and (3) showed no evidence of multiple identical fluorophores, for example, multiple photobleaching steps or overlapping point-spread functions in the CCD image.

In the case of the full Cy3-Cy5-BHQ-2 swinging arm complex, which exhibits a wider variety of behaviors due to the presence of three labels (any of which may be missing or oxidized prior to observation), other observed behaviors were catalogued with interpretations as to the most likely cause of each behavior (Figure S25A). FRET histograms were constructed from the first 400 frames of each molecule. The equilibrium fraction of high-FRET molecules ($f_{high\text{-}FRET}$) was determined by thresholding with a cutoff of FRET = 0.5, which is approximately halfway between the low- and high-FRET states (or quenched and fluorescent states, in the case of the Cy3-Cy5-BHQ2 complex) of 0-0.2 and ~1.0, respectively.

Semi-swinging arm complexes within a given sample exhibited heterogeneous FRET dynamics. Histograms of the number of observed semi-swinging arm complexes spending a given fraction of the time in the high-FRET state are shown in Figure S26 (in contrast, the FRET histograms in Figure 2B represent the total fraction of time spent by *all* complexes of each type in a given FRET state).

5. Determination of equilibrium dissociation constants of DNA hybridization for probe strands for model swinging arm structures by ensemble FRET. Ensemble FRET experiments were performed at 20 °C on an Aminco-Bowman Series 2 Luminescence Spectrometer with an excitation wavelength of 500 nm (0.5 nm bandwidth). As with smFRET experiments, all ensemble FRET measurements were performed in an imaging buffer consisting of 1×TAE-Mg^{2+} + OSS.

To determine the equilibrium dissociation constant (K_d) of hybridization between **Cy3-poly(T)$_{20}$** (5’-Cy3-TTT TTC ACT ATT TTT TTT TTT TTT TTT TTT TTT) and **Cy5-P*-1** or **BHQ2-P*-2**, 0.5 μM **Cy3-poly(T)$_{20}$** was mixed with 0-8 μM of **Cy5-P*-1** or **BHQ2-P*-2** (all are final concentrations), resulting in quenching of Cy3 as determined from fluorescence emission scans. To simulate the duplex that normally holds **Cy5-P*-1** or **BHQ2-P*-2** on the DX tile, a twofold excess of the appropriate capture sequence (**CP-1:** 5’-GGA GGG AGG G; or **CP-2:** 5’-CCA GCC AGC C) was added to each reaction prior to mixing with **Cy3-poly(T)$_{20}$**. Reactions were incubated in the dark at room temperature for 5 min, at which point the hybridization had reached equilibrium as verified by successive fluorescence measurements on the same sample. The intensity of Cy3 fluorescence was plotted as a function of **Cy5-P*-1** or **BHQ2-P*-2** concentration and fit with the equation:

$$y = A\frac{\left((x+T+K_d)-\sqrt{(-x-T-K_d)^2-4\,T\,x}\right)}{2} + y_0 \qquad (1)$$

where T is the concentration of **Cy3-poly(T)$_{20}$**, x is the concentration of **Cy5-P*-1** or **BHQ2-P*-2**, and A and y_0 are constants, yielding K_d estimates of ~0.3 µM for both reactions (Figure S27A). The use of this exact equation was necessary because the relatively large concentration of **Cy3-poly(T)$_{20}$** resulted in significant differences between free and total concentrations of the reactants(*8*).

6. Determination of the inhibition constant of an inhibitor DNA that blocks hybridization of the swinging arm: To determine the inhibition constant K_I of the inhibitor ***I***, 0.5 µM Cy3-**poly(T)$_{20}$** was mixed with 0.5 µM of **Cy5-P*-1** or **BHQ2-P*-2** (pre-bound to **CP-1** or **CP-2**, as described above), and 0-3.2 µM of ***I*** was added, resulting in a concentration-dependent de-quenching of Cy3. The intensity of Cy3 fluorescence was plotted as a function of inhibitor concentration and fit to the logistic function:

$$y = \frac{M-N}{1+I/IC_{50}} + N \qquad (2)$$

where M and N are constants and I is the inhibitor concentration, to determine IC_{50}. The true K_I was estimated to be ~ 0.06 µM (Figure S27B) using the correction(*9*):

$$K_I = \frac{IC_{50}}{1+\frac{T(r_0+2)}{2\times K_d(r_0+1)}} - K_d\left(\frac{r_0}{r_0+2}\right) \qquad (3)$$

where r_0 is the ratio of bound to free **Cy3-poly(T)$_{20}$** in the absence of inhibitor.

The 5-fold increase in the binding affinity of the inhibitor (~0.06 µM) compared to Cy5-P*-1 (~0.3 µM), provided by the 2 extra base-pairs, suffices to inhibit hybridization between the swinging arm and Cy5-P*-1, even at the shortest anchor spacing of 7 nm (see Section 7 and Figure S28).

7. Estimation of effective concentration. The local effective concentration $C_{eff,meas}$ of the swinging arm was estimated by plotting the fraction of time spent in the high-FRET state as a function of inhibitor concentration and fitting with the following equation(*10*):

$$f_{high-FRET} = A * \frac{C_{eff,meas}}{C_{eff,meas} + K_d*\left(1 + \frac{I}{K_i}\right)} + y_0$$

(4)

where A and y_0 are constants, I is the concentration of inhibitor, and K_d and K_I are the equilibrium dissociation and inhibition constants for **Cy5-P*-1** and the inhibitor, respectively, as determined by solution measurements (Figure S28). The estimated local effective concentration of the swinging arm in the vicinity of Cy5-P*-1 is ~ 250 µM for the 7-nm complex and 2.7 µM for the 14-nm complex (Table S4).

Simulation of swinging arm conformation and prediction of local effective concentration. Metropolis Monte Carlo simulations (*11*) were performed using a recently published coarse-grained model of ssDNA that explicitly accounts for excluded volume effects and intra-strand electrostatic repulsion (*12*). Using the parameterization for 10 mM Mg^{2+} (virtual bond angle θ = 57.8 °, virtual bond length l_0 = 0.369 nm, radii of closest approach $a = d$ = 0.56 nm, and charge renormalization factor f = 0.229) and prohibiting chain excursions below the plane of the DX tile, 10^6 chain conformations were sampled. A conformation was considered compatible with hybridization if it placed the proximal end of the sticky-ended probe of the poly$(T)_{20}$ arm within a hemispherical shell S representing the volume swept out by the proximal end of the probe sequence of Cy5-P*-1 (Figure S29). The inner and outer radii of S were estimated as 3.4 + 1.4 ± 1.4 nm, taking into account the rigid 10-bp anchor duplex and two 3T linkers on either side of the duplex, assuming that the 3T linker distal to the tile is rotationally unhindered and using a wormlike chain model with a persistence length of 1 nm to predict the root-mean-square end-to-end distance of ssDNA(*13*). The predicted local effective concentration ($C_{eff,pred}$) was calculated as:

$$C_{eff,pred} = \frac{f_{hyb}}{N_A \times V_S} \tag{5}$$

where f_{hyb} is the fraction of conformations compatible with hybridization, N_A is Avogadro's number and V_S is the volume of S in liters. We find that the value of $C_{eff,pred}$ is rather insensitive to the thickness of S, since any change will affect f_{hyb} and V_S approximately proportionally. The predicted local effective concentration of the swinging arm at the two closest distances is shown in Table S4: ~ 607 μM for the 7-nm complex, and 4.7 μM for 14-nm complex.

To model the double-stranded poly(T)$_{20}$ + poly(A)$_{20}$ arm (Fig. S54), the calculations were performed in an identical manner, except that the swinging arm was instead modeled as a rigid rod of length 6.8 nm (B-type DNA, 20 bp) that isotropically explores a spherical section bounded by a minimum angle φ_{min} above the plane of the tile.

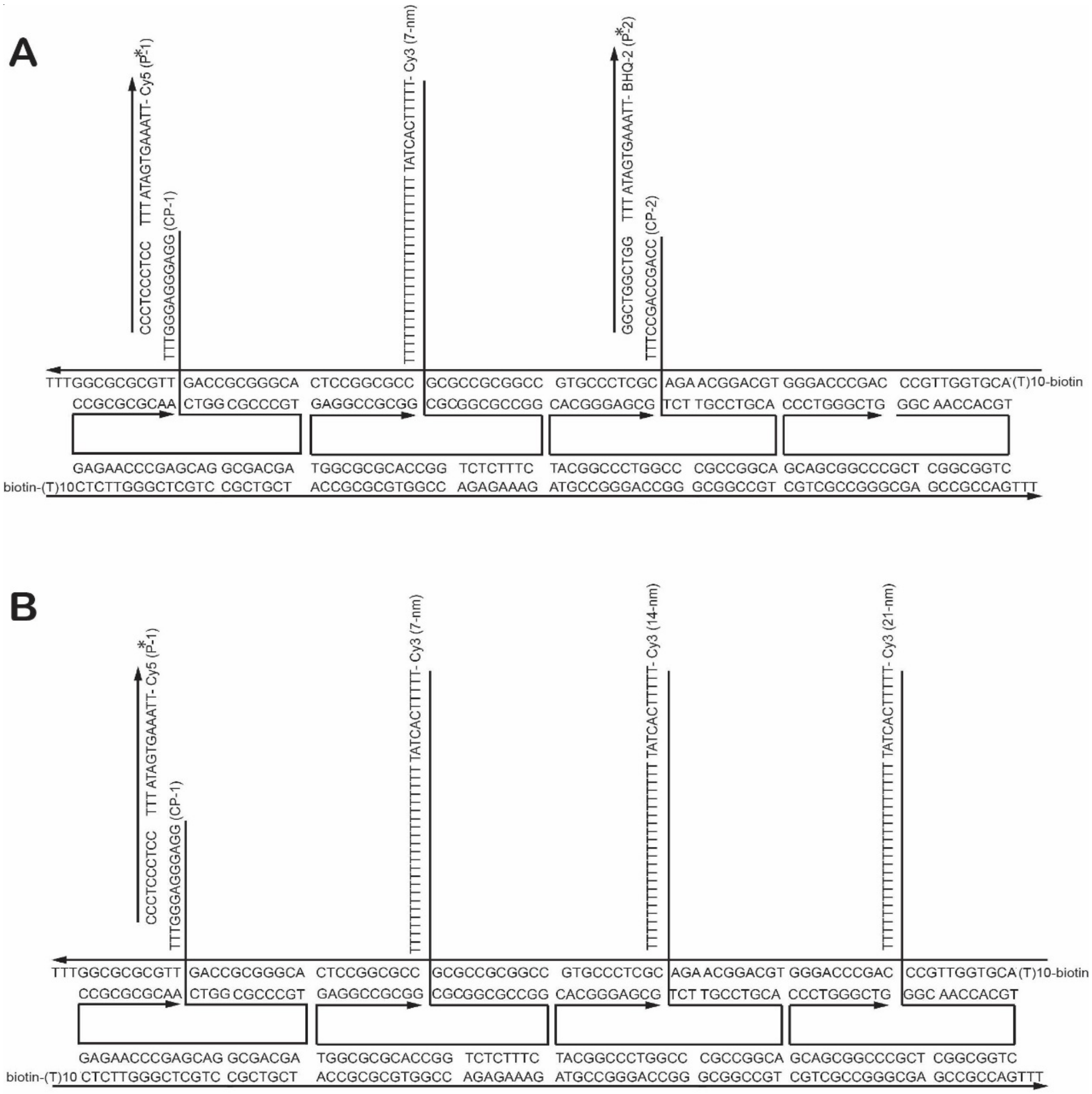

Figure S22. Sequence maps of the DNA-only models of swinging arm structures for single-molecule FRET experiments. (**A**) Cy3-Cy5-BHQ-2 swinging arm complex, in which the Cy5, Cy3 and BHQ-2 labeled strands are designed to extend from the same surface of the tile, with 7 nm between their anchor positions. The 5′-extension of the Cy3-labeled poly(T)$_{20}$ strand is complementary to the 3′-extensions on P*-1 and P*-2, and is designed to swing between the two binding sites in analogy to the G6pDH-NAD$^+$-MDH system (Figure S3), resulting in energy transfer from Cy3 to Cy5 or quenching by BHQ-2. (**B**) Cy3-Cy5 semi-swinging arm complex, designed to test the distance dependence of binding mediated by the poly(T)$_{20}$ in analogy to the systems in Figures S1 and S2. Only one of three scaffold strands (7, 14, or 21 nm from the P*-1 anchor site) bears the 5′-Cy3-poly(T)$_{20}$ extension in a given complex design.

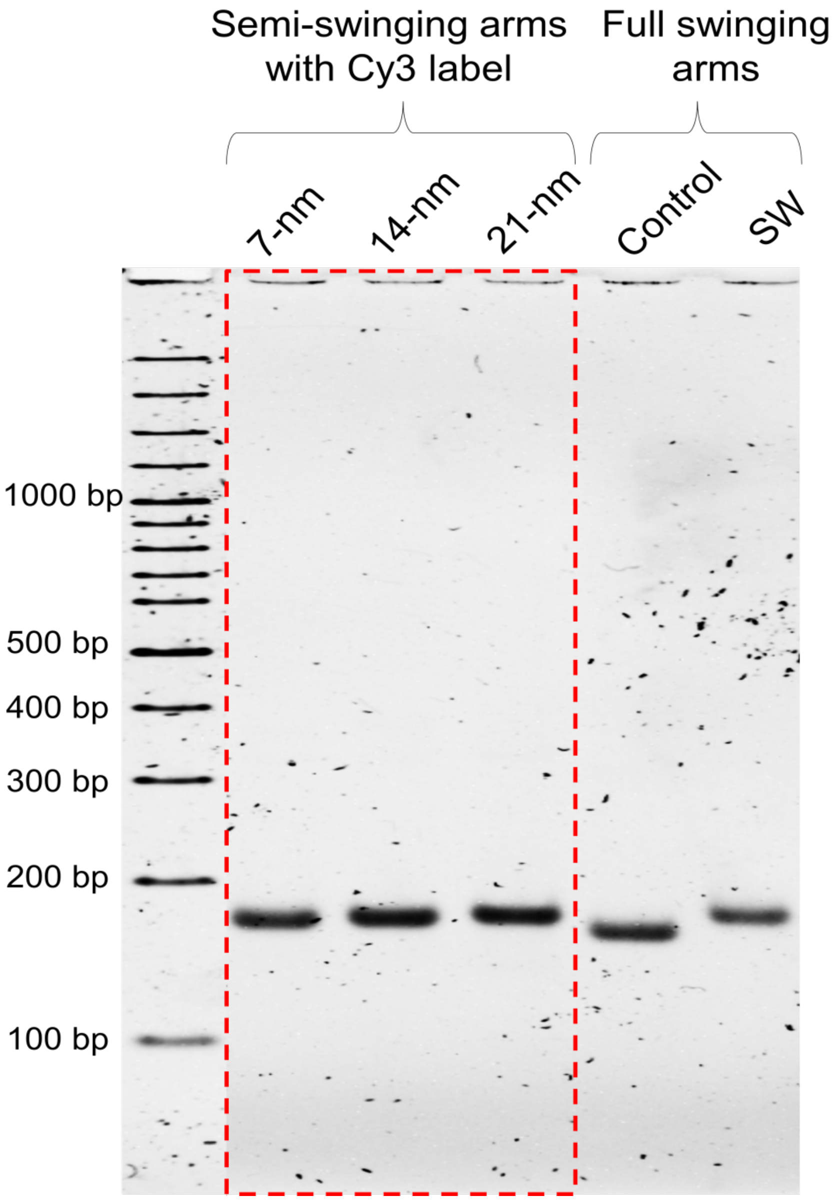

Figure S23. Native 3% PAGE characterization of assembled DNA structures shown in Figure S22. The left three lanes show the Cy3-labeled semi-swinging arms structures with 7, 14 and 21 nm between anchor sites, corresponding to the structures in Figure S22B. The fourth lane from the left is a control structure with the Cy3-poly(T)$_{20}$ as shown in

Figure S22 A but lacking the 3′-extensions of CP1 and CP2. The fifth lane is the same structure as lane 4 but with the capture strands CP1 and CP2.

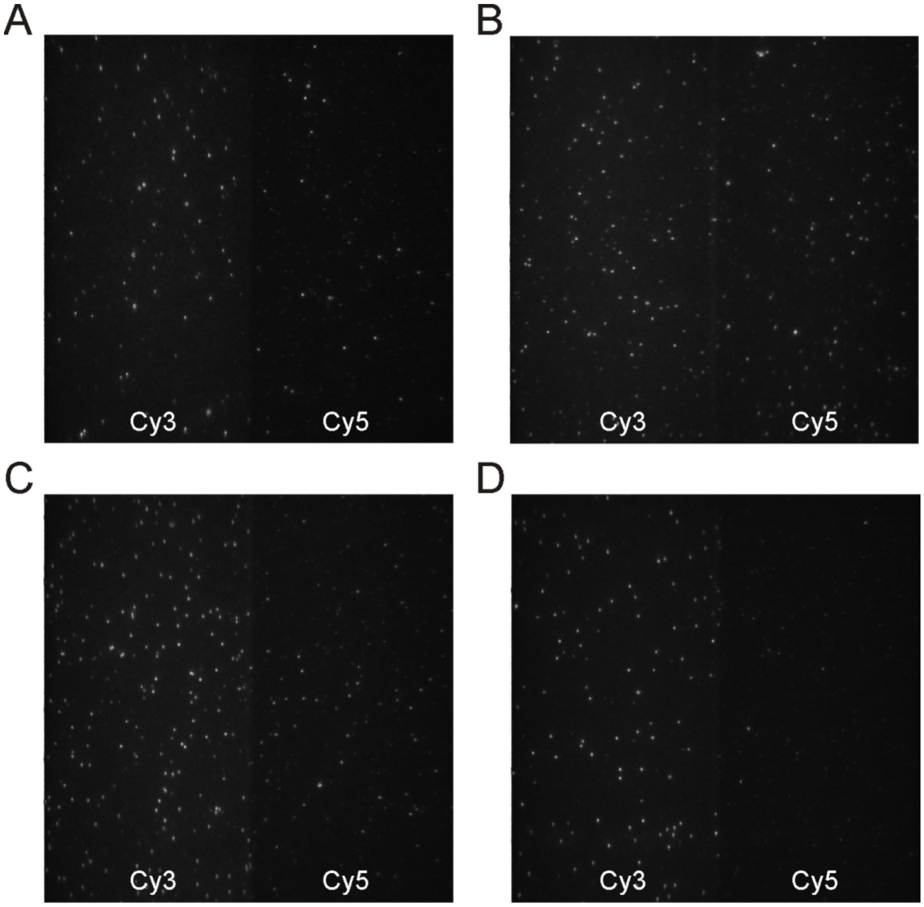

Figure S24. Representative fields of view from smFRET measurements. (**A**) Cy3-Cy5-BHQ-2 swinging arm complex (as shown in Figure S22A). (**B-D**)Cy3/Cy5 labeled semi-swinging arm complexes (as shown in Figure S22B) with distances of 7 nm (**B**), 14 nm (**C**), and 21 nm (**D**) between the anchor positions of the **Cy3 labeled poly(T)$_{20}$** and the **Cy5 labeled P-1 strand**.

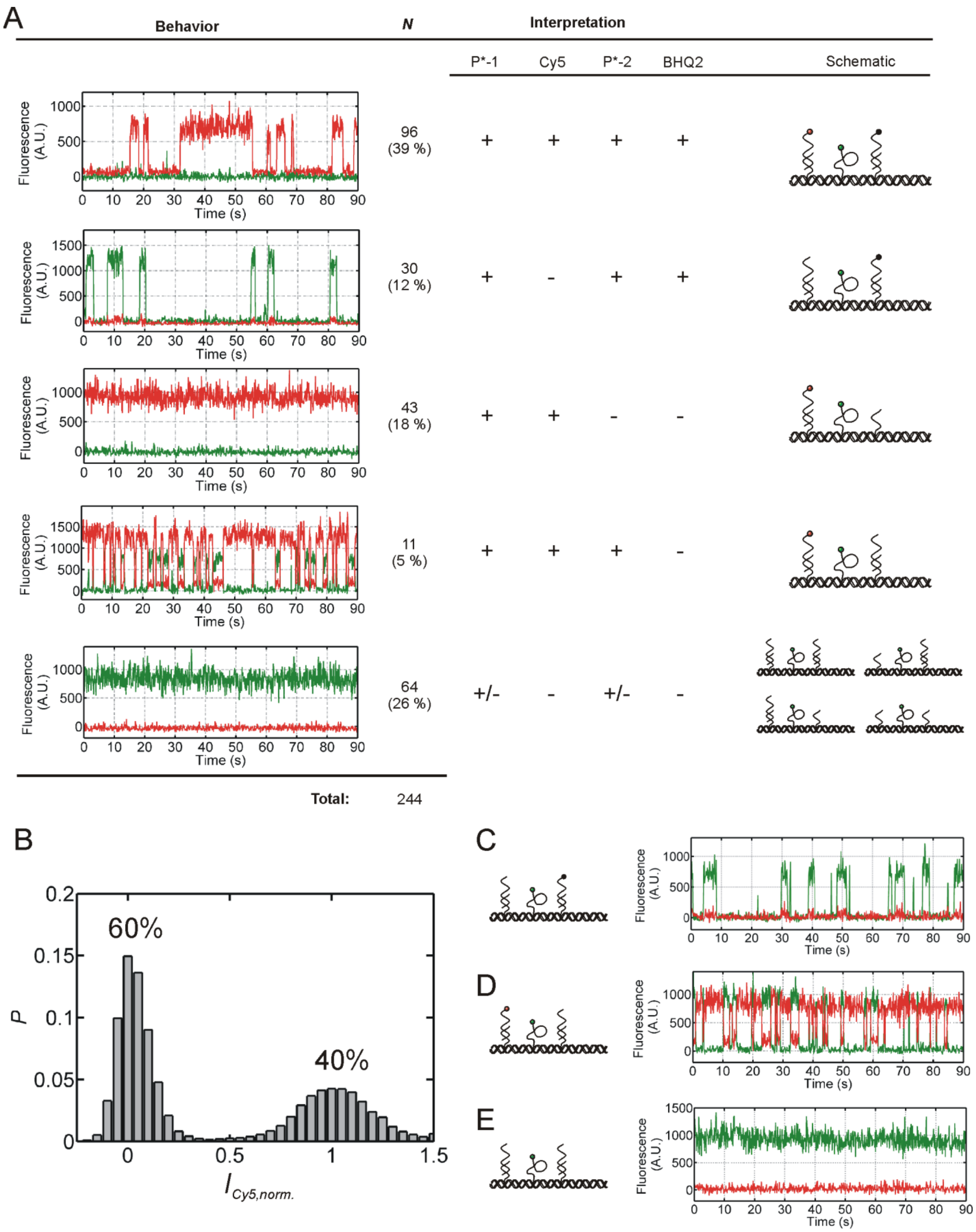
A
Behavior
N
Interpretation
P*-1
Cy5
P*-2
BHQ2
Schematic
Fluorescence (A.U.)
Time (s)
96 (39 %)
+ + + +
30 (12 %)
+ - + +
43 (18 %)
+ + - -
11 (5 %)
+ + + -
64 (26 %)
+/- - +/- -
Total: 244
B
P
60%
40%
$I_{Cy5,norm.}$
0 0.5 1 1.5
0 0.05 0.1 0.15 0.2
C
D
E
Fluorescence (A.U.)
Time (s)

Figure S25. smFRET characterization of fully assembled swinging arm structures with energy transfer between Cy3-Cy5 and Cy3-BHQ-2. (**A**) Tabulated smFRET behaviors of full Cy3-Cy5-BHQ-2 swinging arm complexes, along with representative single-molecule fluorescence intensity trajectories (Cy3 in green, Cy5 in red) and the interpretation regarding the presence or absence of **P*-1**, **Cy5**, **P*-2**, and **BHQ-2**. Complexes with **P*-2** and **BHQ-2** but lacking **P*-1** are not likely to be observable since Cy3 fluorescence will be strongly quenched the majority of the time. (**B**) Histogram of normalized Cy5 intensity for complexes exhibiting alternating high-FRET and quenched states (i.e., "++++" behavior in (A), interpreted as the fully assembled and three-dye labeled complexes). Only the first 20 s of each trajectory whose length exceeded 20 s were included ($N = 81$). (**C**)-(**E**) Representative single-molecule intensity vs. time trajectories of control complexes prepared with (C) unlabeled **P*-1**, (D) unlabeled **P*-2**, or (E) unlabeled **P*-1** and **P*-2**.

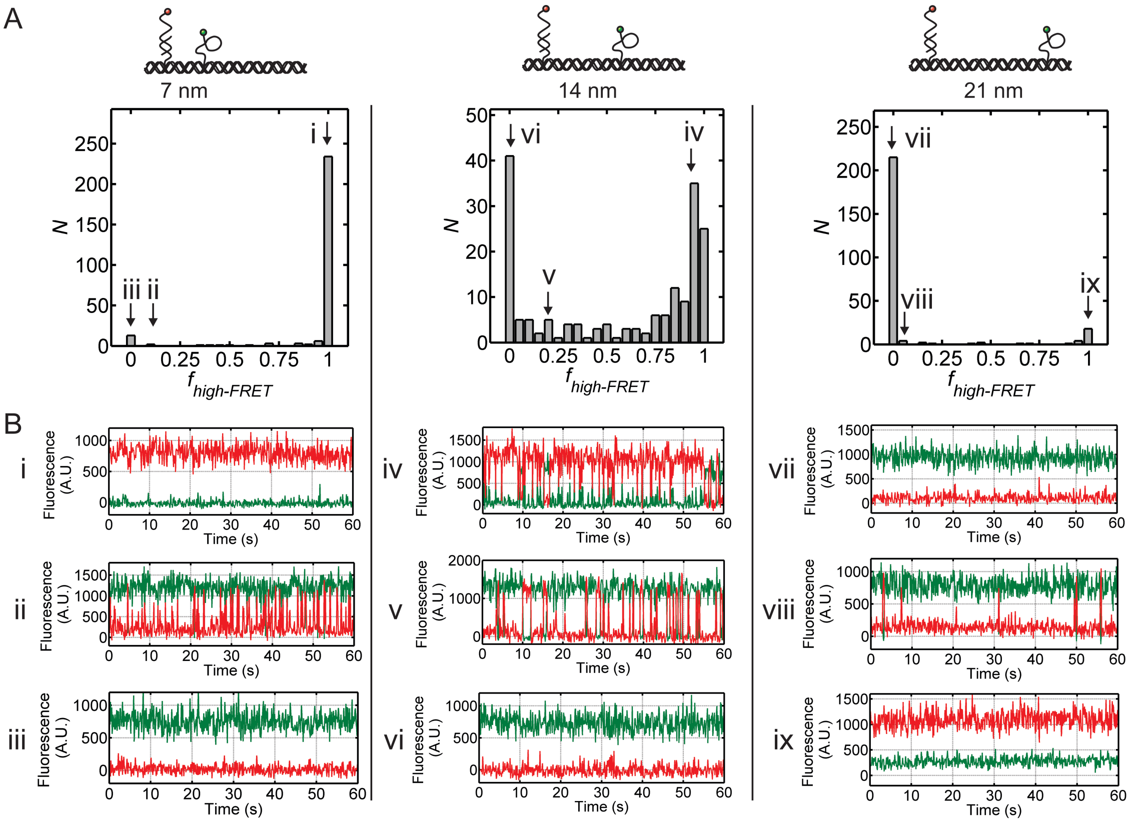

Figure S26. Heterogeneous behavior of single semi-swinging arm complexes. (**A**) Histograms of the number of observed complexes of each type (*d* = 7, 14, or 21 nm) spending a given fraction of time in the high-FRET state (FRET > 0.5). The vertical arrows show the positions of the corresponding molecules whose smFRET trajectories are shown in panel B (i-ix) (**B**) Selected smFRET trajectories showing the diversity of behaviors exhibited by individual complexes of each type. The majority of complexes with a spacing of 7 nm show high FRET, slightly more than half (~ 60%) of the complexes with a 14 nm spacing show high FRET, and only a small fraction (< 10%) of the complexes with a 21 nm spacing show high FRET. Thus, binding between the swinging arm and target probe is most efficient with a 7 nm spacing, somewhat less efficient at 14 nm, and generally not possible at 21 nm.

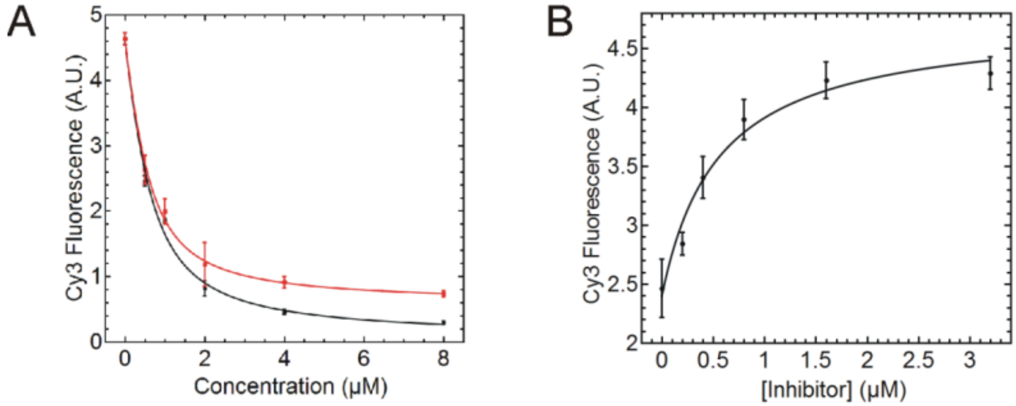

Figure S27. Determination of binding constants of Cy5-P*-1 and BHQ2-P*-2, and the inhibition constant of *I*. (**A**) Ensemble FRET binding titration of free **Cy3-poly(T)$_{20}$** with **Cy5-P*-1** (red) and **BHQ2-P*-2** (black) in 1×TAE-Mg^{2+}. The lines are nonlinear least-squares fits yielding K_d values of 0.31 ± 0.05 μM for **Cy5-P*-1** and 0.36 ± 0.08 μM for **BHQ2-P*-2**. (**B**) Ensemble inhibition of binding between **Cy3-poly(T)$_{20}$** and **Cy5-P*-1** by titration with ***I*** (which forms an 11-bp duplex with **Cy5-P*-1**). Dequenching of Cy3 is modeled by a logistic function (line) yielding an IC$_{50}$ of 0.47 ± 0.24 μM and an estimated K_I of 0.06 μM (calculated as described in the Methods section). Error bars shown are 1 standard error of the mean from three independent measurements.

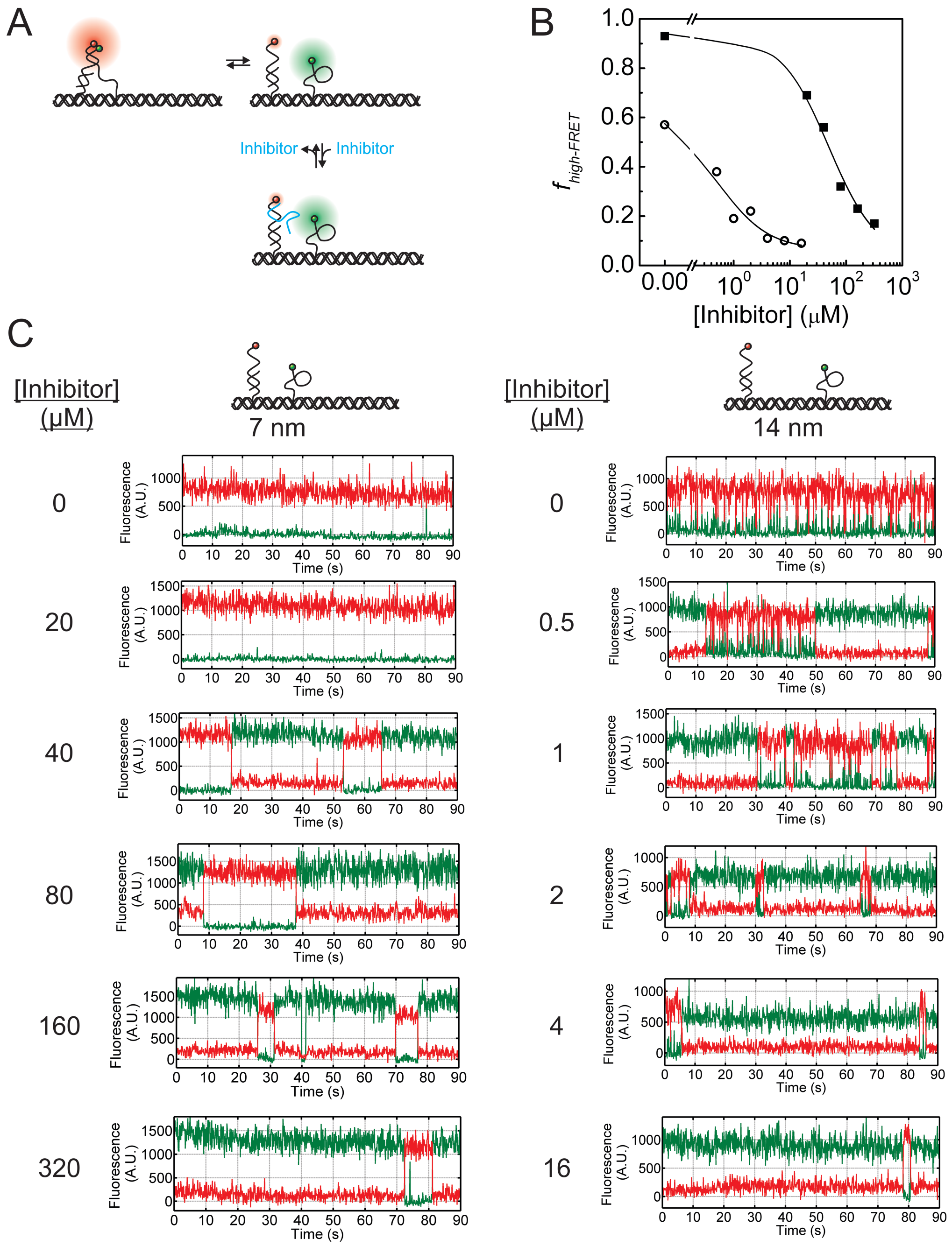

Figure S28. smFRET competition assays. (**A**) Schematic illustration of smFRET competition assays for the determination of local effective swinging arm concentration. (**B**) Determination of the local effective concentration of the Cy3-arm in the vicinity of a **Cy5-**

P*-1 probe displaced by 7 nm (squares) or 14 nm (circles). The fraction of Cy5-labeled probe hybridized to the Cy3-labeled arm (K_d ~ 0.31 μM) in the presence of varying concentrations of Inhibitor strand (K_i ~ 0.06 μM) is fit with a competitive binding model (solid lines) as described in the Methods, yielding the effective concentration estimates in Table S4. (**C**) Representative single-molecule trajectories for the d = 7 nm and d = 14 nm complexes in the presence of varying concentrations of inhibitor.

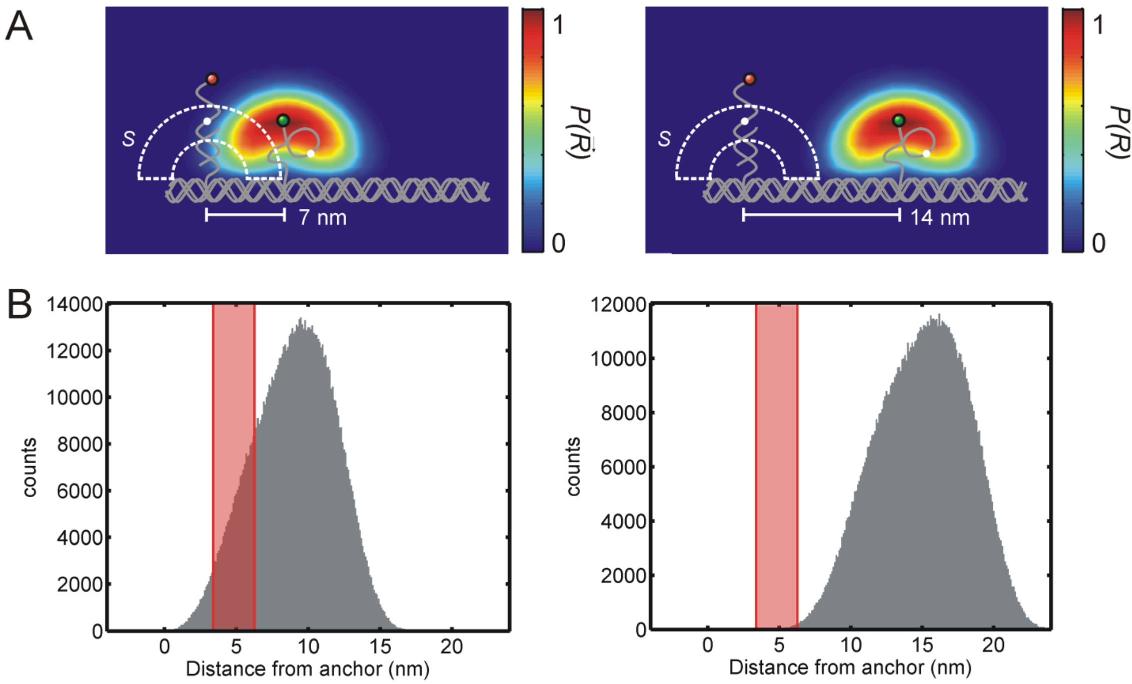

Figure S29. Modeling conformations and local effective concentration of the swinging arm. (**A**) Schematic illustration of the model. The swinging arm (Cy3 labeled) is modeled as a freely rotating chain using the Metropolis algorithm, giving rise to a distribution of conformations. A 5-nm-wide cross-section of the conformational probability distribution is represented by a rainbow color map. The Cy5-labeled probe is assumed to evenly explore a hemispherical shell *S* (white dotted lines). A conformation is considered compatible with hybridization if it can bring the two proximal ends of the arm-probe duplex (white circles) into close proximity. (**B**) Histograms of the distance between the swinging arm and the anchor site for the Cy5-labeled probe as determined by modeling of 10^6 conformations. The red shaded region corresponds to the hemispherical shell *S,* the region compatible with hybridization.

Table S4. Comparison of predicted and measured local effective concentration of the swinging arm in the vicinity of Cy5-P*-1 (DNA-only model structures)

	***d* = 7 nm**	***d* = 14 nm**
$C_{eff,pred}$ (μM)	607	4.5
$C_{eff,meas}$ (μM)	250	2.7

$C_{eff,pred}$ is the predicted local effective concentration of the Cy3-arm in the vicinity of the **Cy5-P*-1 probe**, calculated from the Metropolis Monte Carlo simulations as described in Methods and Figure S29. $C_{eff,meas}$ is the local concentration as estimated from smFRET competition assays (Figure S28).

Section 7: Enzyme activity assay methods and Michaelis-Menten analysis

1) Free enzymes: The activity of freely diffusing dehydrogenases (G6pDH and MDH) is evaluated by the rate of reduction of NAD^+ to NADH (for G6pDH) or oxidation of NADH to NAD^+ (for MDH) as monitored by the change in absorbance at 340 nm.

2) Semi-swinging arm structures: 100 nM G6pDH-NAD^+ or MDH-NAD^+ semi-swinging arm structures (with one enzyme and the swinging arm anchored 7, 14 or 21 nm apart on the DX tile) were prepared into 100 μL total volume with substrate in 1×TBS buffer (pH 7.6) for the activity assay. The assay was performed using a SpectraMax M5 96-well plate reader (Molecular Device, Sunnyvale, CA) following method outlined in (*14*). The activity of semi-swinging arm structures was measured using a coupled assay utilizing PMS (phenazine methosulfate) and resazurin in which PMS first oxidizes NADH to NAD^+, then reduces resazurin to resorufin with the appearance of a fluorescence signal (excitation max ~ 544 nm, emission max ~ 590 nm), as shown in Figure S30A. For a typical reaction, 100 nM G6pDH-NAD^+ structure was incubated with 1 mM glucose-6-phosphate (G6p), 500 μM PMS and 500 μM resazurin; and 100 nM MDH-NAD^+ structure was assayed with 1 mM malic acid, 500 μM PMS and resazurin and 100 nM oxaloacetate decarboxylase (OAD) in 1×TBS buffer (pH 7.5).

3) Fully assembled swinging arm structures: 100 μL reactions containing 100 nM complete G6pDH-NAD^+-MDH swinging arm structures were assayed with 1 mM G6p, 1 mM oxaloacetic acid (OAA) in 100 mM HEPES buffer (pH 8) as shown in Figure S30B. The overall activity of the cascade was measured by monitoring the absorbance decrease at 250 nm due to the reduction of OAA to malic acid (Figure S30C). NAD^+ and NADH have slight difference (~ 10%) at 250 nm as compared to the change between OAA and pyruvate. For example, OD at 250 nm decreases ~ 0.05 for 40 μM NAD^+ converting to NADH, while the G6pDH/MDH cascade reaction with the same concentration of NAD^+ causes an OD decrease of ~ 0.5 in half an hour due to the conversion of OAA to pyruvate. In the experiments, we kept NAD^+ at low micromolar concentration to minimize its interference with the assay. Mg^{2+} and Tris were removed from the solution using size exclusion FPLC with 100 mM HEPES (pH 8) because they would induce the auto beta-decarboxylation of OAA to pyruvate (Figure S31) (*15*).

4) Lactate dehydrogenase (LDH) competition assay: The activity of LDH was characterized using a coupled assay of lactate oxidase (LOX)-horseradish peroxidase (HRP), in which LOX first oxidizes lactate produced by LDH to hydrogen peroxide, then HRP catalyzes the oxidation of Amplex Red to the strongly fluorescent product resorufin (ex 544 nm/ em 590 nm) using hydrogen peroxide (*16, 17*). A typical LDH competition assay was performed with 100-µL reactions containing 100 nM each of LDH and the G6pDH-NAD$^+$-MDH structure 1 mM each of Glucose-6-phosphate, oxaloacetic acid and pyruvate, 10 nM each of LOX and HRP, and 200 µM Amplex Red in 100 mM HEPES (pH 8) buffer.

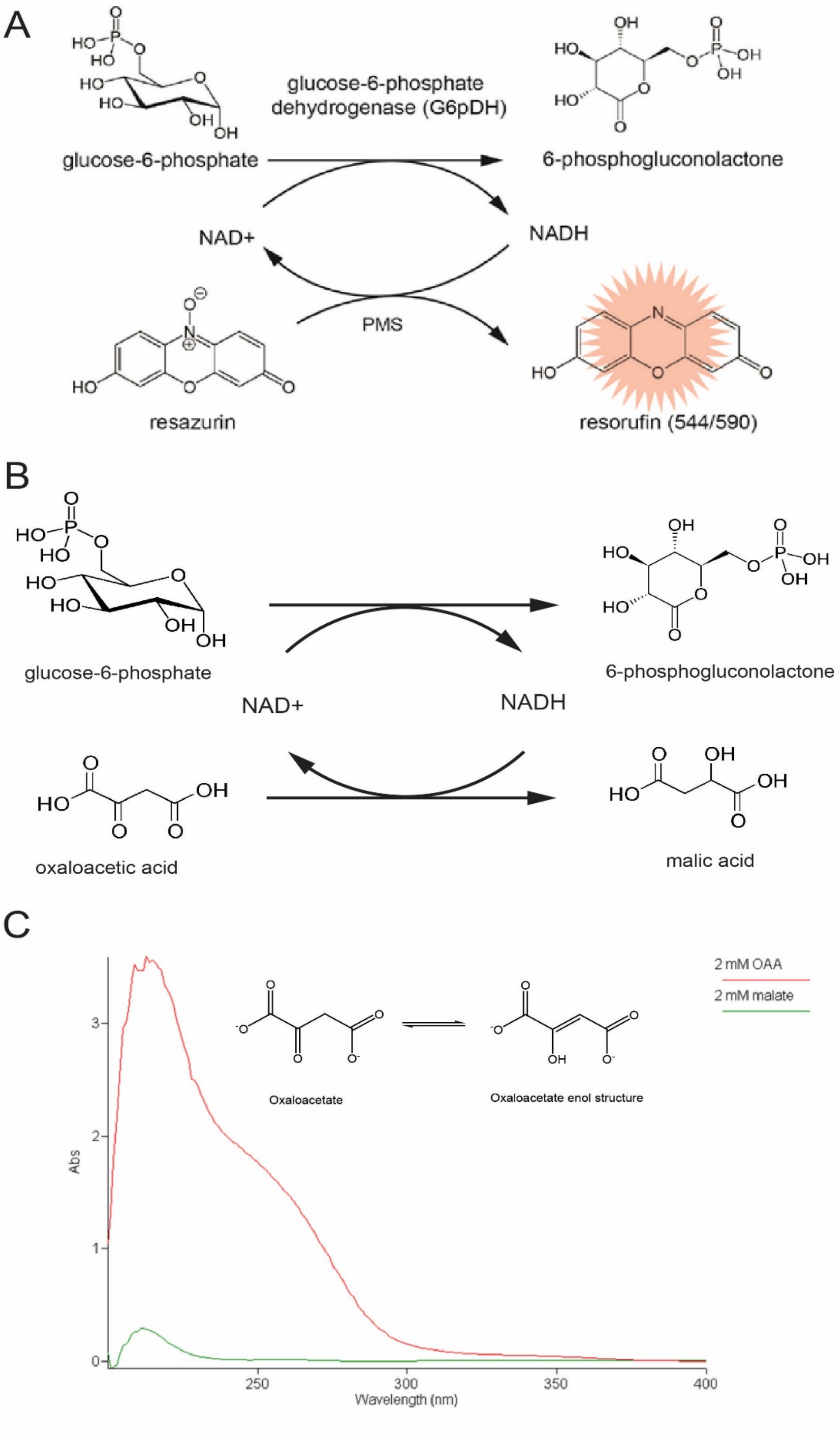
A
glucose-6-phosphate
glucose-6-phosphate dehydrogenase (G6pDH)
6-phosphogluconolactone
NAD+
NADH
PMS
resazurin
resorufin (544/590)
B
glucose-6-phosphate
6-phosphogluconolactone
NAD+
NADH
oxaloacetic acid
malic acid
C
2 mM OAA
2 mM malate
Oxaloacetate
Oxaloacetate enol structure
Abs
0
1
2
3
250
300
350
400
Wavelength (nm)

Figure S30. Reaction schemes for detection of enzymatic activity in the G6pDH-NAD$^+$ semi-swinging arm structure and the G6pDH-NAD$^+$-MDH full swinging arm structure. (**A**) PMS/resazurin coupled assay for G6pDH-NAD$^+$ activity. NAD$^+$ is first reduced to NADH by G6pDH. Next, PMS catalyzes electron transfer from NADH to resazurin producing the strongly fluorescent product resorufin with an emission maximum ~590 nm. MDH-NAD$^+$ activity is assayed similarly using malic acid as the substrate. (**B**) Assay for G6pDH catalyzes the oxidation of glucose-6-phosphate (G6p) and the reduction of NAD$^+$ to NADH. Subsequently, MDH catalyzes the reduction of oxaloacetatic acid (OAA) to malic acid using the NADH produced by G6pDH. (**C**) Oxaloacetic acid absorbs strongly at 250 nm due to its enol resonance structure, while malic acid has very little absorbance at 250 nm. The overall cascade activity of G6pDH-NAD$^+$-MDH can be measured by monitoring the absorbance decrease at 250 nm due to the reduction of oxaloacetic acid to malic acid.

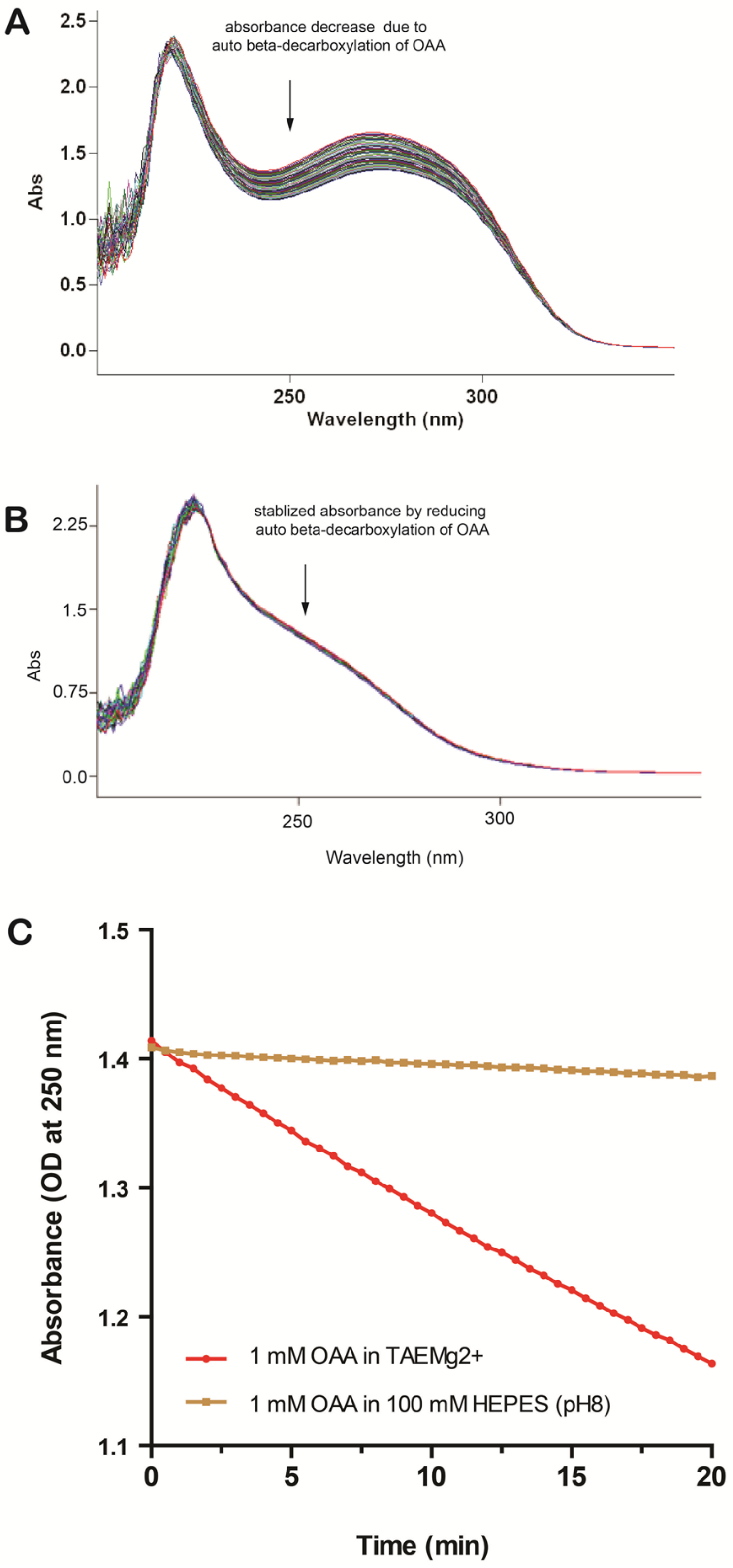

absorbance decrease due to auto beta-decarboxylation of OAA

stablized absorbance by reducing auto beta-decarboxylation of OAA

Figure S31. (**A**) Strong autocatalysis of 1 mM oxaloacetic acid (OAA) in pH 7.5, 1× TAE/Mg^{2+} buffer (12.5 mM $MgCl_2$), due to Mg^{2+}- and primary amine-induced beta-decarboxylation of OAA to pyruvate. (**B**) Weak autocatalysis of 1 mM oxaloacetic acid in pH 8, 100 mM HEPES buffer. (**C**) Comparing the stability of OAA in 1×TAE/Mg^{2+} buffer and HEPES buffer. HEPES buffer was used in all enzyme activity assays involving oxaloacetic acid as substrate.

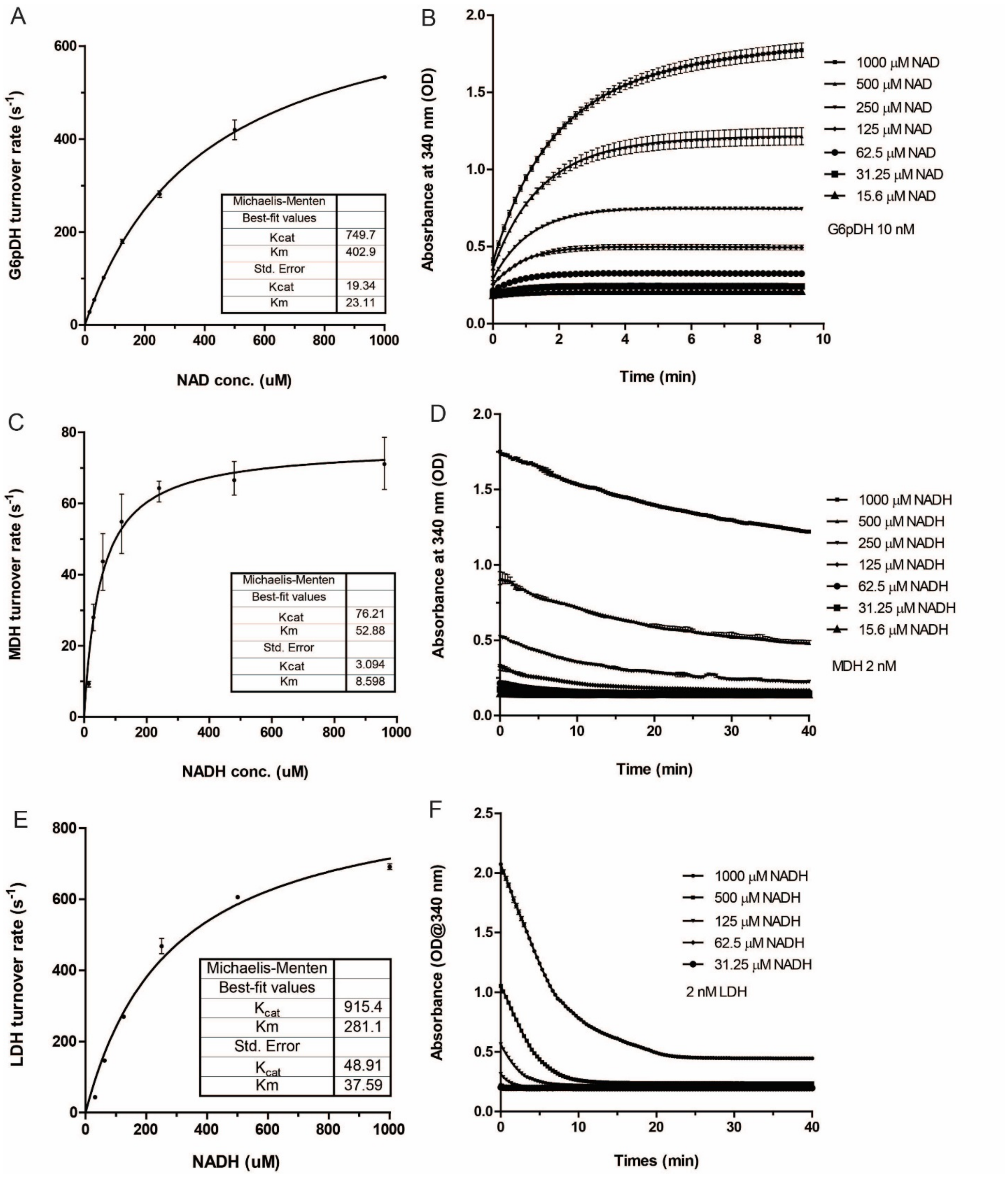
A
G6pDH turnover rate (s^{-1})
NAD conc. (uM)
Michaelis-Menten
Best-fit values
Kcat 749.7
Km 402.9
Std. Error
Kcat 19.34
Km 23.11
B
Absorbance at 340 nm (OD)
Time (min)
1000 μM NAD
500 μM NAD
250 μM NAD
125 μM NAD
62.5 μM NAD
31.25 μM NAD
15.6 μM NAD
G6pDH 10 nM
C
MDH turnover rate (s^{-1})
NADH conc. (uM)
Michaelis-Menten
Best-fit values
Kcat 76.21
Km 52.88
Std. Error
Kcat 3.094
Km 8.598
D
Absorbance at 340 nm (OD)
Time (min)
1000 μM NADH
500 μM NADH
250 μM NADH
125 μM NADH
62.5 μM NADH
31.25 μM NADH
15.6 μM NADH
MDH 2 nM
E
LDH turnover rate (s^{-1})
NADH (uM)
Michaelis-Menten
Best-fit values
K_{cat} 915.4
Km 281.1
Std. Error
K_{cat} 48.91
Km 37.59
F
Absorbance (OD@340 nm)
Times (min)
1000 μM NADH
500 μM NADH
125 μM NADH
62.5 μM NADH
31.25 μM NADH
2 nM LDH

Figure S32. (**A**) Michaelis-Menten plot for determining the Michaelis constant of G6pDH with respect to NAD^+. (**B**) Raw reaction traces of G6pDH in the presence of varying concentrations of NAD^+ and a constant concentration of 1 mM glucose 6-phosphate. (**C**) Michaelis-Menten plot for determining the Michaelis constant of MDH with respect to NADH. (**D**) Raw reaction traces of MDH in the presence of varying concentrations of NADH and a constant concentration of 1 mM OAA. (**E**) Michaelis-Menten plot for determining the Michaelis constant of LDH with respect to NADH. (**F**) Raw reaction traces of LDH in the presence of varying concentrations of NADH and a constant concentration of 1 mM pyruvate. All the assays were performed with unmodified NAD^+ or NADH molecules in 100 mM HEPES (pH 8) buffer.

Discussion: G6pDH has almost 10-fold higher k_{cat} than MDH, which suggests that in the G6pDH-NAD^+-MDH swinging arm structure, the catalytic capacity of G6pDH is not fully exploited; in one catalytic cycle, G6pDH may need to wait for MDH to convert NADH back to NAD^+ before catalyzing another reaction. At the same time, G6pDH has an ~8-fold larger K_m than MDH, suggesting that G6pDH requires a higher local concentration of cofactor than MDH for optimal activity. These differences in turnover number and Michaelis constant led us to design the G6pDH-NAD_2^+-MDH_2 and G6pDH-NAD_4^+-MDH_4 swinging arm structures as shown in Figure 3 (main text), which more effectively utilize the strengths of G6pDH and MDH.

LDH is used to compete with MDH for NADH to demonstrate the specificity of enzyme complexes organized by swinging arm structures. LDH has ~2-fold higher catalytic efficiency (k_{cat}/K_m value) than MDH. Hence, LDH can effectively compete with an equivalent concentration of freely diffusing MDH for NADH. However, the G6pDH-NAD^+-MDH swinging arm structure reduces the ability of LDH to compete with MDH for NADH; as shown in Figure 4 (main text), LDH is effectively out-competed as a larger percentage of MDH is incorporated into swinging arm complexes.

Section 8: Dependence of G6pDH and MDH activity on the length, position, and orientation of the NAD$^+$-modified swinging arm

Since the multi-enzyme complexes rely on local diffusive transport by the swinging arm, we expected their activity to depend on the length of the swinging arm, the distance between the anchor positions of the swinging arm and the enzyme, and the orientation of the swinging arm with respect to the protein anchor site on the DNA tile surface. We therefore investigated and optimized these parameters within our design space.

1. Dependence of the activity of G6PDH-NAD$^+$ on the length of the NAD$^+$-modified polyT swinging arm:

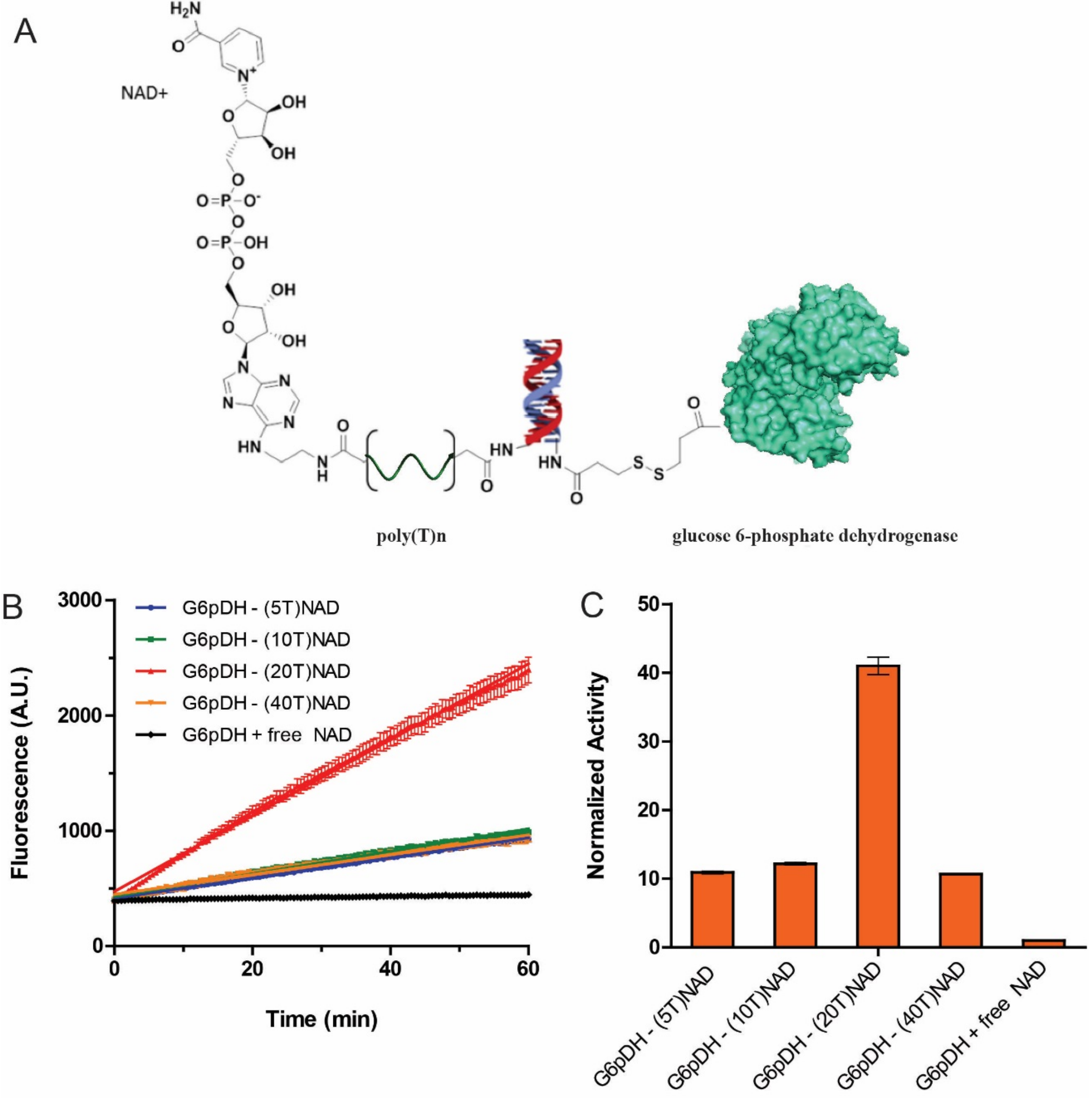

Figure S33. (**A**) Dependence of enzyme activity on arm length was measured by assembling an NAD$^+$-modified DNA strand (the red strand, 5’ AE-NAD$^+$-$(T)_n$ CCC TCC CTC C) with G6pDH labeled with the complementary strand (the blue strand, GGAGGGAGGGATTTTT-G6pDH-3’). The length of the arm was varied (n = 5, 10, 20, 40 nt) to adjust the average distance between the NAD$^+$ and the enzyme. (**B**) Raw activity traces for the G6pDH-NAD$^+$ assembly shown in (A) using different arm lengths. Freely diffusing AE-NAD$^+$ was also tested as a control to react with DNA conjugated G6pDH. (**C**) Normalized activity of the G6pDH-NAD$^+$ arm assemblies shown in (A) as a function of arm length. Activity is normalized with respect to G6pDH in the presence of free AE-NAD$^+$. Assay conditions: 100 nM G6pDH-NAD$^+$ assembly, 1 mM G6p, 500 μM PMS/resazurin in 1 × TBS buffer (pH 7.5). The poly$(T)_{20}$ arm gives the highest activity of the lengths tested.

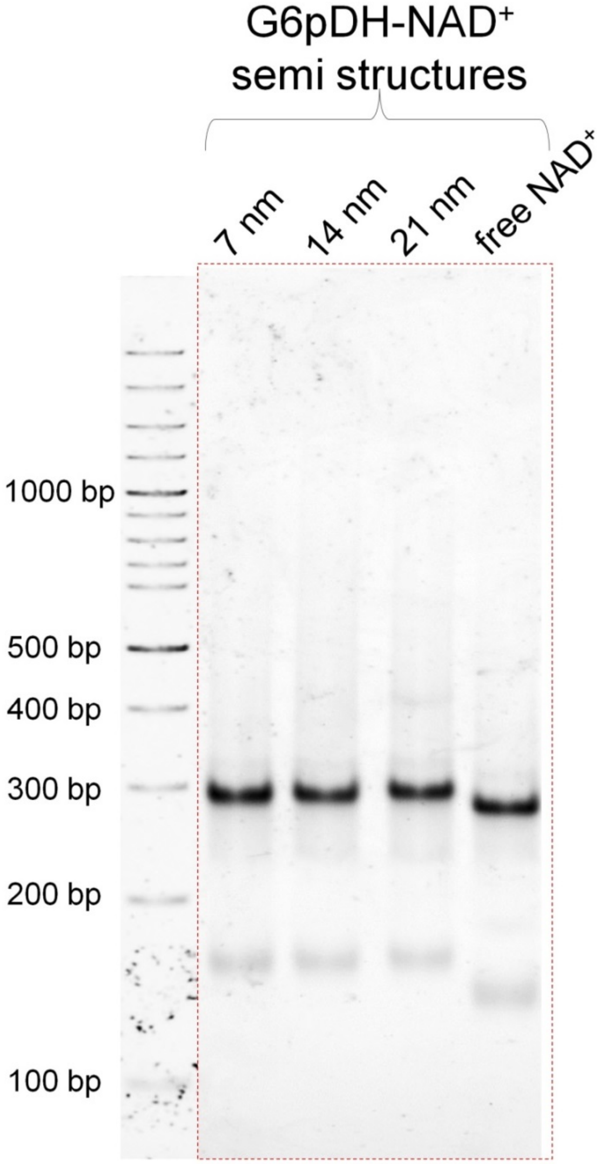

Figure S34. Native 3% PAGE characterization of G6pDH-NAD$^+$ semi-swinging arm structures on DX DNA tiles with distances of 7, 14 and 21 nm between anchor sites. The dark major bands in the gel indicate that the structures (see Figure S1) assemble with high yield. The faint lower band in each lane is the DNA tile lacking G6pDH. A G6pDH-assembled DNA tile lacking the NAD$^+$-labeled poly(T)$_{20}$ and mixed with free AE-NAD$^+$ is also shown as a control.

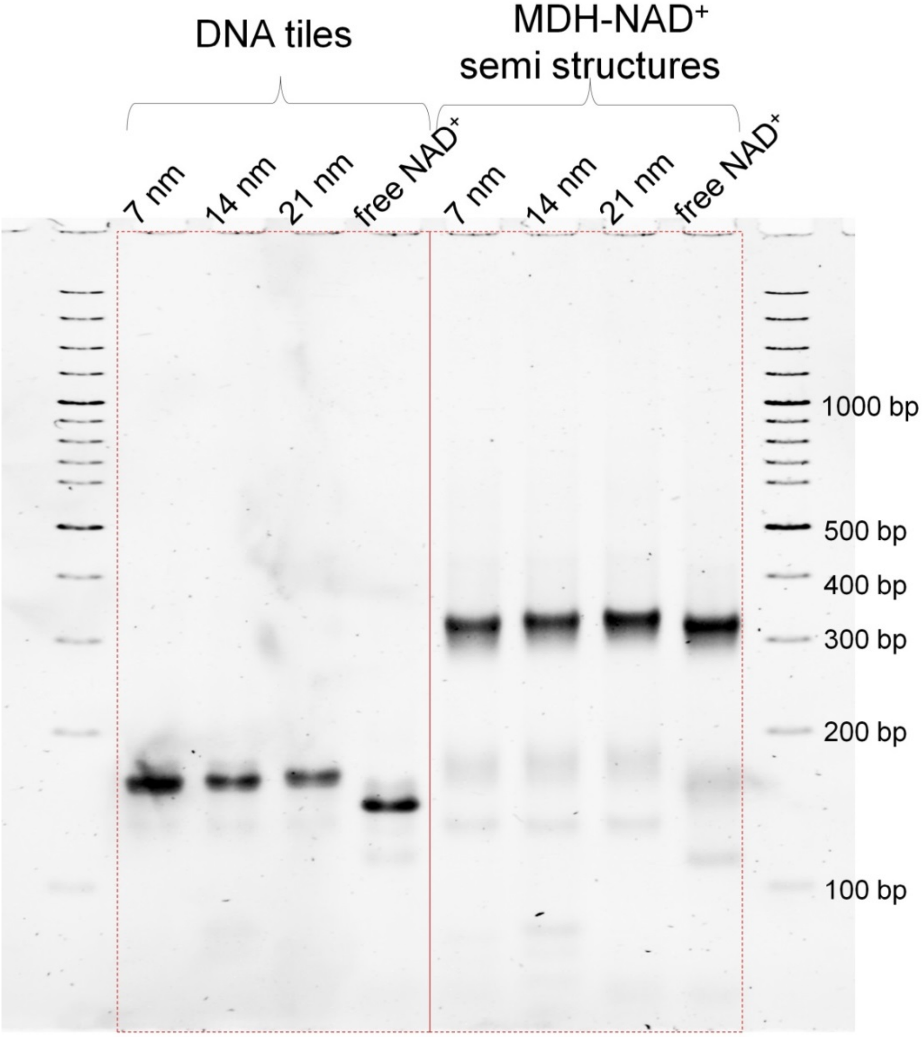

Figure S35. Native 3% PAGE characterization of MDH-NAD$^+$ semi-swinging arm structures without (left) and with (right) assembled MDH. The dark major bands in the gel indicate that the structures (see Figure S2) assemble with high yield. The faint lower band in each MDH-NAD$^+$ lane is the DNA tile lacking MDH. DX tiles lacking the NAD$^+$-labeled swinging arm are also tested the presence of free AE-NAD$^+$ as controls.

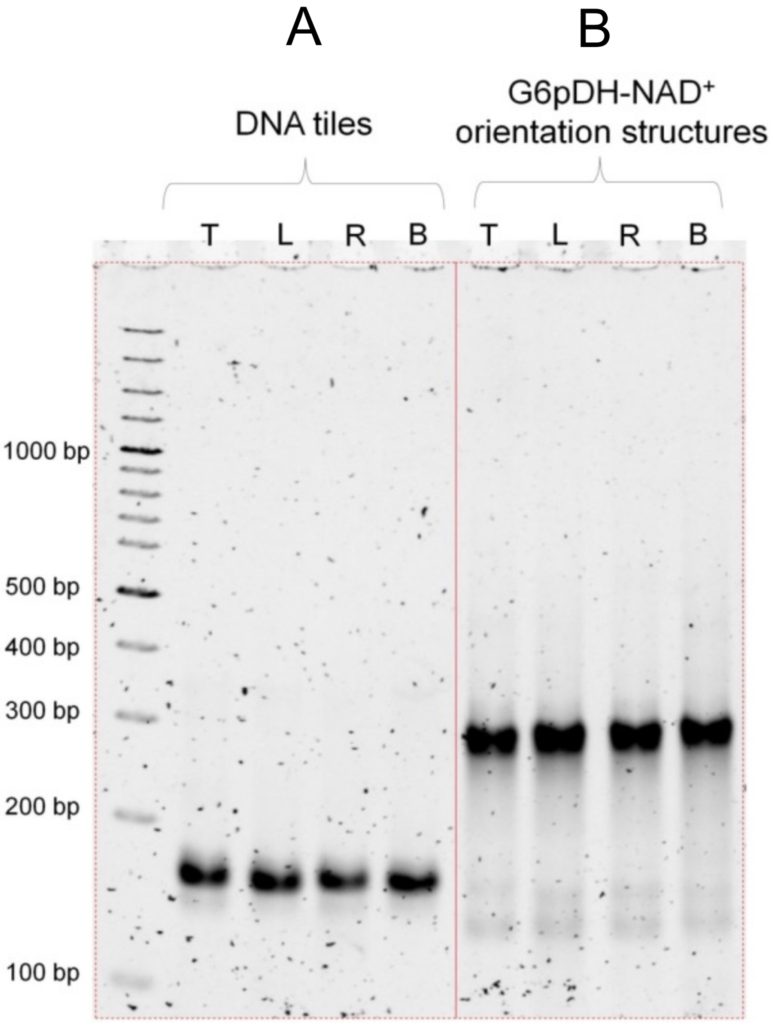

Figure S36. Native 3% PAGE characterization of (**A**) DNA tiles and (**B**) G6pDH-NAD$^+$ semi-swinging arm assemblies with varying orientation of the NAD$^+$ arm relative to the enzyme anchoring position (top): T (top/parallel), L(left), R (right) and B (bottom). Schematics of the structures are shown in Figure S39A and Figure 2E in the main text. The gel shows that all structures form with high yield.

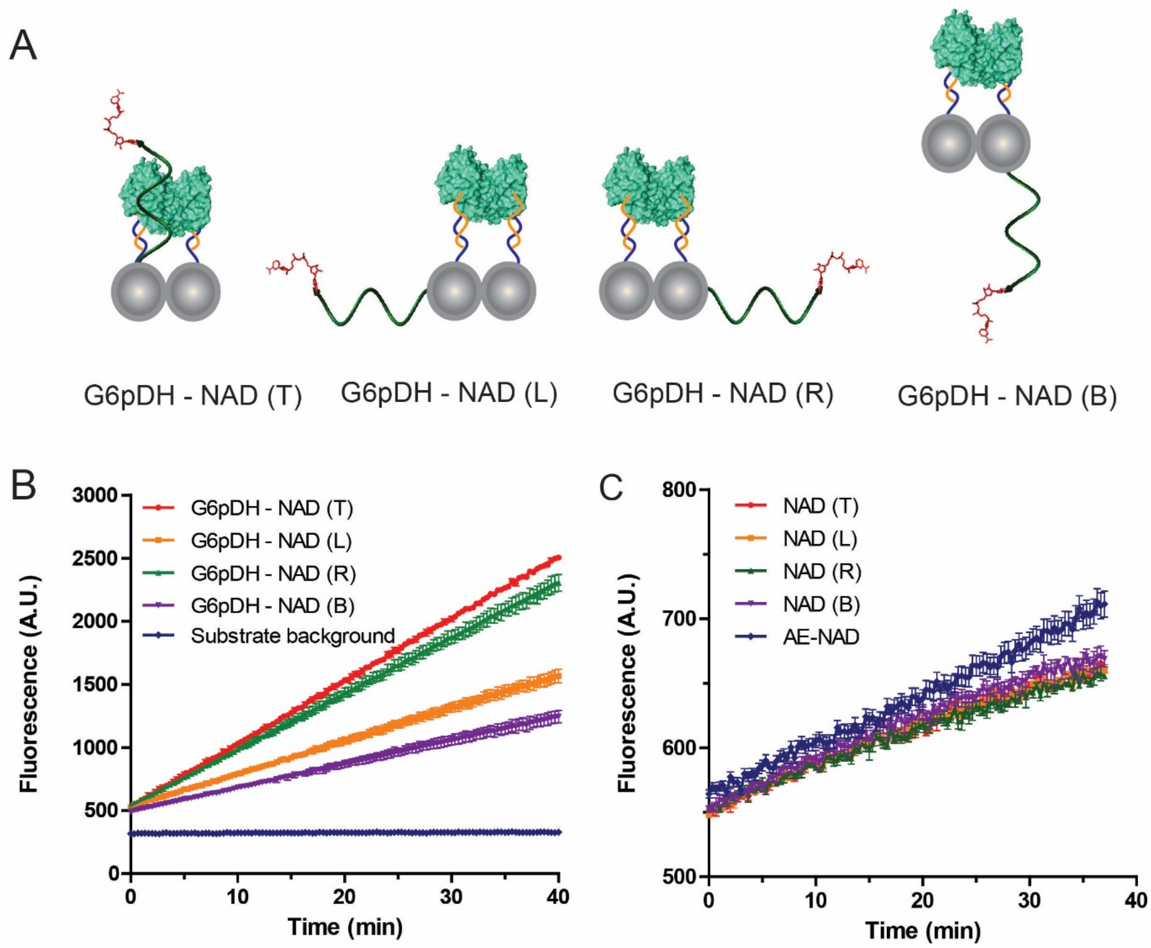

Figure S37. (**A**) Schematics of G6pDH-NAD$^+$ semi-swinging arm assemblies with varying orientations of the anchoring position of the NAD$^+$ arm relative to that of the protein (defined as "top"): T, parallel orientation on the top of the DNA scaffold; L, NAD$^+$ arm oriented to the left; R, NAD$^+$ arm oriented to the right; and B, NAD$^+$ arm oriented to the bottom. These are viewed from the end of the DNA helices with the protein behind the NAD$^+$ arm. (**B**) Raw fluorescence time traces of G6p oxidation catalyzed by G6pDH-NAD$^+$ semi-swinging arm assemblies with different anchoring orientations. Assay conditions: 100 nM G6pDH-NAD$^+$ semi-swinging arm assembly in the presence of 1 mM G6p and 500 μM PMS/resazurin in 1×TBS buffer (pH 7.5). (**C**) Raw fluorescence traces of 100 nM four DNA-NAD$^+$ that are used in constructing orientation assemblies (shown in figure A), reacting with G6pDH in the freely diffusing systems. AE-NAD$^+$ is also tested as control. Assay conditions: 100 nM G6pDH and DNA-NAD$^+$ in the presence of 1 mM

G6p and 500 μM PMS/resazurin in 1×TBS buffer (pH 7.5). The activity of all four conjugates is similar and comparable to that of free AE-NAD^+.

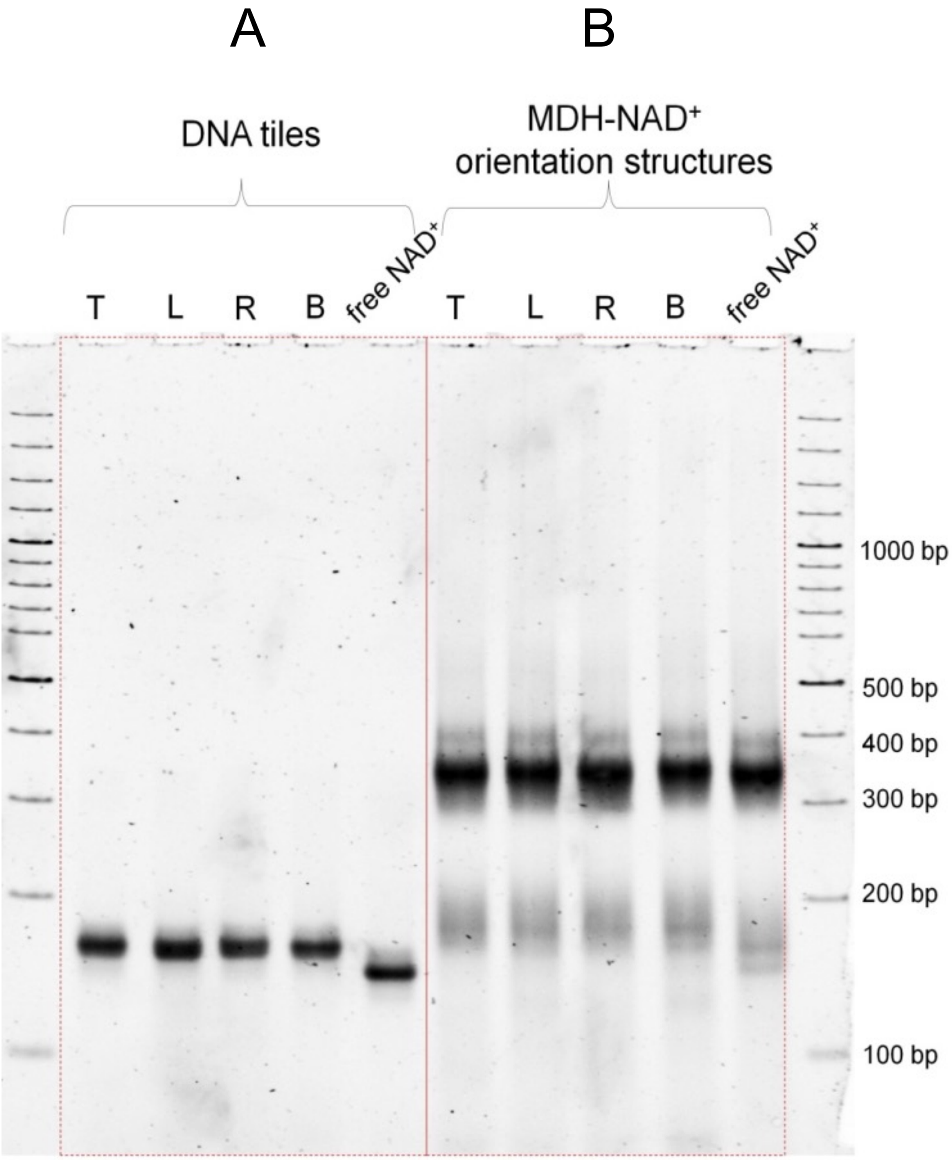

Figure S38. Native 3% PAGE characterization of (A) DNA tiles and (**B**) MDH-NAD^+ semi-swinging arm structures with varying orientation of the NAD^+ arm relative to the enzyme anchoring position (defined as "top"): T (top/parallel), L(left), R (right) and B (bottom). Schematics of the structures are shown in Figure S41A and Figure 2F in the main text. The gel shows that all structures form with high yield.

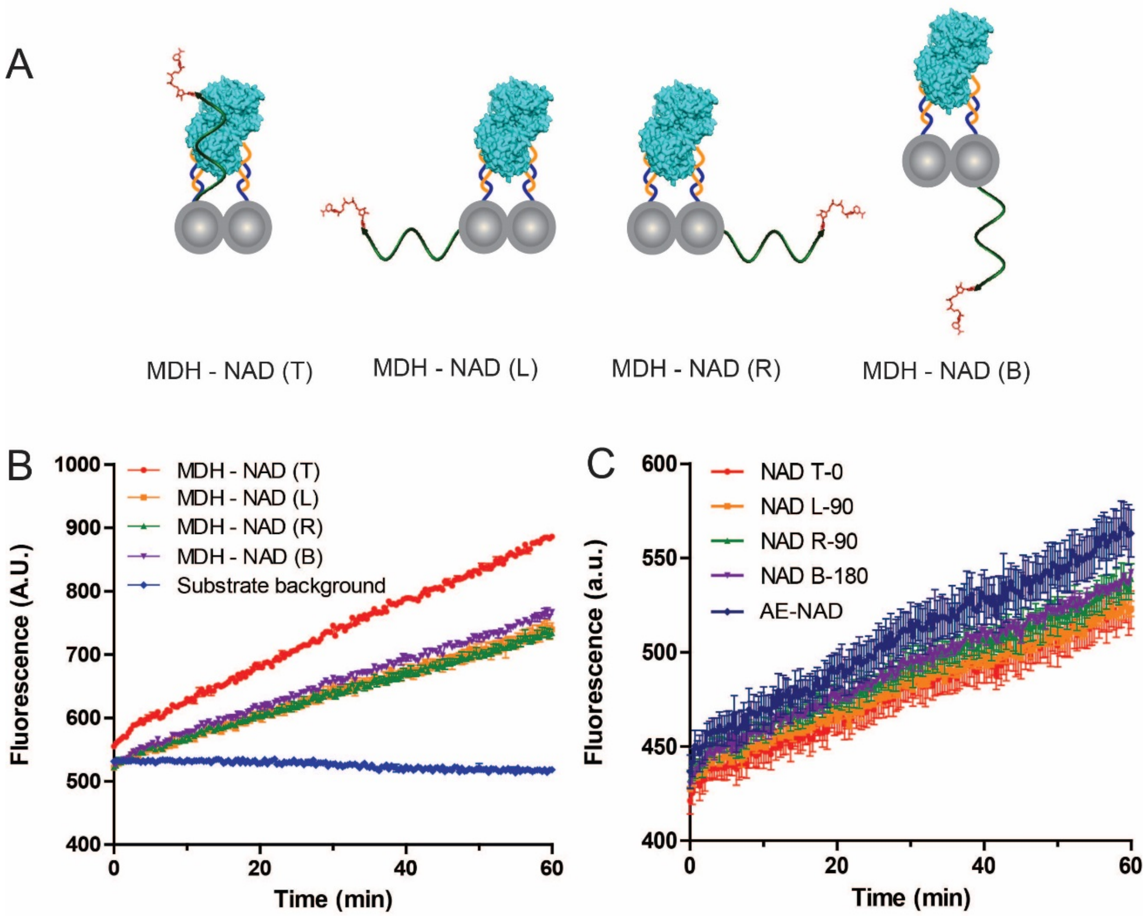

Figure S39. (**A**) Schematics of MDH-NAD$^+$ semi-swinging arm assemblies with varying orientations of the anchoring position of the NAD$^+$ arm relative to that of the protein (defined as "top"): T, parallel orientation on the top of the DNA scaffold; L, NAD$^+$ arm oriented to the left; R, NAD$^+$ arm oriented to the right; and B, NAD$^+$ arm oriented to the bottom. These are viewed from the end of the DNA helices with the protein behind the NAD$^+$ arm. (**B**) Raw fluorescence traces of malic acid oxidation catalyzed by MDH-NAD$^+$ semi-swinging arm assemblies with different anchoring orientations. Assay conditions: 100 nM MDH-NAD$^+$ semi-swinging arm assembly in the presence of 1 mM malic acid and 500 µM PMS/resazurin in 1× TBS buffer (pH 7.5). (**C**) Raw fluorescence traces of 100 nM four DNA-NAD$^+$ that are used in constructing orientation assemblies (shown in figure A), reacting with MDH in the freely diffusing systems. AE-NAD$^+$ is also tested as control. Assay conditions: 100 nM MDH and DNA-NAD$^+$ in the presence of 1 mM malic acid and

500 μM PMS/resazurin in 1×TBS buffer (pH 7.5). The activity of all four conjugates is similar and comparable to that of free AE-NAD$^+$.

Discussion: The results in Figures S38B, S40B, and 2E-F (main text) indicate that orientation of the NAD$^+$ arm parallel to the enzymes on the DNA scaffold gives the highest activity, as expected. Interestingly, even when the NAD$^+$ arm is anchored on the opposite side of the DX tile from the protein (bottom), the assemblies possess ~40-70% of the activity of the (top) type structure. This suggests that the flexibility of the swinging arm, together with the likely heterogeneity of protein orientations (i.e., active sites may face in various directions relative to the swinging arm's anchor position), result in residual activity in structures with a variety of swinging arm orientations. Nevertheless, a parallel orientation permits the swinging arm to reach the active sites of the enzymes most effectively, resulting in the highest activity.

Section 9: Characterization of the assembly and activity of G6pDH-NAD$^+$-MDH (G-NAD$^+$-M) swinging arm structures and stoichiometry-optimized complexes (G-NAD$_2^+$-M$_2$ and G-NAD$_4^+$-M$_4$)

1. Assembly and purification of G6pDH-NAD$^+$-MDH swinging arm structures. G-NAD$^+$-M swinging arm structures, as well as G6PDH-NAD$^+$ and MDH-NAD$^+$ semi-swinging arm structures, were purified using size-exclusion FPLC to remove aggregates, incompletely assembled structures and excess proteins. The fractions collected were characterized using native PAGE to confirm the assignments of the FPLC peaks and to check the purity of the samples.

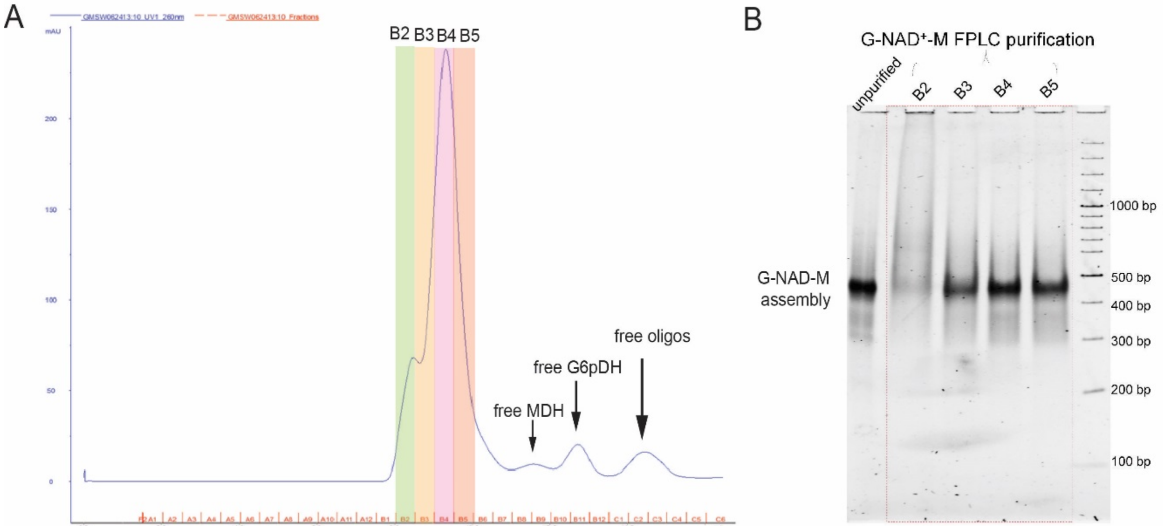

Figure S40. (**A**) Size-exclusion FPLC purification of fully assembled G6pDH-NAD$^+$-MDH swinging arm structures to get rid of excess enzymes and free DNA oligoes. The fractions B2-B5 were collected, representing the fully assembled structure with both the enzymes and the NAD$^+$ on the DX tile. (**B**) Native 3% PAGE characterization the structures collected in size-exclusion FPLC: Faction B2 contains aggregated structures. Fraction B3 to B5 are the fully assembled swinging arm structures and were used for the activity test (raw data shown in Figure S44). Unpurified swinging arm structure is also shown in the left lane as a control, which contains incomplete assemblies, aggregations and free proteins.

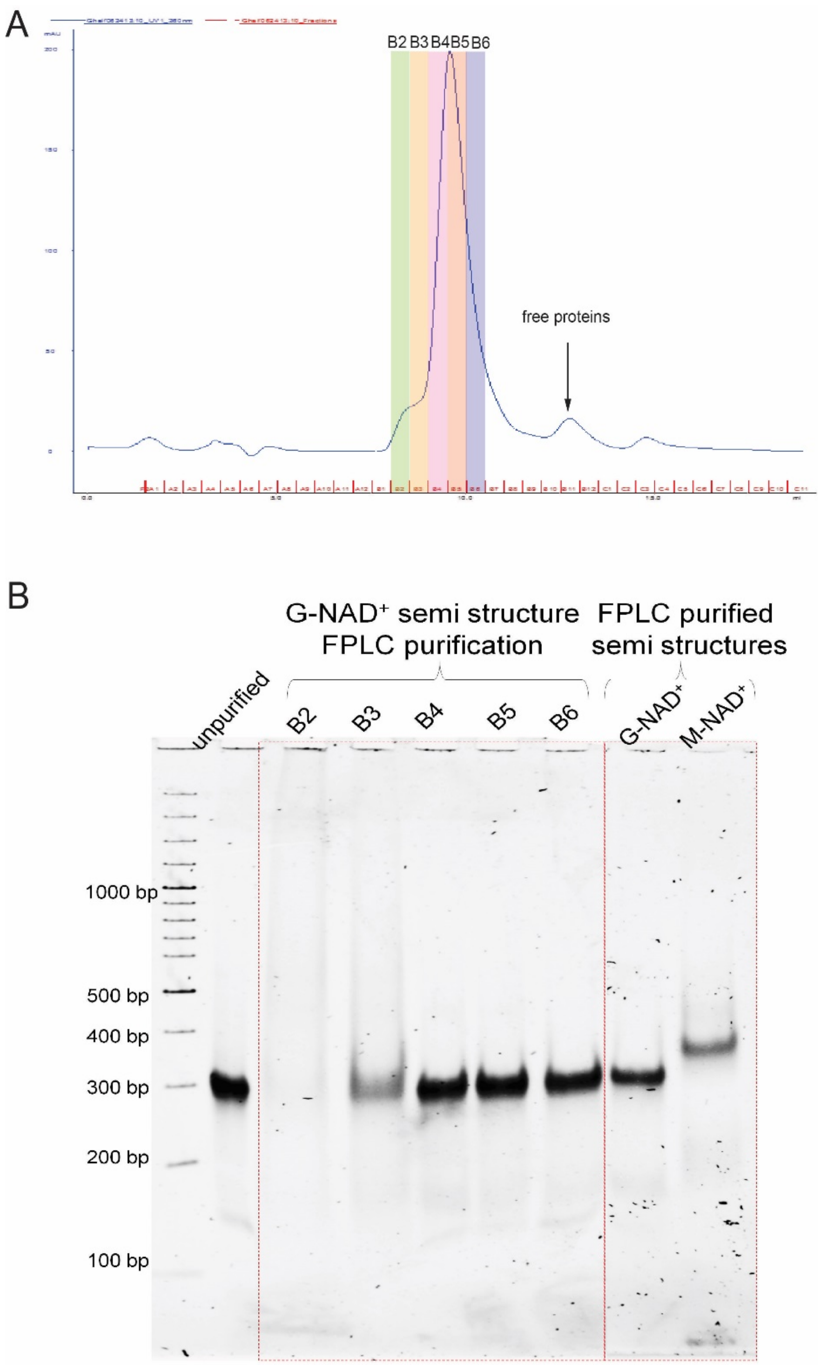

Figure S41. (**A**) Size-exclusion FPLC purification of G6pDH-NAD$^+$ semi-swinging arm structures. Five fractions (B2-B6) were collected. (**B**) Native 3% PAGE characterization of the fractions collected in size-exclusion FPLC. Fractions B2 and B3 contain aggregated structures (significant smear band). Fraction B4, B5 and B6 contain the purified structure and were used in subsequent activity assays (raw data shown in Figure S44). The two rightmost lanes contain FPLC-purified G6pDH-NAD$^+$ and MDH-NAD$^+$ semi-swinging arm structures.

2. Raw activity traces of full swinging arm and semi-swinging arm complexes.

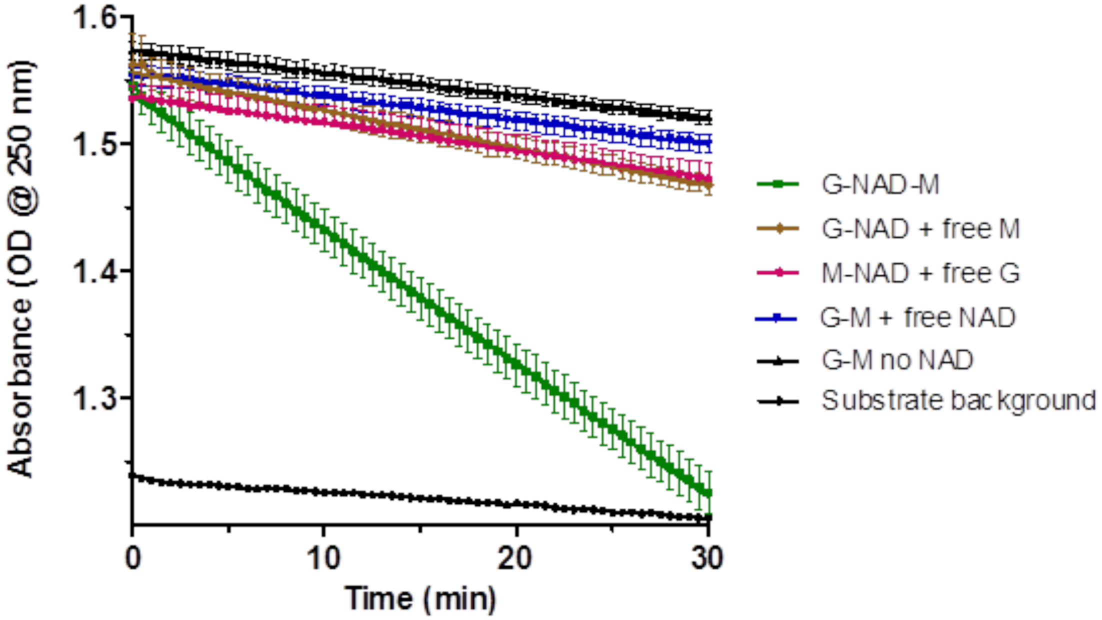

Figure S42. **Raw absorbance traces for evaluating the activity of different swinging arm constructs.** The normalized relative rates of reaction derived from fitting a straight line to each of these plots are shown in main text Figure 3A. Reaction conditions: 100 nM of the assembled enzyme-DX tile structures or free enzymes, 100 nM free AE-NAD$^+$ (when present), 1 mM G6p. and 1 mM OAA in 100 mM HEPES buffer (pH 8). The decrease in absorbance at 250 nm due to conversion of OAA to pyruvate reports on the overall progress of the coupled reactions. Each trace represents the average of three parallel measurements. The full G6pDH-NAD$^+$-MDH swinging arm structure shows significantly higher activity than any of the partially assembled structures, which show reaction rates only slightly above the background autocatalysis of OAA. The higher absorbance at 250 nm for the reaction mixtures than that of the substrates alone (1 mM G6p and 1 mM OAA) is due to the presence of NAD$^+$, proteins and the DNA tile.

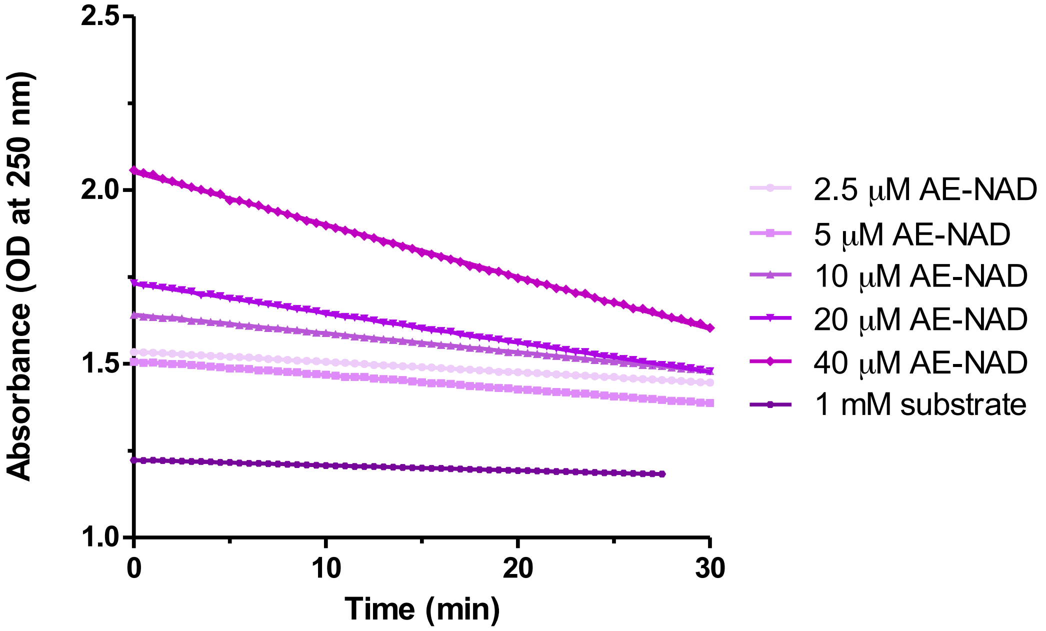

Figure S43. **Raw absorbance traces for determining the effective local concentration of NAD$^+$ on swinging arm structures** by titrating free AE-NAD$^+$ into the G6pDH-MDH assembly (lacking the NAD$^+$ swinging arm) and comparing the initial rates of reaction to that of the G6pDH-NAD$^+$-MDH structure. Assay conditions: 100 nM G6pDH-MDH assemblies with 2.5, 5, 10, 20 or 40 μM free AE-NAD$^+$ and 1 mM each of G6p and OAA in 100 mM HEPES buffer (pH 8).

Discussion:

It is remarked in the main text that the effective local concentration of the NAD$^+$-coupled swinging arm determined by enzyme catalysis (~20 μM at 7 nm) is significantly lower than the swinging arm concentration estimated from competitive hybridization (~250 μM at 7 nm in Fig. S28B). We have suggested two possible reasons for this discrepancy: (1) the stricter orientational and sterical constraints associated with the binding of tethered NAD$^+$ to the active site of a nearby (anchored) enzyme; and (2) the fact that some enzymes or cofactors may be paired together permanently with inactive partners on DNA nanostructures, preventing the formation of an active cascade. As shown in Figure S11, DNA conjugated G6pDH is significantly less active than unmodified enzyme (> 50 % decrease in activity under the assay conditions); it is thus likely that some of the DNA-conjugated enzymes are wholly or partially inactivated. When these inactivated enzymes are assembled into swinging arm structures, many will permanently pair with active NAD^+ molecules, resulting in an incomplete cascade. Similarly in Figure S18, the amino-modified NAD^+ used in this work is less active than unmodified NAD^+, with a ~ 50% decrease in k_{cat} and ~ 2.5 fold increased K_m for G6pDH on average. This suggests that some amino-modified NAD^+ or DNA-conjugated NAD^+ are not active, and may pair with active enzymes and inhibit the catalytic function on the swinging arm structures. Conversely, in a freely diffusing enzyme system, the exchange between enzymes and cofactors happens frequently, and the inactive components can thereby be rapidly replaced by active molecules without inhibiting the entire enzyme/cofactor system. This observation and discussion address one disadvantage of swinging arms and other substrate channeling mechanisms: the malfunction of one assembled component may inhibit the entire multi-enzyme complex. This might be circumvented in part by having redundant copies of enzymes and/or cofactors in a single complex, as in the designs depicted in Fig. 3D.

3. Assembly and characterization of the G6pDH-NAD$^{+}_{4}$ complex based on a 4×4 DNA tile.

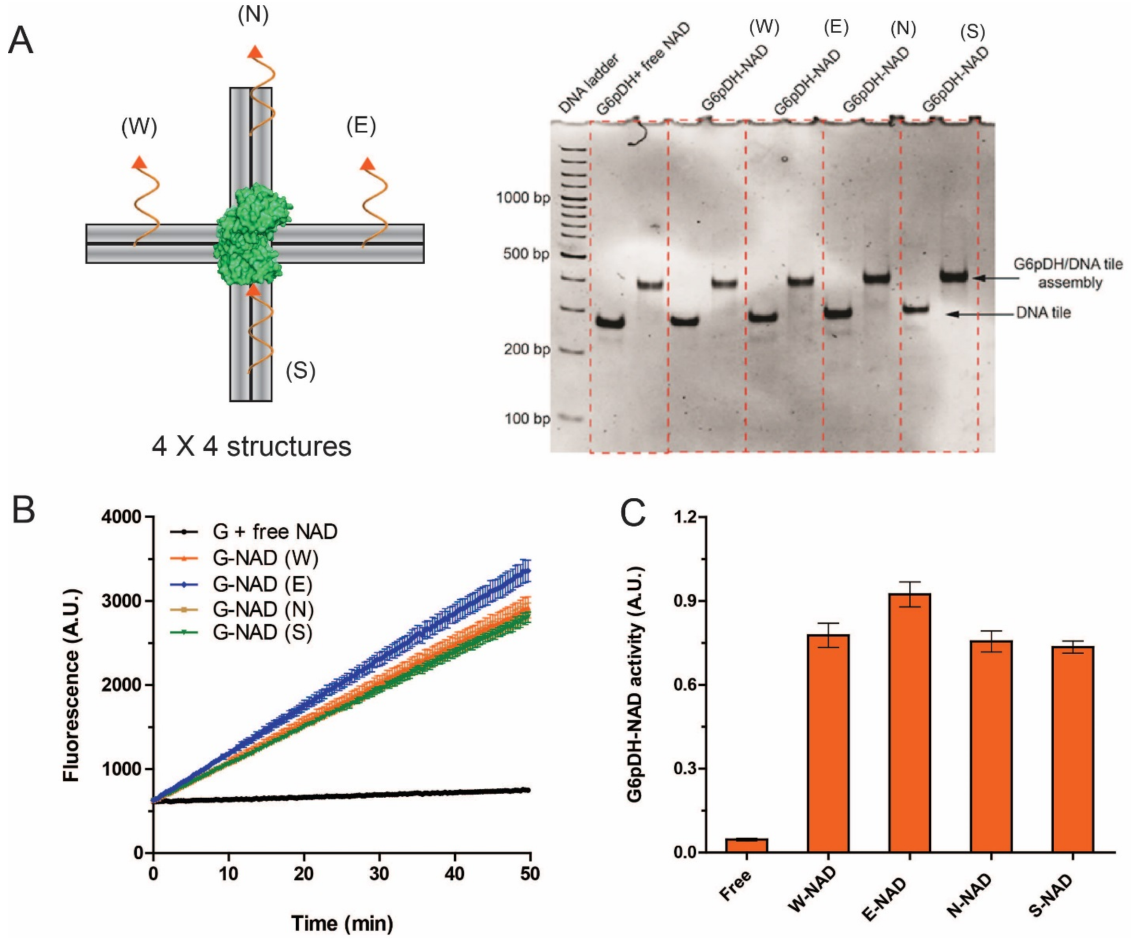

Figure S44. (**A**) Schematic of G6pDH assembly with four NAD^{+}-modified arms on a single 4×4 DNA tile (sequence design shown in **Figure S6**). The right panel shows a native 3% PAGE characterization of G6pDH-NAD^{+} 4×4 tile structures, each containing only one of the four NAD^{+}-modified arms (W, E, N, or S). Binding of G6pDH onto the 4×4 tile causes a mobility shift. (**B**) Activity assay of G6pDH-NAD^{+} 4x4 tile assemblies (each containing only one NAD^{+} arm). (**C**) Enzymatic activity as determined from the initial velocity of the raw fluorescence traces in (B), evaluated by fitting each trace to a straight line. Assay conditions: 100 nM G6pDH-NAD^{+} 4x4 tile structures, 100 nM free AE-NAD^{+} (when present) are 100 nM, 1 mM G6p, and 500 µM PMA/resazurin in 1×TBS buffer (pH 7.5).

Discussion: The activity measured for each of the constructs shown in Figure S46 is similar, varying within 20%. This suggests that there is no strong preference for a particular position of the swinging arm with respect to the enzyme on the 4×4 DNA tile. This may be due in part to the flexibility of the poly(T)$_{20}$ arm and (limited) rotational diffusion of the enzyme by its DNA anchors, but also is likely attributable to the random orientation of G6pDH attachment to the DNA tile. The random conjugation of two P-1 DNA probes to G6pDH *via* two of its many surface lysines (more than 10) is expected to yield a mixture of isomers, giving rise to a variety of orientations of the enzyme on the DNA tile. Since the four anchoring positions of the swinging arm on the 4×4 DNA tile are the same distance (7 nm) from the center of the protein anchoring position, the effective local concentration of NAD$^+$ is almost equal for all four positions when averaged across all isomers of the enzyme-DX tile complex.

4. Assembly of G6pDH and MDH with 1-4 NAD$^+$ swinging arms on the 4×4 DNA tile.

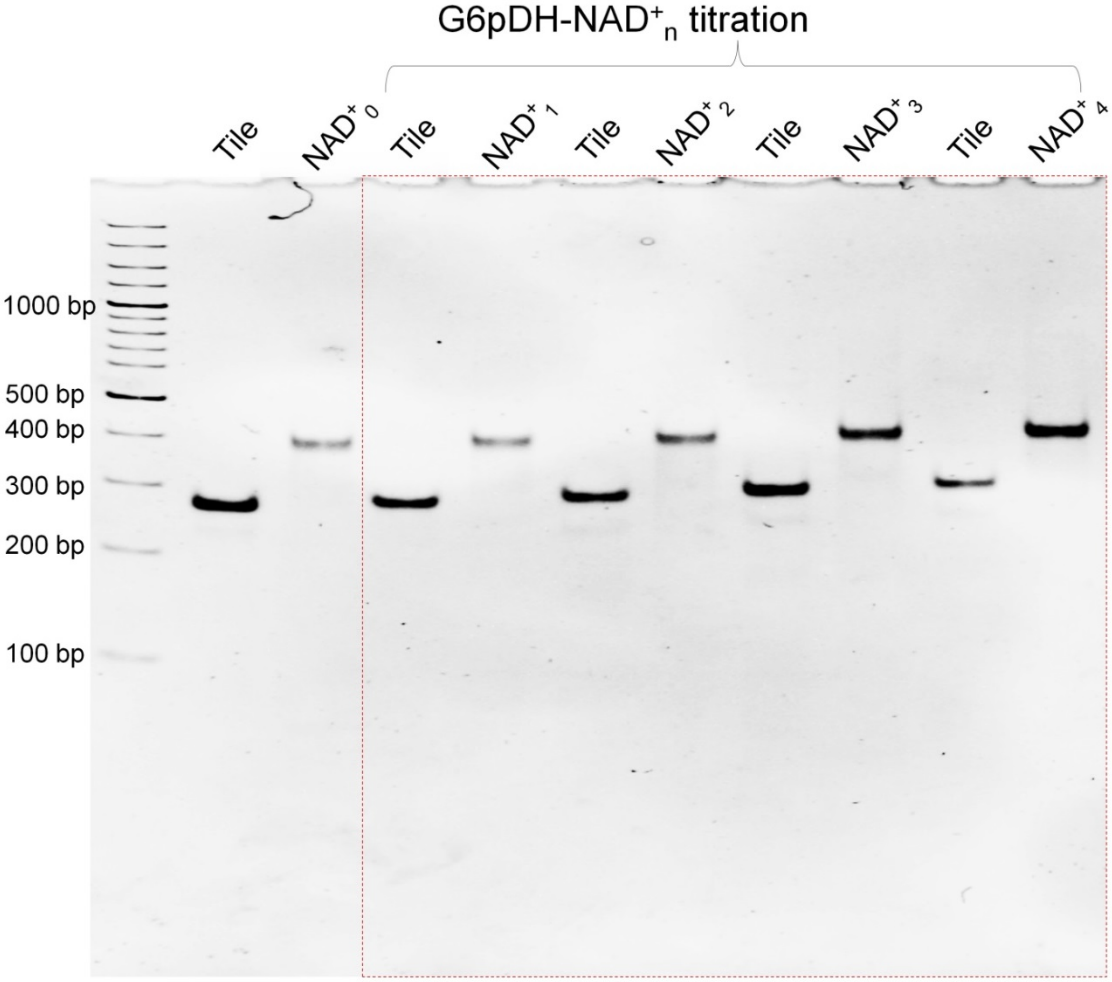

Figure S45. **Native 3% PAGE characterization of the assembly of G6pDH-NAD^+_n (n = 1, 2, 3, 4) structures**, in which G6pDH is located in the center of the 4×4 tile and the each arm of the DNA tile carries one NAD$^+$ swinging arm (or none). Binding of G6pDH to the DNA tile causes a significant mobility shift, while the binding of each additional NAD$^+$ arm causes only a very small decrease in mobility. The gel also indicates that the structures assemble with high yield.

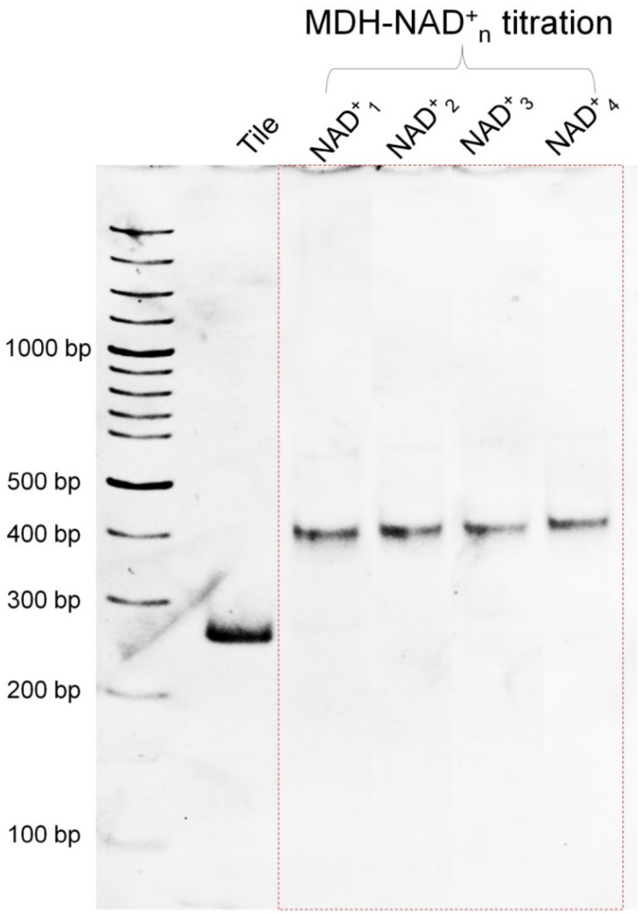

Figure S46. **Native 3% PAGE characterization of the assembly of MDH-NAD^+_n (n = 1, 2, 3, 4) structures**, in which MDH is located at the center of the 4×4 tile and the each arm of the DNA tile carries one NAD$^+$ swinging arm (or none). Binding of MDH to the DNA tile causes a significant gel mobility shift, while the binding of each additional NAD$^+$ arm causes only a very small decrease in mobility. The gel also indicates that the structures assemble with high yield.

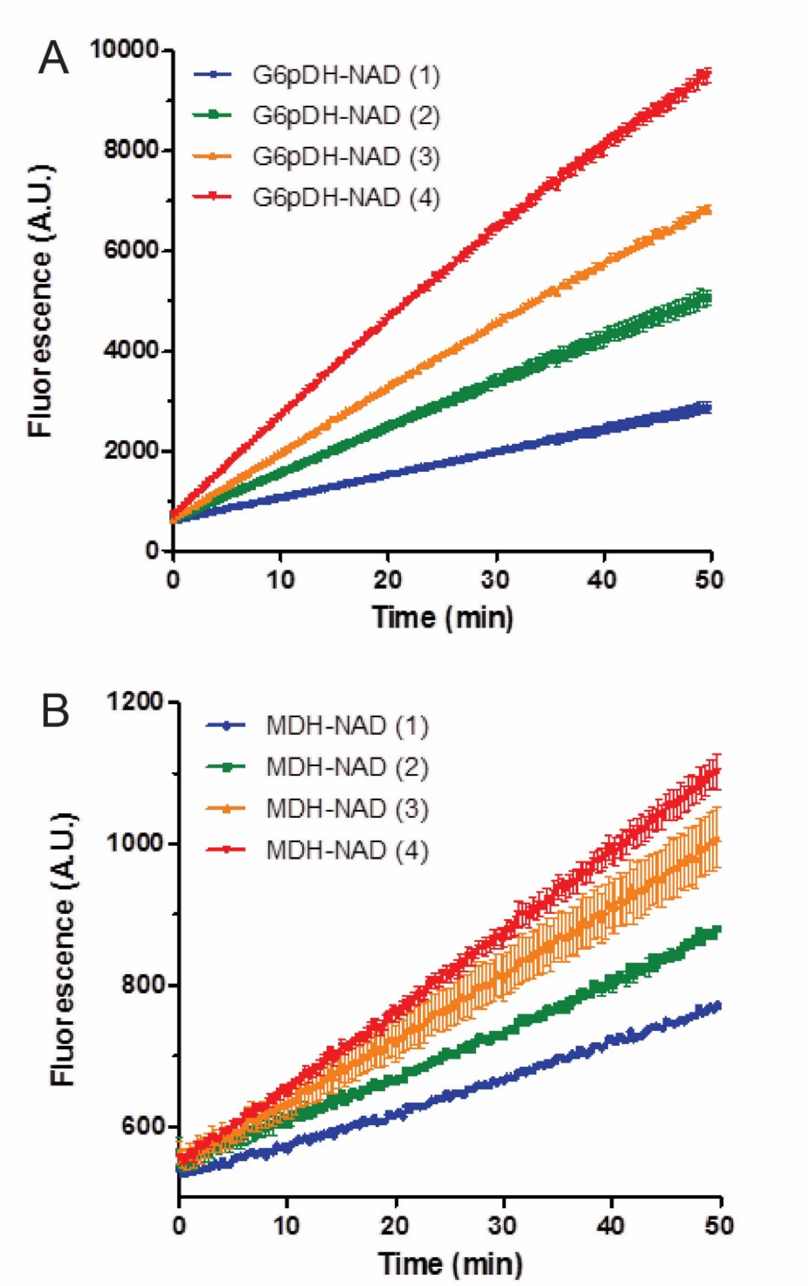

Figure S47. Raw fluorescence traces from reactions catalyzed by G6pDH (A) or MDH (B) with 1-4 NAD$^+$ arms on the 4×4 DNA tile. Assay conditions: 100 nM enzyme-DNA assemblies, 1 mM G6p for the G6pDH assay or 1 mM malic acid for the MDH assay, and 500 µM PMS/resazurin in 1×TBS buffer (pH 7.5). The normalized activity of each complex is determined by fitting a straight line to these traces and is shown in main text Figure 3C.

5. Assembly and purification of the G6pDH-NAD$^+_2$-MDH$_2$ complex based on the DX DNA tile.

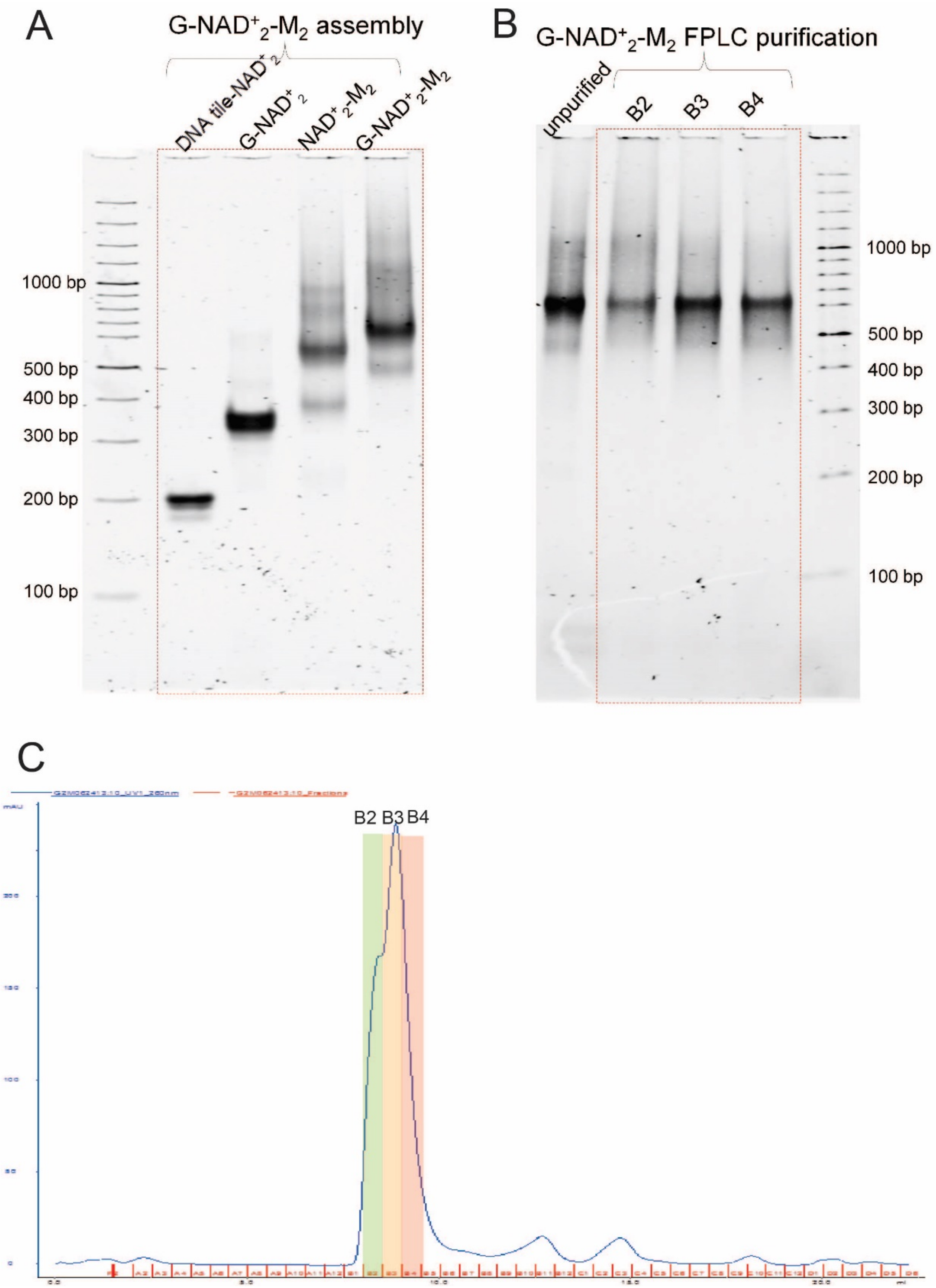

Figure S48. (**A**) Native PAGE characterization of the assembly of G-NAD$^+_2$-M$_2$ structures on the DX DNA tile (shown in Figure S5 and Figure 3D in the main text). Lanes from left to right: DNA tile with two NAD$^+$ arms (DNA tile-NAD$^+_2$), DNA tile with G6pDH and two NAD$^+$ arms (G-NAD$^+_2$), DNA tile with two NAD$^+$ arms and two MDH (NAD$^+_2$-M), and fully assembled G6pDH-NAD$^+_2$-MDH$_2$ structures (G-NAD$^+_2$-M$_2$). (**B**) Native PAGE characterization of the fractions collected from size-exclusion FPLC of the fully assembled G-NAD$^+_2$-M$_2$ structures. Fraction B2 contains aggregates; fractions B3 and B4 were used in subsequent activity assays. (**C**) Chromatogram from the size-exclusion FPLC purification of fully assembled G-NAD$^+_2$-M$_2$ structures, removing excess protein and DNA strands. Three fractions (B2-B4) were collected for the native PAGE characterization shown in (B).

6. Assembly and purification of the G6pDH-NAD$^+_4$-MDH$_4$ complex based on the 4×4 DNA tile.

In this design, the assembly of multiple (1-4) copies of MDH on the 4×4 DNA tile was characterized using PAGE before constructing the complete **G6pDH-NAD$^+_4$-MDH$_4$** structure.

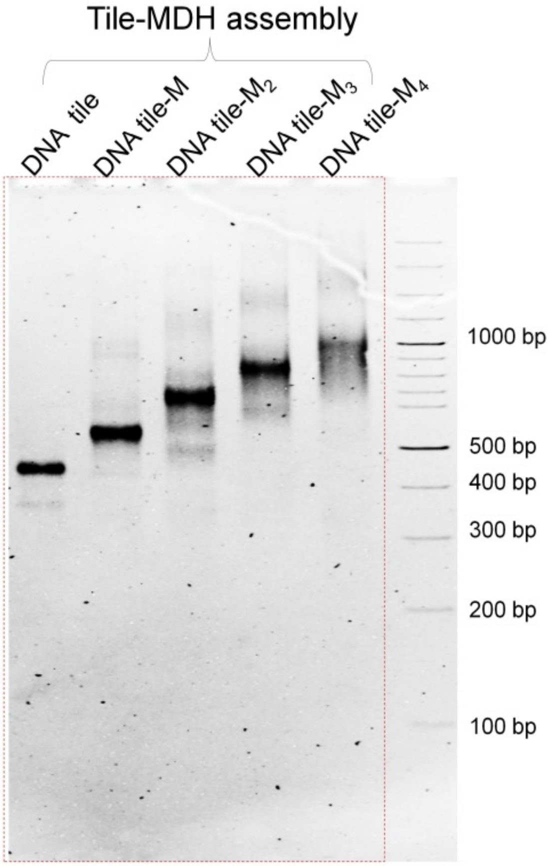

Figure S49. **Native PAGE characterization of the assembly of 1-4 copies of MDH on the 4×4 DNA tile.** Two capture probes for MDH extend from each of the four arms of the 4×4 DNA tile (see Figure S7). To precisely control the number of MDH assembled on each 4×4 DNA tile, the capture probes for MDH are removed from the appropriate scaffold strands during thermal annealing. Lanes, from left to right: 4×4 DNA tile with 0, 1, 2, 3, and 4 copies of MDH.

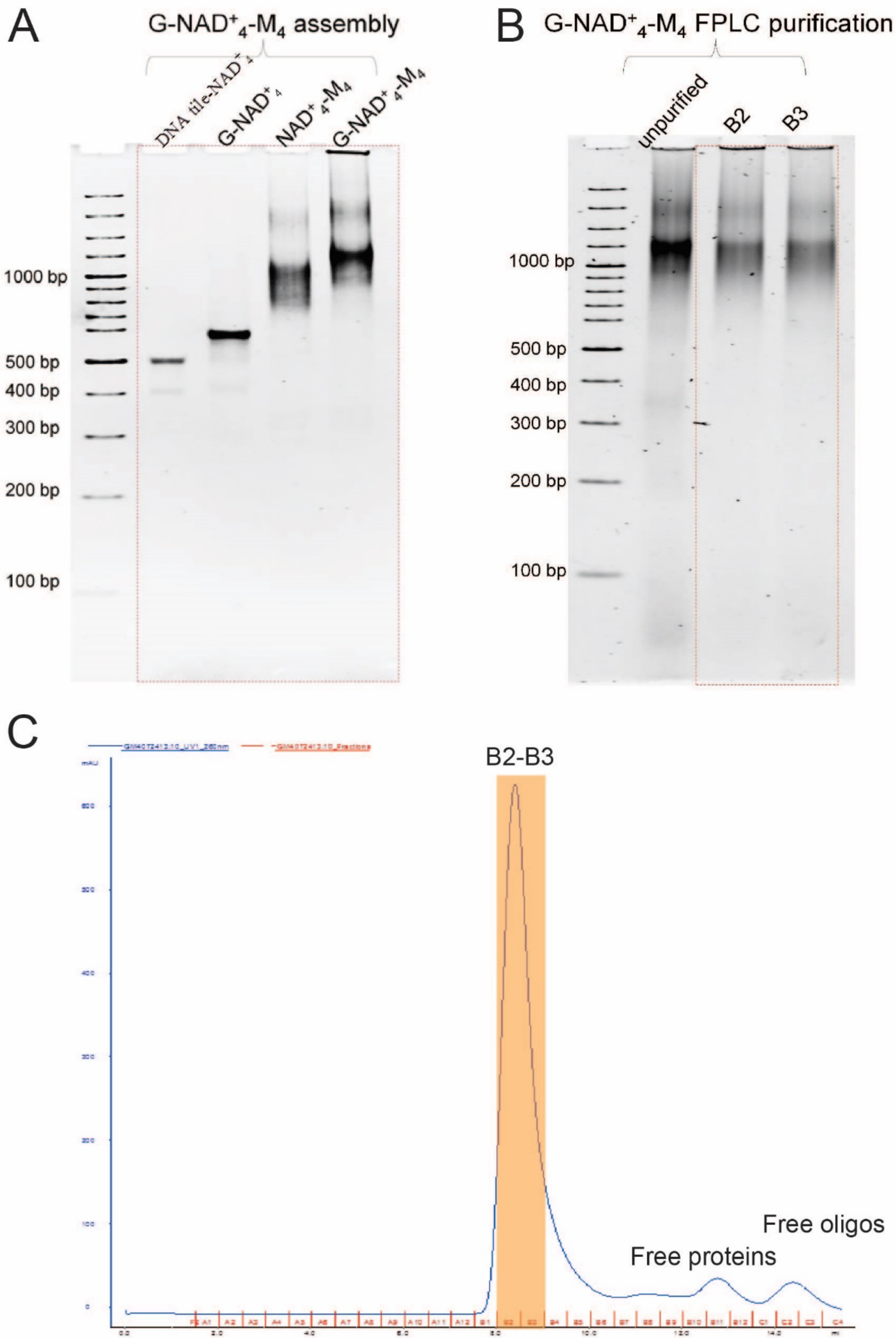A
G-NAD$^+$$_4$-M$_4$ assembly
DNA tile-NAD$^+$$_4$
G-NAD$^+$$_4$
NAD$^+$$_4$-M$_4$
G-NAD$^+$$_4$-M$_4$
1000 bp
500 bp
400 bp
300 bp
200 bp
100 bp
B
G-NAD$^+$$_4$-M$_4$ FPLC purification
unpurified
B2
B3
1000 bp
500 bp
400 bp
300 bp
200 bp
100 bp
C
GM4072412:10_UV1_260nm
GM4072412:10_Fractions
mAU
600
500
400
300
200
100
0
B2-B3
Free proteins
Free oligos
F2 A1 A2 A3 A4 A5 A6 A7 A8 A9 A10 A11 A12 B1 B2 B3 B4 B5 B6 B7 B8 B9 B10 B11 B12 C1 C2 C3 C4
0.0
2.0
4.0
6.0
8.0
10.0
12.0
14.0
ml

Figure S50. **Native PAGE characterization of the assembly of G6pDH-NAD$_4$-MDH$_4$ structures and FPLC purification.** (**A**) Native PAGE characterization of the assembly of G-NAD$_4$-M$_4$ structures on the 4×4 DNA tile (shown in Figure S7 and Figure 3D in the main text). Lanes from left to right: 4×4 DNA tile with four NAD$^+$ arms (DNA tile-NAD$^+_4$), G6pDH-NAD$^+_4$ (G-NAD$^+_4$), NAD$^+_4$-MDH$_4$ (NAD$^+_4$-M$_4$), and fully assembled G6pDH-NAD$^+_4$-MDH$_4$ (G-NAD$^+_4$-M$_4$). (**B**) Native PAGE characterization of the fractions collected from size-exclusion FPLC of fully assembled G-NAD$^+_4$-M$_4$. Fractions B2 and B3 contained few large aggregates and free proteins, and were combined for use in subsequent activity assays. (**C**) Chromatogram from size-exclusion FPLC purification of fully assembled G-NAD$_4$-M$_4$, removing excess proteins and DNA strands.

7. Raw data for comparison of the activity of assemblies with different G6pDH/MDH ratios.

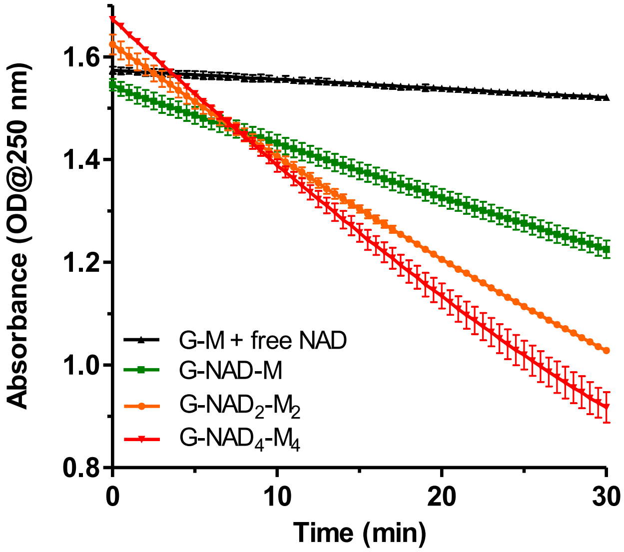

Figure S51. Raw absorbance time traces of reactions catalyzed by each construct. As the number of MDH and NAD$^+$ arms increases from 1 to 2 to 4 per G6pDH, the overall activity of the complex increases. The relative activity of each complex, calculated from the slopes of these absorbance time traces, is shown in Figure 3D in the main text. Assay conditions: 100 nM swinging arm assemblies, 1 mM G6p and OAA in 100 mM HEPES (pH 8).

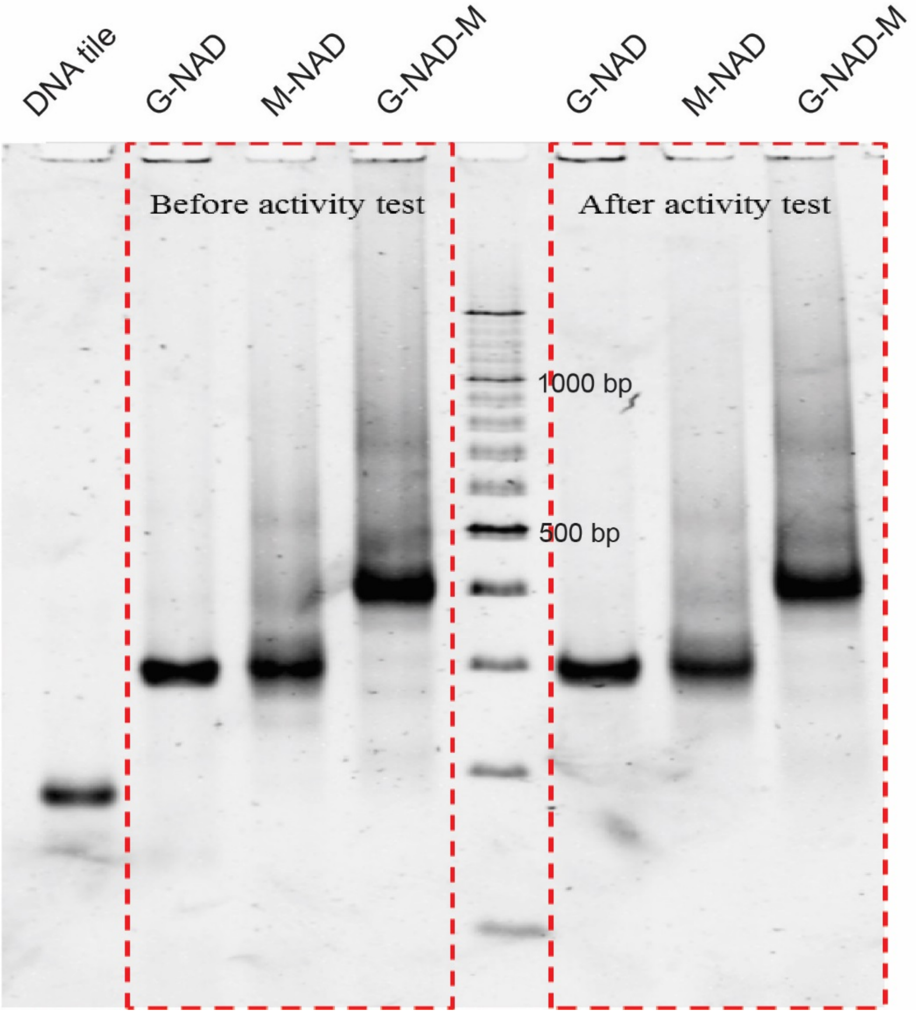

Figure S57.

Figure S52. Native PAGE (3%) characterization of the stability of swinging-arm structures before and after the catalytic reaction. Left: the structures of G-NAD, M-NAD and G-NAD-M before running the reaction. Right: the structures of G-NAD, M-NAD and G-NAD-M after running the reaction. Reaction conditions: 1 mM G6pDH and OAA were incubated with 100 nM enzyme structures for one hour in the pH 7.5 HEPES buffer.

8. Regulation of enzyme complex activity by conversion of the ssDNA arm to dsDNA.

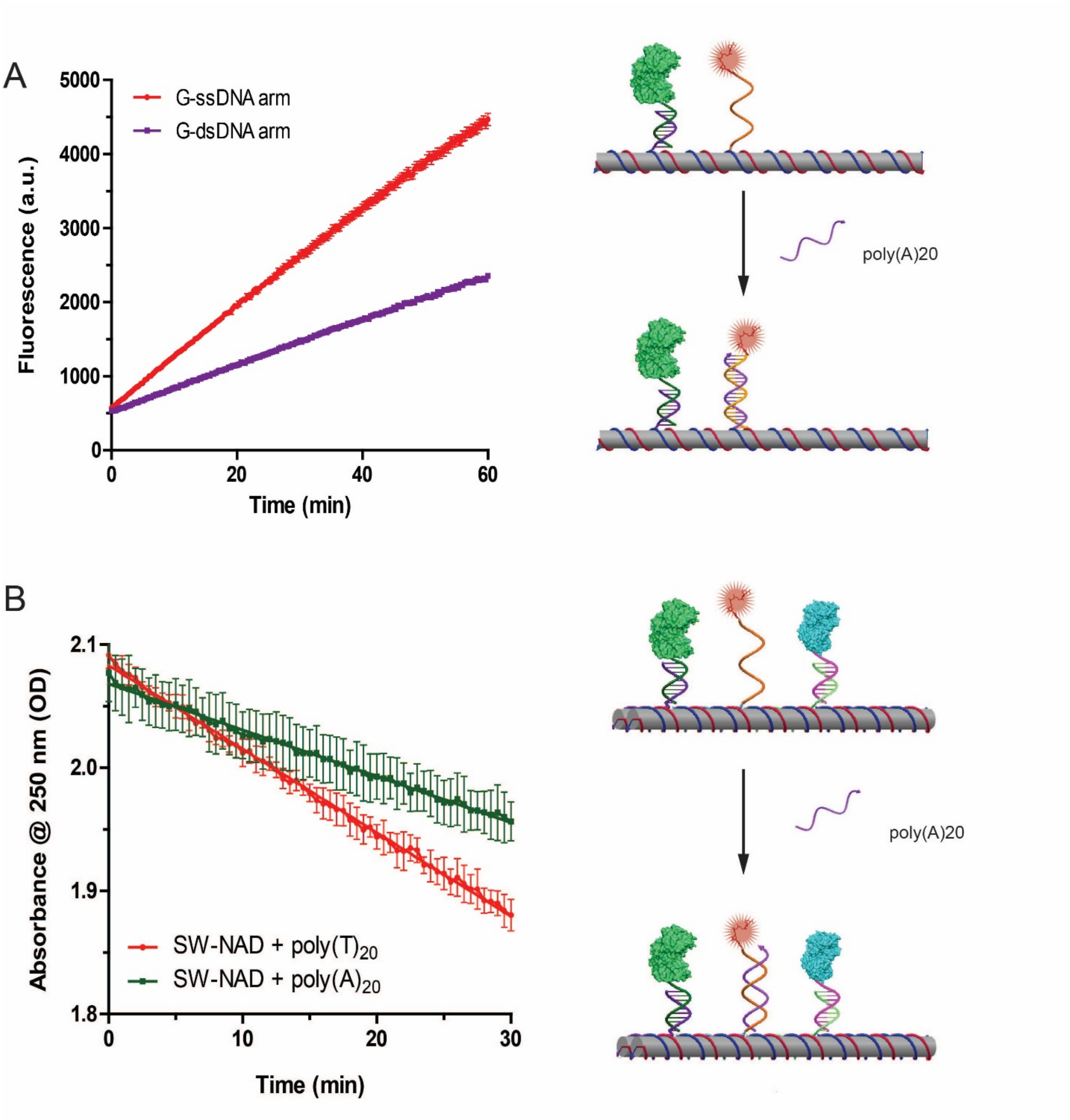

Figure S53. Regulation of enzyme complex activity by conversion of the ssDNA arm to dsDNA. (**A**) Regulating the activity of the G6pDH-NAD$^+$ semi-swinging arm structure by adding a poly(A)$_{20}$ strand to hybridize with the NAD$^+$-poly(T)$_{20}$ arm. The formation of a double-stranded arm results in a ~50% drop in activities, likely by slowing down the diffusion of NAD$^+$ and decreasing the flexibility of the arm (and hence its freedom to explore the space near the enzyme). (**B**) Regulating the activity of the G6pDH-NAD$^+$-MDH swinging arm structures by adding a poly(A)$_{20}$ strand to hybridize with the NAD$^+$-poly(T)$_{20}$ arm. For control reactions in (A) and (B), an equal concentration of poly(T)$_{20}$ (which is unable to hybridize with the swinging arm) is added to the sample. Assay conditions: a 10-fold excess of poly(A)$_{20}$ is added into solution with 100 nM swinging arm complex and incubated for 30 min at room temperature (to allow hybridization to reach equilibrium) before the activity assay. The activity assay conditions are described in Section 7.

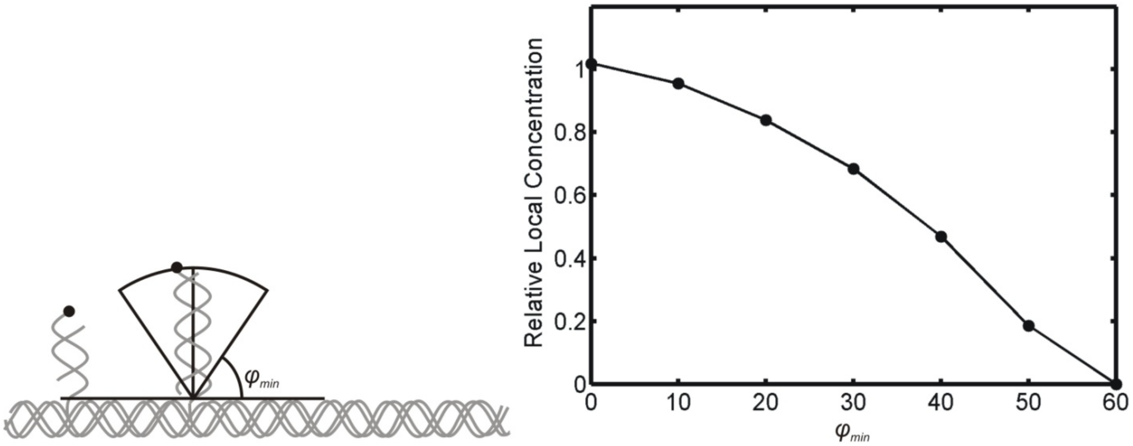

Figure S54. Predicted decrease in local effective concentration with increasing orientational rigidity of a dsDNA arm. When a poly(T)$_{20}$ swinging arm is hybridized to a poly(A)$_{20}$ complement, it forms a fully double-stranded arm that is not separated from the DNA tile by a flexible ssDNA linker, and its rotational diffusion is expected to become more hindered. The dsDNA arm is therefore modeled as a rigid rod (contour length << persistence length) confined to a spherical section defined by a minimum angle φ_{min} above the plane of the DNA tile and the local NAD^+ concentration calculated according to the Monte Carlo procedure described on p. S51. While a completely unhindered dsDNA arm ($\varphi_{min} = 0$) is predicted yield nearly the same local concentration of NAD^+ as the ssDNA arm in the vicinity of the enzyme (Relative Local Concentration ≈ 1), the experimentally determined 30%-50% drop in enzymatic activity (figs. S53 and S55) could be explained by confinement of the dsDNA arm to an angle of ≥ 30-40° above the plane of the tile.

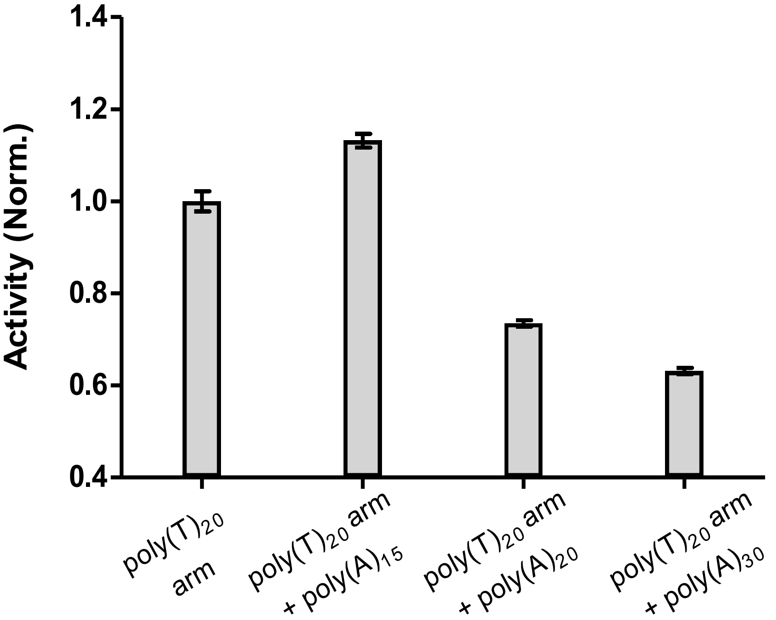

Figure S55. The dependence of swinging arm complex activity on the length of added complementary strands. The activity of the swinging arm decreases as the length of the complements increases, suggesting that the increased rigidity of the double-stranded DNA reduces activity. However, the partially double-stranded arm consisting of $poly(T)_{20}$ and $poly(A)_{15}$ is slightly more active (15%) than the single-stranded $poly(T)_{20}$, suggesting that a partially double-stranded DNA may more effectively present the NAD to the enzyme. The observed the effect of double-stranded DNA rigidity on inhibiting the efficient interaction between the enzyme and the cofactor, is consistent with a previous study that the inhibition and activation of an enzyme-inhibitor complex were regulated by switching the linker between an enzyme and an inhibitor from a single-stranded DNA to a double-stranded DNA.[18] Reaction conditions: 100 nM G6pDH-NAD semi-swinging arm structure was incubated with 1 µM poly(A) complementary strands, and assayed with 500 µM resazurin and PMS in pH 7.5 HEPES buffer.

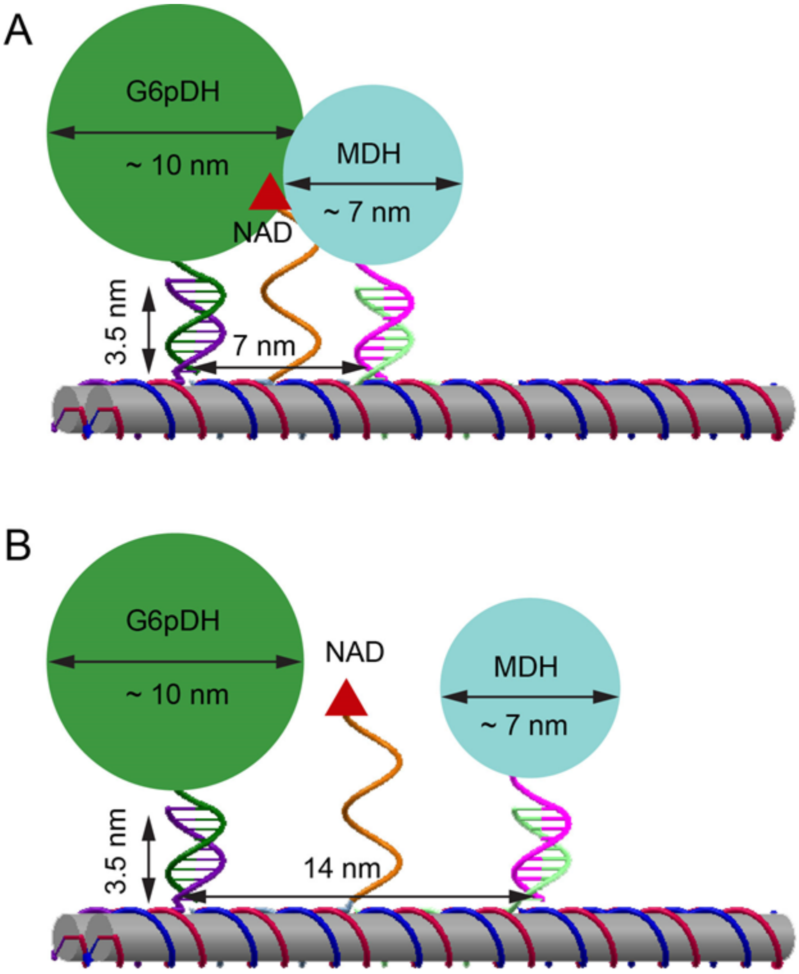

Figure S56. Steric model of G6pDH-NAD-MDH swinging arm structures. Enzymes are anchored to the DNA structures through the hybridization of a short double-stranded DNA (10 bp, ~ 3.5 nm). G6pDH (~ 100 kD) is ~ 10 nm in diameter and MDH (~70 kD) is ~ 7 nm in diameter, according to crystal structures from PDB. (A) At a 7-nm inter-enzyme distance, the two proteins are expected to be in contact (crowded). (B) At a 14-nm inter-enzyme distance, the two proteins are not as crowded, and are thus expected to co-assemble with higher efficiency.

Section 10. AFM images of the fully assembled G6PDH-NAD$^+$-MDH swinging arm complex.

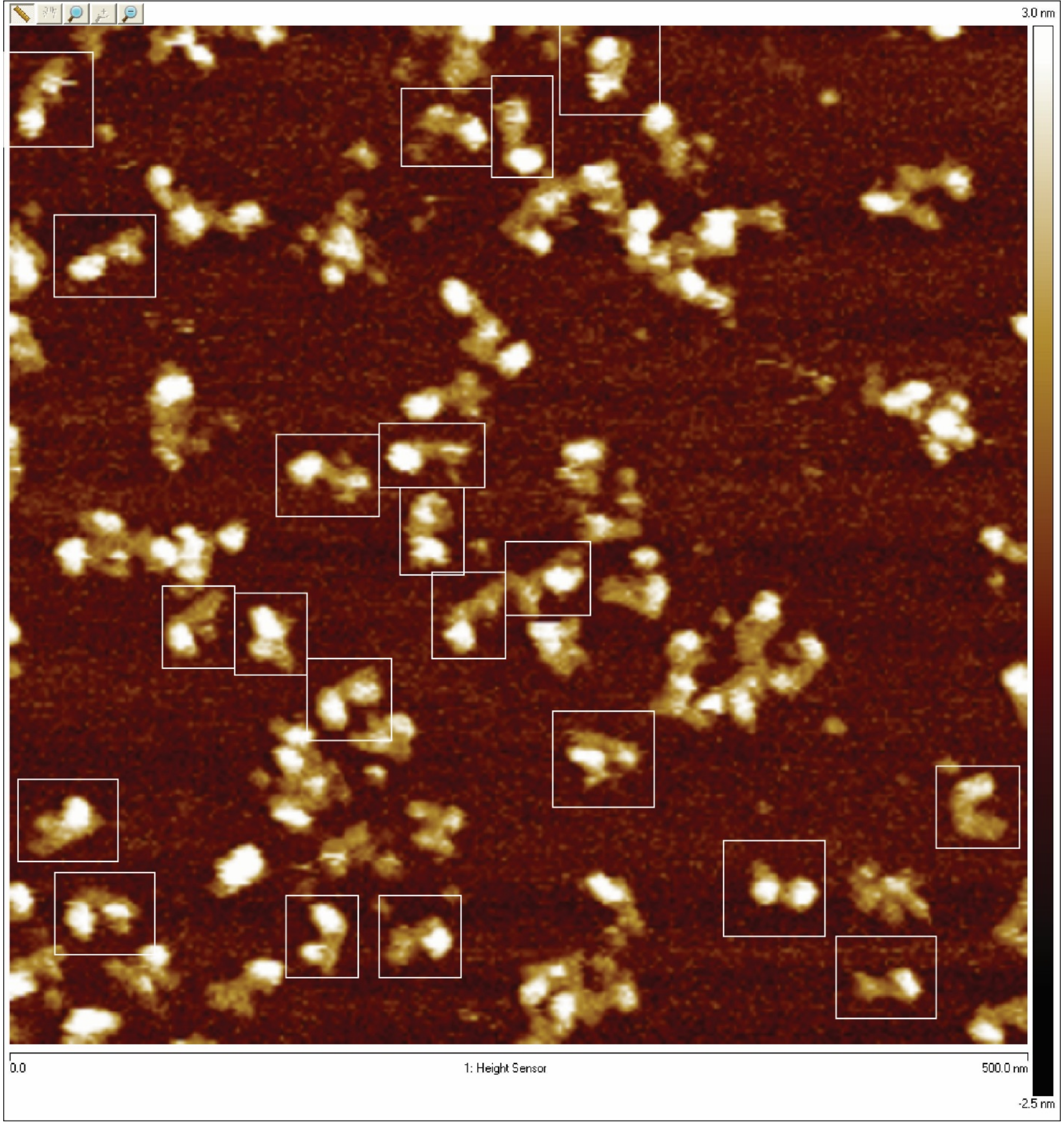

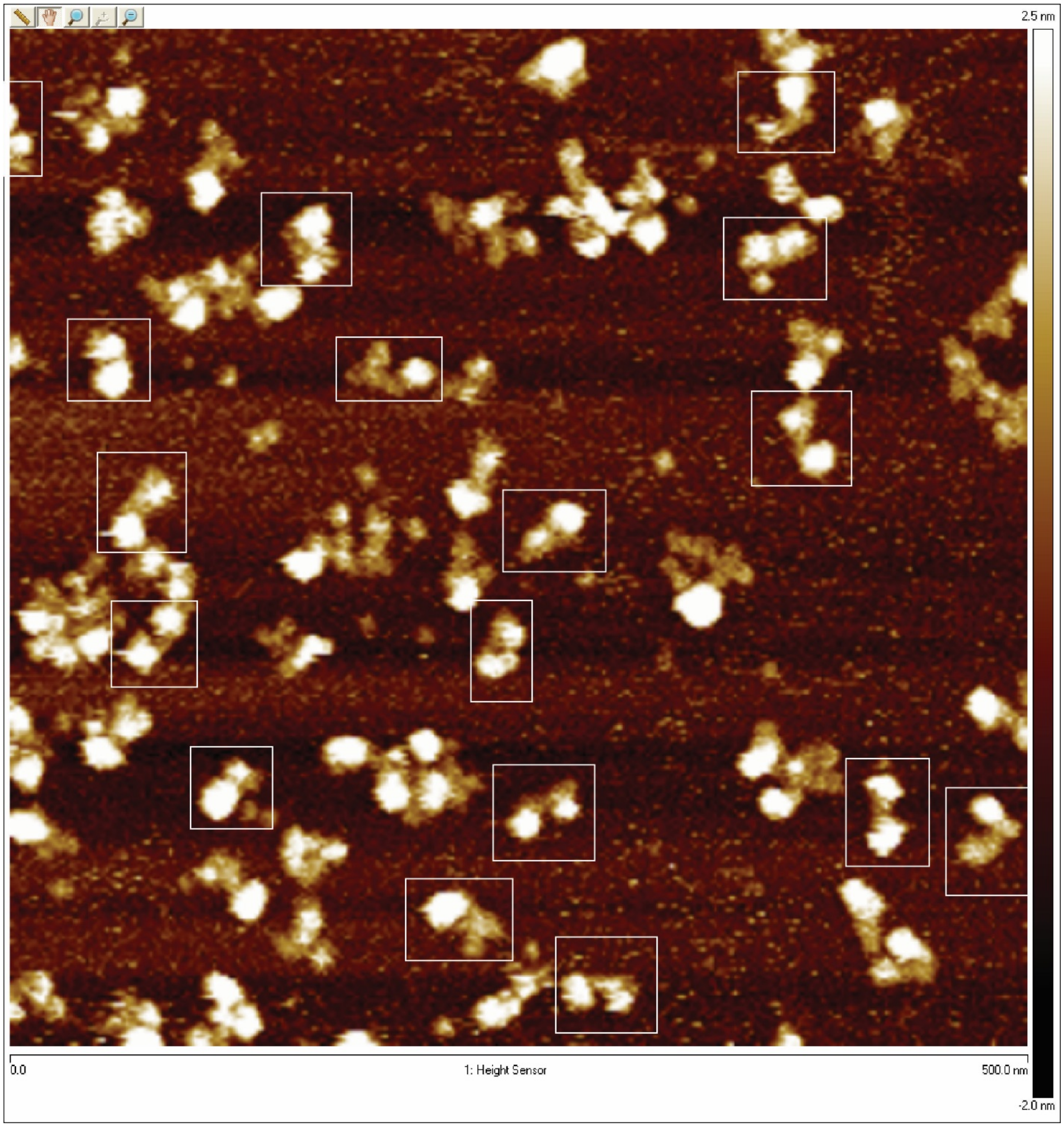

Figure S57. Zoom out AFM images of the fully assembled G6pDH-NAD$^+$-MDH swinging arm complex (Figure S3). The AFM images were obtained using a FastScan AFM (Bruker) under aqueous buffer, in Peak Force mode. The thin white boxes highlight correctly assembled, well-separated structures with both of the proteins clearly distinguished (since MDH is larger than G6pDH, one protein appears brighter than the other in the AFM image of most complexes). The DX tile appears as a rod ~30-40 nm long with one protein at each end. The swinging arm (single-stranded poly(T)$_{20}$ labeled with NAD$^+$ at the 5' end) is not resolved. Some aggregates were also observed. Damage of sample may happen during the AFM imaging process, such as destroyed sample fragments due to strong tip force, overlapped sample deposit and sample aggregation on the mica surface. Thereby, AFM imaging cannot reflect the real yield of structure assembly.

AFM imaging protocol: 2 μL samples were deposited onto a freshly cleaved mica surface (Ted Pella, Inc.) and left to adsorb for 2 minutes. 80 μL of 1 x TAE-Mg^{2+} buffer was added to the sample and 2 μL 100 mM Ni^{2+} was added to enhance DNA adsorption on mica. Extra 40 μL of 1 x TAE-Mg^{2+} buffer was deposited to liquid cell. The samples were scanned using SCANASYST-FLUID $^{+}$ probe (Bruker, Inc.) in “Scanasyst in fluid” mode using a FastScan AFM (Dimension FastScan, Bruker Corporation).

References

1. P. Rowland, A. K. Basak, S. Gover, H. R. Levy, M. J. Adams, The three–dimensional structure of glucose 6–phosphate dehydrogenase from Leuconostoc mesenteroides refined at 2.0 Å resolution. *Structure* **2**, 1073 (1994).
2. A. D. M. Chapman, A. Cortés, T. R. Dafforn, A. R. Clarke, R. L. Brady, Structural basis of substrate specificity in malate dehydrogenases: crystal structure of a ternary complex of porcine cytoplasmic malate dehydrogenase, α-Ketomalonate and TetrahydoNAD. *Journal of Molecular Biology* **285**, 703 (1999).
3. J. Fu, M. Liu, Y. Liu, N. W. Woodbury, H. Yan, Interenzyme substrate diffusion for an enzyme cascade organized on spatially addressable DNA nanostructures. *Journal of the American Chemical Society* **134**, 5516 (2012).
4. M. Liu *et al.*, A DNA tweezer-actuated enzyme nanoreactor. *Nat Commun* **4**, 2127 (2013).
5. C. E. Aitken, R. A. Marshall, J. D. Puglisi, An Oxygen Scavenging System for Improvement of Dye Stability in Single-Molecule Fluorescence Experiments. *Biophysical journal* **94**, 1826 (2008).
6. A. Johnson-Buck, J. Nangreave, S. Jiang, H. Yan, N. G. Walter, Multifactorial Modulation of Binding and Dissociation Kinetics on Two-Dimensional DNA Nanostructures. *Nano Letters* **13**, 2754 (2013/06/12, 2013).
7. M. Blanco, N. G. Walter, in *Methods in Enzymology,* N. G. Walter, Ed. (Academic Press, 2010), vol. 472, pp. 153-178.
8. S. Swillens, Interpretation of binding curves obtained with high receptor concentrations: practical aid for computer analysis. *Molecular Pharmacology* **47**, 1197 (1995).
9. P. J. Munson, D. Rodbard, An Exact Correction to the “Cheng-Prusoff” Correction. *Journal of Receptors and Signal Transduction* **8**, 533 (1988).
10. C. Yung-Chi, W. H. Prusoff, Relationship between the inhibition constant (K_I) and the concentration of inhibitor which causes 50 per cent inhibition (I_{50}) of an enzymatic reaction. *Biochemical Pharmacology* **22**, 3099 (1973).
11. N. Metropolis, A. W. Rosenbluth, M. N. Rosenbluth, A. H. Teller, E. Teller, Equation of State Calculations by Fast Computing Machines. *The Journal of Chemical Physics* **21**, 1087 (1953).
12. S. P. Meisburger *et al.*, Polyelectrolyte properties of single stranded DNA measured using SAXS and single molecule FRET: Beyond the wormlike chain model. *Biopolymers*, (2013).
13. H. Chen *et al.*, Ionic strength-dependent persistence lengths of single-stranded RNA and DNA. *Proceedings of the National Academy of Sciences* **109**, 799 (January 17, 2012, 2012).
14. L. P. Candeias *et al.*, The catalysed NADH reduction of resazurin to resorufin. *Journal of the Chemical Society, Perkin Transactions 2*, 2333 (1998).
15. J. V. Rund, K. G. Claus, Ligand effects on the rate of metal-ion-catalyzed decarboxylation of dimethyloxalacetic acid. *Journal of the American Chemical Society* **89**, 2256 (1967).

16. O. Lockridge, V. Massey, P. A. Sullivan, Mechanism of Action of the Flavoenzyme Lactate Oxidase. *Journal of Biological Chemistry* **247**, 8097 (1972).
17. K. J. Reszka, B. A. Wagner, C. P. Burns, B. E. Britigan, Effects of peroxidase substrates on the Amplex red/peroxidase assay: Antioxidant properties of anthracyclines. *Analytical Biochemistry* **342**, 327 (2005).
18. A. Saghatelian, K. M. Guckian, D. A. Thayer, M. R. Ghadiri, DNA Detection and Signal Amplification via an Engineered Allosteric Enzyme. *Journal of the American Chemical Society* **125**, 344 (2003).